

SURFACE MODIFICATION OF CASE HARDENABLE AISI 8620 STEEL USING TIG ARCING PROCESS

Ph.D. THESIS

by

RAVINDRA KUMAR



**DEPARTMENT OF METALLURGICAL AND MATERIALS ENGINEERING
INDIAN INSTITUTE OF TECHNOLOGY ROORKEE
ROORKEE-247 667, INDIA
JULY, 2017**

SURFACE MODIFICATION OF CASE HARDENABLE AISI 8620 STEEL USING TIG ARCING PROCESS

A THESIS

*Submitted in partial fulfilment of the
requirements for the award of the degree*

of

DOCTOR OF PHILOSOPHY

in

METALLURGICAL AND MATERIALS ENGINEERING

by

RAVINDRA KUMAR



**DEPARTMENT OF METALLURGICAL AND MATERIALS ENGINEERING
INDIAN INSTITUTE OF TECHNOLOGY ROORKEE
ROORKEE-247 667, INDIA
JULY, 2017**



INDIAN INSTITUTE OF TECHNOLOGY ROORKEE ROORKEE

CANDIDATE'S DECLARATION

I hereby certify that the work which is being presented in the thesis entitled “**SURFACE MODIFICATION OF CASE HARDENABLE AISI 8620 STEEL USING TIG ARCING PROCESS**” in partial fulfilment of the requirements for the award of Degree of Doctor of Philosophy and submitted in the Department of Metallurgical and Materials Engineering of the Indian Institute of Technology Roorkee, Roorkee is an authentic record of my own work carried out during a period from January, 2011 to July, 2017 under the supervision of Dr. P.K. Ghosh, Emeritus Professor, Department of Metallurgical and Materials Engineering, Indian Institute of Technology Roorkee, Roorkee.

The matter presented in the thesis has not been submitted by me for the award of any other degree of this or any other Institute.

(RAVINDRA KUMAR)

This is to certify that the above statement made by the candidate is correct to the best of my knowledge.

(P.K.Ghosh)
Supervisor

The Ph.D. Viva-Voce Examination of **Mr. Ravindra Kumar**, Research Scholar, has been held on **6th April 2018**.

Chairman, SRC

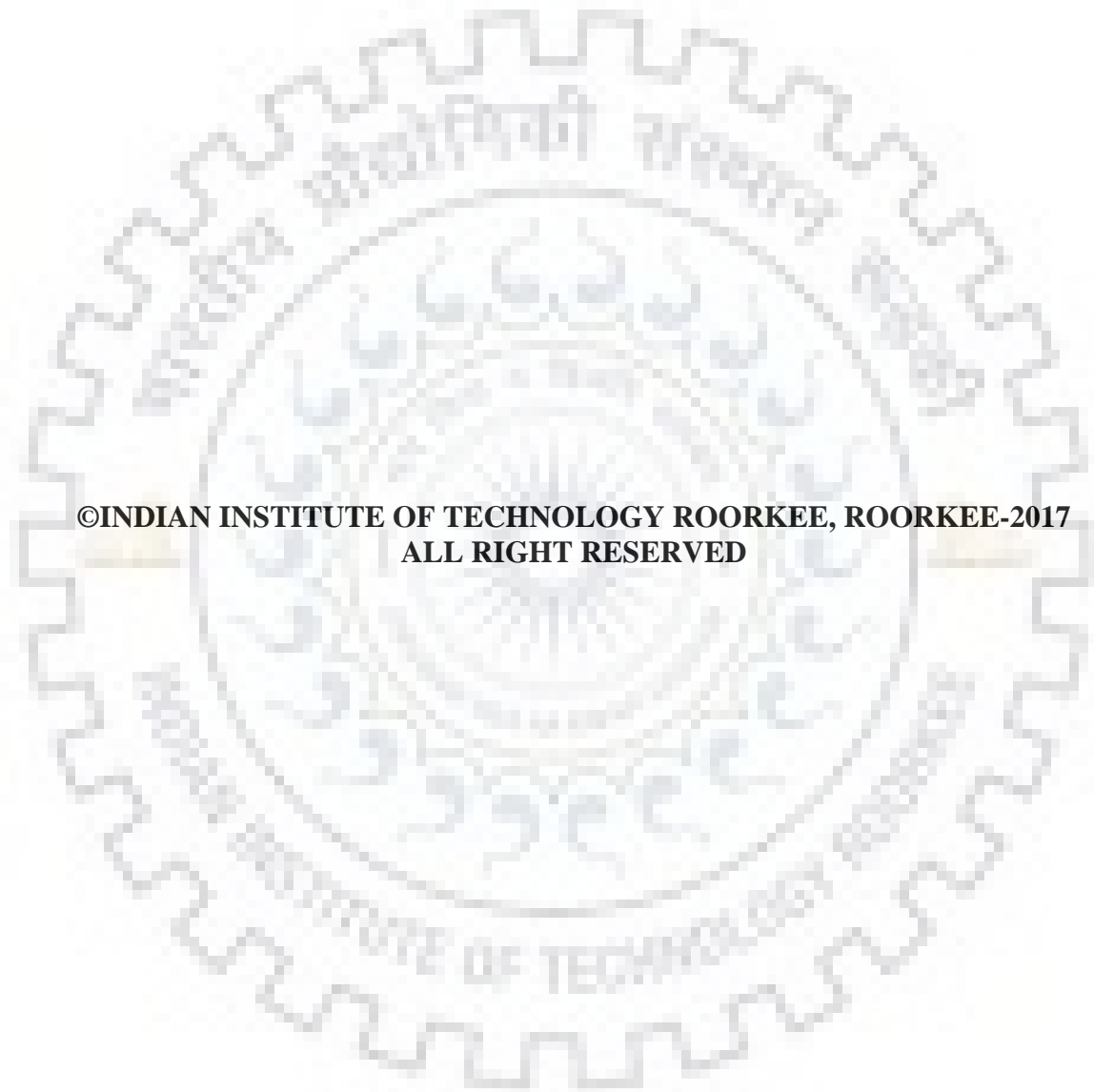
External Examiner

This is to certify that the student has made all the corrections in the thesis.

P.K. Ghosh (Supervisor)

Head of the Department

Dated: _____



**©INDIAN INSTITUTE OF TECHNOLOGY ROORKEE, ROORKEE-2017
ALL RIGHT RESERVED**

ABSTRACT

Surface modification of steel surface is conventionally done by thermal treatment using various thermo-chemicals heating such as flame heating, induction heating, laser heating and electron beam heating. The rapid advancement in the field of surface engineering, conventional techniques for surface treatment like carburizing and flame hardening have been often replaced by the techniques using advanced high energy heat sources such as plasma, laser, and electron beam. These techniques use high energy concentrated beam on the workpiece which generates steep thermal gradients leading to rapid solidification and quick phase transformation in the matrix of limited depth at the substrate surface. The electron beam process is widely used for surface modification of steel, but a shallow case depth (≤ 1.5 mm), need of vacuum and a limited use for relatively small components make this process non-versatile for application at site. The laser beam process also has certain disadvantages like high cost of investment in the equipment, poor laser light absorption in the metal, radiation problem and highly skilled operator requirement. However, a relatively high energy concentration to produce a steep thermal gradient for effective surface treatment by modification of the matrix morphology of metal can also be effectively obtained by using a versatile process of arcing.

In view of the above, the use of readily available autogenous tungsten inert gas arcing (TIGA) process, which requires relatively lower cost of investment, is considered as a new alternative for surface modification of materials. The easy availability at the site, requirement of less skilled worker, support to high heat absorption in metal and less environmental pollution makes TIGA process most favourable for surface modification of steel. In this process, the heat energy is provided by an electric arc maintained between a tungsten electrode and workpiece where a high quality partial melting is ensured under a good inert gas shielding of the molten pool. The TIGA process operates in two modes. The first mode is known as Continuous current TIGA (C-TIGA) and second mode is known as pulse current TIGA (P-TIGA). In C-TIGA process continuous arc is acted over the surface of base plate to modify its surface, whereas in the P-TIGA process the pulsing of arc at a regular frequency creates interruption in arc energy which modifies the substrate surface through controlled melting and solidification.

As compared to C-TIGA process the P-TIGA process may be proved as a better process for surface modification because of using pulse current instead of continuous current facilitates that gives more precise control of energy input along with its distribution in the system. The P-TIGA has number of advantages that primarily include intended operation at relatively low

heating, less distortion of the substrate and more precise control of isotherm and thermal cycle leading to controlled necessary phase transformation and its morphology.

The variable parameters investigated in C-TIGA process were arc current (I), arc voltage (V) and travel speed (S) whereas in P-TIGA process, the operating parameters are frequency (f), pulse time (t_p), base time (t_b), base current (I_b), and pulse current (I_p). The control of pulse arc is comparatively more complicated than control of continuous arc due to the involvement of a large number of simultaneously interactive pulse parameters in it. So, the difficulty in use of pulse parameters can be effectively resolved by using a summarized influence of pulse parameters proposed earlier and defined by a dimensionless hypothetical factor $\phi = \frac{I_b}{I_p} \times f \times t_b$ where, $t_b = \left[\frac{1}{f} \right] - t_p$ derived on the basis of the energy balance concept of the system.

The primary objective of this research is to understand the comparative effect of C-TIGA and P-TIGA processes for industrial application in order to produce more effectively modified surface layer with enhanced hardness and wear properties in AISI 8620 steel substrate. The AISI 8620 steel is the chromium, molybdenum, nickel based case hardenable low alloy steel that gives superior case/core properties after surface modification.

The complete work has been carried out in seven parts. 1. The single pass C-TIGA parameters are optimized with the help of studies on influence of C-TIGA parameters on the thermal behaviour of surfacing including the modified FZ and HAZ geometry. The single pass P-TIGA is applied on the AISI 8620 steel surface at the optimized parameters of the C-TIGA to compare both the processes in terms of modified geometry (Depth of penetration, Width of FZ, HAZ width and FZ area). 2. An analytical thermal model is used to predict the isothermal curve, thermal cycle and cooling rate of the single pass C-TIGA and P-TIGA processes. In order to check the effectiveness of the thermal model, the estimated results (Isothermal curve, thermal cycle and cooling rate) are validated with the experimental results. The effect of single pass C-TIGA and P-TIGA processes on the cooling rate are also compared with respect to each other in this part. 3. Microstructural studies are carried out at optimized parameters of both single pass C-TIGA and P-TIGA processes and correlated to their characteristics cooling rate of the matrix. 4. Effect of both the C-TIGA and P-TIGA parameters on the matrix hardness is studied and compared. 5. Multi-pass TIG arcing process is performed over a larger substrate surface to analyse the effectiveness of both the C-TIGA and P-TIGA processes for industrial application at optimized parameters. 6. The residual stress analysis is performed on the modified zone of both the single and multi-pass TIGA processed surface. 7. The wear analysis

is done to see the effect of C-TIGA and P-TIGA processing on the substrate surface. The characteristics of surface modification obtained by C-TIGA have been compared to those of the surface modified by P-TIGA process in order to find out the utility of the processes used.

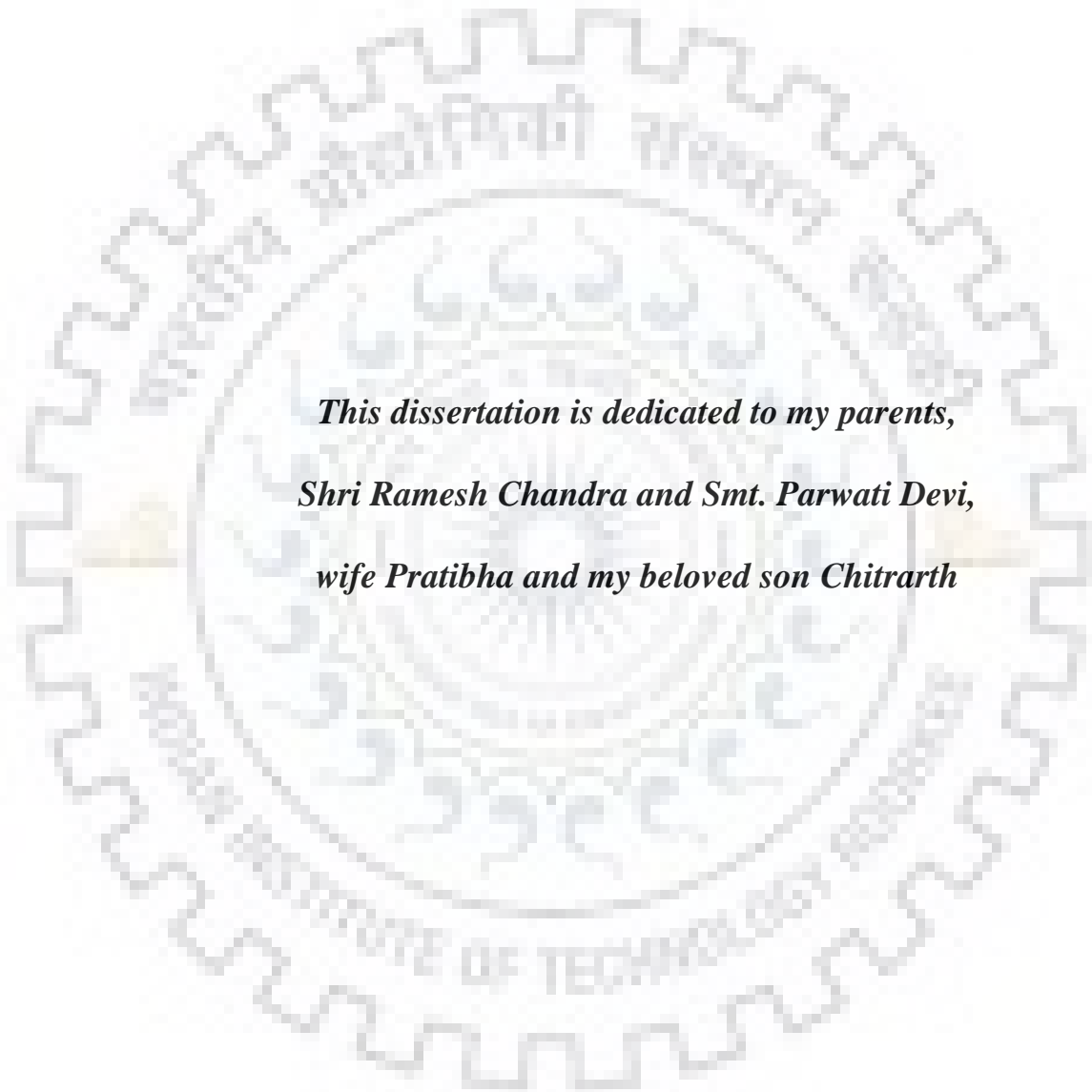
After finding the potentials of P-TIGA process to produce improved surface modification, effort has been made to develop knowledge of critical application of pulse parameters of autogenous P-TIGA process for optimum surface hardening of case hardenable AISI 8620 steel substrates, better than that produced by using C-TIGA process. The knowledge includes appropriate control of pulse parameters primarily in order to manage the thermal cycle and isotherm of the heating zone giving rise to desired surface modification of the substrate primarily defined by its geometry and microstructure. In this regard the relatively low heating characteristics of the pulse current arcing process is also kept under consideration for comparatively lower distortion and residual stresses of the substrate than that observed in case of the conventional non pulse arcing process. The innovation in surfacing is established after carrying out comparative studies using the C-TIGA for the same purpose.

The use of P-TIGA process gives 110 % increment in hardness of the modified zone with respect to that of base metal with adequate depth of modified zone of 2.5 ± 1 mm. The use of P-TIGA process increases 30% hardness in the modified zone as compared to that observed in case of C - TIGA process at the similar heat input, arc current and travel speed. The use of P-TIGA process gives 25 ± 5 % more depth of the modified zone as compared to that happens in case of using C-TIGA process. However nominal difference in compressive stresses of about 5 ± 5 % is established by both of the processes in the modified zone. The increment in hardness with sufficient case depth makes P-TIGA process most suitable for bearing industry. The typical hardness requirement for large case hardenable bearing is 450-650 VHN with the case depth of 10 % of the cage thickness as per the ASTM standards. The use of C-TIGA and P-TIGA processes fulfils the ASTM hardness requirement for large roller bearing with sufficient case depth.

The use of P-TIGA process at appropriate ϕ enhances considerably the depth of hardened layer and hardness with moderate compressive residual stresses in the modified matrix which are observed in case of using the C-TIGA process. The variation in ϕ and pulse frequency has been found to significantly affect the thermal behaviour of fusion and consequently the width and penetration of the modified region along with its microstructure, hardness and wear characteristics. It is found that P-TIGA is relatively more advantageous over the C-TIGA process, as it leads to relatively higher depth of penetration, higher hardness, improved wear resistance, and a better control over surface characteristics. The uses of surface modification

processes develop residual stress over the surface. It is experimentally found that use of TIGA process produces compressive stresses over the surface in case of both the single and multi-pass surface treatment. The development of compressive stresses over the substrate surface is beneficial to improve surface properties like resistance to wear and fatigue.





*This dissertation is dedicated to my parents,
Shri Ramesh Chandra and Smt. Parwati Devi,
wife Pratibha and my beloved son Chitrarth*



ACKNOWLEDGEMENTS

The author has great privilege and gratification to express his heartiest thanks and deep sense of gratitude to his respected supervisors Dr. P.K. Ghosh, Professor, Department of Metallurgical and Materials Engineering, IIT Roorkee, for their valuable guidance and indefatigable efforts throughout the tenure of this work. They have been an inspiring and driving force where targets appeared to be difficult during the course of work. Their timely help, constructive criticism, positive attitude, painstaking efforts, humanistic and warm personal approaches made the author capable to compile the thesis in its present form. Prof. Ghosh helped me grow not only as a researcher, but also as an individual. I am very proud to be one of his students.

Profound sense of appreciation acknowledged to all the members of Student Research Committee (SRC), Dr. Ujjwal Prakash, Chairman SRC, Dr. S. K. Nath, Chairman SRC, Dr. D. K. Dwivedi, External Member and Dr. Vivek Pancholi, Internal Member for their precious assessment throughout.

Deep sense of admiration acknowledged to the Head, Institute Instrumentation Centre (IIC), for their co-operation in extending the necessary facilities and supports during the course of characterization work. A special thanks to all the IIC faculty and technical staff members Mr. Shiv Kumar for giving their full assistance for all characterization facilities.

The author would like to express his sincere thanks to the technical and administrative staff of Department of Metallurgical and Materials Engineering, Mr. H.K. Ahuja, Mr. Ram Singh, Mr. S.M. Giri, Mr. Narendra Kumar, Mr. Shakti Gupta, Mr. Rajender Sharma, Mr. Sanjay, Mr. R. K. Sharma, Mr. Vikram and Mr. Preetam who have helped in all possible ways during the Ph.D work.

The author wishes to thank his friends and colleagues for their moral support and help to keep things in perspective. Thanks are due to Dr. Kaushal Kumar, Mr. Ram Kishore, Mr. Arun Kumar, Mr. Sudhir Kumar, Mr. Nilesh Kumar, Mr. Ankur, Mr. Rahul Rathore, Mr. Deepak Sharma and all the fellows who helped me directly or indirectly during the entire period of this work.

The author expresses his deepest esteem to his father, Shri Ramesh Chandra and mother, Smt. Parwati Devi and for keeping their blessing over me. The special gratitude is due to my wife Pratibha for her continued patience, tolerance, understanding, inspiration,

encouraging and wholehearted moral support during the entire period of this work. The author is highly appreciative to his brother Mr. Sudhir Prashant for their encouragement throughout.

Roorkee

Dated:

RAVINDRA KUMAR



TABLES OF CONTENTS

	Page No.
CANDIDATE'S DECLARATION	
ABSTRACT	i
ACKNOWLEDGEMENT	vii
TABLE OF CONTENTS	ix
LIST OF TABLES	xv
LIST OF FIGURES	xvii
ABBREVIATIONS	xxiii
ACKNOWLEDGEMENTS	vii
TABLES OF CONTENTS	ix
LIST OF TABLES	xv
LIST OF FIGURES	xvii
CHAPTER 1	1
INTRODUCTION	1
CHAPTER 2	7
LITERATURE REVIEW	7
2.1 Surface Modification Processes	7
2.1.1 Thermochemical Processes.....	8
2.1.1.1 Carburizing	8
2.1.1.2 Nitriding and Carbonitriding	8
2.1.1.3 Boronizing	9
2.1.2 Mechanical Surface treatment	9
2.1.2.1 Shot peening	9
2.1.2.2 Deep rolling.....	10
2.1.2.3 Shot blasting.....	10
2.1.3 Thermal Surface Hardening processes.....	11
2.1.3.1 Flame and Induction hardening	11
2.1.3.2 Electron beam hardening.....	11
2.1.3.3 Laser surface hardening	12
2.1.3.4 TIG arcing process	13
2.2 Tungsten Inert Gas Process.....	14
2.2.1 Power source characteristics	15

2.2.2	Process variables and their control	15
2.2.3	Arcing current polarities.....	17
2.3	Pulsed current tungsten inert gas arcing process (P-TIGA)	18
2.3.1	Process variables and their control	20
2.3.2	Ratio of peak current to base current (I_p/ I_b)	23
2.3.3	Heat transferred to fusion zone	23
2.3.4	Estimation of weld pool temperature	24
2.3.5	Concept of summarized influence of pulse parameters	24
2.4	AISI 8620 Steel	25
2.4.1	Properties of AISI 8620 Steel.....	25
2.4.2	Heat Treatment and Surface modification of AISI 8620 steel.....	26
2.4.3	Hardenability	26
2.4.4	Applications of 8620 Steel.....	27
2.5	Factors affecting the properties of AISI 8620 steel.....	28
2.5.1	Effect of alloying elements.....	28
2.5.2	Effect of cooling rate	30
2.5.3	Effect of microstructure	32
2.5.4	Factor affecting the hardenability of AISI 8620 steel.....	34
2.6	Modelling of modified zone	35
2.7	Effect of Residual Stresses on steel.....	39
2.8	Effect of surface modification processes on residual stresses.....	41
2.9	Effect of surface modification processes on wear resistance	42
CHAPTER 3		45
PROPERTIES REQUIREMENT FOR A BEARING COMPONENT		45
3.1	The characteristics of bearing materials	45
3.2	The microstructure requirement for a bearing material.....	46
3.3	Standard specifications for bearing component	47
CHAPTER 4		49
FORMULATION OF PROBLEMS		49
4.1	Formulation of Problem	49
4.2	Objectives.....	50
CHAPTER 5		53
EXPERIMENTATION		53
5.1	Base Material.....	53

5.2 Thermomechanical Simulator	54
5.3 TIGA Power Source.....	55
5.4 Fixture and Torch Manipulator	55
5.4.1 Welding fixture.....	56
5.4.2 Torch manipulator.....	56
5.5 Instrumentation and Recording	56
5.5.1 Measurement of temperature of fusion pool.....	56
5.5.2 Estimation of heat input (Ω)	58
5.5.3 Estimation of average fusion pool temperature.....	58
5.5.4 Estimation of fusion isotherm.....	60
5.6 Single pass TIGA Experimentation	60
5.6.1 Single pass C-TIGA process.....	60
5.6.2 Single pass P-TIGA process.....	61
5.6.3 Measurement of thermal behavior of modified zones (FZ and HAZ)	64
5.6.4 Estimation of single pass modified zone (FZ and HAZ) characteristics	66
5.6.4.1 Geometrical aspects of modified zone	66
5.6.4.2 Metallographic studies	66
5.6.5 Hardness measurement	68
5.7 Multi pass TIGA process	69
5.7.1 Preparation of multipass treatment	69
5.7.2 Metallographic studies on multi-pass modified zone.....	71
5.7.3 Hardness Studies.....	71
5.8 Wear Characteristics of modified zone	71
5.7.2. Estimation of wear rate.....	73
5.9 Residual Stress and distortion studies	73
CHAPTER 6	75
RESULTS AND DISCUSSION	75
6.1 Characteristics of AISI 8620 steel.....	75
6.1.1 Microstructure	75
6.1.2 Effect of heating on microstructure.....	76
6.1.3 Thermo-mechanical simulation of AISI 8620 steel	78
6.1.3.1 Cooling rate estimation.....	78
6.1.3.2 Dilation Curve.....	78
6.1.3.3 CCT Diagram.....	80

6.1.3.4 Effect of cooling rate on microstructure of AISI 8620 steel	80
6.1.3.5 Effect of cooling rate on matrix hardness of AISI 8620 steel	81
6.1.4 Summary	82
6.2 Geometric studies.....	83
6.2.1 Single pass C-TIGA process.....	83
6.2.1.1 Thermal aspects of fusion pool during C-TIGA process	83
6.2.1.2 Geometric studies during single pass C-TIGA process	84
6.2.2 Single pass P-TIGA process.....	88
6.2.2.1 Thermal aspects of weld pool during P-TIGA process.....	89
6.2.2.2 Geometrical aspects of the modified zone using P-TIGA process.....	91
6.2.3 Summary	104
6.3 Analytical estimation of thermal characteristics	105
6.3.1 Analytical estimation of thermal characteristics for single pass C-TIGA process	105
6.3.1.2 Thermal Cycle	114
6.3.2 Analytical estimation of thermal characteristics for single pass P-TIGA process	117
6.3.1.1 Isothermal curve in x-y and y-z plane.....	117
6.3.2.2 Thermal Cycle	127
6.3.3 Summary	131
6.4 Microstructural Studies	132
6.4.1 Microstructural studies for single pass C-TIGA process.....	132
6.4.1.1 Effect of arcing parameters on microstructure of fusion zone.....	132
6.4.1.2 Effect of arcing parameters on microstructure of HAZ.....	135
6.4.2 Microstructural studies for single pass P-TIGA process.....	137
6.4.2.1 Effect of pulse arcing parameters on microstructure of fusion zone	137
6.4.2.2 Effect of pulse arcing parameters on microstructure of HAZ	143
6.4.3 Summary	148
6.5 Hardness Study.....	148
6.5.1 Effect of single pass C-TIGA process on Hardness of FZ and HAZ	148
6.5.2 Effect of single pass P-TIGA process on hardness of FZ and HAZ.....	151
6.5.3 Summary	159
6.6 Multipass TIGA process.....	159
6.6.1 Multi-pass C-TIGA process	159
6.6.1.1 Microstructural studies	159
6.6.1.2 Hardness Study.....	161
6.6.2 Multi-pass P-TIGA process.....	162

6.6.2.1 Microstructural studies	163
6.6.2.2 Hardness Study	168
6.6.3 Summary	169
6.7 Residual stress analysis	169
6.7.1 Effect of single and multi-pass C-TIGA process on residual stresses	170
6.7.2 Effect of single and multi-pass P-TIGA process on residual stresses	172
6.7.3 Summary	174
6.8 Dry sliding wear behavior of TIGA processed AISI 8620 steel plates	175
6.8.1 Effect of C-TIGA process on dry sliding wear	175
6.8.1.1 Effect of C-TIGA process on wear behavior of modified AISI 8620 steel	175
6.8.1.2 Effect of C-TIGA process on Coefficient of friction (COF) of modified AISI 8620 steel	177
6.8.2 Effect of P-TIGA process on dry sliding wear	178
6.8.2.1 Effect of P-TIGA process on wear behavior of AISI 8620 steel.....	178
6.8.2.2 Effect of P-TIGA process on Coefficient of friction (COF).....	182
6.8.3 Wear mechanism	182
6.8.4 The SEM analysis of wear surfaces	183
6.8.5 Summary	186
CHAPTER 7	1877
CONCLUSIONS	1877
CHAPTER 8	1911
SCOPE FOR FUTURE WORK	1911



LIST OF TABLES

Table No.	Description	Page No.
Table 2.1	Minimum mechanical properties of AISI 8620 steel [Tamura et al., 1988].	26
Table 3.1	Typical requirements for bearing application of AISI 8620 steel.....	47
Table 5.1	Typical requirements for bearing application of AISI 8620 steel.....	53
Table 5.2	Parameters used in thermomechanical simulation for CCT curve.....	55
Table 5.3	Parameters used in single pass C-TIGA process.	60
Table 5.4	Pulse parameters used in surface modification of AISI 8620 steel using P-TIGA process at an I_m of 100 A.	61
Table 5.5	Pulse parameters used in surface modification of AISI 8620 steel using P-TIGA process at a I_m of 130 A.....	62
Table 5.6	Pulse parameters used in surface modification of AISI 8620 steel using P-TIGA process at a I_m of 170 A.	63
Table 5.7	Arcing parameters used in multipass treatment using C-TIGA process	70
Table 5.8	Arcing parameters used in multipass treatment using P-TIGA process.....	70
Table 6.1	Comparison of the estimated and measured peak temperatures of FZ and HAZ.	116
Table 6.2	Comparison of the estimated and measured peak temperatures of FZ and HAZ.	129



LIST OF FIGURES

Figure No.	Description	Page No.
Fig. 2.1	Constant current power source characteristic.	15
Fig. 2.2	Effect of polarity in the heat distribution between the tungsten electrode and workpiece [Messeler Jr, 1999].....	18
Fig. 2.3	Arc current characteristics in pulsed current TIGA process.	20
Fig. 2.4	Schematic diagram showing the effect of frequency on fusion track using P-TIGA process.	23
Fig. 2.5	Hardenability curve of the AISI 8620 steel [Apple and Krauss, 1973].	277
Fig. 2.6	CCT curve of AISI 8620 steel [Thompson et al., 1990].	311
Fig. 2.7	Microstructure of AISI 8620 showing (a) decarburized pearlitic surface layer with patches of ferrite and the grain-boundary cementite networks and (b) lath martensite with a minor amount of bainite [Voort and Lucas, 2009].	33
Fig. 2.8	TEM images of single pass laser surface modification of AISI 8620 steel.	333
Fig. 2.9	TEM images of multi pass laser surface modification of AISI 8620 steel.	344
Fig. 5.1	Typical requirements for bearing application of AISI 8620 steel.....	54
Fig. 5.2	Schematic diagram of fixture and work piece for surface modification by TIG arcing process.	56
Fig. 5.3	Diagram showing the calibration of strain buster and thermocouple.	57
Fig. 5.4	(a) Schematic circuit diagram of welding and recording set up along with cooling system of torch head. (b) Photograph of the experimental setup used for TIGA process.....	588
Fig. 5.5	Schematic illustration of double ellipsoidal heat source (volumetric heat source).....	59
Fig. 5.6	Schematic diagram showing (a) location of thermocouples in modified zone. (b) Depth of placement of thermocouple (D_T) and typical macrograph showing placement of thermocouple in FZ. (c) D_T and typical macrograph showing placement of thermocouple in HAZ.	65
Fig. 5.7	Temperature dependent thermo-physical properties of commercial mild steel [Tamura et al., 1988].	65
Fig. 5.8	(a) Schematic diagram showing geometrical aspects of modified zone and (b) typical macrograph of modified bead geometry.	66

Fig. 5.9	Photograph of the Leica optical microscope used for recording microstructure.....	67
Fig. 5.10	Schematic diagram showing FZ and HAZ after modification by TIGA process.....	67
Fig. 5.11	Photograph of the X-ray Diffractometer used for analysis of phases.	68
Fig. 5.12	Photograph of the hardness testing machine used for measurement of hardness.....	699
Fig. 5.13	Typical (a) Schematic diagram and (b) photograph of multi pass TIG arcing processed substrate surface.	70
Fig. 5.14	Typical appearance of transverse section (A-A), representing (I) FZ (II) Reheated FZ (III) Reheat refined FZ (IV) HAZ (V) Reheat refined HAZ of the Multipass TIGA processed surface.	71
Fig. 5.15	Schematic diagram shows the Pin on disc apparatus [Tyagi et al., 2002].	72
Fig. 5.16	Photograph of the Zeiss Scanning Electron Microscope.....	733
Fig. 5.17	(a) Schematic arrangement of strain gages placed at different directions of measuring and (b) Typical view of a three strain gage rosette at a fusion zone.	74
Fig. 6.1	Typical microstructure of AISI 8620 steel used for surface modification in (a) transverse direction and (b) longitudinal direction.....	76
Fig. 6.2	Effect of temperature on the (a) mole fraction of phase transformation (b) volume fraction of phase transformation and (c) Weight % of alloying elements in M_7C_3 carbide.	78
Fig. 6.3	Thermal cycle during thermo-mechanical simulation of AISI 8620 steel.	79
Fig. 6.4	Dilatation curves recorded at different cooling rate of AISI 8620 steel plate. The tangents along the γ -line and α -line detect the inflexion points where the dilatation curve deviates from linearity.....	80
Fig. 6.5	Estimated CCT curve for AISI 8620 steel.	79
Fig. 6.6	Effect of cooling rate on microstructure of AISI 8620 steel.....	81
Fig. 6.7	Effect of cooling rate on hardness of AISI 8620 steel at different heat input.	82
Fig. 6.8	Effect of cooling rate on hardness of AISI 8620 steel at different heat input.	83
Fig. 6.9	At a given arc voltage of $11 \pm 1V$, the effect of I and S on weld pool temperature.....	84
Fig. 6.10	Typical surface appearance of the modified zone using single pass C-TIGA process at variation in arc current from 70 to 200 A and travel speeds from 5 to 15 cm/min.	85
Fig. 6.11	Typical photographs of transverse section of the modified zone using single pass C-TIGA process at variation in arc current from 70 to 200 A and travel speeds from 5 to 15 cm/min.	86

Fig. 6.12	The effect of arc current and travel speed on (a) bead width (b) depth of penetration (c) HAZ width and (d) fusion zone area at an arc voltage of 11 ± 1 V.	88
Fig. 6.13	At a given arc voltage of 11 ± 1 V the effect of ϕ on total heat transfer to weld pool at different I_m of 170, 130 and 100A respectively.....	89
Fig. 6.14	At a given arc voltage of 11 ± 1 V, the effect of ϕ and f on weld pool temperature under different mean current of (a) 100 (b) 130 and (c) 170 A respectively.	91
Fig. 6.15	At a given I_m and arc voltage of 100 A and 11 ± 1 V respectively typical macrographs of weld bead under varied ϕ and f	93
Fig. 6.16	At a given I_m and arc voltage of 130 A and 11 ± 1 V respectively typical macrographs of weld bead under varied ϕ and f	94
Fig. 6.17	At a given I_m and arc voltage of 170 A and 11 ± 1 V respectively typical macrographs of weld bead under varied ϕ and f	95
Fig. 6.18	At a given I_m and arc voltage of 100 A and 11 ± 1 V respectively typical cross sectional macrographs of modified zone under varied ϕ and f	96
Fig. 6.19	At a given I_m and arc voltage of 130 A and 11 ± 1 V respectively typical cross sectional macrographs of modified zone under varied ϕ and f	96
Fig. 6.20	At a given I_m and arc voltage of 170 A and 11 ± 1 V respectively typical cross sectional photographs of modified zone under varied ϕ and f	97
Fig. 6.21	At a given arc voltage of 11 ± 1 V, the effect of ϕ and f on bead width under different mean current of 100, 130 and 170 A respectively.	98
Fig. 6.22	At a given arc voltage of 11 ± 1 V, the effect of ϕ and f on depth of penetration under different mean current of 100, 130 and 170 A respectively.....	101
Fig. 6.23	At a given arc voltage of 11 ± 1 V, the effect of ϕ and f on width of HAZ under different I_m of 100, 130 and 170 A respectively.	102
Fig. 6.24	At a given arc voltage of 11 ± 1 V, the effect of ϕ and f on fusion zone area under different mean current of 100, 130 and 170 A respectively.	104
Fig. 6.25	The effect of arcing current and heat input on estimated isotherms in XY plane at given arc voltage 11 ± 1 V and varied travel speed of (a) 5 cm/min (b) 7.5 cm/min (c) 10 and (d) 15 cm/min.	109
Fig. 6.26	The effect of arcing current and heat input on estimated and measured isotherms in YZ plane at given arc voltage of 11 ± 1 V and varied travel speed of (a) 5 cm/min (b) 7.5 cm/min (c) 10 and (d) 15 cm/min.	113

Fig. 6.27	Comparison of the estimated and measured weld thermal cycle at different combination of arc current and heat input of (a) 100 A; 6.6 kJ/cm (b) 130 A; 8.37 kJ/cm (c) 170A; 12.75 kJ/cm and (d) 200A, 15.24 kJ/cm	116
Fig. 6.28	Comparison of estimated and measured cooling rate at intercritical temperature range (800-5000C).....	1177
Fig. 6.29	Estimated isotherms in XY plane at given I_m of 130 A under varied ϕ from 0.04 to 0.44 and pulse frequency of (a) 2 Hz (b) 10 Hz.....	12020
Fig. 6.30	Estimated isotherms in XY plane at given I_m of 170 A under varied ϕ from 0.04 to 0.44 and pulse frequency of (a) 2 Hz (b) 10 Hz.....	1222
Fig. 6.31	Estimated and measured isotherms in YZ plane at given I_m of 130 A under varied ϕ from 0.04 to 0.44 and f of (a) 2 Hz (b) 10 Hz.....	1244
Fig. 6.32	Estimated and measured isotherms in YZ plane at given I_m of 170 A under varied ϕ from 0.04 to 0.44 and f of (a) 2 Hz (b) 10 Hz.....	1266
Fig. 6.33	Comparison of the estimated and measured weld thermal cycle at different ϕ value of (a) 0.0397 (b) 0.14 (c) 0.29 and (d) 0.44 at a given mean current, arc voltage and travel speed of 170 A, 11 ± 1 V and 10 cm/min respectively.....	1299
Fig. 6.34	Comparison of estimated and measured cooling rate at intercritical temperature range (800-5000 °C).....	13030
Fig. 6.35	Effect of ϕ on cooling rate in the intercritical temperature range with variation of ϕ from 0.04 to 0.44 and f of 2 and 10 Hz at different I_m of (a) 130 A and (b) 170 A.....	13131
Fig. 6.36	Typical microstructure of FZ at FZ at different I of (a) 100 and (b) 170 A where the V and S are kept constant at 11 ± 1 V and 10 cm/min respectively.....	1333
Fig. 6.37	Typical microstructure of fusion zone in single pass C-TIG arcing process under different arc current of (i) 70 (ii) 100 (iii) 130A (iv) 170 and (v) 200 A where the V and S are kept constant at 11 ± 1 and 10 cm/min respectively.....	1344
Fig. 6.38	XRD analysis of the modified surface at S and V of 10 cm/min and 11 ± 1 V.....	1355
Fig. 6.39	Typical microstructure at HAZ using single pass C-TIG arcing process under different arc current of (i) 70 A (ii) 100 (iii) 130A (iv) 170A and (v) 200 A where the V and S are kept constant at 11 ± 1 and 10 cm/min respectively.....	1366
Fig. 6.40	Typical microstructure of FZ showing the effect of ϕ and f at a given I_m of 170A.....	1388
Fig. 6.41	Typical microstructure of fusion zone by single pass P-TIG arcing process under varied ϕ from (i) 0.04 to (v) 0.44 0.44 at an I_m and f of 130 A and 2 Hz respectively.....	1399
Fig. 6.42	Typical microstructure of fusion zone by single pass P-TIG arcing process under different ϕ value of (i) 0.04 (ii) 0.14 (iii) 0.29 (iv) 0.35 and (v) 0.44 at an I_m and f of 130 A and 10 Hz respectively.....	14040

Fig. 6.43	Typical microstructure of fusion zone by single pass P-TIG arcing process under different ϕ value of (i) 0.04 (ii) 0.14 (iii) 0.29 (iv) 0.35 and (v) 0.44 at an I_m and f of 170 A and 2 Hz respectively.....	1411
Fig. 6.44	Typical microstructure of fusion zone by single pass P-TIG arcing process under different ϕ value of (i) 0.04 (ii) 0.14 (iii) 0.29 (iv) 0.35 and (v) 0.44 at a I_m and f of 170 A and 10 Hz respectively.....	1422
Fig. 6.45	XRD analysis of P-TIGA treated surface at I_m of (a) 130 (b) 170 A.	1433
Fig. 6.46	Typical microstructure of HAZ by single pass P-TIG arcing process under different ϕ value of (i) 0.04 (ii) 0.14 (iii) 0.29 (iv) 0.35 and (v) 0.44 at an I_m and f of 130 A and 2 Hz respectively.	1444
Fig. 6.47	Typical microstructure of HAZ by single pass P-TIG arcing process under different ϕ value of (i) 0.04 (ii) 0.14 (iii) 0.29 (iv) 0.35 and (v) 0.44 at I_m and f of 130 A and 10 Hz.	1455
Fig. 6.48	Typical microstructure of HAZ by single pass P-TIG arcing process under different ϕ value of (i) 0.04 (ii) 0.14 (iii) 0.29 (iv) 0.35 and (v) 0.44 at a I_m and f of 170 A and 2 Hz.	1466
Fig. 6.49	Typical microstructure of HAZ by single pass P-TIG arcing process under different ϕ value of (i) 0.04 (ii) 0.14 (iii) 0.29 (iv) 0.35 and (v) 0.44 at I_m and f of 170 A and 10 Hz.	1477
Fig. 6.50	The effect of arc current and travel speed on hardness of (a) FZ and (b) HAZ at an arc voltage of 11 ± 1 V.	15050
Fig. 6.51	Distribution of hardness across the region starting from the fusion zone through HAZ to base metal at different arc current of 70, 130 and 200 A.	1511
Fig. 6.52	Effect of ϕ and f on hardness of fusion zone at I_m and Ω of (a) 100A; 6.9 kJ/cm (b) 130 A; 8.97 kJ/cm and (c) 170 A; 12.75 kJ/cm.	1544
Fig. 6.53	Effect of ϕ and f on the hardness of HAZ at I_m and Ω of (a) 100A; 6.9 kJ/cm (b) 130 A; 8.97 kJ/cm and (c) 170 A; 12.75 kJ/cm.	1555
Fig. 6.54	Distribution of hardness across the region starting from the fusion zone through HAZ to base metal at different f of (a) 2 Hz and (b) 10 Hz at a given I_m of 100 A.	1566
Fig. 6.55	Distribution of hardness across the region starting from the fusion zone through HAZ to base metal at different f of (a) 2 Hz and (b) 10 Hz at a given I_m of 130 A.	1577
Fig. 6.56	Distribution of hardness across the region starting from the fusion zone through HAZ to base metal at different f of (a) 2 Hz and (b) 10 Hz at a given I_m of 170 A.	1588
Fig. 6.57	Microstructures of different modified zones of multi-pass C-TIGA processed substrate at an arc current of 170 A; (i) Reheated FZ (ii) FZ (iii) Reheat refined FZ (iv) HAZ (v) Reheat refined HAZ.	1611

Fig. 6.58	Effect of multi-pass C-TIGA process in the distribution of hardness in the modified zone at an arc current of 170 A.....	1622
Fig. 6.59	Effect of multi-pass P-TIGA process on microstructures of different modified zones designated as (i) FZ (ii) Reheated FZ (iii) Reheat refined FZ (iv) HAZ (v) Reheat refined HAZ at a varied ϕ of (a) 0.04 and (b) 0.44 with f and I_m of 2 Hz and 170 A respectively.	1655
Fig. 6.60	Effect of multi-pass P-TIGA process on microstructures of different modified zones designated as (i) FZ (ii) Reheated FZ (iii) Reheat refined FZ (iv) HAZ (v) Reheat refined HAZ at a varied ϕ of (a) 0.04 and (b) 0.44 with f and I_m of 10 Hz and 170 A respectively.	1677
Fig. 6.61	Distribution of hardness at a varied ϕ of (a) 0.04 and (b) 0.44 at a I_m and f of 170 A and 10 Hz respectively.....	1699
Fig. 6.62	The effect of C-TIGA process on (a) longitudinal and (b) transverse residual stress at the modified zone using single and multi-pass mode.	1722
Fig. 6.63	The effect of P-TIGA process on (a) longitudinal and (b) transverse residual stress at the modified zone using single and multi-pass mode.	1744
Fig. 6.64	Effect of C-TIGA process on volume loss of the modified surface.....	1766
Fig. 6.65	Effect of C-TIGA process at different arcing current on wear rate of the modified surface.	1766
Fig. 6.66	Effect of arc current on the COF of the modified C-TIGA processes substrate surface.	1777
Fig. 6.67	Effect of ϕ on volume loss by Single pass and Multi pass P-TIGA process at the f of (a) 2 and (b) 10 Hz where the I_m is 130 A.	1799
Fig. 6.68	Effect of ϕ on volume loss by Single pass and Multi pass P-TIGA process at the f of (a) 2 and (b) 10 Hz where the I_m is 170 A.	18080
Fig. 6.69	Effect of ϕ on Specific wear rate during Single pass and Multi pass P-TIGA process at f of (a) 2 and (b) 10 Hz with $I_m=130$ A.	1811
Fig. 6.70	Effect of P-TIGA parameters on the COF of the modified P-TIGA processes substrate surface.	1822
Fig. 6.71	The SEM Micrograph of as received base metal.	1844
Fig. 6.72	The SEM micrographs of worn surfaces of the substrate modified by the single and multi-pass C-TIGA processes operated at the arc current of (a) 130 A and (b) 170 A.....	1855
Fig. 6.73	The SEM micrographs of worn surfaces of the substrate modified by single and multi-pass P-TIGA operated at the ϕ of (a) 0.04 and (b) 0.44 while I_m and f are 170 A and 2 Hz respectively.	1866

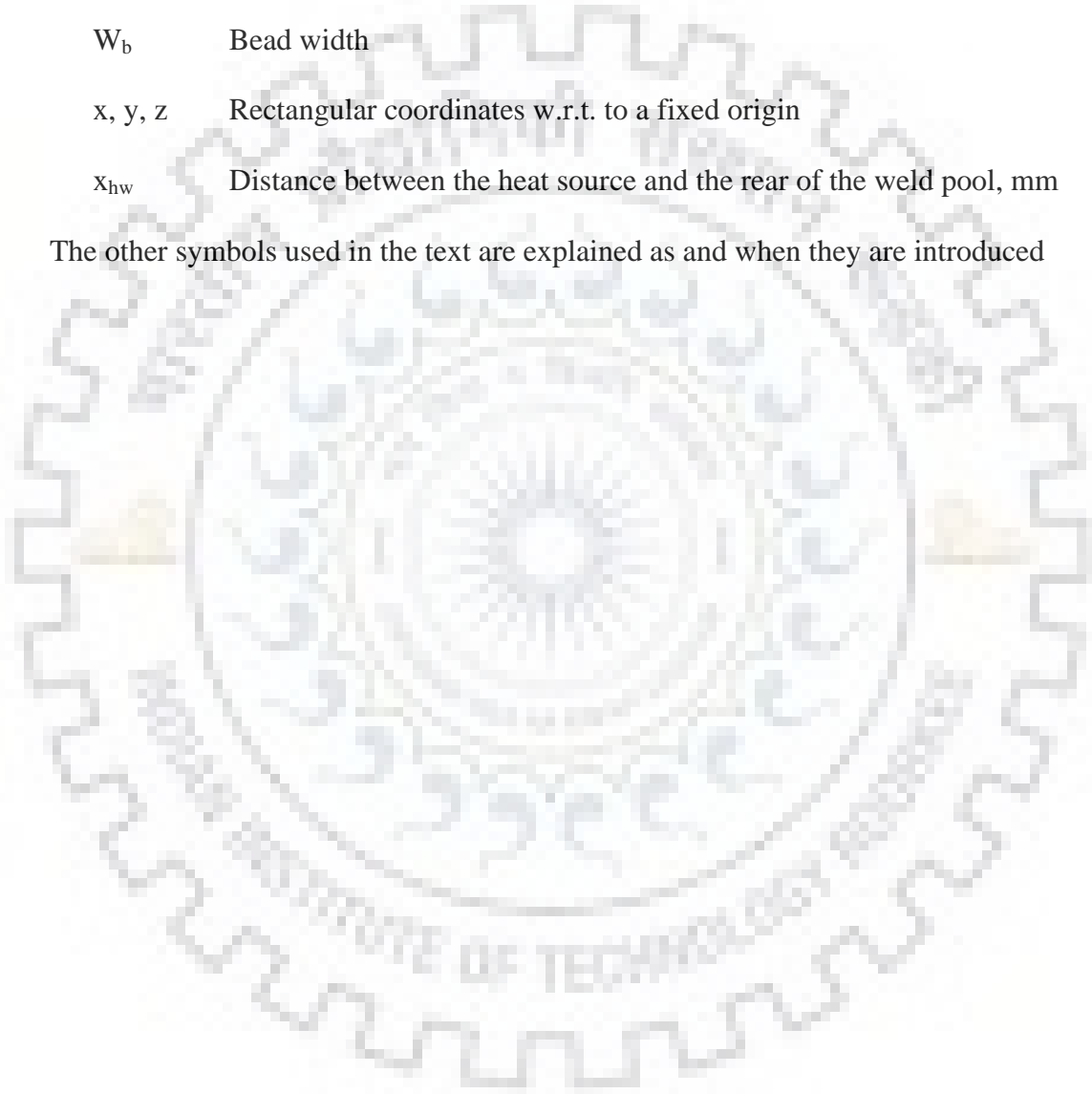
NOMENCLATURE

Symbol	Description
ξ	Distance of the point along the x-axis with respect to the origin of moving heat source, m
Ω	Heat input per unit length of weld, kJ cm^{-1}
ν	Kinematic viscosity of ionized shielding gas ($\text{Kg m}^{-1}\text{s}^{-1}$) (0.0044)
ρ	Mass density of the base metal, kg m^{-3}
σ	Stefan-boltzman constant, $\text{w m}^{-2} \text{K}^{-4}$
σ_{tr}	Transverse shrinkage stress, MPa
ϕ	Summarized influence of pulse parameters factor
λ_a	Thermal conductivity of argon, $\text{J m}^{-1} \text{s}^{-1} \text{K}^{-1}$
η_a	Arc efficiency (%)
$1/2\lambda$	Thermal diffusivity of the base plate
a	Thermal diffusivity of the base plate (m^2/sec) (Al-Mg = 8.418×10^{-5} and Mild Steel = 1.172×10^{-5})
a_1	Width of weld metal deposited in current pass, mm
A_A	Surface area of the arc (m^2)
AC	Alternating current
a_h, b_h, c_h	Ellipsoidal heat source parameters (m)
c_{hf}, c_{hb}	Double ellipsoidal heat source parameters (m)
A_F	Area of fusion, mm^2
b	Plate width, mm
c	Specific heat of the base plate ($\text{J g}^{-1}\text{K}^{-1}$), (Al-Mg = 1.03 and AISI 8620 = 0.475)
CR	Cooling rate, $^{\circ}\text{K}/\text{sec}$
d	Thickness of the base plate, m

D.C	Direct current
E	Young's modulus of base material, $210 \times 10^3 \text{MPa}$
E_w	Electrode extension, m
f	Pulse frequency, Hz
I	Arc current, A
I_b	Base current, A
I_{eff}	Effective current, A
I_m	Mean current, A
I_p	Peak current, A
k	Thermal conductivity of the base metal ($\text{J m}^{-1} \text{s}^{-1} \text{K}^{-1}$) (AISI 8620 steel= 46)
k_p	<i>Pulse duty cycle</i>
L	Arc length, mm and Latent heat of fusion, J kg^{-1}
l_p	Length of fusion pool, mm
Q_{arc}	Arc heat generated by the energy input, J s^{-1}
Q_{AW}	Arc heat transferred to the fusion pool, J s^{-1}
Q_T	Total heat transferred per unit time, J s^{-1}
r_f, r_b	Proportion coefficients in front and behind the heat source
R	Distance (mm) of the point with respect to the central axis
S	Travel speed, cm/min
T_a	<i>Ambient temperature, K</i>
t_b	<i>Base current duration, s</i>
T_d	Temperature at any point in the weld due to arc heating, K
T_m	Melting temperature, K
T_{wp}	Estimated temperature of weld pool, K
T_{ST}	Surface temperature of torch nozzle due to combined heating by convection heat transfer from argon gas plasma and radiation from the arc, K

T_{WP}	Average weld pool temperature, K
T_o	Initial temperature of the base plate, K
t_p	Peak current duration, s
t_{pul}	<i>Pulse cycle time, s</i>
V	Arc voltage, V
VHN	Vickers hardness number
W_b	Bead width
x, y, z	Rectangular coordinates w.r.t. to a fixed origin
x_{hw}	Distance between the heat source and the rear of the weld pool, mm

The other symbols used in the text are explained as and when they are introduced





CHAPTER 1

INTRODUCTION

Surface modification of a material introduces an integrated variation in property to it in terms of various physical, chemical, electronic and mechanical properties. Surface treatment is critically applied to the engineering of modern machine components and tools, where the underlying material is chosen for its bulk properties (elastic modulus, toughness, hot hardness, etc.) while the surface is treated to introduce some new characteristics to it such as improved resistance to corrosion, fracture toughness, wear, resistance to high contact stresses, compressive stresses, fatigue resistance etc. as desired. The majority of components that typically require surface modification include gears, bearings, valves, cams, hand tools, rolls, shafts, machine tools and bearing races.

In order to introduce hard protective coatings to the surface of a material, producers of various components are turning to different surface treatments. General practices for modification of surface primarily follow either changing the surface chemical composition (Thermochemical processes) or modification of surface morphology. The processes of changing chemical composition include carburising, nitriding, carbo-nitriding, cyaniding, PVD, CVD, ion implantation and sputtering processes. Whereas, the localized surface modification by change in matrix morphology is commonly done by thermal treatment using flame heating, induction heating, laser heating and electron beam heating.

The thermochemical processes have been successfully used for surface treatment of steels, but it after gives shallow case depth which is impractical and uneconomical especially when the large parts are to be treated locally. Such as the surface of large gears, large rolls and dies, large bearing cages as well as the ends of valve stems and push rods and wearing surfaces of cams and levers etc.

The local thermal surface hardening by morphological modification is used successfully for surface modification of steel, but it also has certain disadvantages. The use of flame hardening may cause zonal variation of heating and it is difficult to control the temperature of heating of the component. The explosive fuel gases have to be used cautiously in the flame hardening process. The induction hardening process is more complex with relatively poor adaptability where, it is difficult to guarantee the quality of some complex shaped workpiece. The induction heater is quite complex and the cost of inputs is relatively high due to poor

interchangeability and adaptability of the induction coil (inductor). Often it cannot be used for complex shape of the workpiece.

Due to rapid advancement in the field of surface engineering, conventional techniques for surface treatment like carburizing and flame hardening have been replaced by techniques using advanced heat sources such as plasma, laser, and electron beam. These techniques use high energy concentrated beam on the workpiece which generates steep thermal gradients leading to rapid solidification and immediate phase transformation of the surface. The electron beam process is widely used for surface modification of steel, but shallow case depth (≤ 1.5 mm), need of vacuum; limited for the small components makes this process non versatile at site. The laser beam process also has certain disadvantages like high cost of investment in the equipment, poor laser light absorption in the metal, radiation problem and highly skilled operator requirement. However, a relatively high energy concentration to produce a steep thermal gradient for effective surface treatment by modification of matrix morphology of metal can also be effectively obtained by using a versatile process of arcing.

In view of the above the use of readily available autogenous (without filler) tungsten inert gas arcing (TIGA) process is found suitable for surface modification of steel substrate through controlled melting and solidification of the substrate. The easy availability at site, lower cost of investment, less skilled worker requirement, high heat absorption in the metal and less environmental pollution makes TIGA process most favourable for surface modification of steel [Kim and Na, 1988; Kumar et al., 2017]. Here for surface modification, the heat energy is provided by an electric arc maintained between the electrode and workpiece where a high quality partial melting is ensured under a good inert gas shielding of the molten pool. In TIGA process continuous heat source (arc heat source) of double ellipsoidal nature acting at the surface of the base plate, which melts the substrate surface and produces an initial fusion zone in the base metal. In autogenous TIGA process, one can manipulate the arcing process primarily by controlling the voltage, arc current and travel speed influencing the thermal cycle (heating and cooling). Thus it may manipulate the solidification mechanism of fused metal at surface and the characteristics of heat affected zone (HAZ) of the base metal. The control of current enables shaping of fused zone with a wide range of variations.

However, the TIGA process may be proved as a better process of surface modification, especially when it is used with pulse current. This is because the use of pulse current instead of continuous current facilitates more precise control of energy input and its distribution in the system. The pulse current TIG arcing (P-TIGA) has number of advantages that primarily include intended operation at relatively low heating, less distortion of the substrate and precise

control of isotherm and thermal cycle leading to control necessary phase transformation and its morphology. The use of pulse current in TIGA process has been found more effective for control of the arc to use with further precision of desired localized performance. This is because it can operate at a relatively higher energy input of high current but maintains a relatively low net heating of the base metal primarily due to low heat build-up under interruption in arcing causing interrupted fusion and solidification of base metal that consequently also reduces distortion in work piece. It allows greater control of heating with comparatively larger fusion with deeper penetration at a faster speed of arc movement. Thus, it may result in improved quality of thermally modified zone, especially with respect to its microstructure.

The control of pulse arc is comparatively more complicated than control of continuous arc due to involvement of large number of simultaneously interactive pulse parameters in it. Thus, the effect of pulse current TIG arcing (P-TIGA) on characteristics of thermal behavior can be estimated as a function of a summarized influence of pulse parameters such as the frequency (f), pulse time (t_p), base time (t_b), base current (I_b), and pulse current (I_p). The summarized influence of pulse parameters in P-TIGA process can be defined by the following hypothetical dimensionless factor ϕ as it is amply justified in case of the pulse current metal inert gas welding process [Ghosh, 2017, Ghosh et al., 1994, Ghosh 1999, Ghosh et al., 2000, Ghosh et al., 2001 and Ghosh et al., 2007 (a, b)]. The hypothetical factor $\left[\phi = \left(\frac{I_b}{I_p} \times f \times t_b \right) \right]$

where, $t_b = \frac{1}{f} - t_p$, is derived on the basis of the energy balance concept of the system.

The utility of using this concept of Φ in control of pulse current process is amply justified in large amount of work carried out in pulse current gas metal arc welding (P-GMAW) process. The control of this basic nature of the pulsed process with the help of the factor Φ may also remain valid in case of P-TIGA process as it is also primarily based on the basic energy balance concept of pulse control phenomenon. It is successfully tried in case of P-TIGA process by several researchers [Reddy et al., 2013; Suresh et al., 2004; Ghosh and Kumar, 2014]. The use of this concept of Φ to control the P-TIGA process may prove to be significantly effective to add a new dimension to this process in order to introduce for high critical control of weld thermal cycle with considerable flexibility. Thus, this innovative controlled process may be desirably used to improve various properties of modified surface of components for critical applications.

AISI 8620 is a case hardenable low alloy Cr-Ni-Mo steel widely used by all industry sectors for light to medium stressed components and shafts requiring high wear resistance with

reasonably required core strength and impact toughness properties [Lu et al., 2012; Asi et al., 2012]. The typical uses of this steel are Bearings, Arbors, Bushings, Cam Shafts, Differential Pinions, Guide Pins, King Pins, Pistons Pins, Splined Shafts, Ratchets, Sleeves etc. [Arthur et al., 2015; Erdogan et al., 2002; Asi et al., 2007].

The primary objective of this research is to understand the comparative effect of C-TIGA and P-TIGA processes for industrial application in order to produce more effective modified surface layer with enhanced hardness and wear properties in AISI 8620 steel substrate. The AISI 8620 steel is the chromium, molybdenum, nickel based case hardenable low alloy steel that gives superior case/core properties after surface modification. The complete work has been carried out in seven parts. 1. The single pass C-TIGA parameters are optimized with the help of studies on influence of C-TIGA parameters on the thermal behaviour of surfacing including the modified FZ and HAZ geometry. The single pass P-TIGA is applied on the AISI 8620 steel surface at the optimized parameters of the C-TIGA to compare both the processes in terms of modified geometry (Depth of penetration, Width of FZ, HAZ width and FZ area). 2. An analytical thermal model is used to predict the isothermal curve, thermal cycle and cooling rate of the single pass C-TIGA and P-TIGA processes. In order to check the effectiveness of the thermal model, the estimated results (Isothermal curve, thermal cycle and cooling rate) are validated with the experimental results. The effect of single pass C-TIGA and P-TIGA processes on the cooling rate are also compared with respect to each other in this part. 3. Microstructural studies are carried out at optimized parameters of both the single pass C-TIGA and P-TIGA parameters and correlated with the cooling rate. 4. Effect of both the C-TIGA and P-TIGA parameters on the hardness is studied and compared with each other. 5. Multi-pass TIG arcing process is performed over a larger substrate surface area to analyse the effectiveness of both the C-TIGA and P-TIGA process for industrial application at optimized parameters. 6. The residual stress analysis is performed on the modified zone of both the single and multi-pass TIGA processed surface. 7. The wear analysis is completed to see the effect of C-TIGA and P-TIGA processing on the substrate surface. The characteristics of surface modification obtained by C-TIGA have been compared to those of the surface modified by P-TIGA process in order to find out the utility of the processes used.

After finding the potentials of P-TIGA process to produce improved surface modification, effort has been made to develop knowledge of critical application of pulse parameters of autogenous P-TIGA process for optimum surface hardening of case hardenable AISI 8620 steel substrates in comparison to that produced by using C-TIGA process. The knowledge includes appropriate control of pulse parameters primarily in order to manage the

thermal cycle and isotherm of the heating zone giving rise to desired surface modification of the substrate primarily defined by its geometry and microstructure. In this regard the relatively low heating characteristics of the pulse current arcing process is also kept under consideration for comparatively lower distortion and residual stresses of the substrate than that observed in case of the conventional non pulse arcing process. The innovation in surfacing is established after carrying out comparative studies using the C-TIGA for the same purpose.





CHAPTER 2

LITERATURE REVIEW

2.1 Surface Modification Processes

Surface modification of materials has been carried out by use of different methods, technology and procedures. Generally three methodologies are used to improve the surface properties. First one is to change the chemical composition of the substrate surface; second one is to transform the substrate surface without affecting the chemical composition and the third one is to alter the surface properties by some mechanical means. The surface modification processes are used for preparation of components to use in a special condition to reduce the overall cost of the components without affecting its core properties [Bakshi and Harimkar, 2015].

The surface modification (hardening) processes are not basically different from conventional surface treatment processes of materials. The hardness and strength both are achieved by heating the material over the austenite region and then quenched the material in oil or water to form hard phase like martensite. The main difference between the conventional heat treatment processes and surface modification processes is that in case of surface modification process only surface is heated to austenizing temperature before quenching. The core properties like toughness inside the surface remain unaffected by surface modification processes due to the high heat conductivity of ferrous materials. The use of appropriate concentrated heat fluxes to heat the substrate surface over austenizing temperature is necessary without affecting the bulk temperature of the component. The hot intense flames or high frequency induction heating is used to obtain the desire heat input. After using selective surface heating the substrate surface to austenitization temperatures, desired surface hardening is achieved by use of a quench medium to the hot surface, or by self-quenching. The area beneath the surface is act a heat sink to transfer the heat quickly from heated zone to adjacent material (heat sink) by conduction. The process of transfer of heat is known as self-quenching. The rate of transfer of heat should be high enough to allow the formation of hard phases at the surface. So on the basis of methodology, surface modification processes can be divided into three groups [Lampman, 1991; Harimkar et al., 2013; Singh J, 1995].

- (1) Thermochemical processes
- (2) Mechanical Surface Treatment
- (3) Thermal Surface hardening processes

2.1.1 Thermochemical Processes

Thermochemical processes modify the chemical composition of the substrate surface of a part without affecting its core properties [Mencík, 2013]. The thermochemical processes are basically a diffusion method which involves diffusion of hardening elements such as carbon, nitrogen and boron. The thermochemical diffusion processes having advantage of localized heating of workpiece, where the surface modification are desired [Totten and Liang, 2005].

2.1.1.1 Carburizing

Carburizing is one of the important process used for surface modification of steel by the accumulation of carbon into the steel surface [Cajner et al., 2010]. The carburizing is a time and temperature dependent diffusion process which involves heating a component at a temperature in the range of 850-950⁰C for a certain period [Aramide et al., 2009]. Hosseini et al., 2012 described that in carburization process, the carbon atom layer diffuses into the low carbon steel to form a martensitic case to increase the wear and fatigue resistance with a tough, low-carbon steel core. Carburization process includes gas, vacuum, plasma, salt bath and pack carburizing [Asi et al., 2007]. The gas carburization process in which the component is placed in an environment of some carbonaceous gas like Methane, Ethane or any natural gas [Collins et al., 2014]. In the vacuum carburization process the workpiece is placed in a rough vacuum with a hydrocarbon gas under some pressure and then followed by quenching in either gas or oil [Harry W. Antes, 2005]. The plasma ion process uses glow discharge technology under vacuum to introduce carbon bearing ions to the steel substrate [Conrad and Radtke, 1987]. Liquid or salt bath carburization process is implemented in molten salt pots in an environment of carburizing salt such as sodium cyanide. The pack carburizing process is the oldest process in which components are surrounded by a blend of charcoal and activators and then heated in a closed chamber [Foreman, 1990].

2.1.1.2 Nitriding and Carbonitriding

Nitriding is the thermochemical process like carburizing except that instead of carbon here nitrogen is diffused into the metallic surface to produce a hard case [Bernal, 2006]. In this process nitrogen is introduced in a temperature range of 500 to 550⁰ C which is below the austenizing temperature range for steel and quenching is not required in this case [Michalski et al., 2009]. Similar to carburizing process, nitriding process includes gas, liquid and plasma nitriding [Moller et al., 2001]. The gas nitriding process takes place in the presence of ammonia gas which produces nitrogen rich white nitride layer over the surface [Yang, 2012]. The liquid nitriding process is performed in a molten salt bath containing either cyanides or cyanates at a temperature similar to the gas nitriding process. Plasma Nitriding is another approach in which

glow discharge technology is used to introduce elemental nitrogen to the surface of a component in a vacuum using high voltage electrical energy.

Carbonitriding process involves dispersing of both C₂ and N₂ into the surface of steel substrate in a furnace. The process is performed in an environment of carburizing gas (propane or methane) mixed with ammonia followed by gas quenching [Shen et al., 2007]. The advantage of carbonitriding is improvement in fatigue and impact strength. The ferritic nitro carburizing is another approach to modify the steel surface by diffusion of nitrogen and carbon into substrate surface. The process forms a white layer of nitrogen and carbon in steel surface. The process forms the surface having high resistance to wear and significant improvement in fatigue endurance limit [Benedettiet al., 2002].

2.1.1.3 Boronizing

Boronizing is another method to modify the surface properties by introducing boron into the substrate surface. The component is surrounded with the boron containing compound (Boron powder or ferro boron) with some activators like chlorine and fluorine compounds in a temperature range of 850 to 950⁰C for some time [Jain and Sundararajan, 2002]. Mostly the tool steel and heat treated steels are modified by this method [Ozdemir et al., 2008]. Béjar and Henríquez [2009] modified the surface of different steel by a new approach using plasma-electrolysis boronizing. They found that the presence of Cr in the steel promotes the boronizing while C and Ni retard the hardening process. The boronizing process effectively increases the hardness of AISI 8620 from 350 HV to 1610 HV as compared to carburizing process where the typical hardness is achieved around 885 HV [Calik et al., 2009]. However, several disadvantages like inflexibility, high labor intensive and high brittleness of boronizing layers make the process less cost effective [Przybylowicz, 1999].

2.1.2 Mechanical Surface treatment

The elastic-plastic cold working of the substrate surface is the basic methodology of the mechanical surface treatment [Wagner, 1999]. The basic purpose of mechanical surface treatment is to introduce the compressive stresses over the substrate surface to increase resistance against corrosion fatigue, fatigue crack initiation and propagation and improves the structural performance under cyclic loading. Mechanical surface treatment is characterized into Shot peening, deep rolling and Shot blasting processes [Nalla et al., 2003].

2.1.2.1 Shot peening

The shot peening process is a surface modification process in which bombardment of shots (Glass, round metallic or ceramic particles) with sufficient force on a substrate surface to induce the compressive stresses. The process uses the shooting of hardened balls under

controlled parameters on the substrates surface of the workpiece. The use of this process increases the fatigue properties of AISI 8620 steel up to 70 % more than untreated SAE 8620 steel [Matlock, 2005]. The strain hardening of the surface increases the yield stresses of the material [Rice and Rosengren, 1968]. The plastic deformation prompted by shot peening is advantageous for both the soft as well as hard materials [Pandey and Deshmukh]. For hard materials, shot peening produces a hard zone at the surface and somewhat softened layer beneath the surface, whereas for soft materials it produces a homogeneous type of plastic deformation promoting hardening without crack nucleation affinity. Pandey and Deshmukh described that the fatigue life of the component can be improved by shot peening through the increase in hardness of surface (by strain hardening), by microstructural modification, by change in surface conditions and by an optimum spreading of compressive stresses in the surface/subsurface layers. The fatigue properties of AISI 9310 spur gear has been found 1.6 times the life of the standard gears without shot peening [Townsend and Zaretsky, 1982]. However the major disadvantages of this process are bed surface quality and difficulty in thin workpiece deformation [Qandil, 2016].

2.1.2.2 Deep rolling

Deep rolling is an axial-symmetric modification process in which a hardened roller produces plastic deformation in the workpiece. In this process roller is pressed into a fillet to make plastic deformation while the workpiece is revolved with respect to roller [Matlock et al., 2010]. Deep rolling produces a hardened surface with residual compressive stresses which retards the fatigue crack initiation and crack growth [Nikitin, 2007]. Juijerm and Altenberger [2007] studied the combined effect of deep rolling followed by an ageing treatment of Al alloy and found significant increment in hardness and in both low and high cycle fatigue. The effective decrement in the surface roughness with higher rate of work hardening by deep rolling process makes the Ti alloy component more effective in application [R.K. Nalla et al., 2002; Tsuji et al., 1992]. The main drawback of deep rolling is the complex calculation of suitable process parameters for surface treatment [Jeswiet et al., 2008]. Mandal et al., [2016] developed a low carbon micro alloyed steel and modify with thermo mechanical processing (Hot rolling followed by air cooling and water quenching). They found considerably improvement in yield stress and UTS due to the formation of coarse bainite and lath martensite in air cooled sample and a mixture of lath martensite and lower bainite in water quenched sample.

2.1.2.3 Shot blasting

Shot blasting method is another approach to modify the surface properties of materials by introducing compressive stresses in the materials. Shot blasting consists on bombarding a

surface with small, hard particles like alumina, silicon carbide, titanium oxide etc. [Liu et al., 2004]. Xingeng and Jiawen [2003] studied the effect of Shot blasting in Cr-Ni-Mo steel and found coating of chromium oxide with high Cr concentration and reduction in the activation diffusion energy. The shot blasting is effectively used to enhance the surface properties like corrosion resistance, hardness and wear resistance of the steel surface [Xingeng and Jiawen, 2006].

2.1.3 Thermal Surface Hardening processes

Thermal surface hardening processes involve localized heating and quenching of the component without any chemical modification of the surface [Davis, 2002]. The surface modification of steel is mostly carried out by conventional surface hardening processes like flame and induction hardening [Davis, 2004]. Laser beam and electron beam are the new advanced applied energy techniques to modify the surface properties [Picraux and Pope, 1984].

2.1.3.1 Flame and Induction hardening

Flame hardening process is a method of austenizing the surface of the substrate by heating with oxyacetylene gas before quenching the steel in a spray of water [Schneider et al., 2013]. After quenching, the surface of the steel is converted into hard martensitic phase with soft and ductile core. The flame hardening is a simple and cheap process as compare to other hardening process. However, use of explosive gases, difficult to control the heating temperature, coarse martensitic structure due to overheating, high cost per piece in mass production and difficult to control the case depth are some disadvantages of this process [Brockhoff and Brinksmeier, 1999].

Induction hardening is a versatile process where heating is performed by locating a workpiece in the magnetic field produced by high frequency AC current passing through a water cooled Cu coil followed by quenching. The advantages of induction hardening are faster process, less distortion, and small footprints. However, care must be taken when special geometries like hole, corners and complex shapes are treated with this process. Otherwise eddy currents become concentrated at the corners and result in overheating and cracking over the substrate surface [Nemkov, 2004]. It is very difficult to harden the complex shapes by this process and high capital investment is required to harden the workpiece. The conductor coil is designed according to the shape of the substrate and some shapes are very difficult to be induction hardened.

2.1.3.2 Electron beam hardening

The electron beam hardening process uses high velocity focused beam of electron as an energy source to modify the surface properties [Ormanova, 2017]. Modification of surface is

performed under conditions which reduce substrate heating so that after removal of the heat source, the cooling and solidification become rapid into the substrate [Akamatsu, 2003]. The electron beam hardening uses two approaches to modify the surface. The first one is to melt the surface and second one is a transformation hardening in which material is heated upto austenizing temperature range [Bugaev et al., 2002] followed by self-quenching. The process is performed in a high vacuum of 10^{-3} Pa in the region where the electrons are discharged and augmented to avoid oxidizing and scattering of electrons [Boiko et al., 1999]. The Pulse electron beam process is also another approach to modify the substrate surface by allowing energy deposition in a short time [Ivanov et al., 2000]. The advantage of the pulse electron beam process is high surface finishing without any change in the chemical composition and short irradiation time [Ivanov et al., 2002]. The electron beam energy deposition technique makes rapid solidification, fast evaporation, thermally induced compressive stresses, shocking wave, and enhanced diffusion in the substrate surface [Rotshtein et al., 2004]. However, necessity of vacuum, limitation for the bulk component, high capital investment are some limiting factors to use this process for surface modification [Renk et al., 2004]. Ming et al., [2004] developed the wear resistant surfaces by an electron beam process. Walker et al., [2014] studied the effect of large area electron beam melting of the Ti alloy and effectively increase the corrosion resistance of the modified alloy as compared to as received surface. Walker et al., [2013] investigated the effect of pulsing in the electron beam process to increase the surface properties of Co-Cr-Mo alloy for biomedical application.

2.1.3.3 Laser surface hardening

Laser surface modification is primarily used to increase the mechanical properties of extremely stressed machine components like bearings and gears [Damborenea, 1998]. Surface treatment by the laser process raises the wear resistance by improving surface hardness, and induces the residual compressive stresses in the workpiece surface to increase the fatigue properties [Mohseni et al., 2014]. In recent years, industrial lasers are successfully used for surface hardening of steel by melting and transformation hardening approach [Ramadan and Moussa, 2013]. The main advantage of laser that it can produce very concentrated energy fluxes at the substrate surface and the resulting steeper thermal cycle in the workpiece to avoid the need of quenching. Other advantages of laser beam are easy to control, no need of a vacuum, and generate no combustion products. However, laser process also has some difficulties to use this process in situ application. These drawbacks may include the need for complex optics and the use of coatings because of the low infrared absorption characteristics of steel. Barnes et al., [2003] used laser surface hardening for powder metallurgy component and

found a case depth of 0.90 mm with hardness of 952 HV as compared to as received component of 210 HV hardness. Clare et al., [2012] used the laser cladding process to the maintenance, improvement and repair of the surface of a rail material. Grum [2007] compared the different laser surface technique and found that under different conditions different surface layer properties are obtained. Liu et al., [2007] investigated the effect of laser shocked peened process on fatigue life of Al alloy. They pointed out that proper selection of parameters is necessary to increase the fatigue life of materials otherwise internal cracks are developed in the samples. Lu et al.,[2012] investigated the effect of multiple laser processing on mechanical and wear properties of AISI 8620 steel and found remarkable improvement in the mechanical properties and wear resistant. Montross et al., [2002] reviewed the laser shock processing and pointed out that laser shock processing of materials is capable to increase the surface properties and compressive residual stresses into the surface up to 1 mm depth. Pashby et al., [2003] investigated the effect of high power diode laser surface hardening on low alloy steel and found increases in the mechanical properties. Ray et al., [2014] investigated the effect of laser cladding by three Ni base powders with varying chromium, molybdenum, boron and niobium content in lateral rolls of a continuous slab caster. Reich et al.,[2014] describes the effect of laser treatment on clinching of hardened steel. Speidel et al., [2016] developed a new approach to modify the surface of mild steel by using a combination of laser and electrochemical processes. Tewary et al., [2014] successfully applied the laser surface hardening on C-Mn steel with a case depth of 300 μm . Yip et al., [2014] developed a clad layer of Silicon Carbide (SiC) particle reinforced Metal Matrix Composite (MMC) using the iron based alloys (P25) by laser process. Yip and Barnes [2013] applied the laser cladding process to modify the mild steel surface by introducing Silicon Carbide (SiC) particles.

2.1.3.4 TIG arcing process

Tungsten inert gas arcing process is an advancement of the welding process to modify the substrate surface in which an electric arc is struck between a non-consumable tungsten electrode and the substrate surface in a controlled atmosphere of inert gases [Guile, 1984]. The three procedures are used to modify the substrate surface by this process. First one is the tungsten inert gas melting process in which surface is heated up to melting temperature followed by self-quenching [Khan et al., 2000]. Second one is the changing the chemistry of the surface by alloying of various alloying elements such as; Cr, Ti and W using TIGA process [Korkut et al., 2002]. Third one is the deposition of different metals and alloys on the base material by TIGA process. The advantage of TIG cladding is an improvement in performance and long life of the components [Atamert and Bhadeshia, 1989]. The low operating cost, low

maintenance, cheaper labour cost, minimum distortion of the workpiece and higher flexibility at site makes this process more advantageous for surface modification of materials. However, comparatively less effort has been done on the area of surface engineering by this method. Labudovic and Kovacevic [2001] described the combine effect of laser and TIG process for surface modification of Ti alloy. They described that the combination of TIG/ laser is useful in terms of shorter processing time and no need of a vacuum system. Orlowicz and Trytek [2005] studied the effect of TIGA process on cast iron and found the rapid crystallization of melted region with very hard surface. They pointed out that the proper selection of TIGA parameters effectively produce a very high surface hardness and therefore, high wear and abrasion resistance of the surface. Dzedzic and Bylica [2008] used multipass TIGA treatment to modify the surface of high speed steel. Mohamadzadeh et al., [2009] have increased the mechanical and wear properties of cast iron by the use of the TIG melting process. Bochnowski [2010] successfully modified the surface of carbon tool steel by TIGA process. He studied the effect of arcing parameters on the tool steel surface and found the appreciable microstructural modification of the substrate surface up to 3 mm of depth with the precipitation of martensite phase.

2.2 Tungsten Inert Gas Process

The TIG process has been developed in the middle of the twentieth century for fabrication of reactive metals and alloys such as stainless steel, magnesium and aluminum alloys as none of the process (SMAW and Gas welding) available at that time to fabricate successfully primarily due to contamination of atmospheric gases and poor control over the heat input required for welding [Stava, 1990]. In the TIG process the electric arc is established between a tungsten electrode (non-consumable) and base material. The arc gap is kept constant and current is controlled by the power source. The heat of the electric arc produced is employed to achieve coalescence of metals with and without filler metal. Filler metal, generally available in 1 meter length of wire, is added to the leading edge of the weld pool as required. The arcing electrode and molten zones are generally protected by inert gas or gas mixture of argon and/or helium. The current and heat input range of the process are followed of the order of 10-300A and 0.2 to 30 kJ/s respectively [ASM handbook 1994]. However TIG process is a welding process, but successfully used for surface modification of different materials [Carry, 1995]. TIG melting or TIG arcing process involves heating the substrate material over melting temperature followed by self-quenching.

2.2.1 Power source characteristics

The tungsten inert gas arcing process uses constant current power source static characteristic for their application [Venkatramani, 2002]. The volt-ampere output curves are also named as 'drooper' because of significant downward or negative slope of the curves. In the constant current power source characteristics the little variation in arc voltage causes smaller change in arc current (Fig. 9.1). The constant current power source is used for non-consumable tungsten electrode which may sometimes damage during touching of electrode with workpiece for initiation of electric arc. Under this power source characteristics, the short circuiting current shall be limited which would provide safety to power source and the electrode. The constant current power source characteristics are useful to maintain the constant arc length and stable arcing condition.

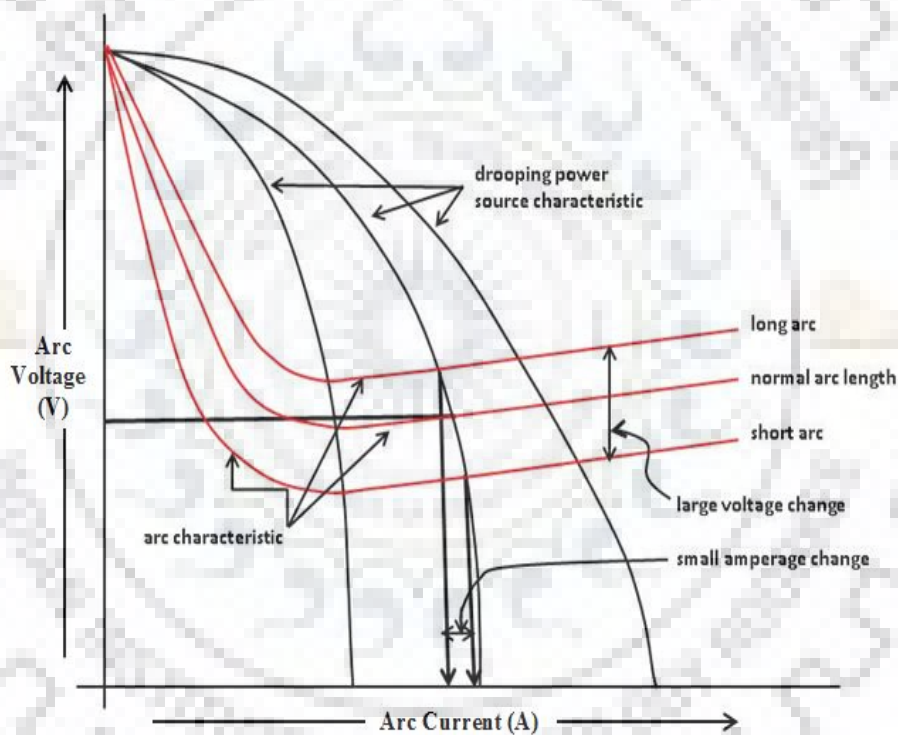


Fig. 2.1 Constant current power source characteristic.

2.2.2 Process variables and their control

The arc current, arc voltage and travelling speed are the primary variable to control the C-TIGA process. The arc current and arc voltage is used to control the energy input into the system while travelling speed is used to control the energy distribution into the system. The control of energy input and energy distribution into the system primarily determine the stability of the process [Liu and Siewert 1989] which is dependent upon the process variables [Choi et al., 1998, Kim and Eagar 1993 (a)]. These have considerable influence on the behaviour of the

FZ and HAZ [Johnson et al., 1989], which in turn affects the properties of modified zones through influence on penetration, solidification mechanism and heat flow.

Arc current

Arc current plays primary role in deciding the thermal and metallurgical behaviour of the modified zone. At a comparatively lower value of it, the size of fusion zone is reduces and at a higher value of arc current, the size of FZ increases. A still higher value of current, the serious distortion and damage of workpiece is possible [Lancaster 1984].

Arc voltage

The arc voltage primarily depends upon the TIG welding apparatus, whether it may fix or adjustable. The arc initiation and arc length are basically controlled by high initial arc voltage. The welding quality or surface modification become poor if the arc voltage is too high [Li and Zhang, 2001]. It is the well-known fact that the arc voltage is primarily controlled by the arc length in TIG process which relatively affects the modified zone's shape and size. The too short arc length causes short circuiting the electrode with workpiece resulting the chances of forming the weld defects and narrow weld bead due to variation in heat input. The disadvantage of shorter arc length is narrow weld bead, The arc length in excess causes a flat and shallow deposit, chances of an electric arc to wander, growth in spattering and may also responsible for porosity in the fusion zone due to air aspiration in the shielding gas jacket [Johnson et al., 1995]. The extended arc length raises the perimeter of electric arc plasma, due to which there is a broader fusion zone. The long arc length also reduces the concentration of heat directly under the tungsten electrode and makes the fusion zone response to weave very sluggish [Matthews et al., 1992]. Smaller arc length advances wetting appearances and control of fusion zone. Hence, it is significant to select the proper arc voltage / arc length to obtain control of the fusion zone resulting in prevailing of the properties of the modified region.

Travel speed

The travel or welding speed plays an important role in TIGA process to improve the properties of modified region. The depth of penetration and arc reinforcement decreases with increasing the travel speed due to a reduction in heat input per unit length or power [Shirali and Mills, 1993]. The depth of modified zone and fusion bead size is primarily controlled by travel speed and arc current. So travel speed and arc current are interdependent to each other. The use of high travel speed reduces the wetting action, increases the irregular bead shape, and increases several defects like porosity and undercut while slower travel speed decreases the porosity in the modified zone [Norman et al., 1999].

Shielding Gas

The selection of shielding gas is very important because it directly affects the welding expenditure, arc stability and electrode life etc. The shielding gas also controls the depth of penetration, fusion zone temperature, surface profile, porosity, physical and mechanical properties of the modified zone [Murphy et al., 2009]. Generally Ar and He gases are used in TIG process [Murphy et al., 2009]. The pure Ar gas is used for welding of thin materials. Ar gas normally delivers more smooth and quiet arc. However, arc penetration is found less when Ar is used. The Ar gas is chosen for most of the applications due to easy availability and lower cost of Ar gas [Durgutlu, 2004]. Helium gas is used where higher depth of penetration and heat is required. So He gas is preferred for welding metals of high thermal conductivity and large thickness [Kah and Martikainen, 2013]. Generally use of He gas is useful for welding of thick sections of Al and Cu. The Ar gas is used for welding of structural steels, stainless steels, micro alloyed steel, Ti and Mg alloy, Cu and Al alloys. Sometimes Ar+H₂ mixture is applied for joining of some grades of stainless steel and Ni alloys [Kumar et al., 2011]. Helium argon mixtures may be used for low alloy steels, aluminium and copper.

2.2.3 Arcing current polarities

The three types of arcing current or polarities (Fig. 2.2) can be used for TIGA process. Each polarity has a distinct characteristic which makes it more anticipated for specific conditions or with certain kinds of materials. The main change among the polarities is in their energy distribution and the degree of arc cleaning.

DCEN (Direct current electrode negative)

In direct current straight polarity mode, tungsten electrode is connected to the negative terminal of the power supply. The total energy transfer from electrode to workpiece is 70 % and 30 % electric energy (Heat energy) remains to the negative terminal. The advantage of DCEN mode is higher depth of penetration with a narrow weld bead profile. Due to high percentage of heat energy transfer to workpiece, this is the most common and widely used polarity mode.

DCEP (Direct current electrode positive)

In DCEP mode the tungsten electrode is coupled to the positive terminal of the power supply. The total heat supply to the workpiece is 30 % and 70 % of heat remains to the positive terminal. The DCEP mode is used very hardly because almost 70 % heat is on the electrode which can easily overheat and burns the tungsten electrode. DCEP mode creates a shallow depth of penetration, wide bead width. The DCEP mode is mainly used for thin and very light material with a low arc current.

AC (Alternating Current):

In AC mode 50 % of energy is transferred to the workpiece and remaining 50 % moved to Tungsten electrode. On the first half of AC cycle where the tungsten electrode is positive, the heat energy is transferred from workpiece to electrode. Similarly in the second half of AC cycle the energy is transferred from the tungsten electrode to workpiece. So the energy input towards the tungsten electrode is averaged out as the AC wave passes from one side of the wave to the other. The AC mode is largely used for white metals like Al and Mg. The first half of the cycle is known as cleaning half because during the first half of the cycle the electrons will flow from workpiece to Tungsten electrode. This will cause the removing of any oxide layer from the base material. The second half of the cycle is known as the penetration half of the AC waveform because in this half mode the electron (energy) is transferred from electrode to workpiece.

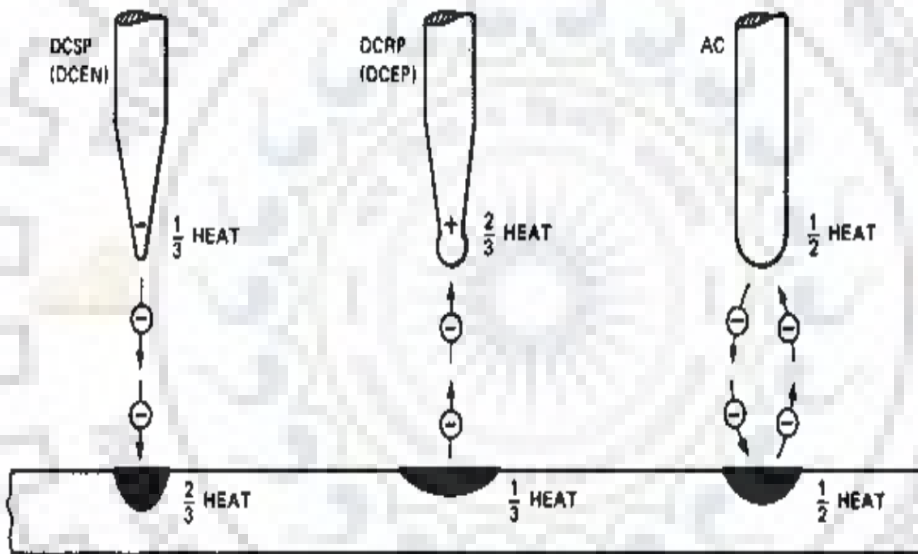


Fig. 2.2 Effect of polarity in the heat distribution between the tungsten electrode and workpiece [Messeler Jr, 1999].

2.3 Pulsed current tungsten inert gas arcing process (P-TIGA)

The pulse tungsten inert gas arcing process is one where the current is pulsed between the low level to the high level as shown in fig. 2.3 [Phillips et al., 1994]. So, this kind of process where current is varied continuously as a function of the time during the arcing is called the pulse arcing. The advanced version of TIGA process uses pulsed current instead of continuous current. Both low frequency pulsation typically (0.1-20Hz) and high frequency pulsation (>100Hz) is often used in this process [Richard, 2001].

The heat input depends on the mean current which is a correlation of the pulse height, pulse duration and frequency [Sakai et al., 2009]. The pulsed current mode of this process offers a better control over the size of fusion zone and its fluidity to manage the pool in position

as well as over the penetration behaviour of the modified zone. The use of autogenous pulse current tungsten inert gas arcing (P-TIGA) has become extremely popular in weld fabrication of relatively thin section and root pass of thick section in various industries due to its ability to precise control of energy input and to introduce control of energy distribution in the process [Tsai and Hou, 2013]. Unique possibility of control of energy distribution in the process may significantly influence the solidification behaviour, nature of phase transformation as well as morphology of various phases in the matrix. This process can be accredited for the possibility of introducing more controlled weld thermal cycle, primarily due to its merit of developing relatively lower heat build-up in weld pool than the conventional TIGA process [Balasubramanian et al., 2008]. Moreover as the P-TIGA is also a relatively low heat process, it may reduce residual stresses and favourably affect the control of dilution and phase transformation in the substrate. In addition, it allows greater control of fusion with enhanced penetration [Kim et al., 1998].

It is generally understood that the total heat input in pulse current arcing process becomes relatively lower than that of conventional arcing because the heat energy required to melt the base metal is primarily supplied at peak current during the pulse on time when a low base current just keeps the arc alive [Chen et al., 2000]. The melting at the stiff arc of peak current gives rise to more penetration which permits more efficient use of arc energy limiting the wastage of heat by conduction into the base metal as it occurs in conventional constant (non-pulsed) current welding. [Nadkarni, 2010]. The heat transfer and fluid flow in the fusion pool can significantly influence its geometry, temperature gradient, local cooling rates, microstructure and mechanical properties. The P-TIGA works at a mean current which is significantly lower than the current used for C-TIGA, but it produces deeper penetration due to high arc pressure at relatively large current of long peak duration [Saedi and Unkel, 1988]. Thus, the effective heat input in P-TIGA becomes considerably lower than the heat input of C-TIGA resulting in lower average fusion pool temperature. Accordingly the P-TIGA exhibits lower thermal distortion than the C-TIGA at a given penetration [Tseng and Chou, 2001]. In other words the P-TIGA process gives an opportunity of using fine-tuned arc wave form and significant energy saving. The P-TIGA has numbers of advantages that primarily include intended operation at relatively low heating, less distortion of substrate and precise control of thermal cycle and isotherm leading to necessary phase transformation and microstructure [Atabaki et al., 2014; Ghosh and Kumar, 2015].

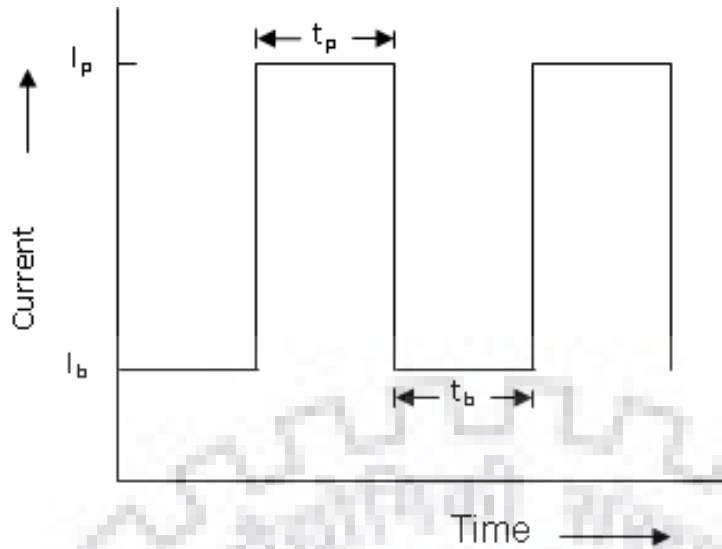


Fig. 2.3 Arc current characteristics in pulsed current TIGA process.

The effective use of pulsing in GMAW process is described by Ghosh and Dorn (1993) and found that use of pulse current effectively controls the metal deposition. The pulsing effect is capable of joining at a relatively low energy input and hence more valuable as compared to GMAW [Ghosh and Dorn 1993]. The similar principle of pulsing is also applied in TIGA process for welding and surfacing [Ghosh and Kumar, 2015] and found comparatively lower heat input and better control of the process. However, it is very difficult to take a combination of accurate pulse parameters, but clear understanding of correlations among pulse parameters and characteristics makes this process easy to use. [Amin, 1983]. In P-GMAW process, mean current, I_m , for a square wave pulse is expressed [Amin1981, Lancaster 1984] as,

$$I_m = \frac{(I_p t_p + I_b t_b)}{(t_p + t_b)} \dots\dots\dots (2.1)$$

Where, t_b is base current duration and t_p is peak current duration, I_p and I_b are pulse current and base current respectively.

Pulse frequency, f , may also be expressed as

$$f = \frac{1}{t_{pul}} \dots\dots\dots (2.2)$$

Where, $t_{pul} = t_b + t_p$

The above mention equations are successfully used to determine mean current and frequency for P-TIGA process by several researchers [Traidia et al., 2010; Stephan et al., 2015].

2.3.1 Process variables and their control

The merits of P-TIGA process is primarily dependent upon the right selection of operating parameters, like mean current (I_m), peak current (I_p), base current (I_b), pulse duration (t_p) and pulse

frequency (f) as they affect the microstructure of fusion zone (FZ) and heat affected zone (HAZ) as well as chemistry due to their influence on weld thermal cycle and weld isotherm [Ghosh and Dorn 1993, Ghosh and Rai 1998, Ghosh and Sharma 1991, Lambentt 1989].

Peak current (I_p)

The peak current is used to proper melting of the material. The level of the high current is decided on the basis of heat that is to be generated for melting the faying surfaces [Farahani et al., 2012]. Higher peak currents will result in greater axial force due to magnetic field generated by the current carried through the electrode due to which distortion of the workpiece is possible. Hence, to ensure appropriate amplitude and duration of peak current, power law relations ($I_p^n t_p = \text{constant}$, $n=2$) have been used for determining the amplitude of peak current and duration [Quintino and Allum 1984, Rajasekaran et.al. 1998, Wang et. al 2004].

Peak current duration (t_p)

The pulse duration is an important operating parameter to control the modified zone. Increase in peak current duration in general, increases the modified zone size and the kind of penetration. So, the higher peak current duration, greater will be the penetration. So, the weld pool size and the penetration requirement govern the pulse current duration [Pal and Pal, 2011].

Base current (I_b)

The base current is required to continue the minimum welding arc between the pulses [Needham, 1965; Nemchinsky, 1997; Praveen et al., 2005]. The fusion zone and geometry of weld bead can be smoothly controlled by the suitable base current level. Sometimes the base current is frequently fixed to a minimum level to control the heat input. Due to which there is a poor fusion geometry and high crowned weld bead. Background current or low level of current must be high enough to maintain the stable arc with lowest possible heat input so that the solidification of the molten weld can take place without any heat build-up [Kumar and Sundararajan, 2009]. So the low level current that is called base current performs the two functions. One, it helps maintain the arc during the welding with the very low heat. During this period, the solidification of the weld metal takes place.

Base current duration (t_b)

The base current duration is required to avoid the additional heat built up into the base material to avoid the excessive distortion of the workpiece [Yousefieh et al., 2011]. During this period the low arc current is maintained to transfer the heat from the fusion zone to adjacent material which causes better control in the cooling rate of the process. However, sometimes due to excessive base current period the cooling rate becomes so much high. Because of the high

cooling rate the gas in trap take place, which in turn leads to the development of the polar city [Manti and Dwivedi, 2007]. So, in which way the solidification of the fusion zone that decides the base current value depends upon the base current duration.

Pulse frequency (f)

The duration of the peak current and the base current determines the pulse frequency [Cook and Hussam, 1985]. The frequency of the pulse is set as per the requirement of the heat input. If we require more heat, than the high frequency pulse should be selected. If we require less heat then, the few pulses of the peak current will be there. That will help in having the lower heat input. Very low pulse frequency (conversely longer background current duration and short peak current period) during Pulse TIGA, reduces heat available for modification which in turn increases the solidification rate. Too high solidification rate increases martensitic transformation in the fusion zone. A fine grained structure can be achieved using both low and high pulse frequencies [Arivarasu et al., 2014]. Fine microstructure is known to improve the mechanical properties of the weld joint. Low pulse frequency (up to 20 Hz) has more effect on the microstructure and mechanical properties [Qi et al., 2013].

Several researchers pointed out that in pulse TIGA process, the weld bead is composed of a series of overlapping fusion spots. Fig. 2.4 shows the effect of frequency on the arc bead. When arcing is done with low frequency, these effects can be clearly observed in the fig 2.4 (a and b). When working with very low pulse frequency the overlapping of fusion nuggets is less. So the heat transfer in between the generated fusion nuggets is high from fusion zone to adjacent workpiece material. When pulse frequency increases the gap between the fusion nuggets are reduces. Due to which fusion zone size increases and heat transfer from fusion zone to adjacent material reduces [Suresh et al., 2004]. So, when the pulse frequency is increased, the peak current is generated at very short intervals. It developed the fusion zone and making possible to solidify quickly at very short interval of the times. So, in the increasing in pulse frequency, the time after which heat is generated; lot of heat is generated and reduced. The continuous, almost very fine with the great overlapping of the molten fusion zone areas with each other. So, increasing the pulse frequency obviously increases the heat input to the base material with more overlapping [Yang et al., 2013]. It has been observed that when we work with the low pulse frequencies, the effect of the pulse TIGA is found more on the structure and on the mechanical properties as compared to the situation, where high pulse frequency is used. When working with high pulse frequency the pulsing takes place very frequently for long period due to which the fusion zone bead being developed like a C-TIGA processed fusion bead [Reddy et al., 2013].

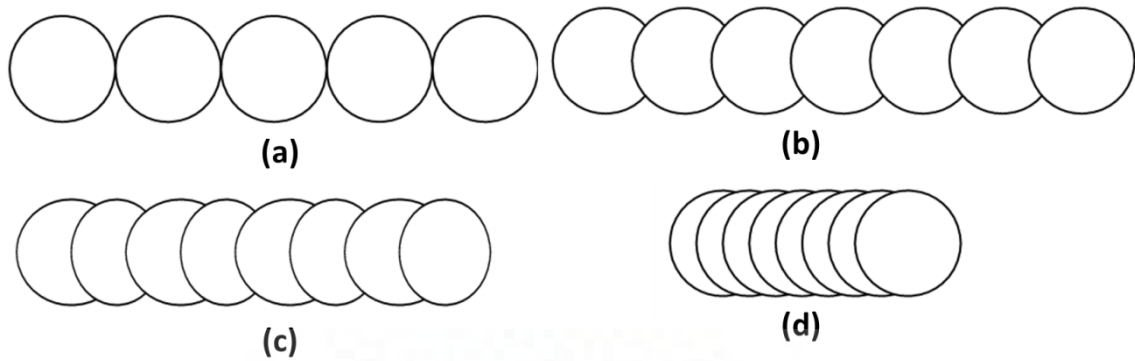


Fig. 2.4 Schematic diagram showing the effect of frequency on fusion track using P-TIGA process.

2.3.2 Ratio of peak current to base current (I_p/I_b)

The peak-to-background current ratios basically provide a means for the welding current to pulse form one level to another. Several researchers describe that for good fusion the peak to base current ratio should be varies from 2:1 to 5:1 ratios. Ghosh and Sharma (1991) investigated the effect of I_p/I_b on the arc pressure. Earlier investigation [Ghosh and Sharma 1991, Ghosh and Gupta 1996] carried out on single pass pulsed current MIG of Al-Zn-Mg alloy have shown the influence of the ratio of I_p/I_b on the porosity content of weld deposit and suggested that the I_p/I_b ratio should be maintained in the range of 7.5 at a mean current of 150 A and around 4 at a mean current of 220 A to achieve a significant reduction in porosity content of the weld deposit.

2.3.3 Heat transferred to fusion zone

The heat transferred (Q_T) to the fusion zone of P-TIGA was estimated in consideration of the arc heat transmitted to the weld pool (Q_{AW} , $J s^{-1}$) and travel speed (S) as follows [Ghosh et al., 2006, Goyal et al., 2008 (b)].

$$Q_T = Q / S \dots\dots\dots 2.3$$

Where, $Q = Q_{AW}$

Q_{AW} may be estimated as ($J s^{-1}$)

$$Q_{AW} = \eta_a (V I_{eff}) \dots\dots\dots 2.4$$

Where, V and I_{eff} are the arc voltage and effective current (root mean square value of the pulsed current wave form) respectively. The I_{eff} is calculated by the following equation [Praveen et al., 2005].

$$I_{eff} = \sqrt{k_p \cdot I_p^2 + (1 - k_p) \cdot I_b^2} \dots\dots\dots 2.5$$

Where, the pulse duty cycle k_p [Ghosh, 2017]

$$k_p = \frac{t_p}{t_{pul}} \dots\dots\dots 2.6$$

2.3.4 Estimation of weld pool temperature

It is assumed that during pulsed current TIG arcing (P-TIGA) method, the energy transfer primarily takes place at peak current (I_p) so the net heat content is mostly directed by it. During arcing the heat transfer to the fusion zone is primarily attributed to the primary arc heating (Q_{AW}). Accordingly the continuous heat source (arc heat source) of double ellipsoidal [Robert W. Messler, Jr., 1999, ASM Handbook 1994] nature acting at the base plate surface, which melts the area of workpiece and produces an initial fusion zone in the workpiece. Thus the distribution of temperature at any place in the fusion zone area may be estimated by the analytical solution of the distributed heat source. The expressions for the temperature, T_d , at any point ($x(\xi)$, y , z) in the modified zone due to arc heating using the distributed heat source expressed as follows:

$$T_d = \frac{3\sqrt{3} \cdot Q_{AW}}{\rho \cdot c \cdot \pi \sqrt{\pi}} \int_0^t \left[\frac{\frac{dt'}{\sqrt{(12a(t-t') + a_h^2)} \cdot \sqrt{(12a(t-t') + b_h^2)}}}{\frac{A'}{\sqrt{(12a(t-t') + c_{hf}^2)}} + \frac{B'}{\sqrt{(12a(t-t') + c_{hb}^2)}}} \right] + T_0 \dots\dots\dots 2.7$$

Where, Q_{AW} is the arc heat transferred to the weld pool.

2.3.5 Concept of summarized influence of pulse parameters

It is very complicated to govern the pulse arc as compared to continuous arc due to envelopment of a huge number of instantaneously collaborating pulse parameters in it. Thus, the consequence of P-TIGA on appearances of thermal characteristics can be expected as a function of a summarized influence of pulse parameters such as frequency (f), peak time (t_p), background time (t_b), background current (I_b), and peak current (I_p). The concise influence of pulse parameters in P-TIGA process can be defined by the following hypothetical dimensionless factor ϕ as it is thoroughly acceptable in case of the pulse current metal inert gas welding process by the hypothetical equation $\left[\phi = \left(\frac{I_b}{I_p} \times (f \times t_b) \right) \right]$ where, $t_b = \frac{1}{f} - t_p$, is derived

on the basis of energy balance concept of the system suggested [Ghosh, 2017, Ghosh et al., 1994, Ghosh 1999, Ghosh et al., 2000, Ghosh et al., 2001 and Ghosh et al., 2007 (a, b)]. Control of basic nature of pulsed process with the help of the factor Φ has also been repeated effective in case of P-TIGA process as it is also primarily based on the basic energy balance concept of pulse control phenomenon. The use of this concept of Φ to control the P-TIGA process may prove to be highly effective to add a new dimension to this process for highly

critical control of weld thermal cycle with considerable flexibility. Thus, this more precisely controlled process may be used to improve various properties of modified surface of components for critical applications of advanced materials.

2.4 AISI 8620 Steel

AISI 8620 is a case hardening steel to provide better mechanical properties and greater resistance to wear than other conventional carbon steels. [AWS handbook 1978, Metals handbook 1979 (a), (b), Rothwell and Malcolm Gray 1976]. AISI 8620 is a low alloy steel having 3-5 weight % of alloying element, including some selective element in order to meet high wear resistance, high strength along with other properties [Suzuki et al., 2001, AWS handbook 1978]. AISI 8620 steel keeps low carbon content (0.18 - 0.23 Wt. %) with varying manganese content up to 1.0 wt%, in order to exhibit sufficient hardenability, ductility and wear resistance. Manganese marginally rises the strength of ferrite, and also rises the hardness of steel during the quenching process by reducing the critical quenching speed. The presence of Cr in the steel significantly increases the toughness and resistance to wear. The Cr also increases the critical quenching temperature in the surface hardening treatment. The presence of Ni in low alloy steel increases the strength of ferrite, toughness and hardenability. During quenching of surface hardening process, Ni effectively reduces the cracking and distortion by converting needle phase martensitic to lath type martensitic structure. The Mo also intensifications the hardness penetration of steel, reduces the critical quenching speed, and rises high temperature tensile strength [Rowan and Sisson, 2009].

2.4.1 Properties of AISI 8620 Steel

AISI 8620 steel must have certain characteristics and properties to use in construction of various advanced components such as wear resistance, core strength, toughness, ductility, formability and weldability so that it can be fabricated successfully by customary methods depending upon applications. In addition to this, improved wear and fatigue resistance is generally required [Pickering 1978]. Generally AISI 8620 steel has higher core strength and toughness than the majority of as rolled or normalized structural carbon steels and has fairly good formability commensurate with their strength level. The wear and fatigue resistance of steel depends upon the method and processing used to modify the surface properties without affecting the core properties.

Mechanical properties

The AISI 8620 is a low alloy steel specially developed for case hardening applications. The mechanical, physical and thermal properties of AISI 8620 steel are primarily dictated by their microstructure and phase transformation. Generally AISI 8620 steel consists of ferrite-

pearlite microstructure, and the properties are affected by changes in the microstructure. The case hardening techniques is used to modify the surface properties, the fineness of the microstructure, and the amount of dispersed phases. The well balanced alloy content permits hardening to produce a hard wear resistant case combined with core strength in the order of 850 MPa [Asi et al., 2007]. The minimum mechanical properties of AISI 8620 steel have been given in Table-2.1.

Table 2.1 Minimum mechanical properties of AISI 8620 steel [Tamura et al., 1988].

Property	Minimum value
Tensile strength	590 MPa
Yield strength	358 MPa
Elongation % in 2"	28.0
Reduction in area, %	61.0
Vickers Hardness	184
Poissons Ratio	0.29
Izod Impact Toughness	115 J

2.4.2 Heat Treatment and Surface modification of AISI 8620 steel

AISI 8620 steel is specially designed case hardened steel having a good response to heat treatment. The thermochemical heat treatment processes are successfully applied to increase the wear resistance, fracture toughness, fatigue resistance, hardness of the surface without affecting the core properties [Thelning, 1984]. The through hardening is not performed for this steel because the tough core requirement. In furnace heat treating process, the surface hardness depends upon the carbon content and hardenability of the material. This steel is hardened by heating to 815 °C followed by a water quenching. AISI 8620 may be given a full anneal at 850 °C and slow cooling at not more than 10 °C per hour down to 450 °C to remove stresses and micro cracks. The tempering of AISI 8620 is done at 120 °C to 150 °C to increase the toughness, minimize the effect of residual stresses and remove the micro cracks after the formation of martensite over the surface after surface hardening process. Arthur et al., [2015] developed a new quenching process for pack carbo-nitride process at 900 °C using cyanide-containing dried cassava leaves (bio-processed waste) to modify the AISI 8620 steel surface. Chatterjee et al., [2014] studied the effect of heat treatment on ductile-brittle transition on Cr-Mo steel and found that heat treatment considerably improve the ductile to brittle transition as compared to as received materials.

2.4.3 Hardenability

The ability of steel to form a martensitic structure after surface hardening is referred to as hardenability. The grain size and composition are the two most significant variables which

affect hardenability. The various researchers describe that due to increase in austenite grain size, there is a reduction in the grain size area. The reduction in grain size area causes the reduction in the number of sites for the nucleation of ferrite and pearlite. Due to which transformations are slowed down, and the hardenability is therefore increased.

Heat treated low-alloy AISI 8620 steel have better hardenability than untreated and carbon steel and therefore can deliver high strength and good toughness in hardened zone. Their alloy content provides improved heat, wear and corrosion resistance [Meyers and Wittman, 1990]. The fig. 2.5 shows the hardenability curves of the as received and hardened 8620 steel which shows the significant improvement in hardness after hardening process as compare to as received unhardened 8620 alloy steel [Apple and Krauss, 1973].

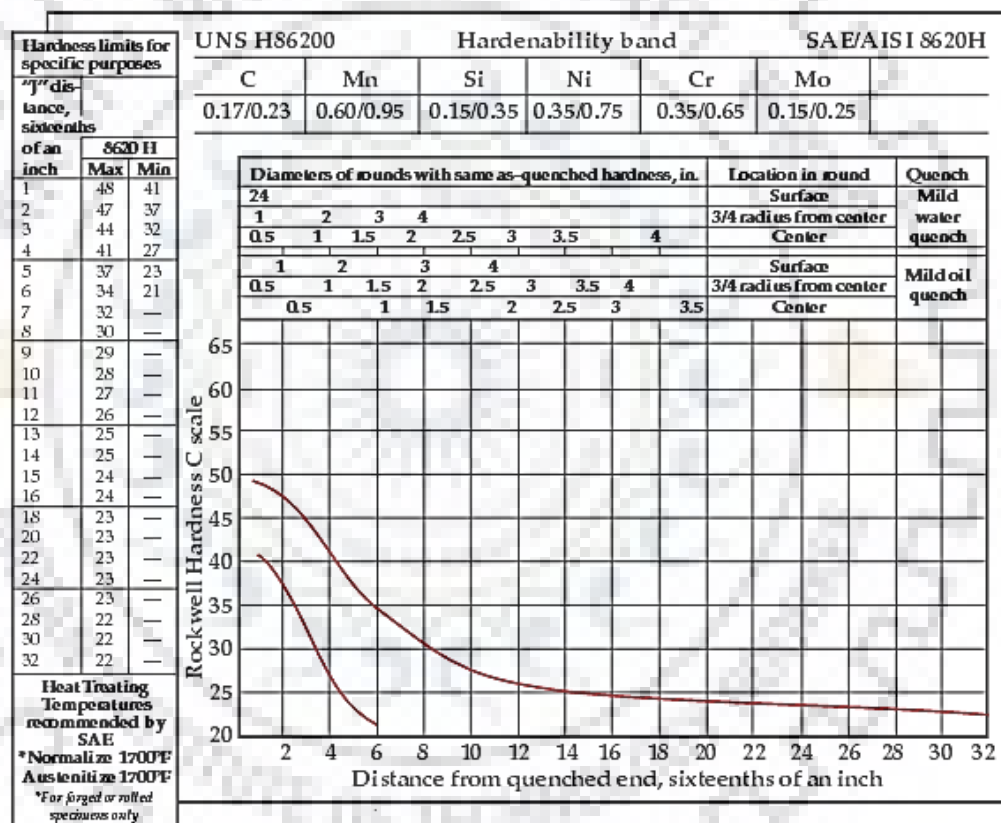


Fig. 2.5 Hardenability curve of the AISI 8620 steel [Apple and Krauss, 1973].

2.4.4 Applications of 8620 Steel

AISI 8620 steel is extensively used in making of components of stationary structure as well as mobile tools and components for example, automotive, earth explorer, mining equipments, large and small scale bearings [ASM Handbook 1992, Kearns AWS handbook 1978, Tamura et al., 1988]. The hard case and a tough core are the primary requirements of case hardened steel components. The permutation of these properties provides the excellent wear resistance, fatigue strength at the surface with the core having good impact strength. The AISI 8620 steel is used

to manufacture several components include almost all types of gears, camshafts, universal joints, driving pinions, link components, axles and arbors. The all these machineries made hardened to resist wear and fatigue with sufficient integral toughness. It is observed that in large wind turbines the flanks and toes bear maximum loads particularly when there is an unexpected change in wind speed. So there is a need of a hard case with a tough core in a wear resistant gear to handle high impact loads. Gear noise increases during life due to abrasion of gear tooth surfaces. Increasing the surface hardness and abrasion resistance of gears will thus decrease gearbox noise. The case hardened AISI 8620 steel is used for manufacturing of gears used in large wind turbine having the advantage of increased core tensile strength and toughness, higher fatigue strength in both core and case, improved hardenability and low distortion. The typical applications of AISI 8620 steel include

- **Transportation:** The case hardened AISI 8620 steel is required in every field of transportation like railways, automobiles, waterways and airways.
- **Energy production:** The AISI 8620 steel is required in power plants to resist the wear and corrosion related problems. The material should be capable to withstand cyclic stress, thermal and mechanical loads. So case hardened AISI 8620 steel is largely used in hydroelectric power stations, wind-turbine generators, and propeller drives of drilling rigs and steam-turbine gears of power stations.
- **General mechanical engineering:** Applications in this area include forging presses, metal rolling equipment, machine tools; drivelines of mining equipment and heavy-duty transmissions; earth exploring equipments and heavy-duty construction cranes.

2.5 Factors affecting the properties of AISI 8620 steel

2.5.1 Effect of alloying elements

The decomposition behavior of steel is governed by the austenite grain size in it. Thus this behavior of steel affects the subsequent microstructure and mechanical properties after surface modification [Rothwell and Malcolm Gray 1976, Shome et al., 2003, Shome et al., 2004, Shome 2007, Stasko et al., 2006, Varughese et al., 1993]. The chemical composition of the steel, time and temperature are the typical surface modification variables to control the austenite grain size [Sufirez et al., 1994, Tamura et al., 1988]. The Cr, Ni, Mo and Mn are the main alloying element in the AISI 8620 steel.

The Ni in AISI 8620 steel works as a austenite stabilizer and as such lowers the temperature at which austenite decomposition will occur on cooling [Isakov, 2009]. The Ni influences the yield behavior by facilitating cross slip resulting a more homogeneous

distribution of the slip throughout the metal crystal, and this is reflected as increased toughness after hardening. The presence of Ni in AISI 8620 steel also decreases the dependence of yield strength on temperature and strain rate with raising the cleavage strength. The Cr and Mo are carbide forming elements in AISI 8620 steel lowered the carbon diffusivity in austenite [Rowan, 2009]. Nickel increases the strength of ferrite, therefore increasing the strength of the steel. It is used in AISI 8620 steel to increase toughness and hardenability [Rollason 1961; Clark and Varney 1962; Aver 1974]. Nickel also tends to help reduce distortion and cracking during the quenching phase of heat treatment.

Manganese endorses deep surface modification in case hardenable steel by powerfully retarding the austenite conversion. Manganese also tends to reduce eutectoid C content and transformation temperature. Several researchers describe that Mn is a most cost effective intensifier [David et al., 2009]. The Mn is used in all types of case hardenable steel to retard the transformation. Generally around 1% Mn is quantified in case hardenable steels. The lower transformation temperature produced by Mn addition encourages reduction in grain size, whether the steel may be either as-rolled or normalized. The reduction in grain size (pearlite, ferrite and bainite) promotes the higher yield strength and impact toughness. The researchers found that the addition of Mn for a given C content increases the pearlite phase in the matrix [Mangonon, 1976]. The increase in the pearlite phase causes the increment in the tensile strength without affecting weldability. The researchers studied the effect of Mn on Ms temperature and found that the Mn reduces the Ms temperature. There is a high probability to contain higher residual austenite in high Mn steel. Although in high Mn steels, Mn promotes to form a carbide phase, which is similar to cementite. The presence of Mn during tempering suppresses the secondary hardening.

Chromium is a strong carbide forming element in steel similar to Mo and W. It has affinity to form a solid solution with both the α and γ phases of iron. The Cr in the presence of Fe and C forms a typical series of carbide compounds. The presence of Cr increases the Ac" critical point and lower down the eutectoid point of carbon [Briant, 1981]. Cr combine with carbon forms the chromium carbide, augmented the tensile strength by precipitation hardening. The grain growth is inhibited by the secondary chromium carbides (second phase particles) by surrounding the grain boundary. Due to grain refinement and second phase particles the dislocation movement becomes very difficult. The presence of chromium carbide in the matrix raises the energy required for elastic /plastic deformation hence causes the improvement in the mechanical and physical properties [Razzak, 2012]. Cr also acts as a hardening element in case hardenable steel and frequently used with Ni to produce higher mechanical properties. The

presence of chromium carbide in the steel increases the wear resistance and cutting ability due to the high hardness.

Molybdenum plays an important role to develop a solid solution with the ferrite phase in steel. It forms a complex carbide phase in the presence of carbon. The addition of Mo in small amount (0.12 to 0.62) increases the Ac₃ critical point in low alloy steel. If there is a presence of Mo in a solid solution of austenite before quenching, the reaction rate for alteration of austenite becomes slowdown as compared to mild steels [Yasumoto et al., 1987]. Due to this there is in depth hardening of low alloy steel. The sufficient amount of Mo in steel causes a higher tempering temperature during quenching and the same degree of softness as compare to carbon steel. So the steel with Mo having ability to retain their mechanical properties specially their strength at high temperature due to high tempering temperature. The steel with Mo has the sufficient resistance to creep under constant loads below their elastic limit at a temperature up to 1150 F. The low alloy steels with a Mo up to 0.40 % shows a minimum affinity to temper embrittlement [Stott et al., 1995]. Some researchers reported that after quenching and tempering some low alloyed steel shows brittleness when gradually cooled from the tempering temperature. The impact resistance is clearly reduced due to this brittleness. This temper brittleness become dangerous when large components are being manufactured by these highly susceptible steels because it is very difficult to fast cooling of large components to prevent damage. Mo additions in the amounts noted prevent temper brittleness and allow usual cooling rates to be used after tempering.

2.5.2 Effect of cooling rate

The wear resistance and other mechanical properties of AISI 8620 steel are improved by surface modification methods through phase transformation, grain refinement, dislocation hardening, and inducing compressive stresses over the surface [Bardelcik et al., 2010]. The variation in the cumulative amount of deformation, temperatures of working and cooling rates can produce a variety of microstructures as per the requirement. The rapid heating up to and over from austenitic temperature and then cooling with different cooling rates results in various types of microstructures, along with different combinations of properties. The dendrite formation in the steel is the distinctive technique of solidification, which is reliant on the heating and cooling cycle. The researchers reported that the precipitation starts simultaneously during the solidification from liquid to solid and dependent on the cooling rate.

A continuous-cooling-transformation (CCT) diagram (Fig. 2.6) is used to predict the phase transformation in low alloy steel (Thompson et al., 1990). The CCT diagram describes the substantial suppression of polygonal ferrite creation and a noticeable transformation area,

usually recognized to bainite formation, at the temperatures in between to ferrite and martensite formation. In the area between the ferrite and martensite transformation, the ferrite having the groups of equally oriented particles around 1 μm of size and high dislocation density conquered the significant conversion of austenite during continuous cooling. The ferrite grains anticipated two types of phase in the matrix during continuous cooling leading to the “acicular ferrite” and “granular ferrite”. The phase transformation from austenite region depends upon the cooling cycle. At high cooling rate the austenite is transformed into the complete martensite structure. At medium cooling rate the austenite is transformed into martensite and bainite and at slow cooling rates, polygonal ferrite and Widmanstätten ferrite formed. Uzlov and Danchenko [1971] studied the effect of cooling rate in the mechanical, physical properties and phase transformation of different carbon steels up to cooling rate of 6 $^{\circ}\text{C}/\text{sec}$. They found that the properties of carbon steel with different C percentage differ to each other.

Tomita and Okabayashi, in an investigation of quench rate effects in low carbon 4320 steel versus med/high carbon 4340 steel, proposed that rapidly quenching low carbon steels reduced the amount of fine globular and rod Fe_3C (carbide) phase at prior austenite grain boundaries in the as quenched condition. As a result of eliminating the grain boundary rods, martensite packet size was increased, along with associated material strength. The effect is less pronounced in higher carbon steels. This suggests a number of important factors. The quench rate / strengthening effect is carbon dependent, with low carbon alloy steels being more sensitive to quench rate strengthening than high carbon steels.

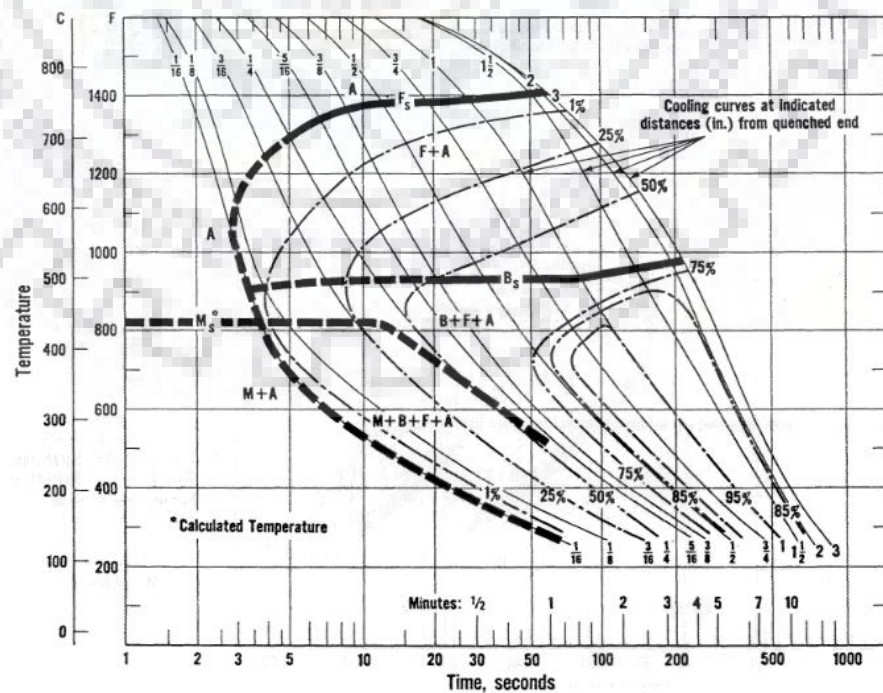


Fig. 2.6 CCT curve of AISI 8620 steel [Thompson et al., 1990].

The material strengthening effect is carbide related, and limited by steel chemistry and subgrain structure (i.e. martensite laths). Material case strengthening in the case due to quench rate is likely minimal. Consequently, the fatigue Stage I crack initiation for carburized Pyrowear53 may be more controlled by surface residual compressive stresses arising from the differences in quench rate than by material strength. Calik A. [2009] studied the effect of cooling rate in AISI 1020, AISI 1040 and AISI 1060 Steels. The effective phase transformation and solid solution hardening due to increase in percent carbon and cooling rate is the main key factor of increasing mechanical properties. Davis and King [2013] reported the appreciable refinement of microstructure and improvement in the toughness due to change in cooling rate in low alloy steel. Karmakar et al., [2017] studied the effect of different range of cooling rate (0.07 to 3.33 K/s) for micro-alloyed and plain C-Mn steel. They described that high cooling rate increases the formation of hard phase like martensite and bainite by reducing the austenite to ferrite transformation temperature and ferrite grain size.

2.5.3 Effect of microstructure

The different cooling rates give rise to variation in microstructure resulting in different mechanical properties of AISI 8620. Erdogan et al., [2002] investigated oil quenched carburized 8620 steel from the temperature of 731 °C. They pointed out that the oil quenching converts the ferrite-pearlite microstructure into martensitic phase transformation at the surface and dual phase microstructure having ferrite and martensite at the subsurface. The initial microstructure of specimen produced coarse, nodular martensite particles restricted to the former pearlite colonies and a quasi-continuous network of martensite along the ferrite grain boundaries. Guguloth et al., [2002] describes the effect of low cycle fatigue on the Cr-Mo steel and found that modified Cr-Mo steel, having tempered martensitic structure containing coarse-precipitates (such as Cr_{23}C_6) and fine-precipitates (such as Mo_2C , NbC and VC), showed the continuous softening to failure under cyclic loading both at ambient and at elevated temperatures. Samanta et al., [2013] studied the effect of quenching and partitioning (Q&P) treatment of low alloy steel to produce a higher fraction of retained austenite by carbon partitioning from supersaturated martensite.

Voort and Lucas [2009] has shown in his studies the effect of carburisation followed by water quenching on the microstructure of gear teeth surface made by AISI 8620 steel. Figure 2.7 (a) shows that the gear teeth surfaces were decarburized during heat treatment after carburizing, resulting in a 15-18 μm thick layer of pearlite with patches of ferrite. Below this layer the structure shown in Fig. 2.7 (b) consists of plate martensite and substantial retained austenite with irregularly dispersed patches containing inter- granular carbide networks.

J.Z. Lu et al., investigated the microstructural evolution of single and multiple laser treated of AISI 8620 steel. The Fig. 2.8 shows the TEM images of single laser shock processing treated surface at different depth from the substrate surface. Fig. 2.8(a) depicts the distinctive TEM image in the modified zone at the cross sectional depth of 20 μm from the substrate surface. The figure clearly shows the submicron equiaxed grains of size 320 nm. The Fig. 2.8 (b & c) shows the fragmented pearlites with average length of 300-500 nm at the depth of 200 and 300 μm respectively. Fig. 2.8 (d) depicts the sufficient parallel lamellar pearlites in the unmodified zone.

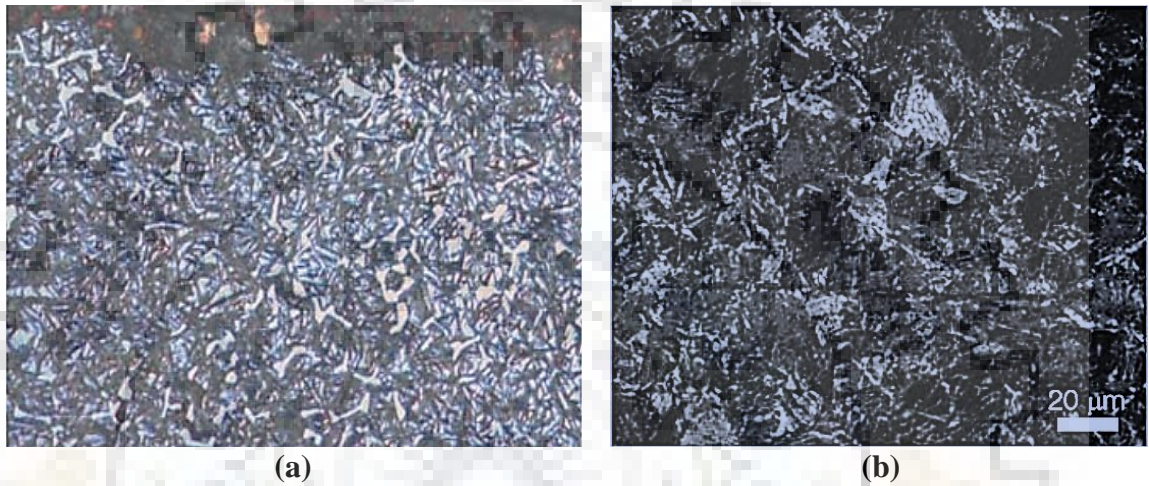


Fig. 2.7 Microstructure of AISI 8620 showing (a) decarburized pearlitic surface layer with patches of ferrite and the grain-boundary cementite networks and (b) lath martensite with a minor amount of bainite [Voort and Lucas, 2009].

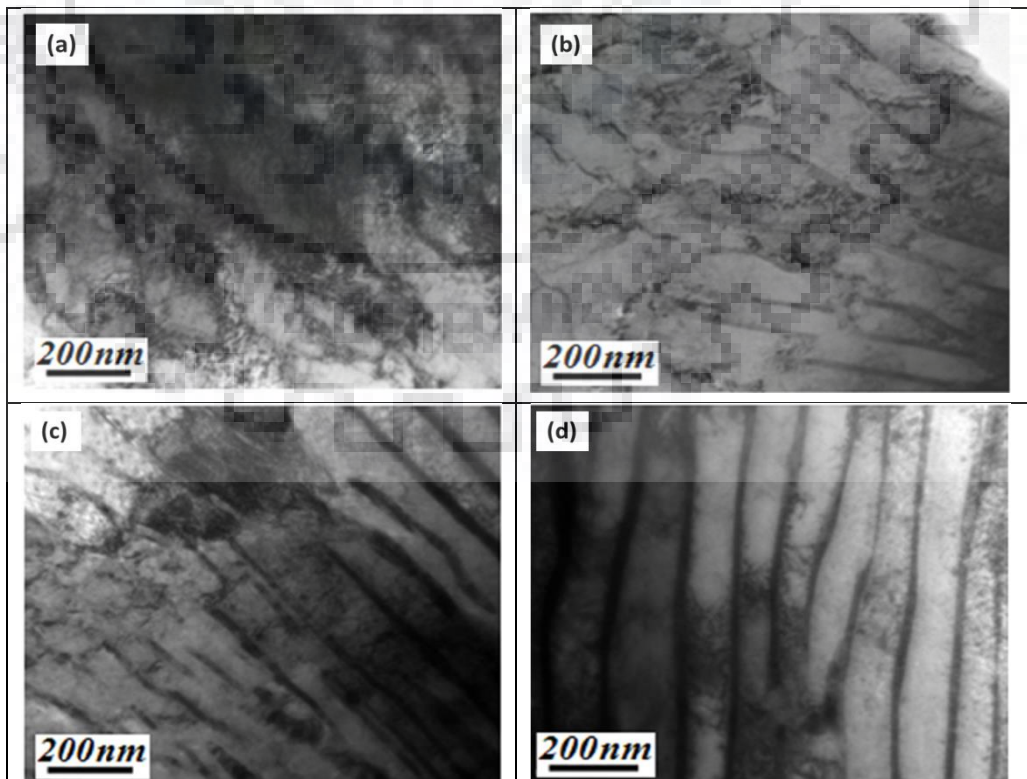


Fig. 2.8 TEM images of single pass laser surface modification of AISI 8620 steel.

Fig. 2.9 displays the typical TEM images of multi laser shock processed region at the different depth. Fig. 2.9 (a) shows the plenty of submicron equiaxed grains having size of 220 nm which is slightly smaller than the single LSP impacts at the depth of 20 μ . Fig. 2.9 (b) shows the typical TEM image in the modified zone at the cross sectional depth of 200 μ m from the substrate surface subjected to multiple laser shock processing and found many tiny pearlites in the modified zone. Fig. 2.9(c) shows the lamellar pearlites broken into small segments having average length of 100 nm due to effect of multipass LSP at the depth of 300 μ m. Fig. 2.9 (d) shows the plenty of parallel lamellar pearlites in the non-modified zone similar to single pass LSP. So the microstructure of AISI 8620 effectively controlled by the surface hardening process. However there is difference in the microstructure with an increase of cross sectional depth from the substrate surface. The refinement of the grains is observed in the modified zone due to dislocation movement by multipass LSP treatment. The multipass treatment on AISI 8620 steel surface make appreciable grain refinement and dispersion strengthening of C atoms.

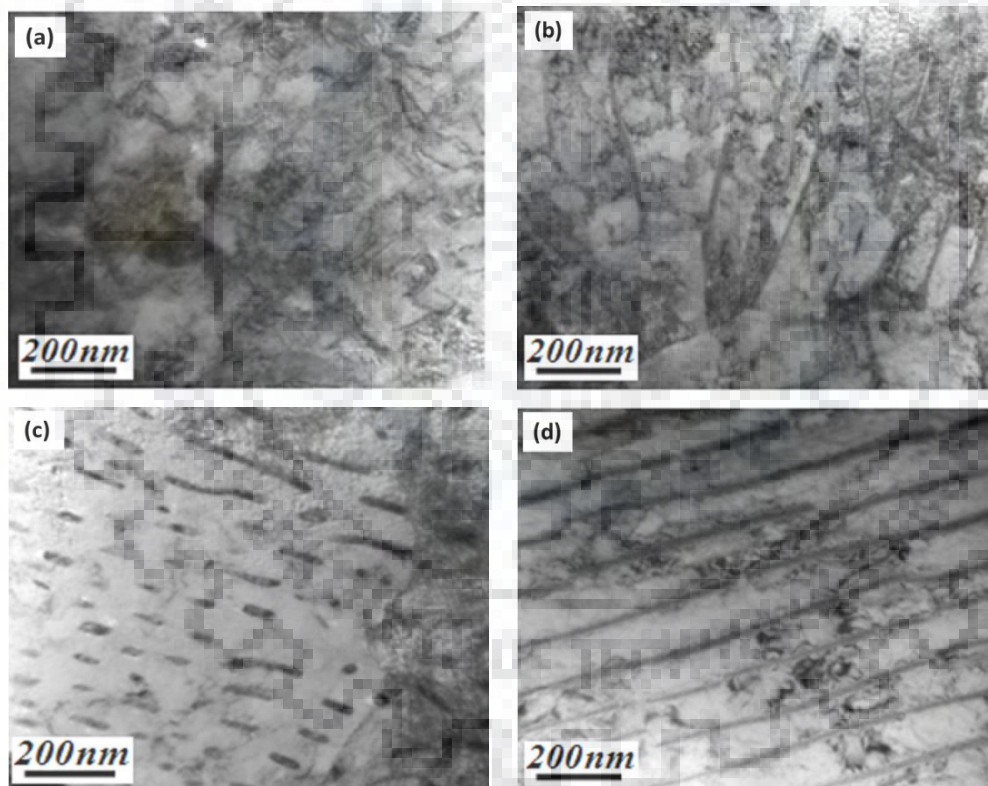


Fig. 2.9 TEM images of multi pass laser surface modification of AISI 8620 steel.

2.5.4 Factor affecting the hardenability of AISI 8620 steel

The hardenability of steel depends upon the carbon content, all alloying element except cobalt and austenite grain size. Bain [1979] described that the transformation rate at which the austenite in the steel converted into fine pearlite at the defined temperature controls the hardenability of steel. The composition of the steel is the main key factor to control the rate of

transformation at a precise temperature. The maximum transformation rate is observed at temperature of 510 °C which is used to predict the critical quenching speed and the temperature must be exceeded to become steel hardened.

The AISI 8620 steel consists of Mn, Cr, Ni, Mo and Al as an alloying constituent. The manganese, chromium and nickel contribute directly to deep hardening by increasing the hardening rate and molybdenum appears to induce shallow hardening though restricting grain growth. The hardenability is reduced if the austenite is rapidly transformed into fine pearlite. The hardenability is effectively influence by the grain size and controlled largely, for any specified temperature, by the obstruction to grain growth offered by large numbers of very finely dispersed particles, of exceedingly small aggregate mass, comprised presumably of stable oxides such as alumina, vanadium, and probably silica or silicates.

2.6 Modelling of modified zone

Rosenthal et al., 1946 has used the Fourier partial differential equation of heat conduction and introduced the moving coordinate system to develop solutions for the point and line heat sources and applied it successfully to address a wide range of welding problems. In his solutions, quasi steady state condition (an observer stationed at the point heat source fails to notice any change in the temperature around him as the source moves on) was assumed which can also be justified experimentally for a long weld. Starting from the partial differential equation of heat conduction, expressed in rectangular coordinates (x, y, and z) w.r.t. a fixed origin in the solid, he applied it successfully for welding by considering a moving coordinate system. It is well known that Rosenthal's solutions are valid at locations away from the heat source but are subjected to considerable error at or near the heat source due to assumption of a point or line heat source.

Wells et al., 1952, considered a two-dimensional moving rectangular heat source with a uniform distribution of heat intensity. He proposed the estimation of heat input and welding speed by examining the finished weld. Paley et al., 1975, investigated the heat flow in welding thick steel plates by considering the effects of boundary surfaces (bottom or edge of the plate) assuming them adiabatic based on the Rosenthal's solution for point heat source. Christensen et al., [1965], developed generalized plots of temperature distribution in dimensionless form at surface as well as at different depths of any substrate, which was found useful for estimation of HAZ, cooling rate and residence time between two temperatures. Pavelic et al., [1969] developed a finite difference method to determine the temperature distribution in a 2-D plate using line heat source. By using melting temperature isotherms as a boundary condition, the shape of the weld pool was correlated with the welding variables. In this method experimental

work is required to determine the boundary conditions. The details of the weld pool shape could not be correlated using line source theory therefore distributed heat source with Gaussian distribution of heat flux (W/m^2) was suggested. Friedman [1975] developed a thermo mechanical analysis of welding process using FEM. The model enables calculation of temperatures, stresses, and distortions resulting from the welding process. Friedman and Glickstein [1976] developed FEM analysis for transient heat conduction to investigate the effect of various welding parameters such as heat input and its duration from the arc and its distribution at the surface of the weldments on the thermal response characteristics, in particular the weld bead shape and the depth of penetration. Tsai et al., [1992] developed a semi empirical 2-D finite element heat transfer model that treats the melting interface as an inner boundary to calculate the quasi steady state temperature field and cooling rate in HAZ. Eager and Tsai [1983] modified the Rosenthal's model considering a 2-D Gaussian distributed heat source after assuming (i) no convective or radioactive heat flow, (ii) constant average thermal properties, and (iii) a quasi-steady state semi-infinite medium. They also developed its solution for the temperature of a semi-infinite body using a constant distribution parameter and obtained results were compared with their experimental values on various metals. Goldak et al., [1984] developed a mathematical model based on a Gaussian distribution of the power density and proposed a three-dimensional double ellipsoidal moving heat source. Finite element modelling was used to calculate the temperature field for bead on plate study and found that the use of 3-D heat source can predict the temperature of the weld joints with much deeper penetration compared to the 2-D model. The computed results of temperature distributions for submerged arc welds in thick work pieces were compared with the experimental values of Christensen et al., [1965].

Tekriwal and Mazumder [1988, 1986] developed a 3-D transient heat conduction model for arc welding using FEM analysis and compared the predicted size of the weld pool and HAZ with the experimental results and found good agreement. Na and Lee [1987] conducted 3-D finite element analysis of the transient temperature distribution in GTA welding by introduced a solution domain which moves along with the welding heat source and it was verified with the experiments on medium carbon steel under various welding conditions. Boo and Cho [1990] developed an analytical solution of 3-D heat conduction equation with convective boundary conditions at welding surface to predict the transient temperature distribution in a finite thick plate. The results were compared with the experimental values of GTA bead on plate weld on medium carbon steel. Vishnu Ravi et al., [1991] developed an analytical model of heat flow during pulsed current GTAW considering Gaussian distributed heat source and the results were

compared with mild steel weld. The investigation shows that pulsed current welding refines the grain structure of the weld metal. Kumar Subodh et al., [1992] developed three dimensional finite element modelling of gas metal arc welding. He has considered volumetric distribution of heat content of transferring droplets. The model is validated by predicting weld bead dimensions and comparing them with experimental data. Ghosh et al., [1993, 2006 and 1999] developed a model to predict the thermal and metal transfer behaviour during P-GMAW process and validated the model considering a summarized influence of pulse parameter factor ϕ . Prasad S. and Sankara N. [1996] developed a technique involving finite element analysis of temperature distribution during arc welding by using a transient adaptive grid technique. It gives a finer mesh around the arc source, where the temperature gradients are high, and a coarser mesh in other places to increase computational efficiency of the analysis. Fan et al., (1997) proposed a two-dimensional model using the boundary fitted coordinate system to simulate the P-TIG process. Kim and Na (1998) used the FDM to analysis the fluid flow and heat transfer in partially penetrated fusion zone under P-TIG process.

Nguyen et al., [1999], Nguyen et al., [2004] developed the analytical solutions for transient temperature field of a semi-infinite body subjected to a double ellipsoidal power density moving heat source with conduction only. The results were compared with the bead on plate deposition on HT-780 plates using GMA welding. The model failed to predict the shape of the weld pool in the transversal cross section. Pathak and Datta [2000] presented a three-dimensional transient finite element analysis of heat flow in arc welding using Gaussian distributed heat source and the results were compared with the published values. It was found that arc length significantly affects the temperature of weld pool and adjacent base metal. Komanduri and Hou [2000] developed an analytical solution for the temperature rise distribution in short work pieces in arc welding considering the arc beam as a moving plane (disc) heat source with a pseudo-Gaussian distribution of heat intensity. Christensen et al., has proposed a neural network approach [2003] for GMA butt joint welding. Mahaptra et al., [2006] developed 3D finite element analysis to predict the effect of shielded metal arc welding process parameters on temperature distribution, angular distortion and weldment zones in butt and one sided fillet welds. The predicted temperature distributions in butt bead on plate and one sided fillet weld under various conditions of welding are compared with experimental results and found to be in good agreement.

Bag and De [2008] have developed a finite element based 3 dimensional quasi steady heat transfer model to compute temperature field in gas tungsten arc welding process. The welding heat has been considered as volumetric heat source. The model is validated with

experimentally measured weld dimensions. Goyal et al., [2008] has developed analytical solution to find the temperature distribution in weld pool for pulse current gas metal arc welding considering two types of heat source acting simultaneously. Arc heat source has been considered as double ellipsoidal while transfer of heat by super-heated metal droplets as point heat source. The results are validated by comparing the results of bead on plate study. The equation is unable to determine the temperature within a radius of 2mm from arc centre. Bag S. and De [2009] have developed efficient numerical heat transfer model coupled with genetic algorithm based optimization for prediction of process variables in GTA spot welding. Genetic algorithm identifies suitable value of process variable for a target weld dimensions. A B Murphy et al., [2009] reviewed the thermal modelling in plasma generated in TIG welding process and found that the thermo physical properties affects the characteristics of welding arc, including the weld pool depth and geometry.

Schnick et al., (2010) proposed a mathematical model for arc welding process to to predict the local central minimum in the radial distributions of temperature and electric current density which is caused by a high concentration of metal vapour in the arc core and its high radioactive emission. They also described the effect of the metal vapour in increasing electrical conductivity at low temperatures, which leads to lower heat flux density and current density at the weld pool, implying a shallower weld pool. M. Chiumenti et al., [2010] developed a FEM model to describe the material behavior when the material transforms from liquid (purely viscous) to solid (elasto-plastic) in the multi pass welding process.

Anca et al., (2011) developed a FEM model to predict the thermal and mechanical phenomena in the arc welding process. Traidia and Roger (2011) proposed the unified time-dependent model to define the fluid flow, heat transfer and electromagnetic fields in the modified zone by P-TIG process. Tseng and Huang [2013] performed a FEM analysis by Gaussian distribution of the heat flux with an effective arc radius to describe the distributive nature of the heat source provided by the welding arc. They pointed out that arc efficiency has an effect on temperature history during welding. Tong et al., 2013 developed a time dependent heat source model (dynamic model) according to the characteristics of P-TIG process. However many investigations have been accompanied, but far less work has been done on the development of the welding heat source model under P-TIG process. Adak et al., 2015 developed the multiple linear regression equations to predict different results (weld bead geometry, as a function of multiple input variables for 'bead-on-plate' type GMAW process. Bag and De [2008] developed a three dimensional quasi steady heat transfer model to estimate the temperature distribution in gas tungsten arc welding (GTAW) process. De et al., [2003]

developed an analytical model to predict the cooling rate and microstructure in laser spot welds. Häßler et al., [2015] developed a FEM model to characterization of the arc for narrow gap welding. The model allows the specific improvement of the shielding gas flow and the prediction of the temperature profile of the workpiece for real component applications. Hertel et al., [2014] simulated the plasma-MIG process to investigate the influence of process parameters and thus helps to improve the properties of the weld. Manvatkar et al., [2011] developed a three-dimensional (3-D) heat transfer analysis based on the finite element method to predict the weld pool geometry, thermal cycle and mechanical properties in laser assisted shaping process for ASS. Schnick et al., [2012] developed a numerical model to study the arc behaviour and interaction phenomena between a plasma arc and a superimposed laser beam. M. Shome [2007] used Ashby–Easterling analytical model based on Gaussian heat source distribution to determine the peak temperature at different locations of the HAZ in a butt welded situation by considering a disc diameter proportional to the electrode diameter and limiting conditions defined by the current density. Shome et al., [2004] developed an analytical model to accurately predict the grain size of the HAZ that experience thermal cycles with large kinetic strengths, taking into consideration the transition in grain growth kinetics following precipitate dissolution. Shome et al., [2006, 2004] simulated the HAZ using the Rykalin-3D (thick plate) heat-transfer model and generated a continuous cooling transformation (CCT) diagrams for HSLA steel. Tadamalle et al., [2014] estimated the weld pool geometry and cooling rate in laser welding. Yang et al., [2008] simulated the laser shock peening of Al alloy by FEM modelling to provide the overall numerical assessment of the characteristic physical processes and transformations. Zähr et al., [2012] simulated the effect of process gases in the TIG welding process.

2.7 Effect of Residual Stresses on steel

Residual stress is defined as the non-uniform plastic flow due to application of manufacturing operations like welding, surface hardening, cold and hot working, forging and so on [Mohanty, 1994]. The residual stresses are generated to balance the force system inside the workpiece. It means if the component is affected by residual compressive stress in one of the side than another side must be balanced by the residual tensile stresses. The researches explained that the residual stresses generated into the system may be destructive or constructive. If the nature of stresses is tensile, it adversely affects the fatigue and wear properties. The compressive nature of stresses is beneficial same for wear and fatigue properties. It is very essential for a design engineer to know the beneficial and adverse effects of residual stresses so that he could maintain the prescribe safety limit of applied force for an

engineering component. Sometimes residual stresses are induced into the components to increase the wear, corrosion and fatigue properties [Totten, 2002].

The residual thermal stresses are introduced by the surface hardening processes into the substrate surface. The thermal gradient during heating and cooling also make the substantial change in the volume of the component. There is the expansion of the surface during heating due to thermal gradient. The heat is rapidly transferred to core by conduction due to which the cooling of surface becomes very fast compared to interior [Dieter, 1988]. The temperature difference between the interior and surface increase upto maximum limit and then reduces. As a result when the heat is transferred from the surface to core the surface shrinks more than the interior which creates the pressure against the interior. Since the core is heated at the same time due to transfer of heat so interior is not much shrink by the same volume. This condition builds the tension in the substrate surface and compression in the interior region. Due to this irreversible plastic flow occurs into the system. The further reducing of temperature with time, there is a change in situation. The compressive stresses are generated at the surface with decrease of temperature and tensile stresses in the interior side [Dieter, 1992].

The various factors are involved to introduce residual stresses into the system. The surface hardening processes also increase the volume due to phase transformation. However, every product of austenite decomposition, i.e., martensite, bainite or pearlite would be associated with a volume increase [Inoue et al., 1981]. The martensite forms promptly on the substrate surface of steel after quenching. The martensitic formation is primarily associated with the volume expansion, whereas for a certain time the interior remains as austenite because of it is still hot. After some time when the austenite phase beneath the surface transform into martensite, the expansion of volume due to conversion is constrained by the hardened surface layer causing in compression in the core and tension at the surface [Leggatt, 2008]. The thermal shrinkage in the interior is delayed by the hard surface layer. Researchers described that this type of volume expansion and contraction may cause severe plastic deformation leading to distortion of the workpiece or even localized braking which is known as quench cracking. The component of large size have a high cooling rate due to rapid heat transfer contribute to high thermal contraction and suppresses the volumetric expansion. The researchers studied that for a fix cooling rate there is a decrease in the residual stress if the thermal gradient decreases with the decreasing cross section. So the residual stresses are primarily depend upon the size of workpiece, cooling rate, phase transformation and hardenability of steel [Shipley and Moore, 2002]

2.8 Effect of surface modification processes on residual stresses

The use of surface modification process introduces the residual stresses on the material by phase transformation and non-uniform deformation during heating and cooling cycles [Shipley and Moore, 2002]. If the transfer of phase is ferrite to pearlite or martensite, the volume increases hindered by the bulk material produces compressive residual stresses. Collins [1993] described that the compressive residual stress is induced by surface hardening process to retard the nucleation and propagation of surface cracks. Researchers [Kobasko et al., 2007; Kobasko, 2010 Kobasko, 2012] investigated that thermochemical treatment like carburizing introduces the compressive stresses by delay in surface martensite formation due to the high surface carbon content. Kobasko et al., described that carburizing followed by intensive quenching produces the compressive stresses on the surface with subsequent increase in fatigue and fracture properties of steel. Farfan et al., [2004] found that the fatigue strength is effectively increases by the hardening case depth and brittle fracture is observed in a hard case layer and ductile fracture in the core of the specimen.

Terent et al., investigated the effect of nitriding on residual stress and fatigue strength of structural steel. He pointed out that the ion nitriding essentially increases fatigue resistance of all structural steels due to the saturation of metal surface by nitrogen and causing in surface layer compressive stresses. Kanchanomai et al., studied the effect of residual stress on fatigue behavior and mechanism of carbonitrided AISI 1015 steel under uniaxial cyclic loading and found higher fatigue resistance due to the presence of compressive stresses in case layer. Leskovsek, V. et al., have studied the effect of plasma nitriding and nitrocarburizing for surface treatment of AISI H11 steel and found residual compressive stresses in the diffusion zone.

Lee et al., [2006] have investigated the effect of flame hardening of 12 Cr steel and found that tensile stresses are produced due to a phase transformation and compressive stresses due to thermal contraction. Researchers [Schöpfel et al., 1997; Grum et al., 2001; Lin and Ericsson, 1992; Kristoffersen and Vomacka, 2001] have studied the effect of induction hardening on the residual stresses and found the compressive stresses at the surface followed by tensile residual stresses at the core. Sochalski-Kolbus et al., [2015] have investigated the residual stresses in Inconel 718 by neutron diffraction technique and found compressive stresses over the surface due to precipitation of different phases and thermal shrinkage developed by high heating and cooling rate. De and Debroy [2011] described in a perspective way the effect of residual stresses in welding and concluded that residual stresses occur in the welding process due to difference in cooling rates in the distinct regions of the welding, non-

uniform instantaneous thermal cycle, and volume change due to phase transformations. Wavare and Ramgir [2015] studied the effect of magnetic arc blow on the stresses during arc welding processes.

2.9 Effect of surface modification processes on wear resistance

Wear is commonly defined as the undesirable deterioration of a component by the removal of material from its surface. It generally happens because of detachment and displacement of constituent particles from the substrate surface. The deterioration of materials rapidly increases with the wear and significant reduction in the properties of the materials. There are various reason of wear in the material. It may be due to rubbing of materials against each other, eroding effect of gaseous and liquid media, scratching of solid particles from the surface and due to corrosion effect. The surface modification processes are used to increase the wear resistance of the substrate surface by appreciable phase transformation of the surface.

Kikuchi et al., developed a high-frequency induction heating (IH) with fine particle peening (FPP) system to increase the wear resistance of the steel. Chen et al.,[2008] studied the wear conditions of the rolling element bearings with the developed statistical monitoring charts of occupation probability (OP) in the clusters. Buchely et al.,[2005] studied the effect of microstructure on hardfacing alloy and find that W-rich hardfacing alloys have the high wear resistance due to unique combination of tough M_6C and hard, massive MC carbides in a eutectic matrix. Chatterjee and Pal [2003] developed a new hardfacing electrode by adding niobium as carbide forming element and molybdenum as a matrix hardening agent and successfully reduces the wear rate of cast iron. Chatterjee and Pal [2006] studied the effect of hardfacing on cast iron to increase the erosive wear resistance and find that use of modified electrode increases one and half times erosion resistance of hardfacing deposits than that of commercial hardfacing electrodes. Murray and Clare [2016] studied the morphology and wear behaviour of electric discharge coatings and found that the single layer coating of TiC produces the high wear resistance as compared to double coating of Si and TiC. Gautham et al., [2013] used the plasma spraying of Ni-Cu-Cr-Al multi-component coatings to increase the wear resistance of steel surface. Rajeev et al., [2014] developed stelite coatings on valve steel material to improve the wear resistance and service life of component. They used Plasma Transferred Arc (PTA) and Cold Metal Transfer (CMT) techniques for deposition of coatings on the surface. Shariff et al., [2013] studied the effect of laser surface modification on rail steel and found that the laser surface modification effectively increases the wear resistance by phase transformation as compared to as received pearlitic rail steel. Singh et al., [2010] investigated the effect of spark plasma sintering for surface modification of Al alloy and found superior

wear resistance as compared to base material. Wang et al., [2008] studied the metal to metal sliding contact and its effect on wear resistance of steel.





CHAPTER 3

PROPERTIES REQUIREMENT FOR A BEARING COMPONENT

The present chapter deals with the detailed description of various properties required for industrial application of AISI 8620 steel as a bearing component. The commercial requirements (standards) of the characteristics/properties of bearing component of the AISI 8620 steel have been studied to form the target of this work to achieve. AISI 8620 is a case hardenable low alloy steel and generally used for automotive and large bearing cages. Typical requirement of bearing is hardened faying surface with tough core according to the service industry. However thoroughly hardened bearings component is also used in industry, but they have a relatively low service life, high production and maintenance cost compared to a case hardened bearing component.

3.1 The characteristics of bearing materials

The rolling elements and bearing rings are generally affected by the cyclic large pressure with a certain extent of sliding. The cages of bearing experienced sliding contact, tension and compression due to cyclic loading against the rolling elements in either single or double bearing cages. Thus, materials should have following characteristics for working as bearing ring, rolling element and cages.

1. High hardness
2. High wear resistance
3. High dimensional stability
4. High mechanical strength
5. High traction (rolling contact) fatigue strength

Beside these characteristics, resistance to deterioration under frictional heating, impact loading and corrosive environment also required depending upon particular applications. In view of these the relevant properties primarily required for good bearing materials are stated below.

1. Hardness

The hardness plays most important role in designing the bearing components. The lower hardness materials used for bearing component cause premature failure of the components. Hardness of a material primarily depends upon the metallurgical phases present in the matrix of the surfaces. In this regard the type, amount and distribution of phases in the matrix plays most

significant role. So material should be hard enough to increase the life cycle of the bearing components by resisting under cracking and material loss in service.

2. Wear Resistance

The bearing components are largely affected by the cyclic motion, pressure and high impact. The wear adversely affects the service conditions of the bearing components. The wear in the bearing components causes the changes in the dimensions of the metallic bearing surface. Due to the presence of foreign particle, metal to metal contact, mechanical and chemical phenomena worn the surface up to such an extent that it makes the bearing unserviceable.

3. Dimensional stability

Dimensional stability is one of the prime necessary characteristics of a bearing component. Conventional heat treatments used for modification of microstructure with hard phase transformation are often known as major instability in dimension. These structural changes largely occur due to development of tensile residual stresses prompted by phase transformation that results inappropriate failure of a bearing component. Control of microstructure and residual stresses provide long service to the bearing component.

4. Mechanical strength

The mechanical strength should be enough to prevent pull out of material from the bearing component. A low mechanical strength of faying surface causes local yielding in the matrix of bearing component resulting distortion in it.

5. Fatigue strength

Fatigue occurs due to having dynamic loading that exceeds the fatigue strength of the bearing component. Under severe conditions, the surface may be damaged due to propagation of surface fatigue cracks. These surface cracks may cause premature failure of a bearing component. Thus the bearing should have high fatigue strength.

Besides these properties, low cost of material, low coefficient of friction, corrosion resistance, high thermal conductivity, low thermal expansion and compressive residual stresses of the surface are some other properties necessary for a bearing component.

3.2 The microstructure requirement for a bearing material

The properties of a case hardened bearing component basically depend upon the final microstructure of the substrate surface. In case of bearing component the high hardness is required on the substrate surface. Martensite is a hard phase forms in carbon steel after rapid cooling from its intercritical temperature range. . The martensite phase has the needle type and

lath type morphology, which largely depends upon the C content of the steel. In high carbon steel, it is found as needle type where as in low carbon steel appears as lath type. The lath martensite structure in the matrix of the substrate surface is desirable for a bearing component as it provides relatively high hardness along with good combination of fatigue, wear and mechanical properties. The needle type martensite is generally undesirable due to its relatively lower fatigue properties and proneness to micro cracks over the surface.

3.3 Standard specifications for bearing component

As per ASTM F-2431 and F-2436 following specifications are used for bearing component as shown in table 3.1. Other properties like mechanical strength, fatigue strength depends upon the application of the material.

Table 3.1 Typical requirements for bearing application of AISI 8620 steel.

Application	Minimum Depth of Surface Modification	Case Hardness	Core Hardness	Surface roughness	Hardening Processes
Rolling bearing Rings (Cages)	10% of Thickness of bearing rings	470-600 Hv	250-350 Hv	0.51 μm	Diffusion Processes
					Advance Energy methods
					Flame/Induction Hardening

Typical hardening processes used in industry for case hardening of bearings are diffusion, advance energy methods, flame and induction hardening. The present study involves the use of TIGA process for modify the surface properties in according to the large bearing applications.



FORMULATION OF PROBLEMS

4.1 Formulation of Problem

It is a worldwide demand to replace a costlier material by a cheaper material without affecting the working capabilities. The average economic loss due to wear and corrosion alone in United States is reported as 500 billion USD per year at current prices, which is about 4.2 % of the gross national product. Therefore lots of research is carried on to develop cheaper materials and processes to save the economic losses. In this regard surface modification process plays an important role primarily to modify the properties of service interactive surface to increase its wear and corrosion resistance without affecting the core properties. The surface modification by Tungsten Inert Gas Arcing (TIGA) process is a comparatively new approach to modify the surface properties by introducing an arc between the non-consumable tungsten electrode and workpiece under an inert shield environment. In this process a rapid heating and cooling of the substrate introduces desirable phase transformation to the surface to increase its wear and corrosion resistance up to a certain depth. It is generally understood that high hardness materials are good wear resistant as compared to soft materials.

Surface modification of steel through TIGA process creates different zones (FZ and HAZ) on the surface. The phase transformation of these zones depends upon their thermal cycle defined by heating rate, peak temperature and cooling rate. Several researchers have found that cooling rate effectively controls the phase transformation in steel surface. Higher cooling rates make the hard phase transformation from austenite into the steel surface. Integrity of the modified zone in critical applications is largely adjudged by its relevant properties, which primarily depends upon microstructure of the fusion zone (FZ) and heat-affected zone (HAZ). The morphology of modified zone is largely dictated by its cooling rate, which is primarily governed by the efficiency of the sink depending on temperature distribution (isotherm) in the fusion zone (FZ) and heat affected zone (HAZ) of the base metal. The temperature distribution of modified zone, affected by the heat content and geometry of the fusion zone, dictates its thermal cycle and influences the solidification behaviour of the melt. Hence a suitable control of these aspects of fusion zone often becomes a matter of great interest.

. In autogenous TIGA process, one can manipulate the arcing process primarily by controlling the current, voltage and arc travel speed influencing the isotherm (temperature

distribution) and thermal cycle, and thus it has capacity to manipulate the solidification mechanism of fused metal at the substrate surface and the characteristics of heat affected zone (HAZ) of the base metal. The control of current enables shaping of a fused zone with a wide range of variations.

However, the TIGA process may be proved as a better process of surface modification, especially when it is used with pulse current. This is because the use of pulse current instead of continuous current facilitates more precise control of energy input and its distribution in the system. The pulse current TIG arcing (P-TIGA) has number of advantages that primarily include intended operation at relatively low heating, less distortion of the substrate and precise control of isotherm and thermal cycle leading to control necessary phase transformation and microstructure. The use of pulse current in TIGA process has been found more effective for control of the arc to use with further precision of desired localized performance. This is because it can operate at a relatively higher energy input of high current but maintains a relatively low net heating of the base metal primarily due to low heat build-up under interruption in arcing causing interrupted fusion and solidification of base metal. It also consequently reduces distortion in work piece. It allows greater control of heating with comparatively larger fusion with deeper penetration at a faster speed of arc movement. Thus, it may result in improved quality of thermally modified zone, especially with respect to its microstructure. The knowledge can be used in various industries including electrical power generation, bearing manufacturing, turbine manufacturing and Gear manufacturing where surface modification of steel provides superior wear resistance that gives more reliability and longer life of the system.

4.2 Objectives

After finding the potentials of P-TIGA process to produce an improved surface modification, effort has been made to develop knowledge of critical application of pulse parameters of autogenous P-TIGA process for optimum surface hardening of case hardenable AISI 8620 steel substrates in comparison to that produced by using C-TIGA process. The knowledge includes appropriate control of pulse parameters primarily in order to manage the thermal cycle and isotherm of the heating zone giving rise to desired surface modification of the substrate primarily defined by its geometry and microstructure. In this regard the relatively low heating characteristics of the pulse current arcing process is also kept under consideration for comparatively lower distortion and residual stresses of the substrate than that observed in case of the conventional non pulse arcing process. The innovation in surfacing is to be established after carrying out comparative studies using the C-TIGA for the same purpose. The characterization of improvement in properties of substrate is primarily defined by its

characteristic properties resulting in longer life with higher service capacity and safety. It is primarily approached from the following angles as stated below.

1. Mathematical modeling of thermal behavior of autogenous continuous and pulse TIGA surfacing as a function of process parameters and their effect on profile of heating and phase transformation in AISI 8620 steel.
2. Setting a target to improve the surface characteristic/properties of AISI 8620 steel in reference to their minimum requirement available in a commercial product of this steel as a bearing component.
3. Experimental verification of the control of isotherm and thermal cycle and behavior of phase transformation in autogenous P-TIGA surfacing up to desired depth of AISI 8620 steel substrates to achieve required properties superior to those found in case of using the C-TIGA process.
4. To develop a thorough understanding of the scientific and technological aspects of the C-TIGA and P-TIGA process to explore the possibilities of its applications in more challenging areas of producing wear resistant hard surfacing of steels especially with respect to control of microstructure.
5. To study the effect of the factor ϕ , mean current (I_m) and heat input (Ω) of P-TIGA process by analyzing their influence on thermal behavior and geometry of weld pool in substrate surface in order to develop an understanding of efficient use of them to produce high wear resistant substrate surface.
6. To study the effect of arcing parameters on the residual stresses generated during C-TIGA and P-TIGA.
7. To study the effect of TIGA parameters on tribological characteristic of the modified surface produced by both the continuous and pulsed TIGA surface modification process using the single and multipass procedures.
8. Finally to establish superiority of the P-TIGA process to improve the bearing properties of AISI 8620 steel over those recommended in commercial standard.



CHAPTER 5

EXPERIMENTATION

The chapter consists of the analytical and experimental procedures employed in the present work and describes details of the processing route employed for surface modification of AISI 8620 steel substrate. The surface modification of AISI 8620 steel is carried out by C-TIGA as well as P-TIGA processes using single and multi-pass procedures. Further, various equipments/ instruments and procedures used to investigate composition, hardness, mechanical properties, wear behavior and residual stress analysis of the modified surface are discussed.

5.1 Base Material

The surface modification has been carried out on a 18 mm thick plate of control rolled low alloy AISI 8620 steel as base material using direct current electrode negative (DCEN) continuous tungsten inert gas arcing (C-TIGA) and pulsed tungsten inert gas arcing (P-TIGA) processes using 3.2 mm diameter tungsten electrode of specification AWS EWTh-2 grade. Chemical composition as per ASTM of the base plates as per test certificates given by the supplier as well as obtained through spark emission optical spectroscopy have been shown in Table 5.1. The results of chemical analysis obtained by using spark emission spectroscopy are found to be in good agreement with the results of the test certificates given by the supplier. The surface modification of AISI 8620 steel was performed with DCEN polarity under commercial Ar (99.98%) gas shielding at a flow rate of 18 L/min.

Table 5.1 Typical requirements for bearing application of AISI 8620 steel.

Materials	Grade	Chemical composition (Wt. %)										
		C	S	P	Mn	Si	Cr	Ni	Mo	Al	Cu	Fe
Base Plate 18mm Thick (TC)	AISI 8620	0.23	0.002	0.01	0.69	0.21	0.63	1.19	0.19	0.02	0.02	rest
Base Plate 18mm Thick (SEOS)	AISI 8620	0.21	0.002	0.01	0.68	0.19	0.63	1.15	0.19	0.02	0.02	rest

TC-Test certificate, SEOS-Spark emission optical spectroscopy

During surface modification the plate was tightly placed in a fixture to avoid distortion. The surface modification of plate was executed in horizontal position by a perpendicularly positioned centrally located welding gun, which was travelling on an automated trolley. Surface modification was performed by maintaining the gap of 2 mm between the electrode tip and the

substrate surface. The flow rate of gas was controlled with the help of a flow meter and a pressure regulator fitted to the gas cylinder.

5.2 Thermomechanical Simulator

The Gleeble 3800 thermomechanical system is used to predict the CCT curve and dilation curve of AISI 8620 steel plate. The Gleeble-3800 as shown in figure 5.1 is a fully integrated digital closed-loop control thermal and mechanical testing system. Easy to use Windows based computer software, combined with an array of powerful processors, provide an extremely user friendly interface to create, run and analyze data from thermal mechanical tests and physical simulation programs. The cylindrical sample of 6 mm diameter and 65 mm length is used in thermomechanical simulator to estimate CCT curve. Thermocouples were attached to the samples thus prepared by spot welding technique using thermocouple welder, which comes with the Gleeble system. Thermocouples were of K type and attached maintaining a distance of 1mm from each other. The sample thus prepared was put in the Gleeble 3800 system for the experiment. Data as required for the simulation was entered into the computer system in the Rosenthal 3-D dialogue box, while the sample was inserted into the vacuum chamber and tightened accordingly. The experiment was initiated after satisfactory vacuum pressure of 10^{-3} Torr. The parameter used to estimate the CCT curve and dilation curve has been given in Table 5.2.



Fig. 5.1 Typical requirements for bearing application of AISI 8620 steel.

Table 5.2 Parameters used in thermomechanical simulation for CCT curve.

Heating rate:	200 C/s
Specific heat:	0.475
Thermal conductivity:	0.46
Density :	7.84
Holding time :	0.01 sec
Peak temperature :	1300 °C
Temperature regime to estimate cooling rate($T_{8/5}$)	800°C to 500°C
Cooling rate (°C/s)	Heat input (kJ/cm)
30	34.87
50	20.92
70	14.92
100	10.46
120	8.72
150	6.97
170	6.14

5.3 TIGA Power Source

A, DC (direct current) arcing/welding power source made by ESAB (Model no. Aristo 2000-LUD 450 UW) was used in the current study. The power source was having an advantage of operating different arcing and welding operations such as MIG, GMAW, SMAW, GTAW, C-TIGA and P-TIGA. The machine can be operated in synergic and non-synergic modes by using several commands in respect to different materials, electrode diameter and filler wire in the presence of protective environment. During operation with the C-TIGA and P-TIGA the non-synergic mode is used to operate the power source where all the parameters are manually settled with maintenance of appropriate correlations among them. The power source was fitted with a control panel along with screen for displaying different set of parameters as well as soft push buttons to input different parameters of arcing process. The power source was connected with 3-phase electrical supply for its operation as per requirement.

5.4 Fixture and Torch Manipulator

The fixture and torch manipulator are required to hold the base material properly and guide the welding torch during operations of surface modification by TIGA process.

5.4.1 Welding fixture

To fix the base plate rigidly in order to avoid distortion during TIGA process, a fixture was used as shown in Fig. 5.2. The fixture consists of a thick mild steel supporting plate of size $450 \times 350 \times 40$ mm and two clamping plates of dimension $300 \times 150 \times 40$ mm. During TIGA process the base plate was tightly stable and clamped in the fixture. The clamping force was released after the plates naturally cool down to ambient temperature.

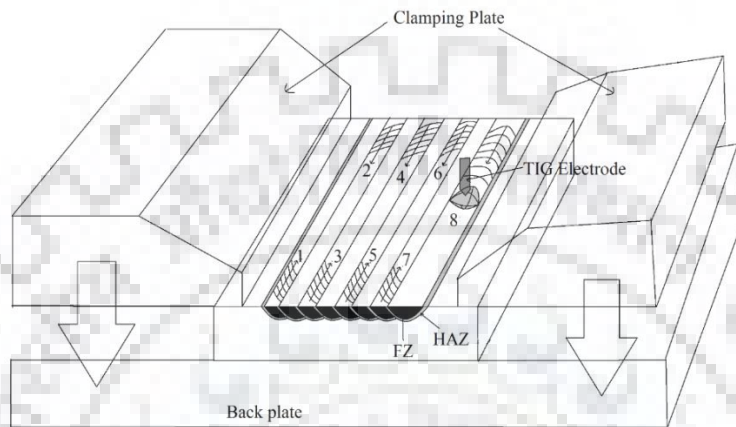


Fig. 5.2 Schematic diagram of fixture and work piece for surface modification by TIG arcing process.

5.4.2 Torch manipulator

A mechanized TIGA torch manipulator, “Gulco make KAT” travel carriage has been used in this work. It was capable to grip the torch strictly in the arms and clamping pivots to regulate it at any anticipated position with the help of rack and pinion arrangement. The torch manipulators were also capable to increase the travel speed in the range of 2.5 to 85 cm/min with an electronic display during surface treatment. The reliability of the digital reading of travel speed of the carriage was verified before use by measuring the length and time of travel with the help of a scale and a stopwatch of least count of 0.01 second respectively at different speeds.

5.5 Instrumentation and Recording

Instrumentation and recording include recording of thermal characteristics of the fused pool at different operating parameters.

5.5.1 Measurement of temperature of fusion pool

The temperature of the fusion pool was recorded with the help of an R-Type thermocouple (Pt-13 % Pt-Rh) of 0.25 mm diameter. The thermocouple was connected with a computer through a “Strain Buster” (decentralized strain/temperature measuring module) for recording the output. The Strain buster was capable of recording the output of the thermocouple at a time interval of 10 ms in both of its two channels. Before using the thermocouples and

“strain buster” for recording of temperatures, they were calibrated within the required temperature range by a known heating source. The output of thermocouple in terms of volt was converted to temperature. The output of the thermocouple as a function of temperature considered through its calibration has been shown in Fig. 5.3. The circuit diagram along with cooling system of welding torch head and the photograph of complete welding and recording setup have been shown in Fig. 5.4 (a) and (b) respectively.

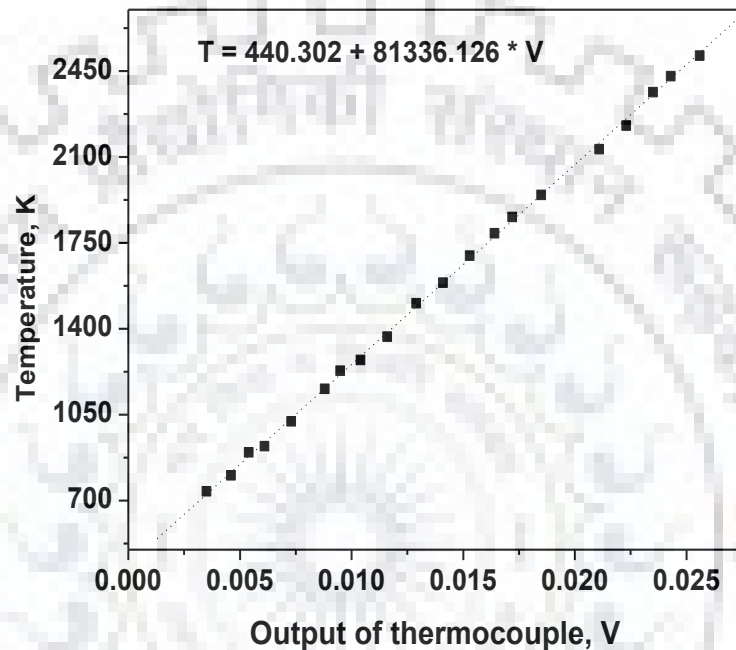
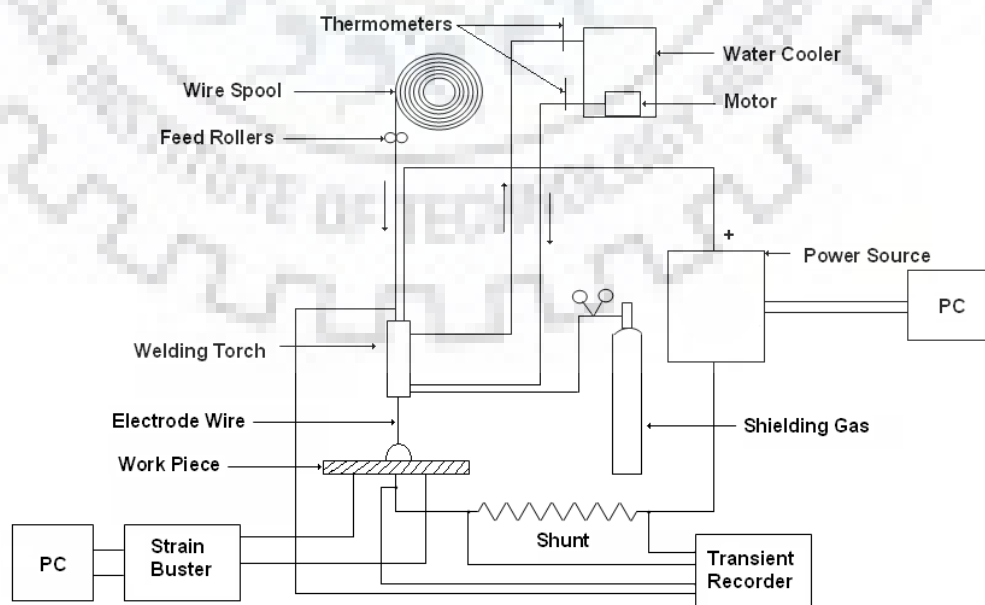


Fig. 5.3 Diagram showing the calibration of strain buster and thermocouple.



(a)



(b)

Fig. 5.4 (a) Schematic circuit diagram of welding and recording set up along with cooling system of torch head. (b) Photograph of the experimental setup used for TIGA process.

5.5.2 Estimation of heat input (Ω)

The heat input (Ω) during C-TIGA and P-TIGA processes can be predicted as a function of arc voltage (V), travel speed (S) and arc current or mean current (I or I_m), and arc efficiency (η_a) as follows [Maruo et. al, 1984].

$$\Omega = \frac{\eta_a \times V \times [I(or)I_m]}{S} \dots\dots\dots(5.1)$$

The mean current (I_m) of the P-TIGA process as a function of background current (I_b), pulsing current (I_p), duration of background current (t_b) and peak current duration (t_p) may be obtained as [Lancaster, 1984] as

$$I_m = \frac{(I_b t_b + I_p t_p)}{(t_b + t_p)} \dots\dots\dots(5.2)$$

In case of AWS EWTh-2 grade electrode under protection of argon gas the η_a of TIGA process was taken as 70% to 85% [Dupont and Marder, 1995].

5.5.3 Estimation of average fusion pool temperature

The average fusion pool temperature ($T_{WP} = T_d$) generated during TIGA process was estimated [Goyal et al., 2008] by considering the temperature (T_d) of the point (x(ξ), y, z) due to concentrated arc heating using double ellipsoidal heat source as follows (Fig.5.5).

$$T_d = \frac{3\sqrt{3} \cdot Q_{AW}}{\rho \cdot c \cdot \pi \sqrt{\pi}} \int_0^t \left[\frac{dt'}{\left(\frac{A'}{\sqrt{(12a(t-t') + c_{hf}^2)}} + \frac{B'}{\sqrt{(12a(t-t') + c_{hb}^2)}} \right)} \right] + T_0 \dots\dots\dots(5.3)$$

Where,

ρ , c and a are mass density, specific heat and thermal diffusivity of the workpiece. The a_h , b_h , c_{hf} and c_{hb} are the ellipsoidal heat source parameters defined by a location having at least a power density of 5% to that of the center on surface of the ellipsoid. Q_{AW} is the arc heat transferred to the weld pool and estimated by the following equation.

$$Q_{AW} = \eta.V.I \text{ Joule} \dots\dots\dots(5.4)$$

The η is arc efficiency, V is arc voltage and I is arc current respectively,

$$A' = r_f \cdot \exp\left(-\frac{3(x - v.t')^2}{12a(t - t') + c_{hf}^2} - \frac{3y^2}{12a(t - t') + a_h^2} - \frac{3z^2}{12a(t - t') + b_h^2}\right) \dots\dots\dots(5.5)$$

$$B' = r_b \cdot \exp\left(-\frac{3(x - v.t')^2}{12a(t - t') + c_{hb}^2} - \frac{3y^2}{12a(t - t') + a_h^2} - \frac{3z^2}{12a(t - t') + b_h^2}\right) \dots\dots\dots(5.6)$$

Where, r_f and r_b are the proportion coefficients in front and behind the heat source, estimated as:

$$r_f = \frac{2 \cdot c_{hf}}{(c_{hf} + c_{hb})} \dots\dots\dots(5.7)$$

$$r_b = \frac{2 \cdot c_{hb}}{(c_{hf} + c_{hb})} \dots\dots\dots(5.8)$$

The arc efficiency for the TIG arcing process is considered as 75% and the suitable values of the ellipsoidal axes parameters are selected by measurement of fusion pool geometry. The c_{hf} (in front of the heat source) and c_{hb} (behind the heat source) are considered as $c_{hf} = a_h$ and $c_{hb} = 2 c_{hf}$ described by Goyal et al., [2009].

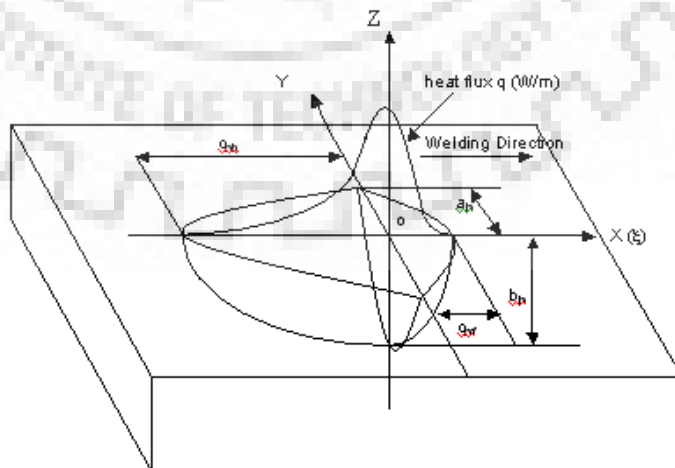


Fig. 5.5 Schematic illustration of double ellipsoidal heat source (volumetric heat source).

5.5.4 Estimation of fusion isotherm

The fusion isotherm as a function of arc current (I) and travel speed (S) of different temperature for C-TIGA process has been estimated and plotted in longitudinal (XY) and transverse (YZ) direction using the software origin 8 using Eq. 5.3. Similarly, the fusion isotherm as a function of ϕ and f at different I_m at different temperature for P-TIGA process has been estimated and plotted using the software origin 6.1 using Eq. 5.3. The fusion isotherm dictates the geometrical and thermal aspects of fusion pool ultimately governing the properties of the modified zone.

5.6 Single pass TIGA Experimentation

The single pass TIGA experimentation gives a thorough understanding of thermal and geometrical aspects of modified zone through which it is possible to identify an optimized arcing condition to apply in substrate surface for desired phase transformation and properties. The single pass treatment is applied over the surface to optimize the arcing parameters in terms of higher hardness, high depth of modified zone and minimum distortion of the workpiece.

5.6.1 Single pass C-TIGA process

The surface modification of AISI 8620 steel was carried out by single pass C-TIGA process. The base plate was thoroughly mechanical and chemically cleaned before carrying out surface modification to remove any corrosion product or foreign particles adhering to the surface. The single pass TIGA process was carried out at a constant arc voltage of 11 ± 1 V considering increment of arc current from 70 A to 200 A with variation of travel speed from 5 to 15 cm/min. The heat input was varied through a variation of arc current and travel speed. The arcing parameters used during single pass C-TIGA process has been shown in Table 5.3.

Table 5.3 Parameters used in single pass C-TIGA process.

Arc Voltage (V)	Arc Current (I) A	Travel Speed (S) (cm/min)
11±1	70	5
		7.5
		10
		15
	100	5
		7.5
		10
		15
	130	5
		7.5
		10
		15

	170	5
		7.5
		10
		15
	200	5
		7.5
		10
		15

5.6.2 Single pass P-TIGA process

In case of P-TIGA process at a known I_m and travel speed (S), the pulse parameters I_p , I_b , t_p and f were varied to get different values of summarized influence of pulse parameters defined by the factor ϕ [Ghosh, 2017, Ghosh et al., 1994, Ghosh 1999, Ghosh et al., 2000, Ghosh et al., 2001 and Ghosh et al., 2007] of 0.04 to 0.44 respectively. For every set of arcing parameters five single pass bead, each of 65 mm in length, were applied and properties were studied to ensure reproducibility of the process. The combinations of parameters were facilitated to study and correlate the effect of pulse parameters and heat input on various features of modified surface. The P-TIGA parameters used during the single pass surface modification at different I_m has been shown in Tables 5.4, 5.5 and 5.6 respectively.

Table 5.4 Pulse parameters used in surface modification of AISI 8620 steel using P-TIGA process at I_m of 100 A.

Arc Voltage (V)	Travel speed (cm/min)	Heat Input (kJ/cm)	I_m (A)	I_{eff} (A)	ϕ	Pulse Parameters				
						I_p	I_b	t_p (sec)	t_b (sec)	f (Hz)
11±1	10	6.64	100	131	0.04	185	15	0.25	0.25	
				122	0.09	171	29	0.25	0.25	
				115	0.14	156	44	0.25	0.25	
				108	0.21	141	59	0.25	0.25	
				104	0.29	127	74	0.25	0.25	
				102	0.35	117	83	0.25	0.25	
				101	0.44	107	94	0.25	0.25	
				131	0.04	185	15	0.10	0.10	5
				122	0.09	171	29	0.10	0.10	
				115	0.14	156	44	0.10	0.10	
				108	0.21	141	59	0.10	0.10	
				104	0.29	127	74	0.10	0.10	
				102	0.35	117	83	0.10	0.10	
				101	0.44	107	94	0.10	0.10	

				101	0.44	107	94	0.10	0.10	
				131	0.04	185	15	0.05	0.05	
				122	0.09	171	29	0.05	0.05	
				115	0.14	156	44	0.05	0.05	
				108	0.21	141	59	0.05	0.05	10
				104	0.29	127	74	0.05	0.05	
				102	0.35	117	83	0.05	0.05	
				101	0.44	107	94	0.05	0.05	
				131	0.04	185	15	0.03	0.03	
				122	0.09	171	29	0.03	0.03	
				115	0.14	156	44	0.03	0.03	
				108	0.21	141	59	0.03	0.03	15
				104	0.29	127	74	0.03	0.03	
				102	0.35	117	83	0.03	0.03	
				101	0.44	107	94	0.03	0.03	

Table 5.5 Pulse parameters used in surface modification of AISI 8620 steel using P-TIGA process at a I_m of 130 A.

Arc Voltage (V)	Travel speed (cm/min)	Heat Input (kJ/cm)	I_m (A)	I_{eff} (A)	ϕ	Pulse Parameters				
						I_p	I_b	t_p (sec)	t_b (sec)	f (Hz)
11±1	10	8.97	130	171	0.04	241	19	0.25	0.25	2
				159	0.09	222	38	0.25	0.25	
				149	0.14	203	57	0.25	0.25	
				141	0.21	184	76	0.25	0.25	
				135	0.29	164	96	0.25	0.25	
				131	0.35	152	107	0.25	0.25	
				130	0.44	139	122	0.25	0.25	
				171	0.04	241	19	0.10	0.10	5
				159	0.09	222	38	0.10	0.10	
				149	0.14	203	57	0.10	0.10	
				141	0.21	184	76	0.10	0.10	
				135	0.29	164	96	0.10	0.10	
				131	0.35	152	107	0.10	0.10	
				130	0.44	139	122	0.10	0.10	
				171	0.04	241	19	0.05	0.05	
				159	0.09	222	38	0.05	0.05	

				149	0.14	203	57	0.05	0.05	10
				141	0.21	184	76	0.05	0.05	
				135	0.29	164	96	0.05	0.05	
				131	0.35	152	107	0.05	0.05	
				130	0.44	139	122	0.05	0.05	
				171	0.04	241	19	0.03	0.03	
				159	0.09	222	38	0.03	0.03	15
				149	0.14	203	57	0.03	0.03	
				141	0.21	184	76	0.03	0.03	
				135	0.29	164	96	0.03	0.03	
				131	0.35	152	107	0.03	0.03	
				130	0.44	139	122	0.03	0.03	

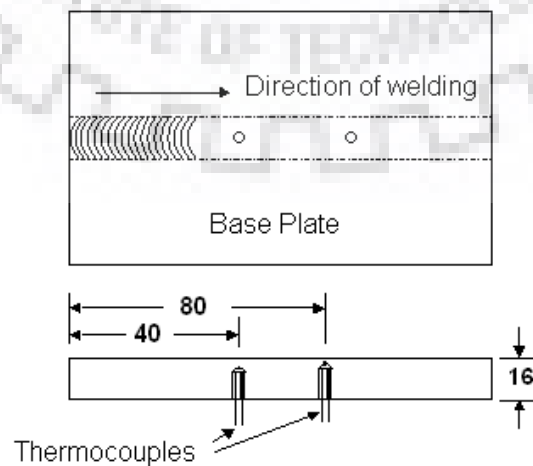
Table 5.6 Pulse parameters used in surface modification of AISI 8620 steel using P-TIGA process at a I_m of 170 A.

Arc Voltage (V)	Travel speed (cm/min)	Heat Input (kJ/cm)	I_m (A)	I_{eff} (A)	ϕ	Pulse Parameters				
						I_p	I_b	t_p (sec)	t_b (sec)	f (Hz)
11 ± 1	10	12.75	170	223	0.04	315	25	0.25	0.25	2
				208	0.09	290	50	0.25	0.25	
				195	0.14	265	75	0.25	0.25	
				184	0.21	240	100	0.25	0.25	
				176	0.29	215	125	0.25	0.25	
				173	0.35	200	140	0.25	0.25	
				170	0.44	180	160	0.25	0.25	5
				223	0.04	315	25	0.10	0.10	
				208	0.09	290	50	0.10	0.10	
				195	0.14	265	75	0.10	0.10	
				184	0.21	240	100	0.10	0.10	
				176	0.29	215	125	0.10	0.10	
				173	0.35	200	140	0.10	0.10	10
				170	0.44	180	160	0.10	0.10	
				223	0.04	315	25	0.05	0.05	
				208	0.09	290	50	0.05	0.05	
				195	0.14	265	75	0.05	0.05	
				184	0.21	240	100	0.05	0.05	

				176	0.29	215	125	0.05	0.05	
				173	0.35	200	140	0.05	0.05	
				170	0.44	180	160	0.05	0.05	
				223	0.04	315	25	0.03	0.03	15
				208	0.09	290	50	0.03	0.03	
				195	0.14	265	75	0.03	0.03	
				184	0.21	240	100	0.03	0.03	
				176	0.29	215	125	0.03	0.03	
				173	0.35	200	140	0.03	0.03	
				170	0.44	180	160	0.03	0.03	

5.6.3 Measurement of thermal behavior of modified zones (FZ and HAZ)

At a selected set of C-TIGA and P-TIGA parameters, the temperature of fusion pool was measured during single pass TIGA process in order to verify validity of the analytical expression of Eq. 5.3. To get fusion pool temperature after achieving its stability two thermocouples were inserted from the bottom of the workpiece in two dissimilar locations at distances of about 40 and 80 mm from the run on position of arcing as schematically shown in Fig. 5.6(a). The two wires of the thermocouple are kept separate with the help of sleeve and beads. The beads were push fitted in the hole prepared by drilling process. Thermocouples were placed at different depths corresponding to FZ and HAZ from the substrate bottom surface as shown in Fig. 5.6(a). The depth of placement, D_T , of thermocouple as schematically shown in Fig. 5.6 (b and c) respectively was calculated according to the estimation of fusion isotherm matching with melting temperature of the AISI 8620 steel as substrate plate using the analytical Eq. 5.3 given earlier [Goyal et al., 2008], so that the tip of the thermocouple wire fits under FZ and HAZ without having a direct contact with the arc.



(a)

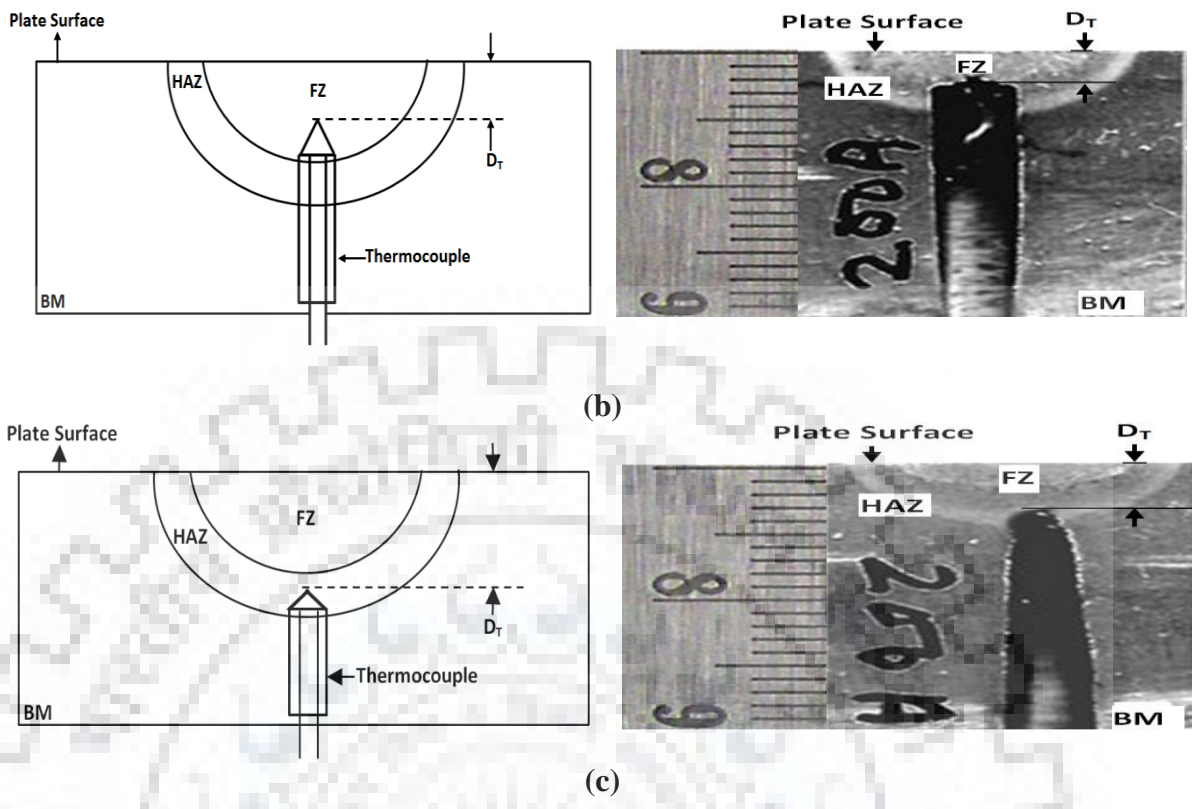


Fig. 5.6 Schematic diagram showing (a) location of thermocouples in modified zone. (b) Depth of placement of thermocouple (D_T) and typical macrograph showing placement of thermocouple in FZ. (c) D_T and typical macrograph showing placement of thermocouple in HAZ.

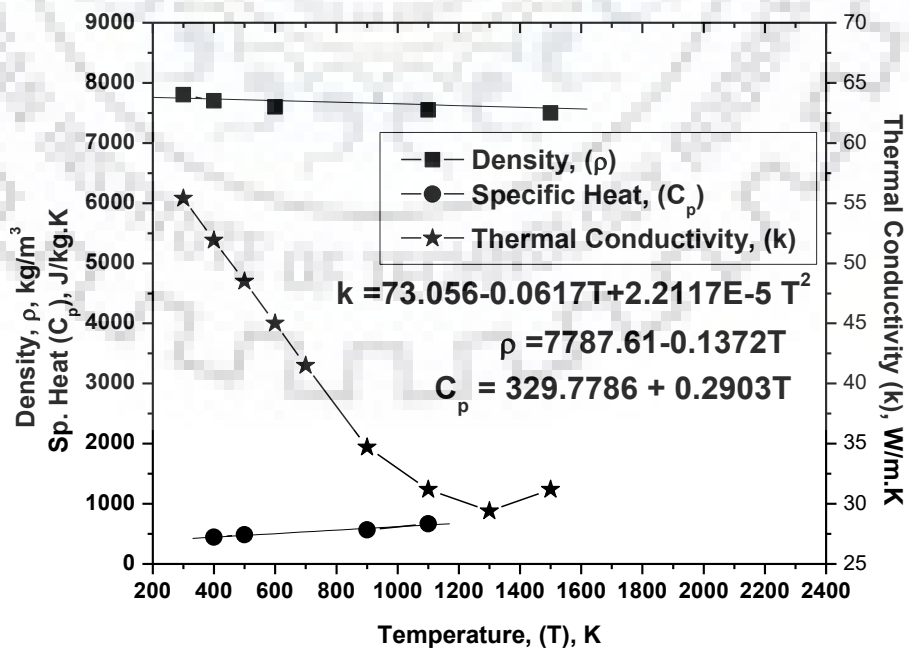


Fig. 5.7 Temperature dependent thermo-physical properties of commercial mild steel [Tamura et al., 1988].

The isotherm was estimated by considering the temperature dependent thermo-physical properties of materials [Tamura et al., 1988] as shown in Fig. 5.7 for commercial mild steel which are assumed to be in close approximation to those of the AISI 8620 steel used in this work. The thermal cycle was measured by using computerized data recorded as output of the thermocouples through “Strain Buster” as explained in section 5.4.

5.6.4 Estimation of single pass modified zone (FZ and HAZ) characteristics

The characteristics of modified zones observed at various arcing parameters of TIGA processes were analyzed with respect to geometrical aspects of modified zones (FZ and HAZ) as well as the microstructure of modified zones. The different aspects of the studies on modified zone characteristics have been detailed out as below.

5.6.4.1 Geometrical aspects of modified zone

The transverse section of the modified zone collected from its central part of fusion track assuring a stable arcing was polished by standard metallographic procedure and etched in 3% nital solution to reveal the FZ and HAZ geometry and its microstructure. The schematic diagram of geometrical aspects of FZ and HAZ and its typical macrograph was shown in Figs. 5.8 (a) and (b) respectively. The characteristics of different aspects of modified zone were studied by measuring the bead width (W_b), depth of penetration (P_d), HAZ width (W_{HAZ}) and area of fusion (A_F) with the support of image analyzer software.

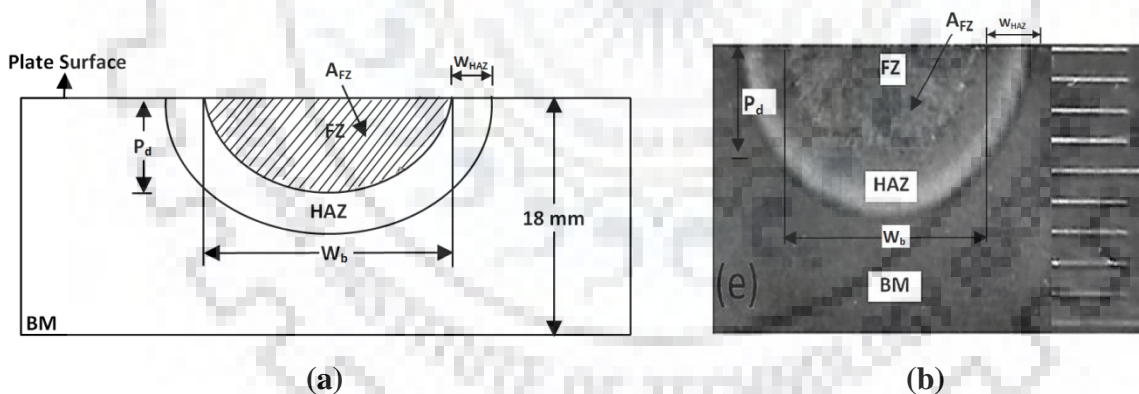


Fig. 5.8 (a) Schematic diagram showing geometrical aspects of modified zone and (b) typical macrograph of modified bead geometry.

5.6.4.2 Metallographic studies

Metallographic studies include the study of morphology of the FZ and HAZ with respect to its microstructure.

Studies on FZ and HAZ

The microstructures of FZ and HAZ at different arcing parameters were studied on the metallographically prepared transverse section etched in 2% nital solution. It was studied

qualitatively with respect to phase transformation as revealed under Leica make (Fig.5.9) optical microscope primarily at centre of the FZ. The specific features of the microstructure were recorded in the computer using Leica Application Suit software.

The HAZ of modified zone near to the fusion contour was studied using metallographically prepared and etched specimens of the modified zone at different C-TIGA and P-TIGA parameters. The different zones of a modified area have been shown in Fig. 5.10. The width of HAZ (W_{HAZ}) perpendicular to the fusion line was measured at several locations along it. The adobe photoshop 7.0 was used to analysis the captured images. The accuracy of the measurements was also confirmed by studying the same under optical microscope at suitable magnifications. Average of all the values of the width of HAZ measured on several specimens prepared at a given arcing parameter has been reported as its characteristic feature.



Fig. 5.9 Photograph of the Leica optical microscope used for recording microstructure.

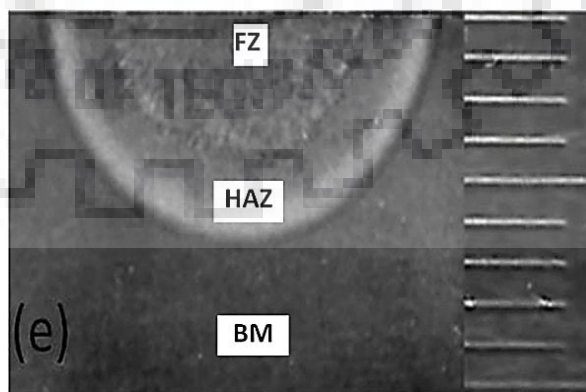


Fig. 5.10 Schematic diagram showing FZ and HAZ after modification by TIGA process.

The XRD analysis was carried out directly on the TIGA processed substrate surface. XRD analysis was carried out with 40 kW, 30 mA CuK α radiation (λ -1.504) at 2⁰/min scan rate within the scan angle between $0^0 \leq 2\theta \leq 90^0$ to analyze the different phases. The Fig. 5.11 shows the instrument used for XRD analysis made by Rigaku smartlab. Prior to XRD analysis the substrate surface was polished upto 1000 grit paper and properly cleaned by chemical (acetone) to remove any dust and corrosion particle.



Fig. 5.11 Photograph of the X-ray Diffractometer used for analysis of phases.

5.6.5 Hardness measurement

The Vickers micro hardness (VHN) of C-TIGA and P-TIGA has been studied at different locations of their etched transverse section revealing the FZ and HAZ. The Vickers micro hardness (VHN) of base metal, FZ and HAZ was measured by diamond indentation using a load of 300 gm. A photograph of the hardness testing machine used for measurement of hardness has been shown in Fig. 5.12. The hardness of FZ and HAZ was randomly measured at least on 10 locations of its central region. The indentations on FZ and HAZ were randomly made to obtain the true characteristics of hardness distribution. The average hardness observed in FZ and HAZ for the given set of parameters were found out for both C-TIGA and P-TIGA process. The average hardness was correlated with heat input Ω and Arc current (I) in case of C-TIGA whereas for P-TIGA it was correlated with the summarized influence of pulse parameters of arcing defined as ϕ , I_m and f .



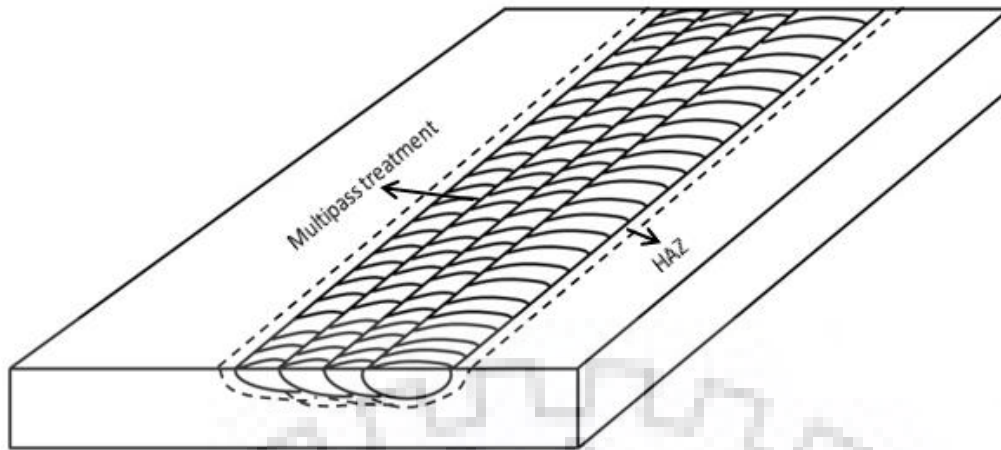
Fig. 5.12 Photograph of the hardness testing machine used for measurement of hardness.

5.7 Multi pass TIGA process

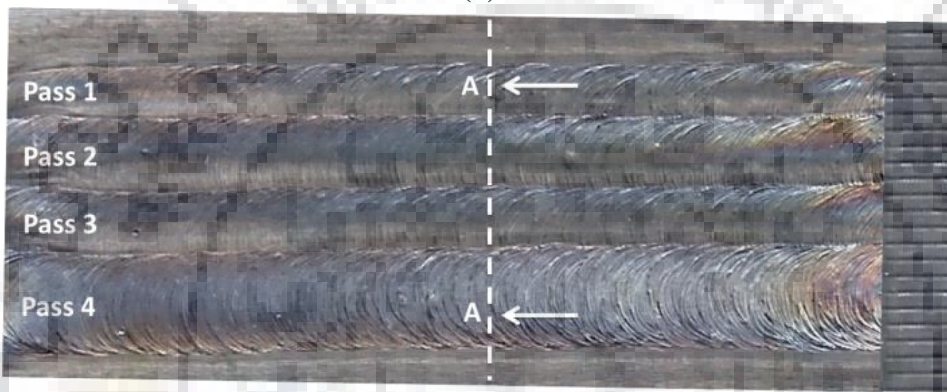
The single pass TIGA process is applied over the substrate surface to optimize the arcing parameters in terms of depth of penetration, hardness. The multipass TIGA process is applied over a substrate surface in reference to commercial perspective especially in bearing applications. The effect of multipass treatment by both the processes (C-TIGA and P-TIGA process) is studied and compared in terms of microstructural features and hardness distribution in its different thermally affected regions.

5.7.1 Preparation of multipass treatment

The controlled rolled AISI 8620 steel of 18 mm thick plate of size 65 x 100 mm has been used in preparation of multipass treatment. Multi-pass treatment of surface with 50% overlapping of fusion zone as shown in Fig. 5.13 (a and b) was carried out at optimum arcing parameters of single pass fusion, which was found to create maximum penetration and a width of fusion in both of the processes (C-TIGA and P-TIGA). Proper cooling of the substrate surface upto room temperature is insured after every pass to avoid excessive heat built up into the substrate surface. The schematic diagram (Fig. 5.13 (a)) is representing the modified surface after multi-pass treatment. The multipass treatment was carried out by direct current electrode negative polarity as stated earlier. Prior to multi pass treatment, the base plate was carefully scrubbed to remove the extra oxide film and any corrosion product adhering to the faying surface. The arcing parameters used during multi pass treatment under C-TIGA and P-TIGA processes are shown in Tables 5.7 and 5.8 respectively.



(a)



(b)

Fig. 5.13 Typical (a) Schematic diagram and (b) photograph of multi pass TIG arcing processed substrate surface.

Table 5.7 Arcing parameters used in multipass treatment using C-TIGA process

Arc Voltage (V)	Travel speed (S) (cm/min)	Arc Current (I) A	Heat Input (kJ/cm)
11±1	10	100	7.02
		130	9.28
		170	11.12

Table 5.8 Arcing parameters used in multipass treatment using P-TIGA process.

Arc Voltage (V)	(Ω) (kJ/cm)	S (cm/min)	I_m (A)	f	ϕ
11±1	8.97	10.0	130	2	0.04
					0.44
				10	0.04
					0.44
12.75		170	2	0.04	

		10.0			0.44
				10	0.04
					0.44

5.7.2 Metallographic studies on multi-pass modified zone

The transverse sections of the modified region prepared by using the multi-pass C-TIGA and P-TIGA processes were prepared for microstructural studies by standard metallographic technique and etched with 5% chemical (Nital) solution. Metallographic studies under optical microscope were carried out on the different thermally affected regions produced at multi-pass treated modified zone. The thermally affected regions are divided into five zones as shown in Fig. 5.14 respectively.

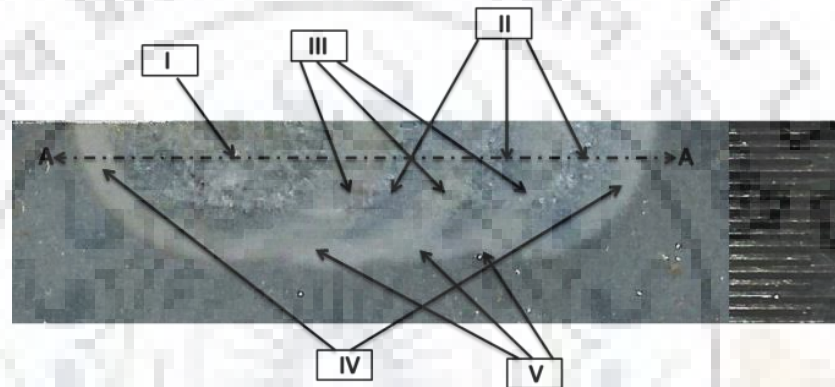


Fig. 5.14 Typical appearance of transverse section (A-A), representing (I) FZ (II) Reheated FZ (III) Reheat refined FZ (IV) HAZ (V) Reheat refined HAZ of the Multipass TIGA processed surface.

5.7.3 Hardness Studies

The distribution of hardness along the line A-A as shown in Fig. 5.14 was measured by Vickers micro hardness testing (Fig. 5.12) of Leitz Wetzlar Germany at a load of 300 grams having provision of magnification of image upto X500. Prior to carrying out testing the machine was calibrated by measuring the hardness of a standard sample at the same load.

5.8 Wear Characteristics of modified zone

The effect of optimized TIGA parameters for both the processes (C-TIGA and P-TIGA) on wear characteristics of modified zone have been studied and compared with non-treated AISI 8620 steel sample. Cylindrical pin samples (15mm × 6 mm ϕ) were used for the current study of wear characteristics. The pin samples that had horizontal surfaces in the contact area and rounded at the corners. The surface of the sample was polished using (100-1200) grit paper and cleaned by acetone to remove corrosion product and foreign particles from the pin surface.

The dry sliding wear tests were operated at a relative humidity of 35 to 45 % at ambient temperature and pressure.

The dry sliding test was conducted against the counter face of a hardened and polished round disk made of 52100 steel that had a hardness of 65 HRC. The Fig. 5.15 shows the schematic diagram of pin on disc apparatus. The losses of pin weight at different intermissions of time were measured. The pin is detached from the holder after each course, cooled down to room temperature, eliminates unattached wear particles, weighed, and stable further in exactly the similar situation in the sample holder so that the alignment of the sliding surface remained unchanged. The weight loss was taken by a weight weighing machine within an accuracy of 1×10^{-7} kg. The sample weight was measured five times, once after every 5 minutes of throughout an 30 minute period. Each test was performed at a constant load of 20 N and sliding velocity of 2.55 m/s and repeated three times with identical new samples. The investigation of wear rate was carried out by the final volume loss after stabilized period of time. The friction force as indicated on the wear machine was used to calculate the torque applied on the sample using the stable distance of apparatus lever arm. Finally the average coefficient of friction was calculated from frictional force and applied load.

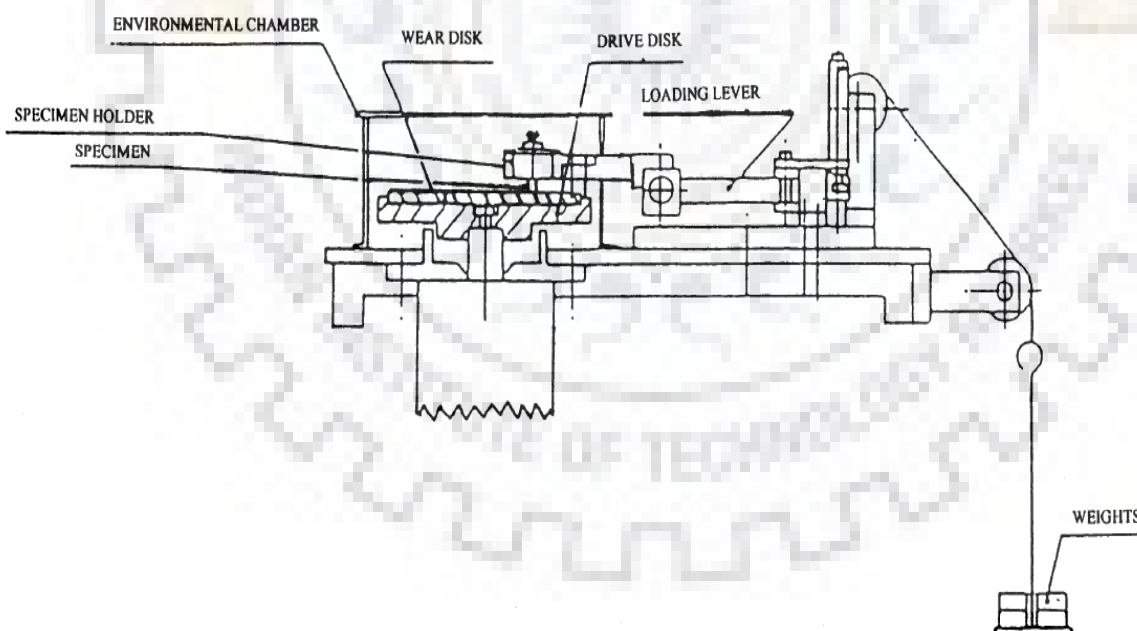


Fig. 5.15 Schematic diagram shows the Pin on disc apparatus [Tyagi et al., 2002].



Fig. 5.16 Photograph of the Zeiss Scanning Electron Microscope.

5.7.2. Estimation of wear rate

The analysis of wear rate and coefficient of friction (COF) is estimated through measurement of mass loss and friction force at different TIGA parameters in the modified zone as follows.

$$\text{Volume loss, mm}^3 = \frac{\text{mass loss, g}}{\text{density, g/cm}^3} \times 1000 \dots\dots\dots (5.9)$$

$$\text{Specific wear rate, mm}^3 \text{ N}^{-1} \text{ m}^{-1} = \frac{\text{Wear Volume (mm}^3\text{)}}{\text{Force (N) X Sliding Distance (m)}} \dots\dots\dots (5.10)$$

$$\text{COF} = \frac{\text{Applied Load}}{\text{Friction Force}} \dots\dots\dots (5.11)$$

5.9 Residual Stress and distortion studies

Residual stress analysis of modified fusion zone in single and multi-pass C-TIGA process and P-TIGA process has been studied with respect to effect of arcing parameters. stresses Residual stresses of the matrix adjacent to the surface of the modified zone were studied by the central drill hole technique as described in ASTM E-837 where a rosette type (A) strain gauge is used as shown in Fig. 4(a and b). Prior to fixing strain gauge the modified surface was properly cleaned by degreasing and chemical etching with 2% Nital solution to reveal the fusion zone. The three strain gages were oriented in the radial direction within the rosette and placed at equidistant from the rosette center. The two strain gages were positioned perpendicular to each other and the third one was positioned along its bisector. Drilling was carried out up to a depth of 1.2 mm using a diamond drill bit of 1.5 mm diameter. The depth of

drilling was measured with the help of a linear variable differential transformer having at least count of 0.001 mm connected to a digital displacement indicator. Prior to starting the incremental drilling operation, a zero setting of each strain gage was always confirmed.

The longitudinal and transverse residual stresses were calculated from the measured strains ϵ_1 , ϵ_2 and ϵ_3 using following equations.

Longitudinal Residual Stress

$$= P - Q \dots \dots \dots (5.12)$$

Transverse Residual Stress

$$= P + Q \dots \dots \dots (5.13)$$

P and Q are two combination stresses corresponding to the three measured strains. P and Q are calculated as:

$$P = -\frac{E(\epsilon_3 + \epsilon_1)}{2\bar{a}(1 + \nu)} \dots \dots \dots (5.14)$$

$$Q = -\frac{E(\epsilon_3 - \epsilon_1)}{2\bar{b}} \dots \dots \dots (5.15)$$

Where, E is Modulus of Elasticity, ν is Poisson’s ratio, \bar{a} and \bar{b} are calibration constants. The E and ν have been taken as 205 GPa and 0.29 for SAE 8620 steel. The \bar{a} and \bar{b} have been taken as corresponding to the ratio of hole diameter (D_o) and gage circle diameter (D).

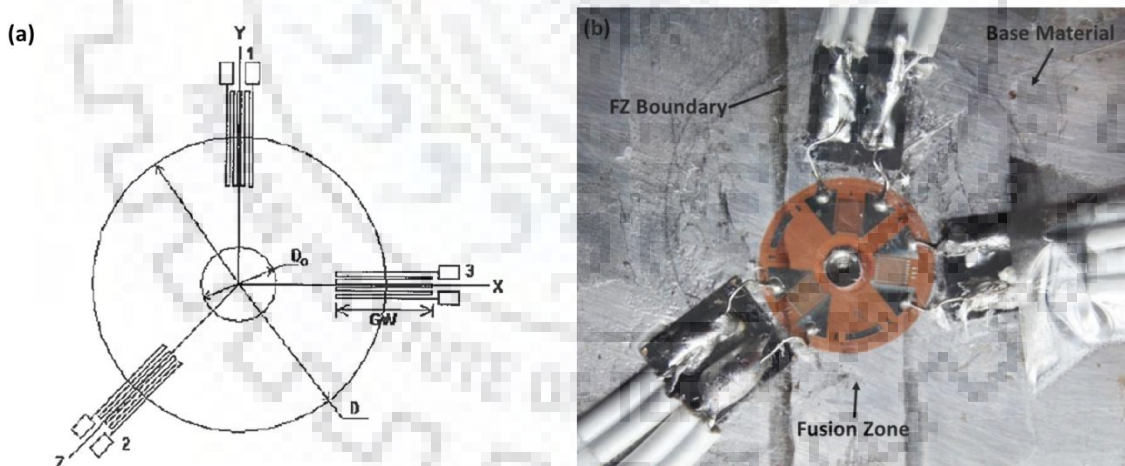


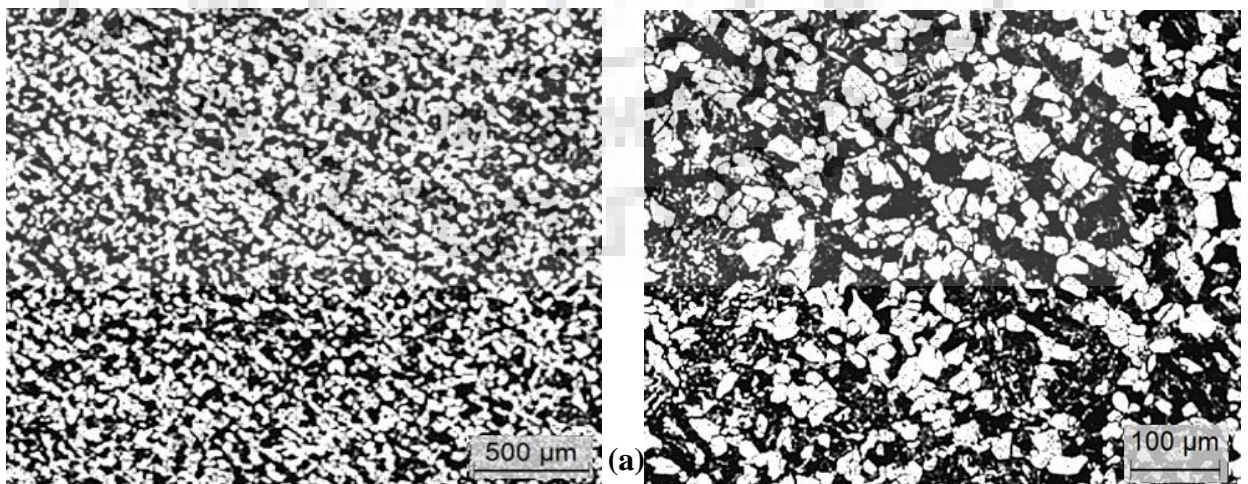
Fig. 5.17 (a) Schematic arrangement of strain gages placed at different directions of measuring and (b) Typical view of a three strain gage rosette at a fusion zone.

This chapter presents detailed discussions of the results obtained in the present work for preparation of higher wear resistant with a tough core substrate using Continuous and Pulsed current TIG arcing process. The chapter presents the results and their discussion of a large variety of experiments described in the chapter 5 and examine them in order to understand the influence of C-TIGA and P-TIGA process, parameters and procedure on modification of AISI 8620 steel substrate. Analyzing the characteristics of the modified zone with respect to their mechanical, metallurgical, residual stresses, wear and friction properties, the necessary control of operating parameters and procedure to improve the surface properties have been established. Necessary control of the operating parameters to improve the surface properties is analyzed in the light of a prescribed model.

6.1 Characteristics of AISI 8620 steel

6.1.1 Microstructure

The typical microstructures of the transverse and longitudinal section of the AISI 8620 low alloy steel base plate having homogeneously distributed grains in the matrix has been shown in Fig. 6.1 (a-b) respectively. The microstructures consist of uniformly distributed proeutectoid ferrite and pearlite in the matrix. The average grain size in transverse and longitudinal direction has been found to be of the order of $8.5 \pm 1 \mu\text{m}$ and $7 \pm 1 \mu\text{m}$ respectively.



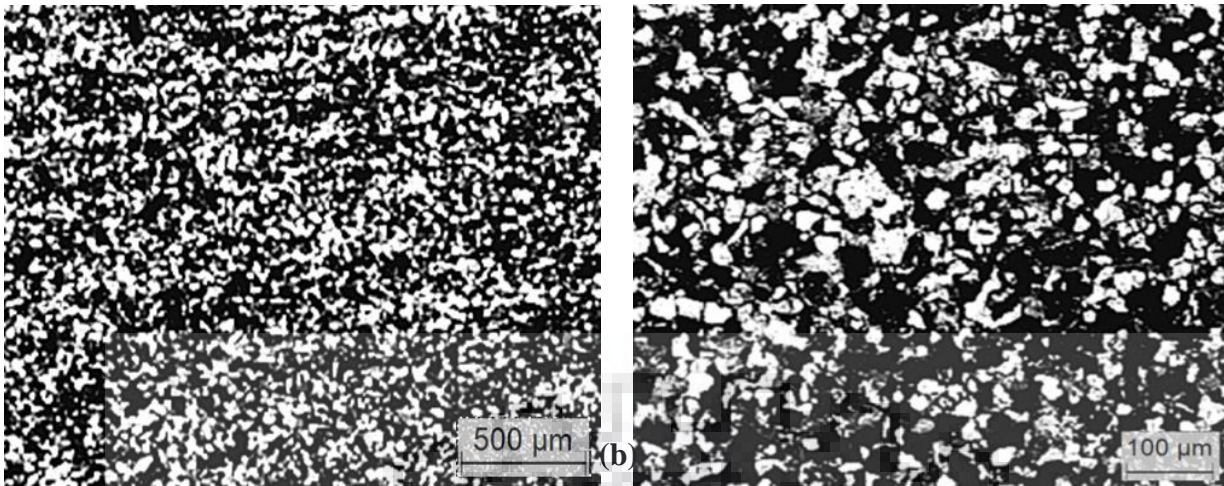


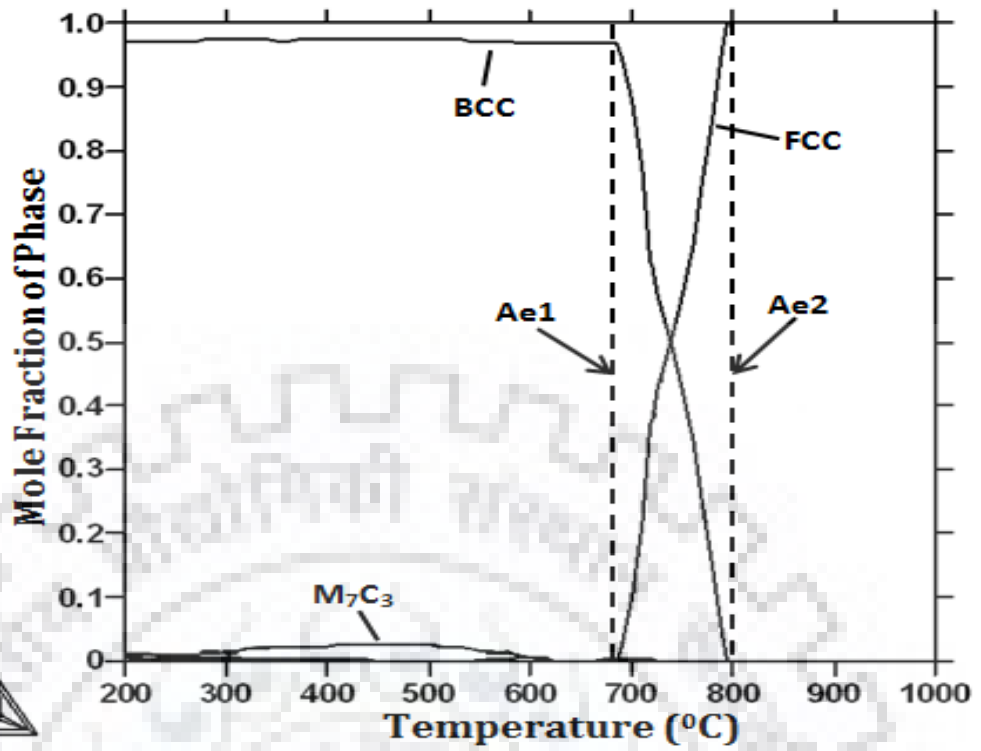
Fig. 6.1 Typical microstructure of AISI 8620 steel used for surface modification in (a) transverse direction and (b) longitudinal direction.

6.1.2 Effect of heating on microstructure

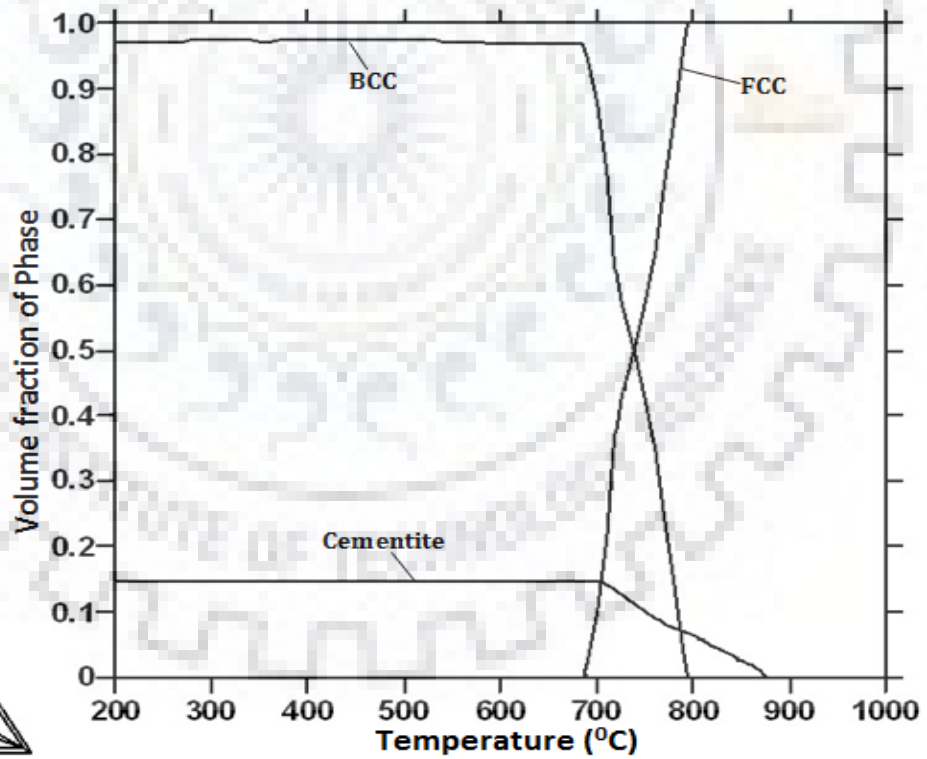
The effect of heating on starting microstructure and intercritical temperature range of the steel were estimated by the computational alloy thermodynamic software Thermocalc. The observed thermodynamically stable phases and their critical temperatures of formation are summarized in Fig. 6.2 (a, b and c). The thermodynamically stable phases like bcc (ferrite), fcc (austenite), cementite and M_3C , $M_{23}C_6$, M_7C_3 , M_3C_2 and M_5C_2 carbides that can form in this system were chosen where M in these carbides could be any of metallic elements of the alloy (Fe, Cr, Mn or Ni).

The Fig. 6.2 (a) depicts the critical temperature of transformation line Ae1 and Ae3 representing transformation temperatures of 680 and 800 °C respectively. In this temperature range the ferrite phase is converted into austenite phase. It is noted that the initial stable phases are ferrite and the M_7C_3 carbide. The M_7C_3 phase is completely dissolved at 640 °C. Thus, the observed carbides in the starting microstructure of the steel are more likely to consist of cementite (M_3C), rather than the equilibrium M_7C_3 carbide.

Fig. 6.2 (b) shows the major stable cementite phase, reaching a volume fraction of 14%. Cementite may be dominant carbide up to that temperature range throughout the measured range of C content. The Fig. 6.2 (c) shows the weight fraction of alloying elements in this carbide phase as a function of temperature. It is observed from the figure that at a relatively lower temperature of 200-400 °C the carbide contains mainly chromium. At the relatively high temperature range of 400-700 °C the carbide contains Cr with a substantial amount of Mn and Fe.



(a)



(b)

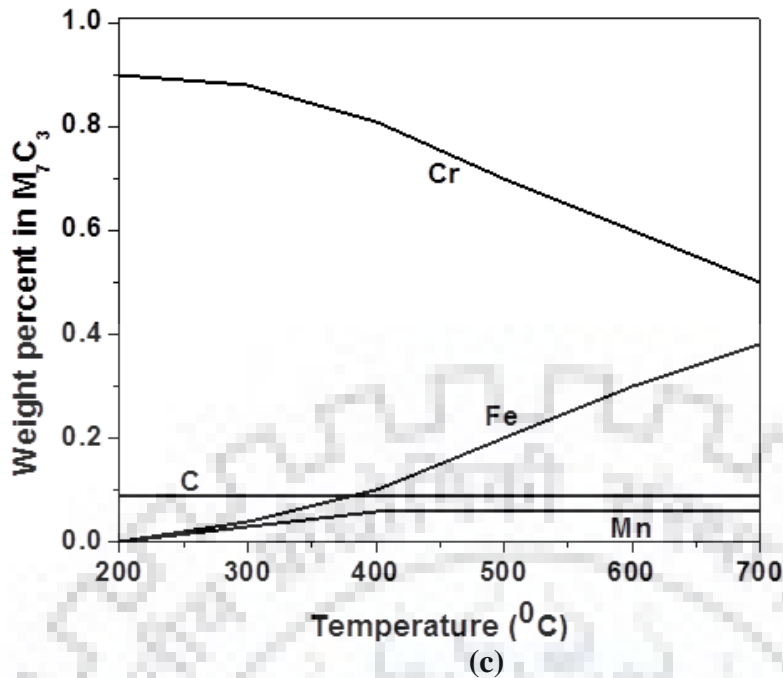


Fig. 6.2 Effect of temperature on the (a) mole fraction of phase transformation (b) volume fraction of phase transformation and (c) Weight % of alloying elements in M_7C_3 carbide.

6.1.3 Thermo-mechanical simulation of AISI 8620 steel

6.1.3.1 Cooling rate estimation

The thermal profile corresponding to heat input of 6.1 kJ/cm to 104.6 kJ/cm and peak temperature of 1300 °C has been shown in fig. 6.3. The cooling rate (CR) is calculated in the inter critical temperature range of 800 °C to 500 °C. It is observed from the figure that increase of heat input from 6.1 to 104.6 kJ/cm significantly reduces the cooling rate from 170 °C/s to 10 °C/s. The steeper thermal gradient at the lower heat input is due to availability of bulk of the material to act as a heat sink to provide rapid heat transfer.

6.1.3.2 Dilation Curve

The Fig. 6.4 shows the dilation curves achieved while cooling at different cooling rates and at a given peak temperature of 1300 °C. The reduction in temperature causes a nearly linear contraction in the γ and α phase. The specimen experiences an increment in circular dilation until the complete transformation of γ phase into α phase is attained. The transformation start (T_s) and finish (T_f) temperatures are decided on the basis of deviation of tangents from the γ and α lines respectively. The increase in cooling rate from 10 °C/s to 170 °C/s shows a relative reduction of T_s and T_f temperature. This is because slower cooling rates require a longer incubation period to nucleate to the product phases and provide more time for the austenite to ferrite transformation to continue.

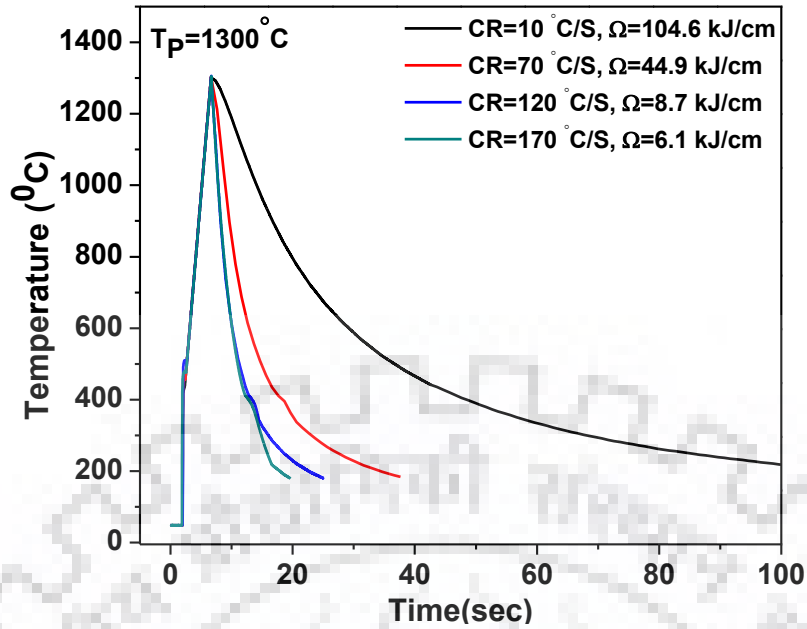


Fig. 6.3 Thermal cycle during thermo-mechanical simulation of AISI 8620 steel.

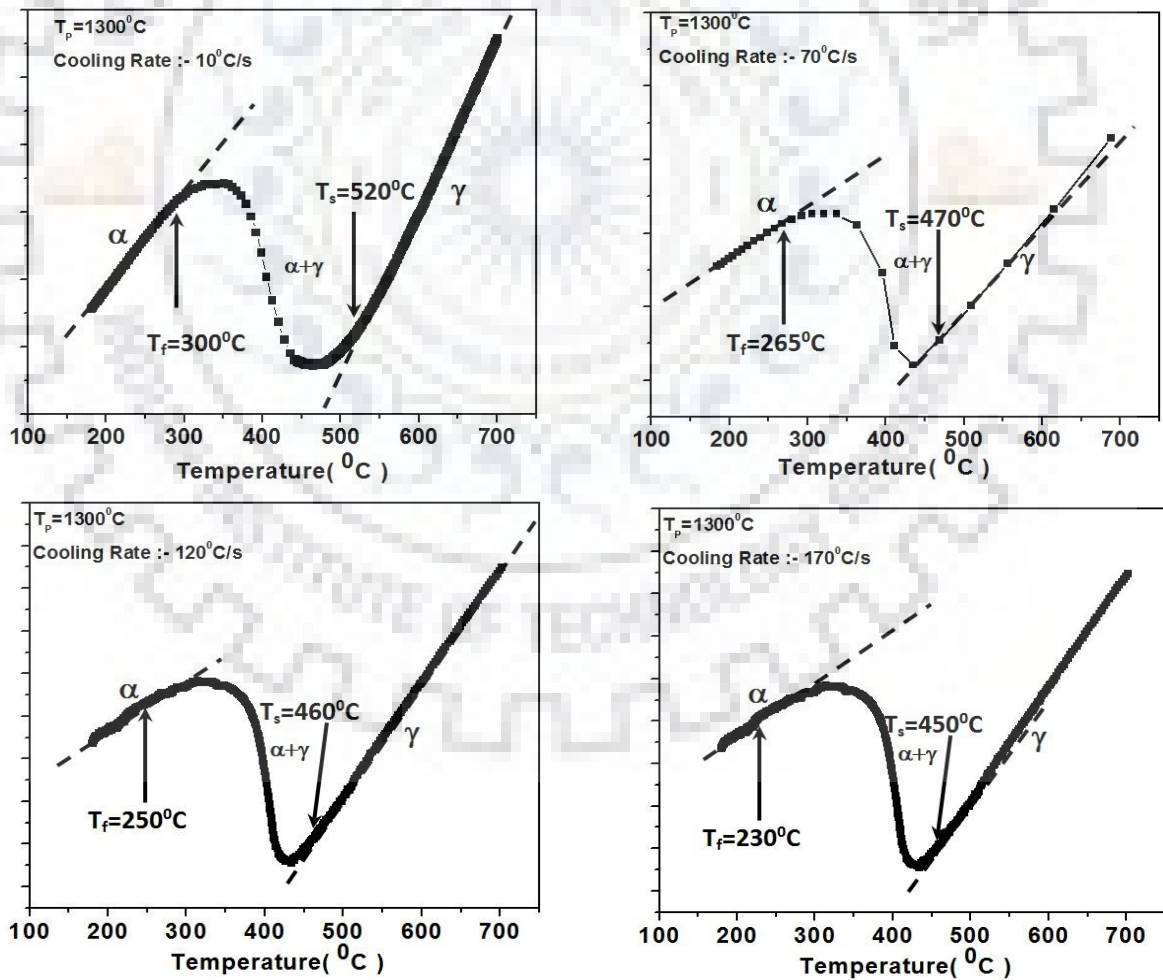


Fig. 6.4 Dilatation curves recorded at different cooling rate of AISI 8620 steel plate. The tangents along the γ -line and α -line detect the inflexion points where the dilatation curve deviates from linearity.

6.1.3.3 CCT Diagram

The CCT diagram for AISI 8620 steel is estimated by the TMS system and is shown in Fig 6.4. It can be observed from the figure that the martensitic start (M_s) and martensitic finish (M_f) temperature for AISI 8620 steel are 683 K (410°C) and 583 K (280°C) respectively. The estimated M_s and M_f values are closed to the values determine by the researchers for similar type of low alloy steel [Barkoula et al., 2008]. The total time required to form the fully martensitic structure is 10.2 second. Further, it can be observed from the figure that at relatively slower cooling rate ranging from 10°C/s to 70°C/s , there is the formation of typical bainite structure and at a higher cooling rate beyond 70°C/s , there is a possibility of formation of fully martensite structure.

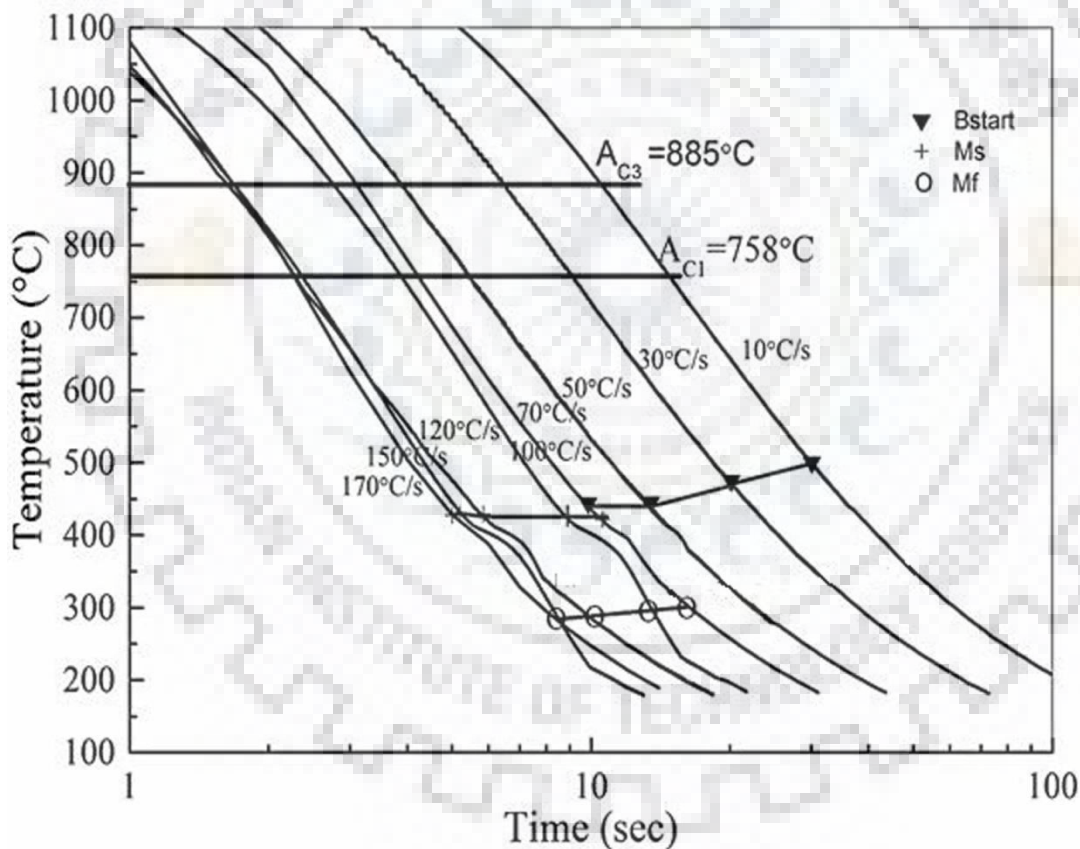


Fig. 6.5 Estimated CCT curve for AISI 8620 steel.

6.1.3.4 Effect of cooling rate on microstructure of AISI 8620 steel

Microstructures resulting from phase transformations in the AISI 8620 steel at different rates of cooling from peak temperature of 1300°C are shown in Fig. 6.6. At comparatively slow cooling rate of 10°C/s the microstructure reveals the presence of some retained austenite and mixer of lower and upper bainite in the matrix. A mixture of bainite and lath martensite is

appeared at cooling rate of $70\text{ }^{\circ}\text{C/s}$. The fully lath type of martensitic structure in the matrix is observed at the cooling rate of 120 and $170\text{ }^{\circ}\text{C/s}$. The martensitic structure observed at high cooling rate is lath type due to relatively lower percentage of carbon. The confirmation of microstructure is made by the CCT diagram as shown in Fig. 6.4.

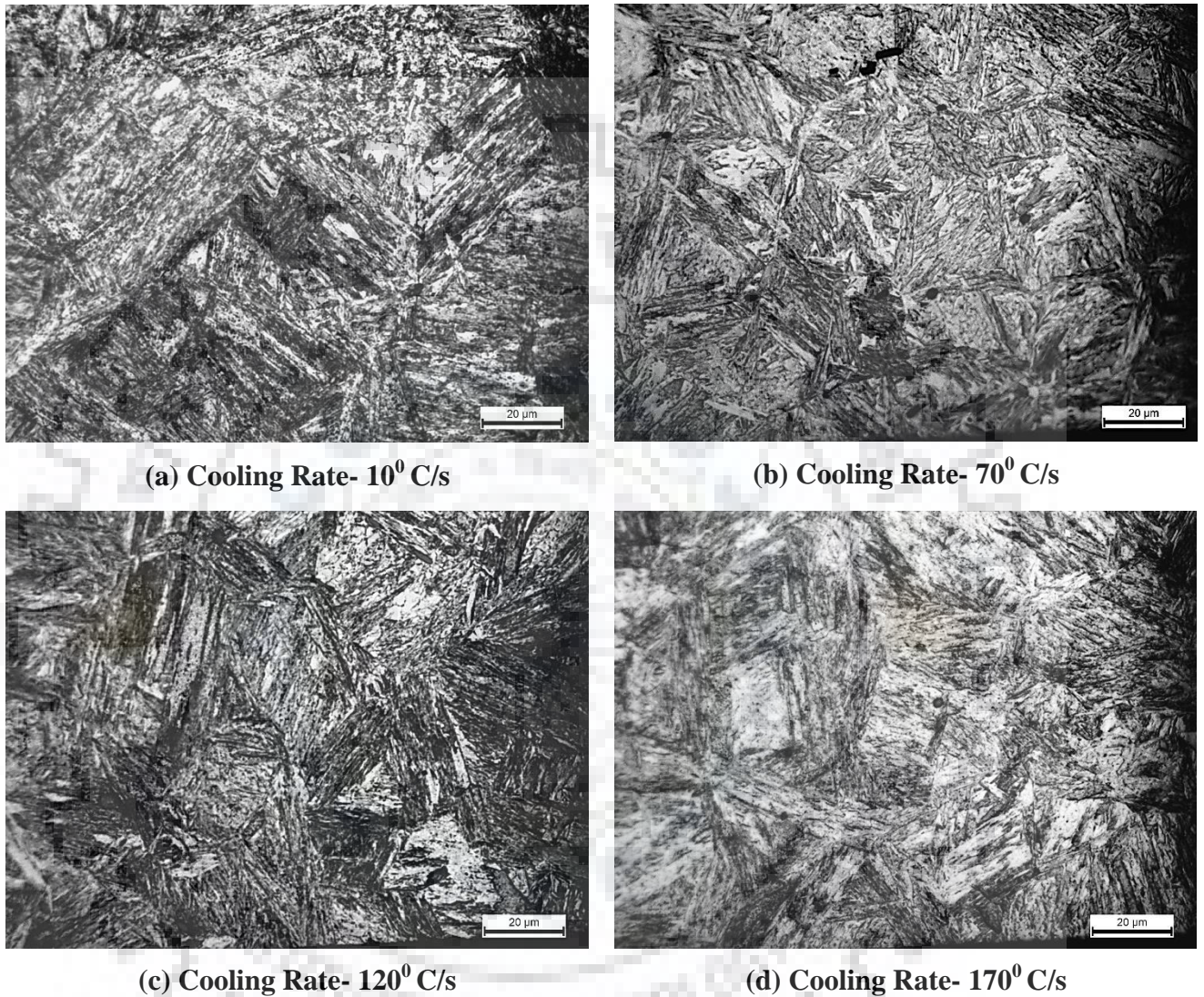


Fig. 6.4 Effect of cooling rate on microstructure of AISI 8620 steel.

6.1.3.5 Effect of cooling rate on matrix hardness of AISI 8620 steel

The Fig. 6.7 depicts the effect of cooling rate on hardness of AISI 8620 steel. The hardness of base material has been found as $210\pm 10\text{ VHN}$. The presence of varied amount of different phases in the modified zone as discussed above is clearly reflected in their matrix hardness. The figure shows that the increase of cooling rate from 10 to $170\text{ }^{\circ}\text{C/s}$ increases hardness rapidly from 310 ± 5 to $520\pm 8\text{ VHN}$. The increase of hardness with the increase of cooling rate is primarily attributed to hard phase transformation. The increase in hardness confirms the formation of bainitic structure at a lower cooling rate in the range of about $10\text{ }^{\circ}\text{C/s}$

to 50 °C/s. The fully martensitic structure is confirmed by its characteristics hardness at higher cooling rates from 70 to 170 °C/s.

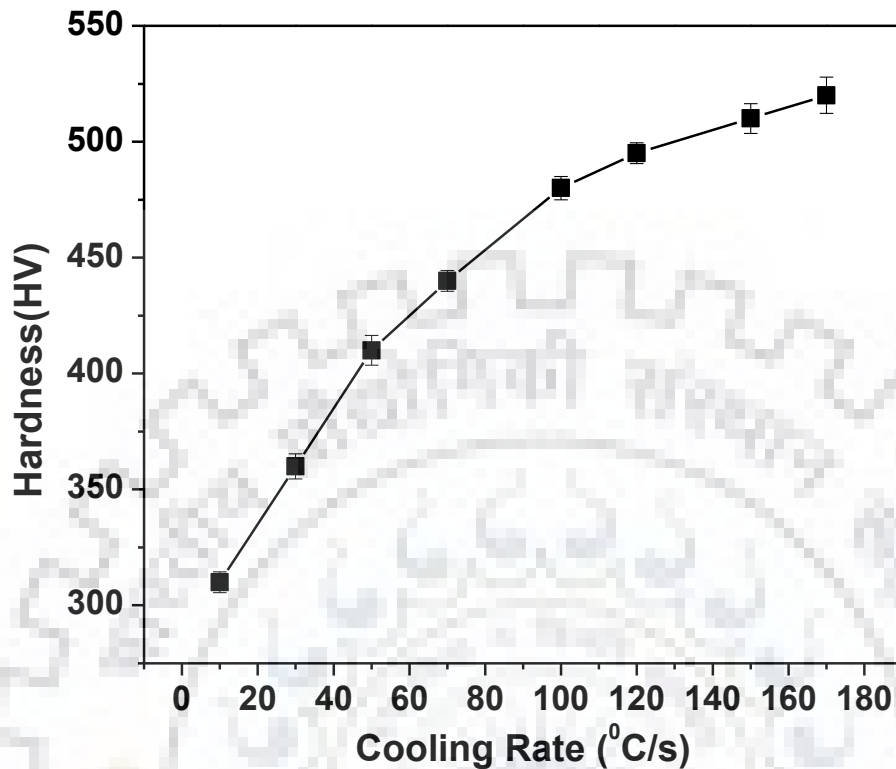


Fig. 6.5 Effect of cooling rate on hardness of AISI 8620 steel at different heat input.

6.1.4 Summary

The effect of heating on phase transformation in reference to the intercritical temperature range is estimated and confirmed by characteristic changes in microstructure with the help of computer software. The increase in matrix temperature makes significant changes in the thermodynamically stable phases. The CCT diagrams have been generated to predict the microstructures of the entire modified zone in AISI 8620 steel. The microstructures of modified zone consist of a mixture of lath martensite, lower and upper bainite where their proportion and morphology vary with the change in cooling conditions of the weld thermal cycle. A full martensitic structure is obtained under low heat input and high cooling rate conditions in the AISI 8620 steel, while a mixed microstructure is present in the AISI 8620 steel at relatively high heat input and low cooling rate. The consequent change in hardness is observed in the modified zone with the variation of cooling rate.

6.2 Geometric studies

6.2.1 Single pass C-TIGA process

The studies on thermal and geometrical aspects of the modified zone as a function of arcing parameters provide the knowledge to understand and analyze the effect of C-TIGA parameters on bead geometry, temperature of the weld pool and heat input into the modified zone. This may play a leading role in deciding the parameters for multipass modification of extended surface of AISI 8620 steel. In addition to this the single pass C-TIGA process is also a deciding factor to optimize the single pass P-TIGA process parameters in terms of depth of modified zone. At a given arc voltage (V) the geometrical characteristics have been studied at varying arc current of 70 to 200 A and travel speed (S) of 5 to 15 cm/min. The C-TIGA parameters used for single pass study have been shown in Tables-5.3 (chap. 5).

6.2.1.1 Thermal aspects of fusion pool during C-TIGA process

At a given arc voltage of $11 \pm 1V$ the influence of arc current on theoretically estimated energy transfer (Q_T) has been depicted in Fig. 6.8. The figure shows that total energy transferred to weld pool linearly increases with the increment of arc current. The empirical correlation of Q_T with the arc current (I) at a given arc voltage has been worked out as follows.

$$Q_T = 11.53I + 20.35 \quad (6.1)$$

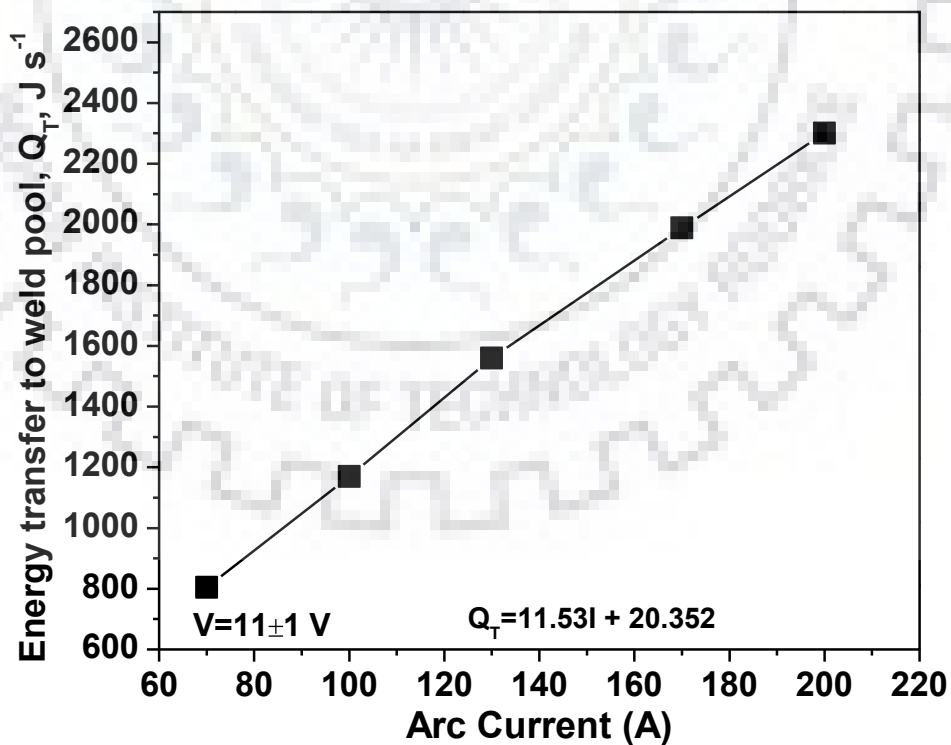


Fig. 6.6 Effect of cooling rate on hardness of AISI 8620 steel at different heat input.

At a given arc voltage of $11 \pm 1V$ the effect of arc current on theoretically estimated weld pool temperature, T_{WP} at a depth of about 1.5 mm from its surface and about 1.5 mm from the arc center under different travel speed has been shown in Fig. 6.9. It has been observed that at a given arc voltage and travel speed (S) the T_{WP} increases significantly with the increase of arc current. The figure also depicts that the T_{WP} decreases with the increase in travel speed from 5 to 15 cm/min at a given arc current (I) and arc voltage. The empirical correlation of T_{WP} with the I and S has been worked out as follows.

$$T_{WP} = -2.34 S + 10.47 I - 0.18 SI + 1065 \quad (6.2)$$

The mathematical expression (Chap-5, eq.5.3) used for estimation of weld pool temperature has been successfully verified by several researchers in their studies [B.P. Aggrawal, 2010; Goyal et al., 2008 (b)].

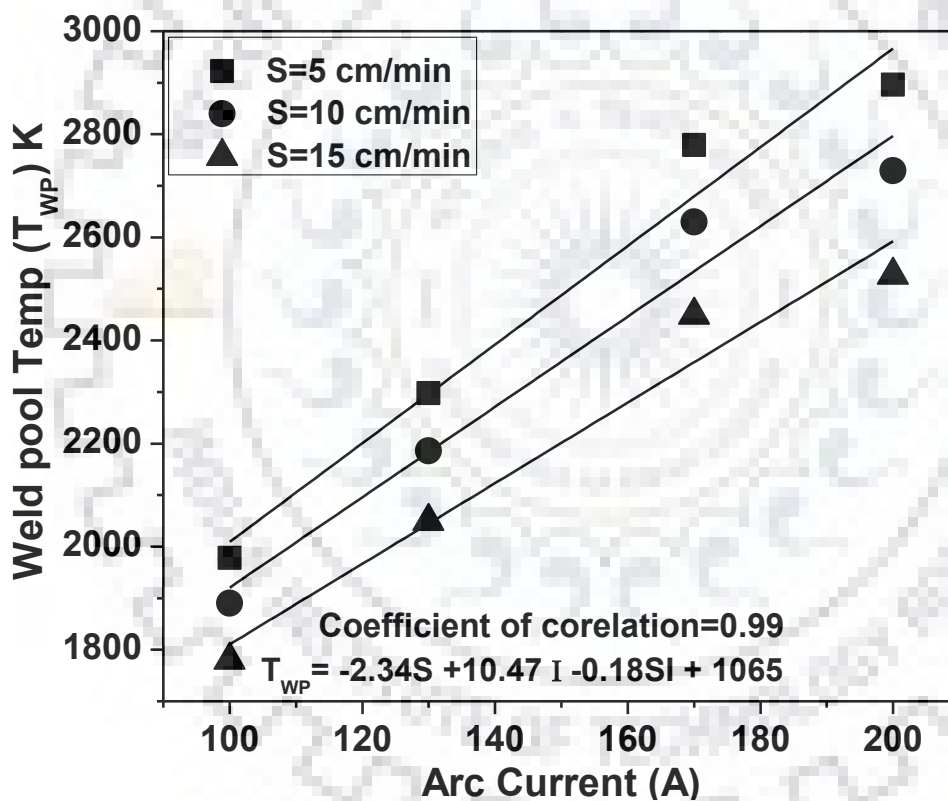


Fig. 6.7 At a given arc voltage of $11 \pm 1V$, the effect of I and S on weld pool temperature.

6.2.1.2 Geometric studies during single pass C-TIGA process

The typical appearance of the surface and transverse sections of the single pass C-TIGA at varying arc current and travel speed is shown in Figs. 6.10 and 6.11 respectively. Figures show that at a given arc voltage, the increase of arc current and decrease of travel speed significantly affects the geometry of fusion bead. It is depicted from the figure that the increase

in arc current from 70 to 200 A and decrease in travel speed from 15 to 5 cm/min increases the heat input into the workpiece. The increase in heat input (Ω) significantly affects the geometrical aspect of fusion zone, such as bead width (W_b), penetration (P_d), HAZ width (W_{HAZ}) and fusion zone area (A_{FZ}). It is a well-known fact that the increase in heat content in the workpiece is obtained through the reduction in the travel speed (S) and increment in the arc current (I). The net increase in the heat input increases the temperature of the fusion pool and fluidity of the molten metal [Fan and Kovacevic, 2004].

I(A) S	5 cm/min		7.5 cm/min	
	70			
100				
130				
170				
200				
	10 cm/min		15 cm/min	
70				
100				
130				
170				
200				

Note: All dimensions are in mm.

Fig. 6.8 Typical surface appearance of the modified zone using single pass C-TIGA process at variation in arc current from 70 to 200 A and travel speeds from 5 to 15 cm/min.

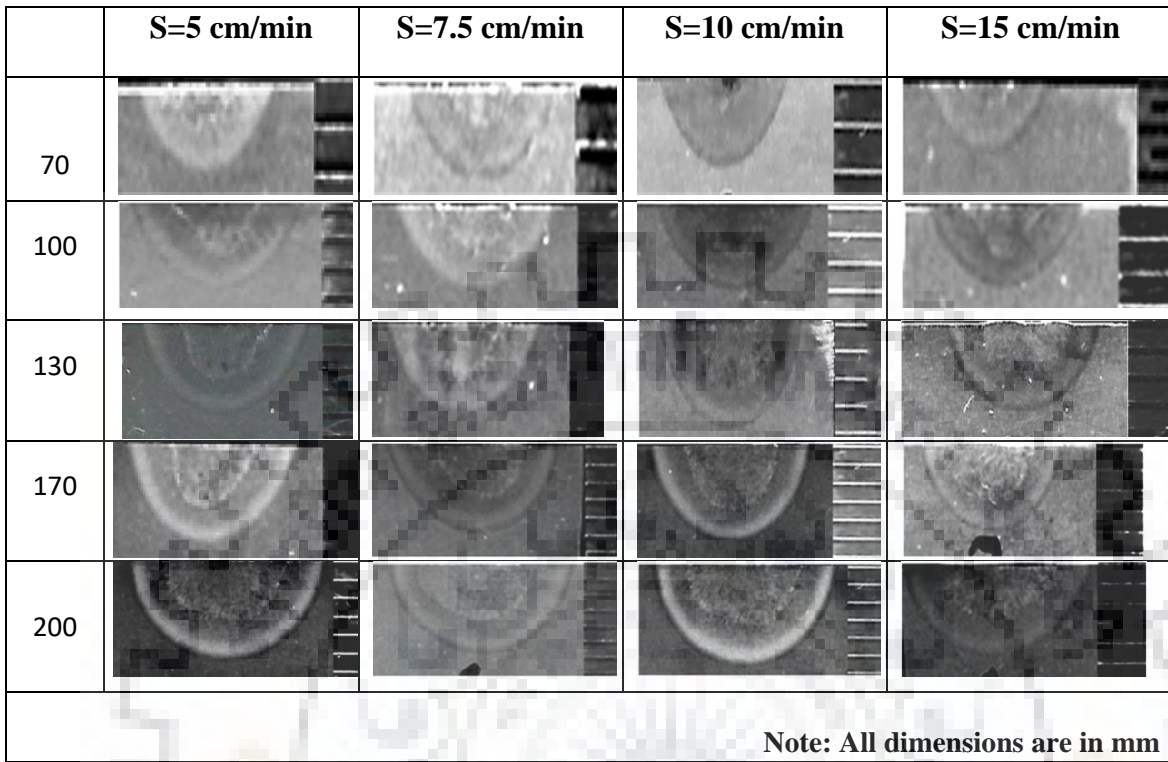


Fig. 6.9 Typical photographs of transverse section of the modified zone using single pass C-TIGA process at variation in arc current from 70 to 200 A and travel speeds from 5 to 15 cm/min.

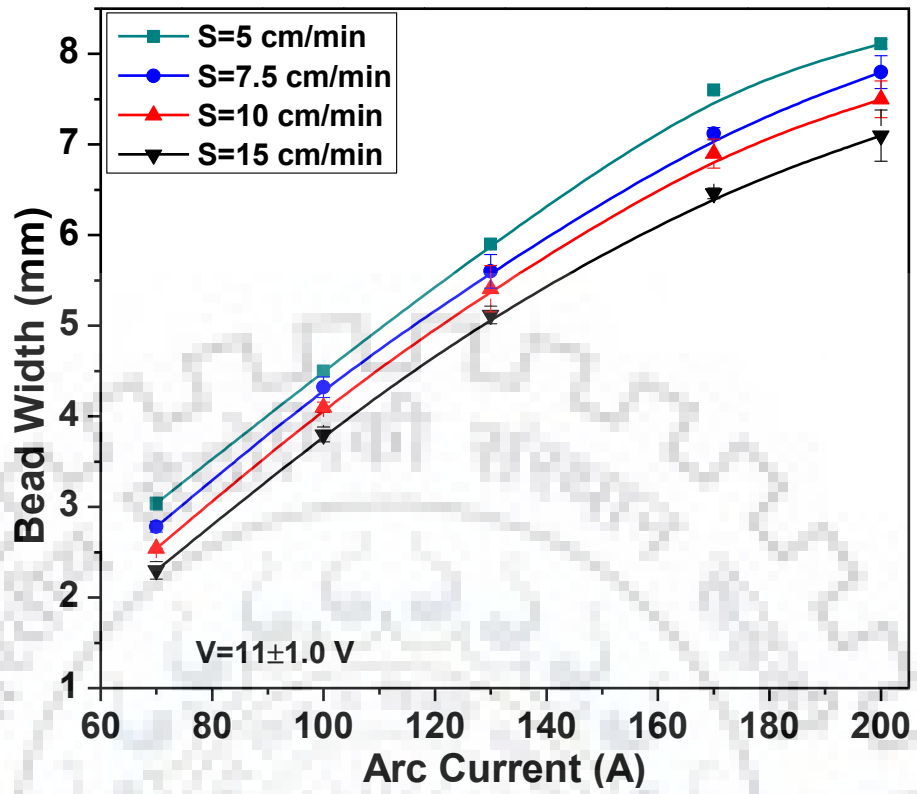
The effect of variation in arc current (I) and travel speed (S) at a given arc voltage of $11\pm 1V$ has been shown in Figs 6.12 (a-d). The figures show that the increase in arc current from 70 to 200A significantly increases the bead width (W_b), depth of penetration (P_d), Width of HAZ (W_{haz}) and area of FZ (A_{FZ}). It has been further observed that the W_b , P_d , W_{haz} and A_{FZ} increase appreciably with the reduction of travel speed. Such a variation in W_b , P_d , W_{haz} and A_{FZ} as a function of arc current (I) and travel speed (S) may be primarily attributed to the variation in heat transfer to the fusion zone governing its pool size and fluidity [Robert W Messler, 1999]. The empirical correlations of W_b , P_d , W_{haz} and A_{FZ} as a function of I and S depicted in Figs 6.12 (a-d) respectively have been given below.

$$P_d = -0.051s + 0.019I - 3.20 \times 10^{-4} Is + 0.482 \quad (6.3)$$

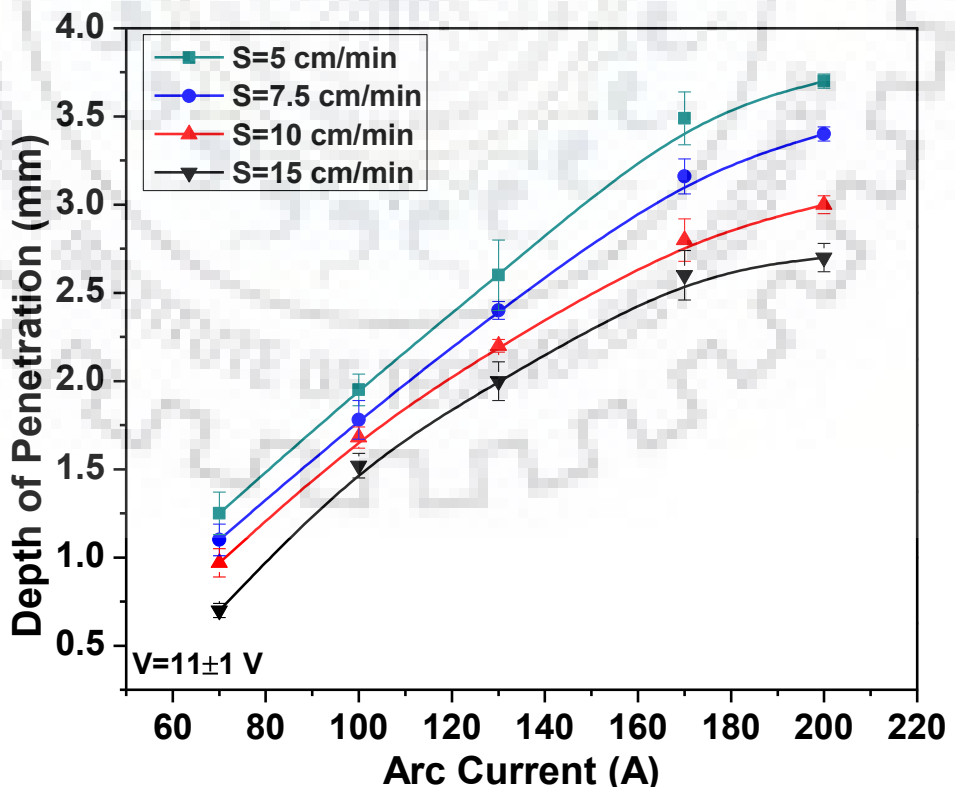
$$W_b = -0.063s + 0.042I - 3.86 \times 10^{-4} Is + 0.78 \quad (6.4)$$

$$W_{haz} = -0.014s + 0.012I - 3.23 \times 10^{-4} Is + 0.29 \quad (6.5)$$

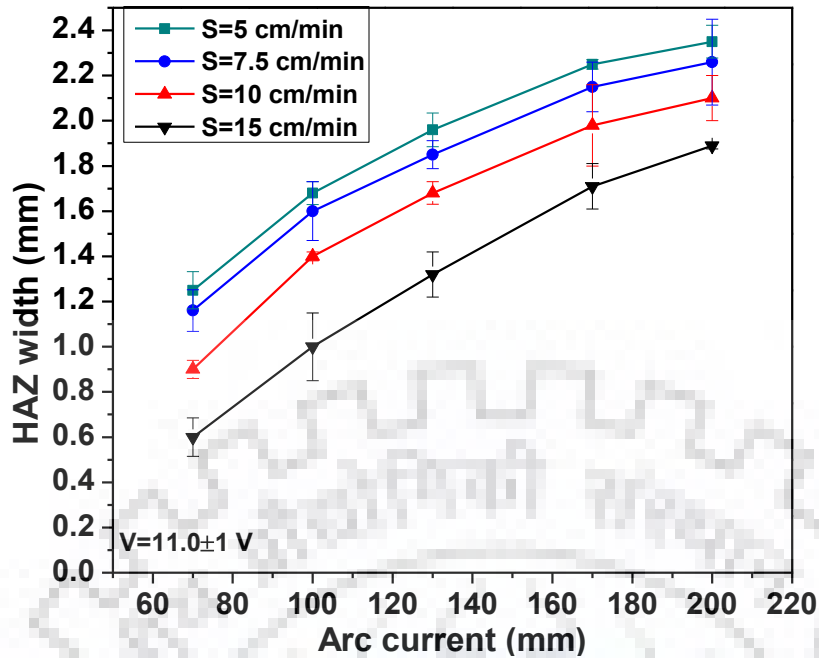
$$A_{FZ} = 0.57s + 0.25I - 1.11 \times 10^{-2} Is - 13.62 \quad (6.6)$$



(a)



(b)



(c)

Fig. 6.10 The effect of arc current and travel speed on (a) bead width (b) depth of penetration (c) HAZ width and (d) fusion zone area at an arc voltage of 11 ± 1 V.

6.2.2 Single pass P-TIGA process

The acceptability of the hardened region in TIGA process is largely governed by its required depth of penetration at an optimum thermal exposure giving rise to a minimum heat affected zone (HAZ). The extent of modification of the base metal largely depends upon nature of energy transfer and thermal behavior of the fusion zone dictating shape and size of the molten pool and its temperature. The heat content of weld pool is largely governed by its molten mass per unit length and temperature. The shape and size of weld pool affect the properties of the fusion zone and HAZ. Achieving all these aspects can be more precisely addressed by using P-TIGA process controlled by the summarized influence of pulse parameters proposed earlier [Ghosh et al., 2000, Ghosh and Kumar, 2014] and defined by a hypothetical factor ϕ derived on the basis of the energy balance concept of the system. This is because it more thoroughly facilitates controlling the fusion characteristics including its microstructure [Ghosh 1996, Ghosh et al., 2006, Ghosh et al., 2008, Goyal et al., 2008 (b), Hussian et al., 1996, Randhawa et al., 1998, Randhawa et al., 2000].

The thermal behavior of fusion has been studied considering heat transfer to the fusion zone by the arc, [Goyal et al., 2008 (b), Ghosh et al., 2006], heat input (Ω), temperature of weld pool (T_{WP}) and weld isotherm governing the shape and size of fusion pool. Therefore, to control the P-TIGA process in order to get desired modified zone and phase transformation, it

is required to have an understanding of correlation among the Ω , T_{WP} , ϕ and I_m and fusion zone characteristics. The P-TIGA parameters used for single pass study have been shown in Tables-5.4, 5.5 and 5.6 (chap. 5).

6.2.2.1 Thermal aspects of weld pool during P-TIGA process

The thermal behavior of energy transfer being dictated by ϕ and I_m may affect the total heat transferred to the fusion zone. The total energy transferred to the weld pool may govern the temperature (T_{WP}) and the shape and size of the fusion zone consequently affecting the weld isotherm which ultimately influences the thermal behavior of modified zone. Thus, the thermal behavior of fusion zone has been studied considering the total energy transfer to the fusion pool, average weld pool temperature (T_{WP}) and fusion isotherm under different pulse parameters.

At a given arc voltage of $11 \pm 1V$ the influence of ϕ on theoretically estimated Q_T at different mean currents (I_m) of about 170, 130 and 100 A has been depicted in Fig. 6.13. The figure shows that the total energy transferred to weld pool reduces with an increment of ϕ at a given I_m and enhances with I_m at a given ϕ . The total heat transferred to weld pool Q_T is primarily dictated by the arc heat, largely depending upon the effective mean current, which is having a similar trend of variation with (at a given I_m and with I_m at a given ϕ). The empirical correlation of Q_T with ϕ and I_m at a given arc voltage have been worked out as follows.

$$Q_T = 11.09I_m + 21.93\phi - 6.60I_m\phi - 3.01 \quad (6.7)$$

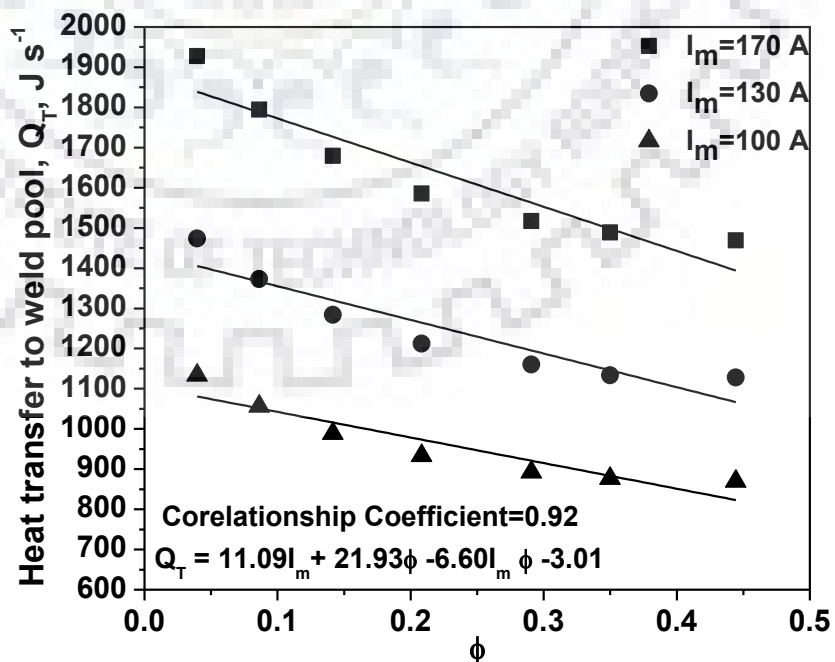


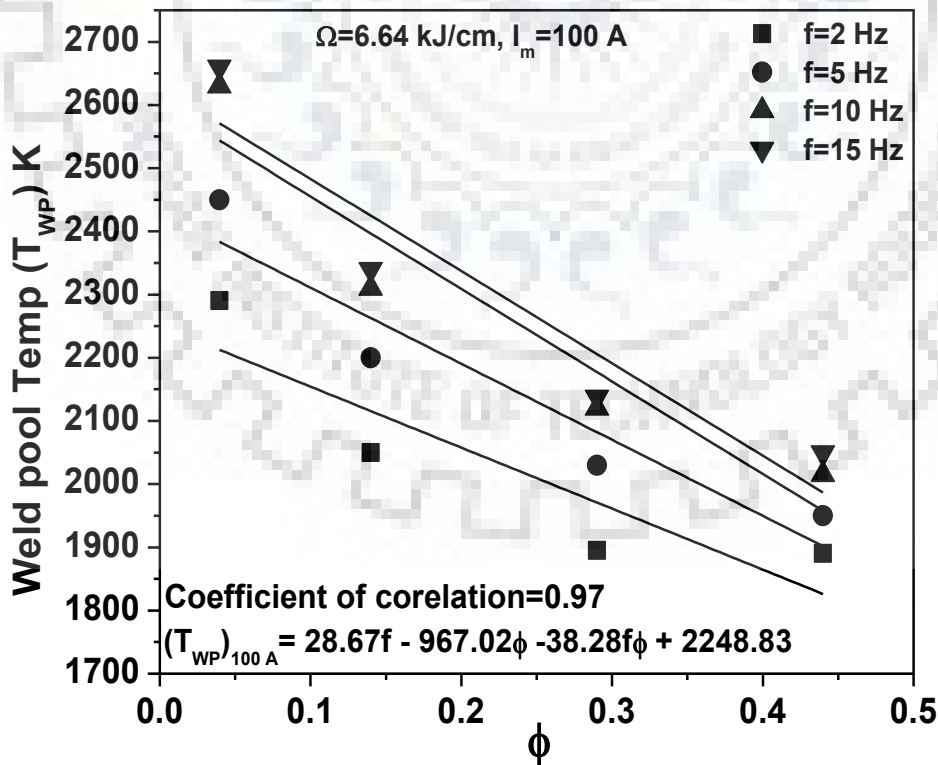
Fig. 6.11 At a given arc voltage of $11 \pm 1V$ the effect of ϕ on total heat transfer to weld pool at different I_m of 170, 130 and 100A respectively.

At a given arc voltage of $11\pm 1V$ the effect of ϕ on theoretically estimated weld pool temperature, T_{WP} , at a depth of about 1.5-2 mm from its surface and about 1.5 mm from arc center, under different I_m of 100, 130 and 170 A at different pulse frequency (f) varied in the range of 2 to 15 Hz has been shown in Fig. 6.14 (a-c) respectively. It has been observed that at a given I_m and f the T_{WP} reduces significantly with the increase of ϕ , the T_{WP} enhances with increase of Ω at a given f and ϕ and it also increases appreciably with enhancement of f at a given I_m and ϕ . At a given I_m and f , the reduction of T_{WP} with the increase of ϕ may have primarily happened due to decrease of fusion zone size as explained earlier. While, the enhancement of T_{WP} with increase of I_m at a given f and ϕ is accredited to increase of total heat transferred to the weld pool (Q_T) per unit length. However the appreciable increment of T_{WP} with enhancement of f at a given I_m and ϕ has primarily happened due to increase of energy input per pulse with the increase of f . The empirical correlation of T_{WP} as a function of f and ϕ at different I_m have been worked out as follows.

$$(T_{WP})_{100A} = 28.67f - 967.02\phi - 38.28f\phi + 2248.83 \quad (6.8)$$

$$(T_{WP})_{130A} = 21.55f - 1122.73\phi - 15.59f\phi + 2423.89 \quad (6.9)$$

$$(T_{WP})_{170A} = 27.72f - 954.43\phi - 32.32f\phi + 2773.18 \quad (6.10)$$



(a)

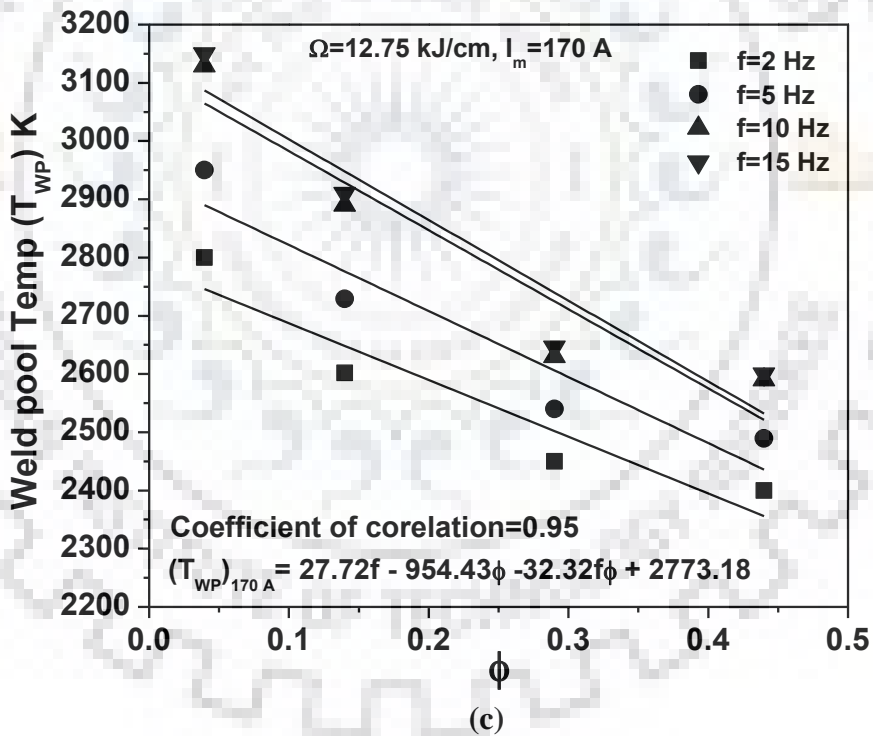
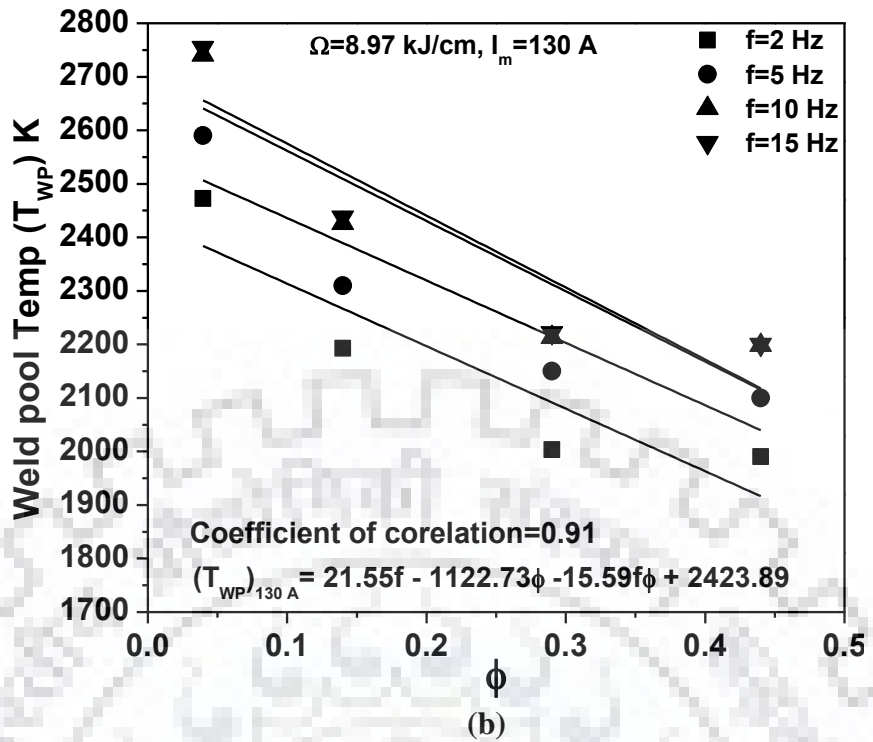


Fig. 6.12 At a given arc voltage of $11 \pm 1 \text{ V}$, the effect of ϕ and f on weld pool temperature under different mean current of (a) 100 (b) 130 and (c) 170 A respectively.

6.2.2.2 Geometrical aspects of the modified zone using P-TIGA process

The parameters I_m , T_{WP} and fusion isotherm, which to a great extent dictate the geometrical aspects of fusion pool, are largely dictated by various pulse parameters of the P-


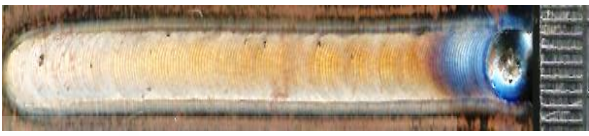


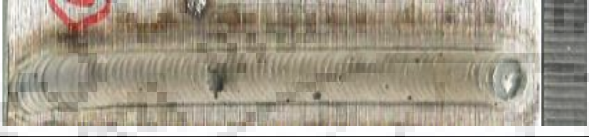


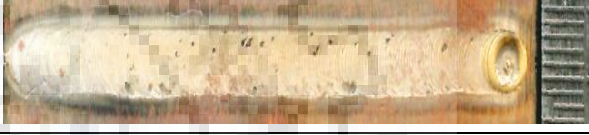












TIGA process. Thus, the geometrical aspects of fusion pool with respect to its bead width (W_b), depth of penetration (P_d), HAZ width (W_{HAZ}) and area of fusion (A_F) has been studied as a function of pulse parameters so that optimum pulse parameters can be revealed to ensure the characteristics of the modified zone as per the requirement of industrial applications especially in bearings. At a given arc voltage of $11\pm 1V$ the typical photographs of the surface appearance of the bead geometry of the fused zone observed in P-TIGA process at different I_m respectively, of 100 A, 130 A and 170 A have been shown in Figs. 6.15, 6.16 and 6.17 respectively, where the ϕ and f are varied in the ranges of 0.04 to 0.44 and 2 to 15 Hz. Similarly, at a given arc voltage of $11\pm 1 V$ the typical photographs of transverse section of the modified zone observed in P-TIGA process at different I_m of 100 A, 130A and 170 A have been shown in Figs. 6.18, 6.19 and 6.20 where ϕ and f are varied in the ranges of 0.04 to 0.44 and 2 to 15 Hz.

Observations on geometrical features of the modified zone in the substrate as revealed in the Figs. 6.15-6.20 clearly indicate that at a given I_m the variation in pulse characteristics governed by the ϕ and f has significant influence on fused bead width, depth of penetration of fusion, area of fusion and width of HAZ in the substrate. At this juncture, it may be noted that the heat input (Ω) is varied by changing the mean pulse current (I_m) at given arc voltage of $11\pm 1 V$ and arc travel speed (S) of 10 cm/min. Thus, it is inferred that the entire change in geometrical characteristics of fusion in substrate is happened primarily by the influence of pulse parameters. The nature of variation of these geometrical features of the modified zone as a function of pulse parameters considered as ϕ and f of the P-TIGA process has been studied in detail as discussed below. At different I_m of 100, 130 and 170 A respectively, the effect of variation in ϕ and f in the range of 0.04 to 0.44 and 2 to 15 Hz respectively on the measured bead width (W_b) of fusion zone has been shown in Figs. 6.21(a-c) respectively. Under the same given conditions of I_m of 100, 130 and 170 A the effect of ϕ and f on the depth of penetration (P_d), width of HAZ (W_{HAZ}) and area of the fusion zone (A_{FZ}) has been shown in Figs. 6.22 (a-c), 6.23 (a-c) and 6.24 (a-c) respectively. The Figs. 6.21 (a-c) depict that W_b reduces significantly with the increase of ϕ at a given f while the I_m remains constant. But it is observed that the W_b appreciably enhances with the increase of f from 2 to 10 Hz followed by an insignificant change in it with a further increase of f to 15 Hz. Such a variation in W_b as a function of ϕ and f may be primarily attributed to increase of heat buildup in molten pool [Pal and Pal, 2011] enhancing its size and fluidity. The empirical correlations of W_b as a function of f and ϕ at different I_m has given below.

$$\text{At } I_m=170 \text{ A} \quad W_b = 0.05f - 3.85\phi - 0.16f\phi + 8.14 \quad (6.11)$$

At $I_m=130$ A $W_b = 0.05f - 2.37\phi - 0.06f\phi + 5.80$ (6.12)

At $I_m=100$ A $W_b = -0.05f - 2.39\phi - 0.07f\phi + 5.59$ (6.13)

$I_m=100$ A and $\Omega= 6.6$ kJ/cm		
ϕ	$f=2$ Hz	$f=5$ Hz
0.04		
0.14		
0.29		
0.35		
0.44		
ϕ	$f=10$ Hz	$f=15$ Hz
0.04		
0.14		
0.29		
0.35		
0.44		

Note: All dimensions are in mm.


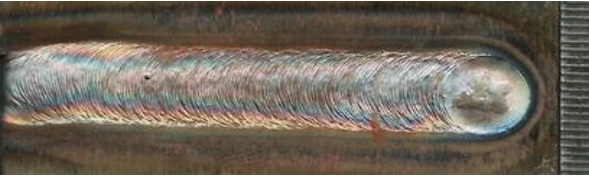




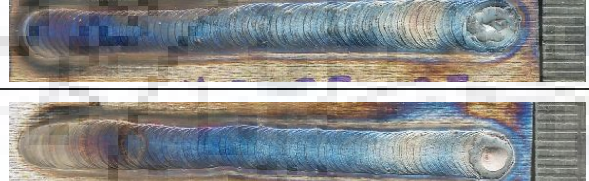
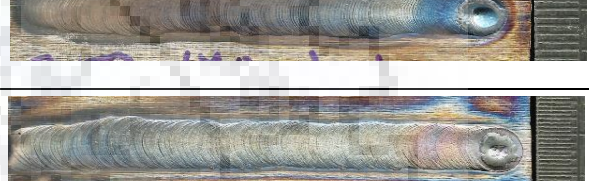
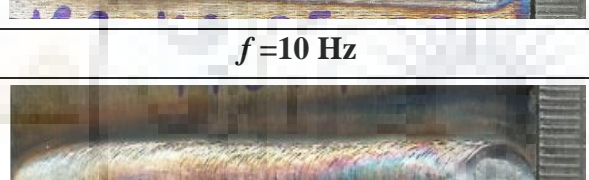
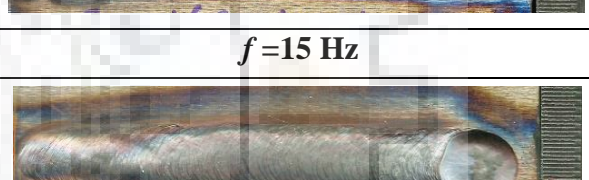

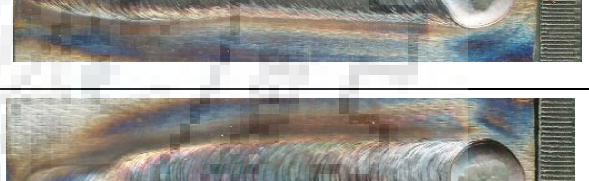
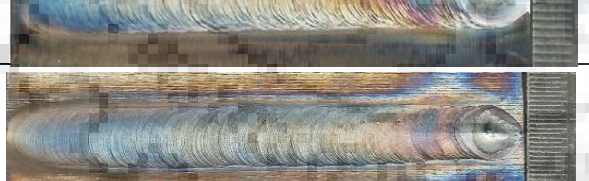



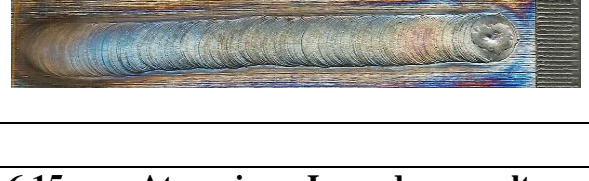
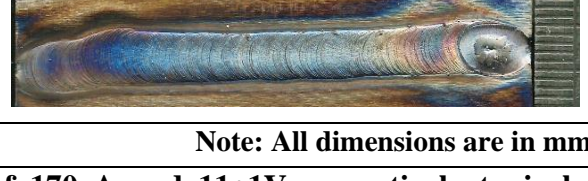
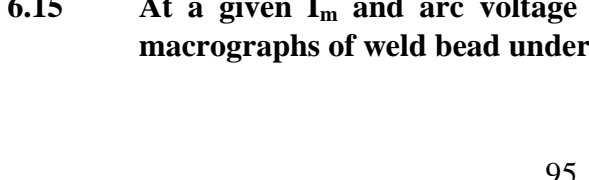

Fig. 6.13 At a given I_m and arc voltage of 100 A and 11±1V respectively typical macrographs of weld bead under varied ϕ and f .

$I_m=130$ A and $\Omega=8.97$ kJ/cm

ϕ	$f=2$ Hz	$f=5$ Hz
0.04		
0.14		
0.29		
0.35		
0.44		
ϕ	$f=10$ Hz	$f=15$ Hz
0.04		
0.14		
0.29		
0.35		
0.44		



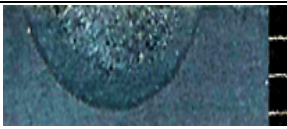



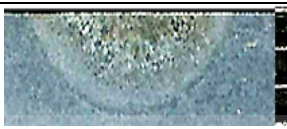






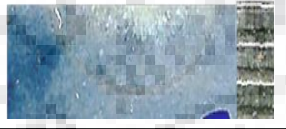






Note: All dimensions are in mm

Fig. 6.14 At a given I_m and arc voltage of 130 A and $11\pm 1V$ respectively typical macrographs of weld bead under varied ϕ and f .

$I_m=170\text{ A}$ and $\Omega=12.75\text{ kJ/cm}$		
ϕ	$f=2\text{ Hz}$	$f=5\text{ Hz}$
0.04		
0.14		
0.29		
0.35		
0.44		
ϕ	$f=10\text{ Hz}$	$f=15\text{ Hz}$
0.04		
0.14		
0.29		
0.35		
0.44		


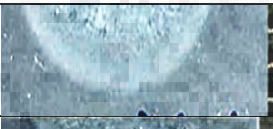







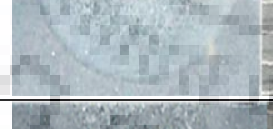








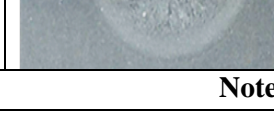

Note: All dimensions are in mm

Fig. 6.15 At a given I_m and arc voltage of 170 A and 11±1V respectively typical macrographs of weld bead under varied ϕ and f .

$I_m=100 \text{ A}$ and $\Omega=6.6 \text{ kJ/cm}$				
ϕ	$f=2 \text{ Hz}$	$f=5 \text{ Hz}$	$f=10 \text{ Hz}$	$f=15 \text{ Hz}$
0.04				
0.14				
0.29				
0.35				
0.44				

Note: All dimensions are in mm

Fig. 6.16 At a given I_m and arc voltage of 100 A and $11\pm 1V$ respectively typical cross sectional macrographs of modified zone under varied ϕ and f .

$I_m=130 \text{ A}$ and $\Omega=8.97 \text{ kJ/cm}$				
ϕ	$f=2 \text{ Hz}$	$f=5 \text{ Hz}$	$f=10 \text{ Hz}$	$f=15 \text{ Hz}$
0.04				
0.14				
0.29				
0.35				
0.44				

Note: All dimensions are in mm

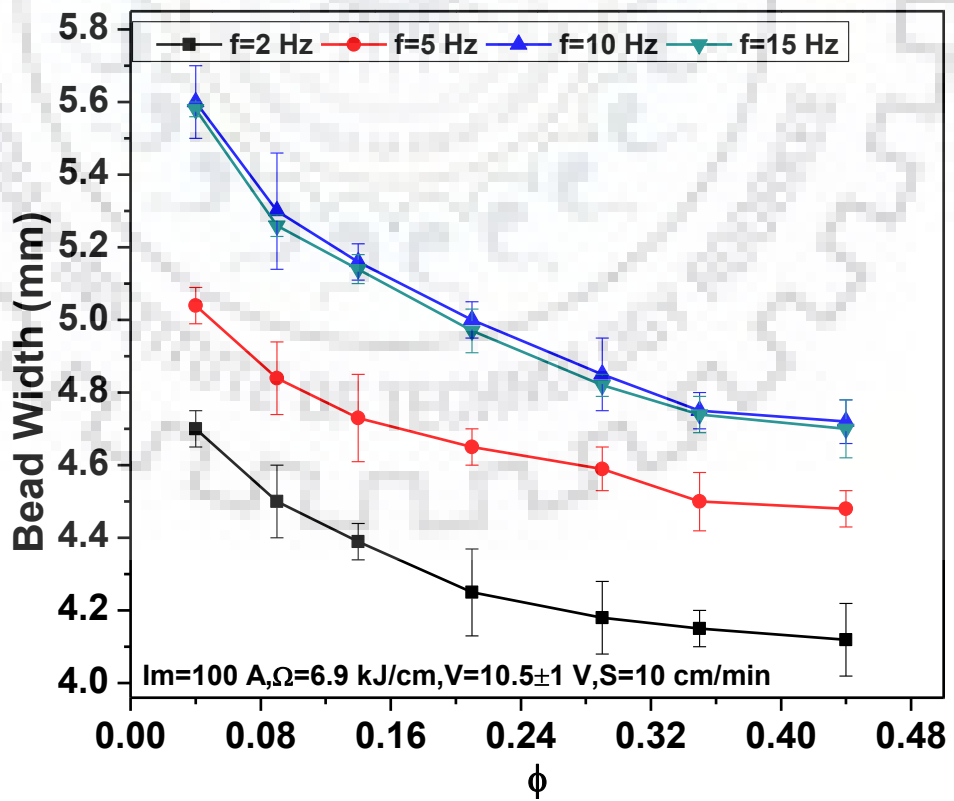
Fig. 6.17 At a given I_m and arc voltage of 130 A and $11\pm 1V$ respectively typical cross sectional macrographs of modified zone under varied ϕ and f .

$I_m=170 \text{ A}$ and $\Omega=12.75 \text{ kJ/cm}$				
ϕ	$f=2 \text{ Hz}$	$f=5 \text{ Hz}$	$f=10 \text{ Hz}$	$f=15 \text{ Hz}$
0.0 4				
0.1 4				
0.2 9				
0.3 5				
0.4 4				

Note: All dimensions are in mm

Fig. 6.18

At a given I_m and arc voltage of 170 A and $11 \pm 1 \text{ V}$ respectively typical cross sectional photographs of modified zone under varied ϕ and f .



(a)

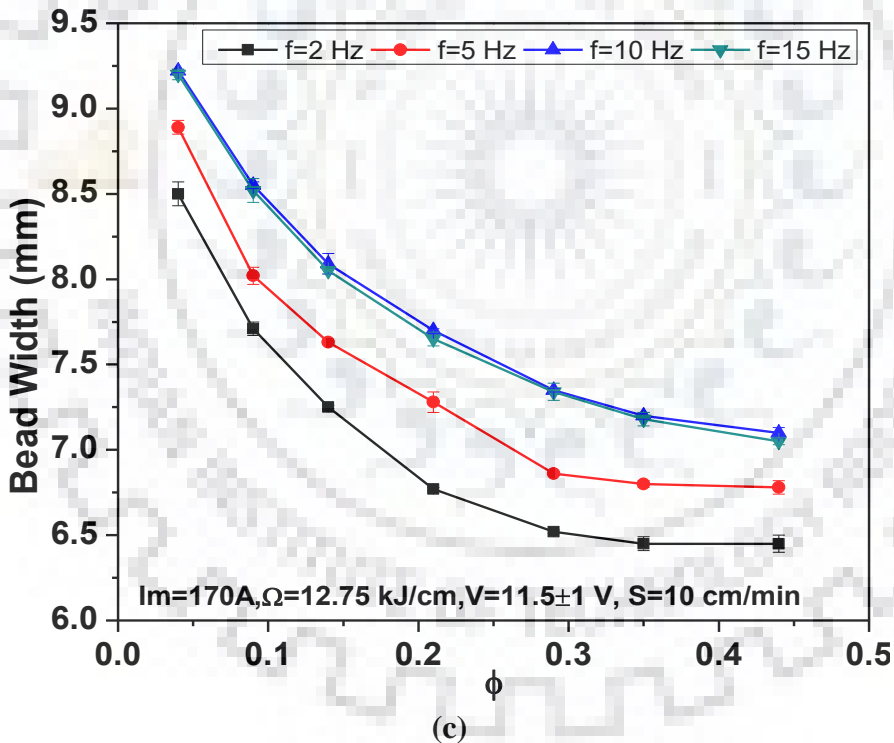
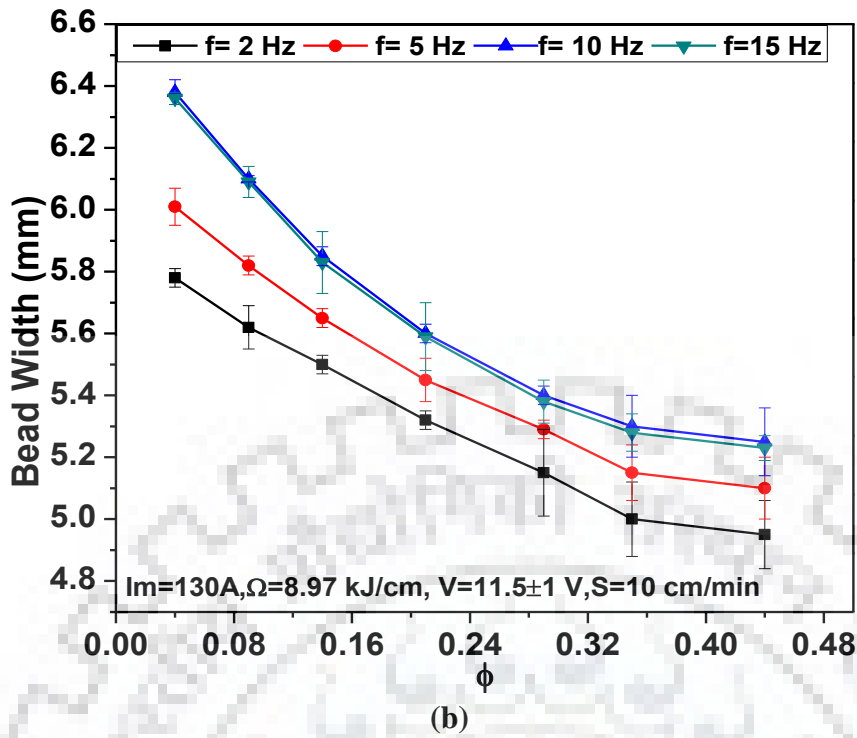


Fig. 6.19 At a given arc voltage of $11\pm 1V$, the effect of ϕ and f on bead width under different mean current of 100, 130 and 170 A respectively.

Similarly at I_m of 100, 130 and 170 A the effect of ϕ at different pulse frequency (f) on depth of penetration (P_d), width of HAZ (W_{HAZ}) and area of fusion (A_{FZ}) of single pass TIG arcing process is shown in Figs. 6.22 (a-c), 6.23 (a-c) and 6.24 (a-c) respectively. It is observed from the figures that at a given Ω the increase of ϕ from 0.04 to 0.44 reduces P_d , W_{HAZ} and A_{FZ} when f remains constant. However, here it is also observed that at a given ϕ the increase in f

from 2 to 10 Hz significantly enhances the P_d , W_{HAZ} and A_{FZ} and is then marginally reduces with a further increase of f to 15 Hz. At a given f and I_m the reduction in the P_d , W_{HAZ} and A_{FZ} with the increase of ϕ may have also primarily happened due to the reduction of heat build-up in the fused zone of the workpiece. Whereas, at a given ϕ and I_m the increase of f from 2 to 10 Hz enhances the P_d , W_{HAZ} and A_{FZ} , which may have attributed to the enhancement of weld pool temperature (T_{WP}) due to increase of heat build-up in it. Whereas the further increase of frequency from 10 Hz to 15 Hz insignificantly affects those characteristics, possibly due to lowering of heat build-up in the fused zone. This may be realized that at a given heat input the heat build-up is a function of heat loss primarily due to heat consumed in remelting of primary solid forms during pulse off time and heat dissipation through conduction to the substrate, apart from the heat loss by convection and radiation processes. It may be broadly assumed that the heat lost in remelting of primary solids formed during interruption of arcing governed by pulse frequency predominantly dictates the heat build-up in the fused zone under the practically constant capacity of heat loss by conduction to the base metal. Thus, it is understood that when the increase of pulse frequency allows relatively less time of arc interruption promotes heat build-up in the fusion zone. Finally, at a certain pulse frequency the heat builds up in the fused zone becomes practically constant under insignificant loss of heat in remelting of less primary solids formed at a low period of interruption in arcing at a high pulse frequency. The situation remains similar at further higher pulse frequency. The observed characteristics of fused zone shown in Figs. 6.21 (a-c) - 6.24 (a-c) are in agreement to the understandings as stated above.

The empirical correlations of P_d , W_{HAZ} and A_{FZ} as a function of ϕ and f under different I_m has been given below.

$$\text{At } I_m = 100 \text{ A} \quad P_d = 0.005f - 0.90\phi + 0.02f\phi + 1.76 \quad (6.14)$$

$$\text{At } I_m = 130 \text{ A} \quad P_d = 0.03f - 1.5\phi - 0.02f\phi + 2.27 \quad (6.15)$$

$$\text{At } I_m = 170 \text{ A} \quad P_d = 0.02f - 1.52\phi + 0.011f\phi + 2.82 \quad (6.16)$$

$$\text{At } I_m = 100 \text{ A} \quad W_{HAZ} = 0.005f - 0.42\phi - 0.002f\phi + 0.88 \quad (6.17)$$

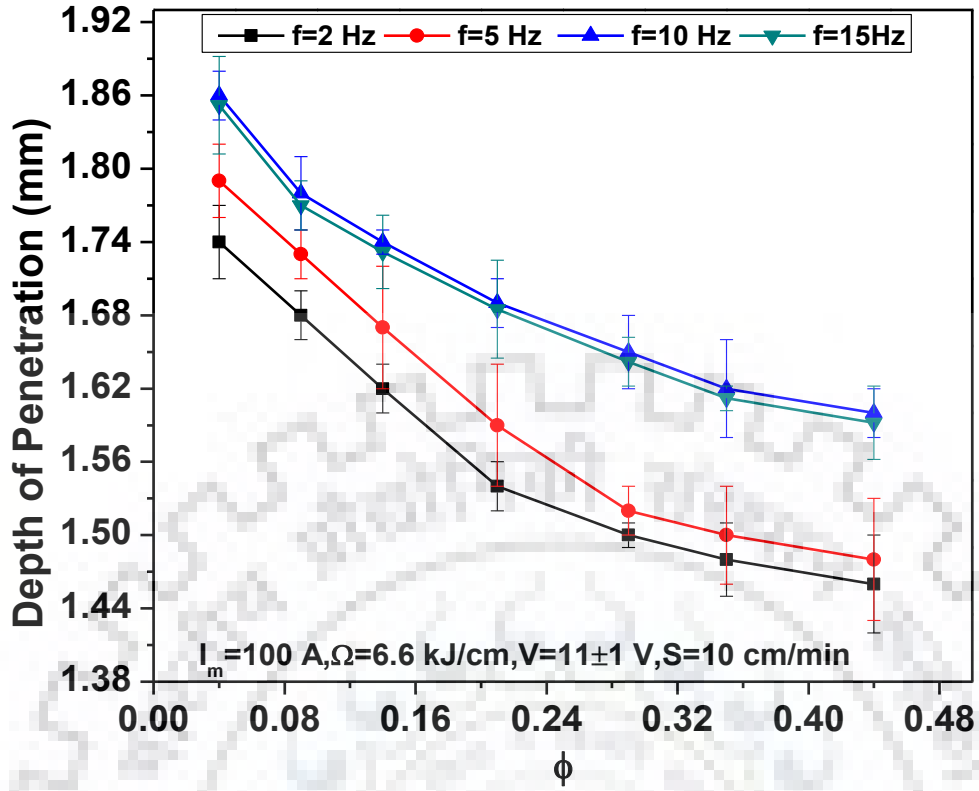
$$\text{At } I_m = 130 \text{ A} \quad W_{HAZ} = 0.006f - 0.47\phi - 0.001f\phi + 0.96 \quad (6.18)$$

$$\text{At } I_m = 170 \text{ A} \quad W_{HAZ} = 0.01f - 0.72\phi - 0.004f\phi + 1.78 \quad (6.19)$$

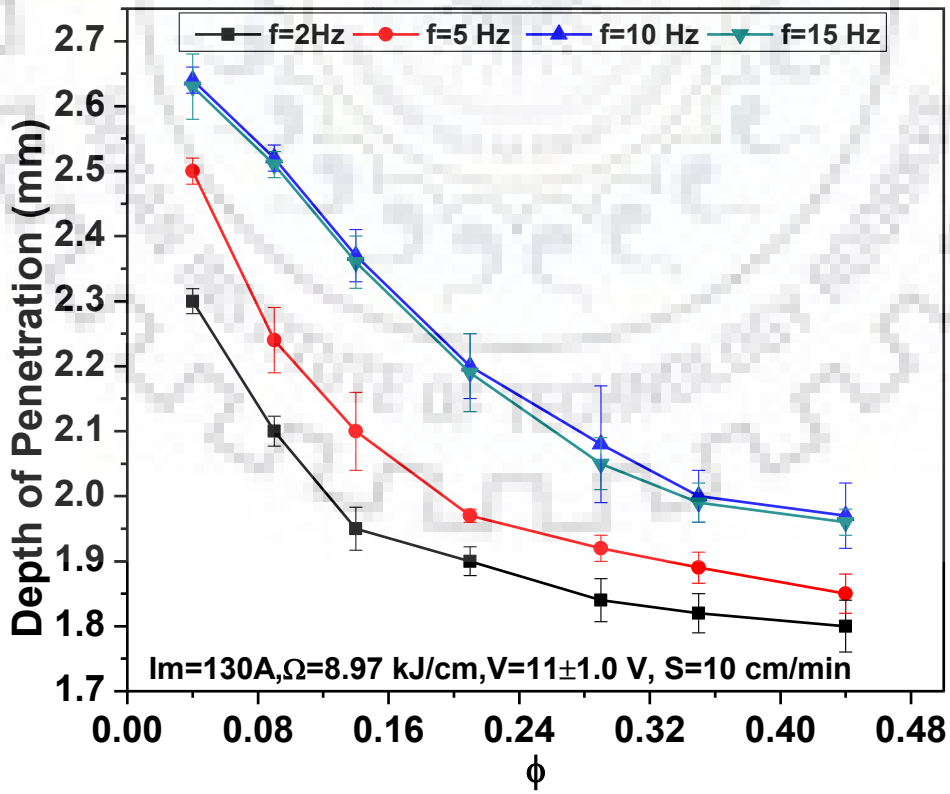
$$\text{At } I_m = 100 \text{ A} \quad A_{FZ} = 0.28f - 3.92\phi - 0.33f\phi + 8.27 \quad (6.20)$$

$$\text{At } I_m = 130 \text{ A} \quad A_{FZ} = 0.18f - 8.64\phi - 0.32f\phi + 13.16 \quad (6.21)$$

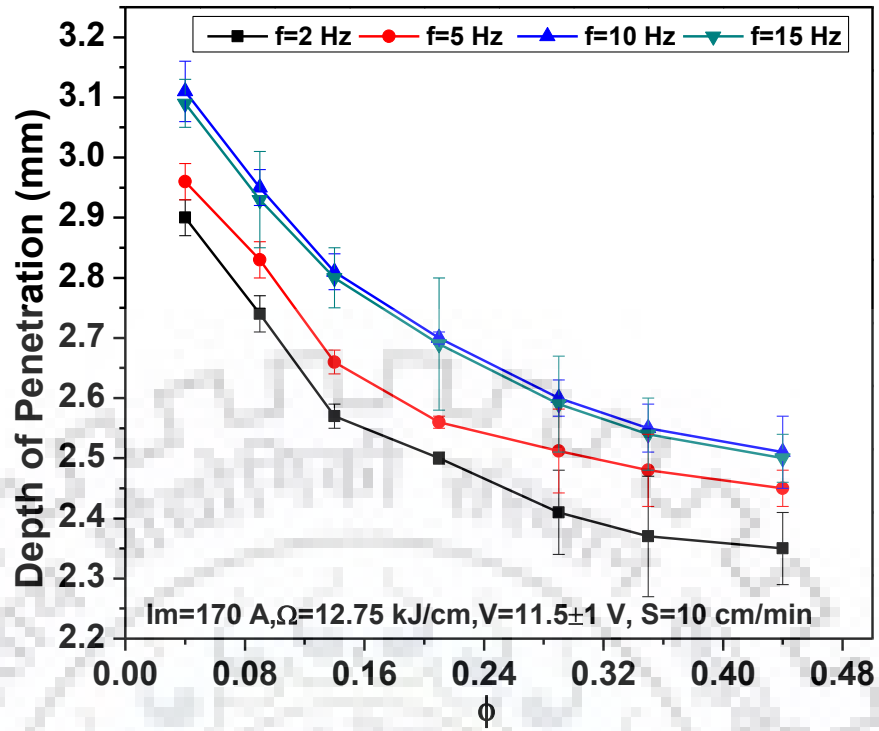
$$\text{At } I_m = 170 \text{ A} \quad A_{FZ} = 0.43f - 27.56\phi - 0.34f\phi + 27.84 \quad (6.22)$$



(a)



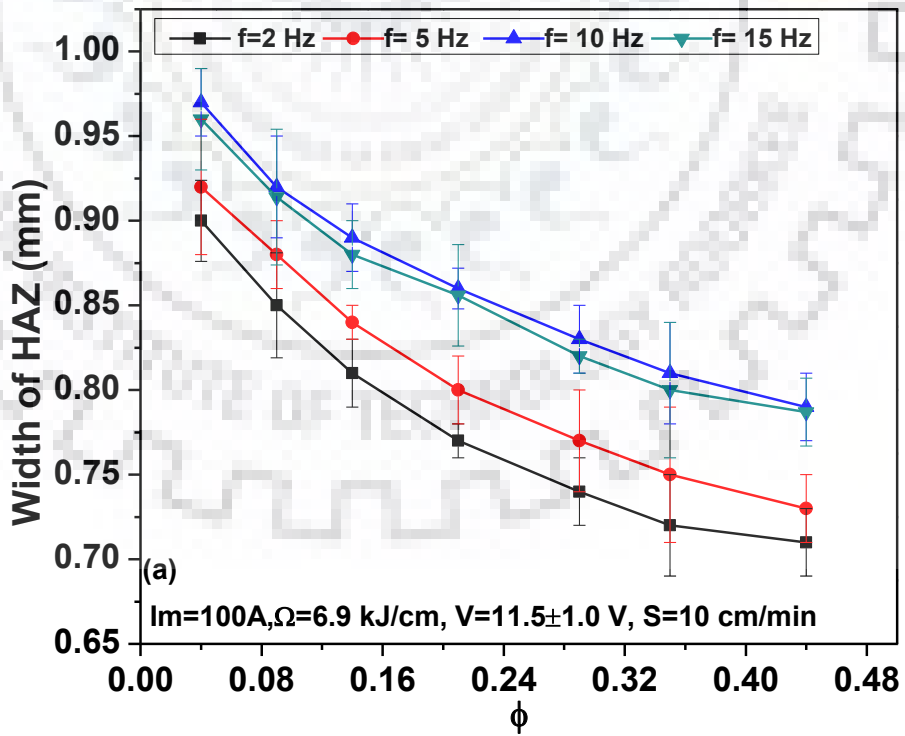
(b)



(c)

Fig. 6.20

At a given arc voltage of 11 ± 1 V, the effect of ϕ and f on depth of penetration under different mean current of 100, 130 and 170 A respectively.



(a)

(a)

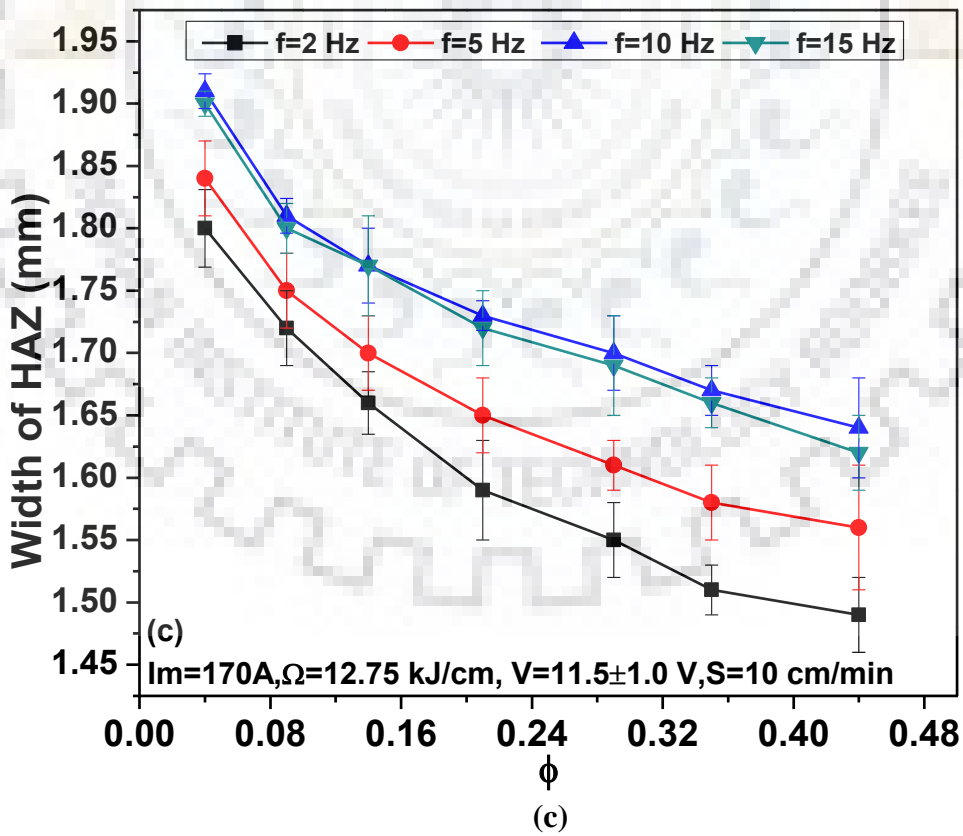
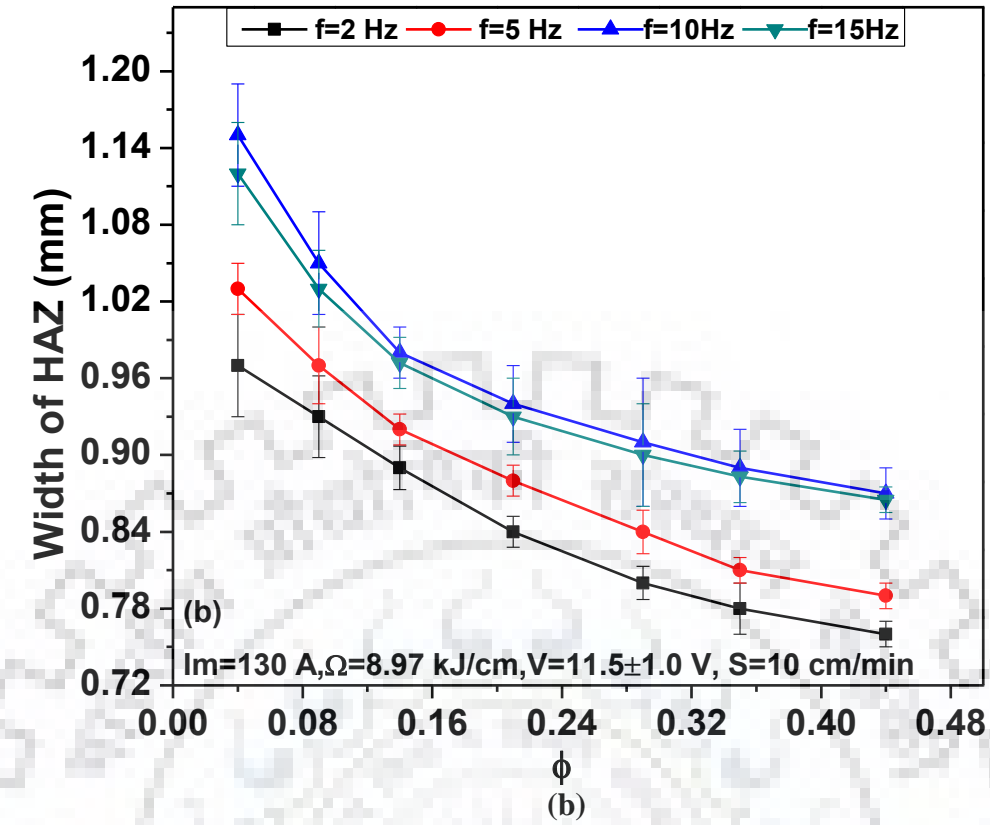
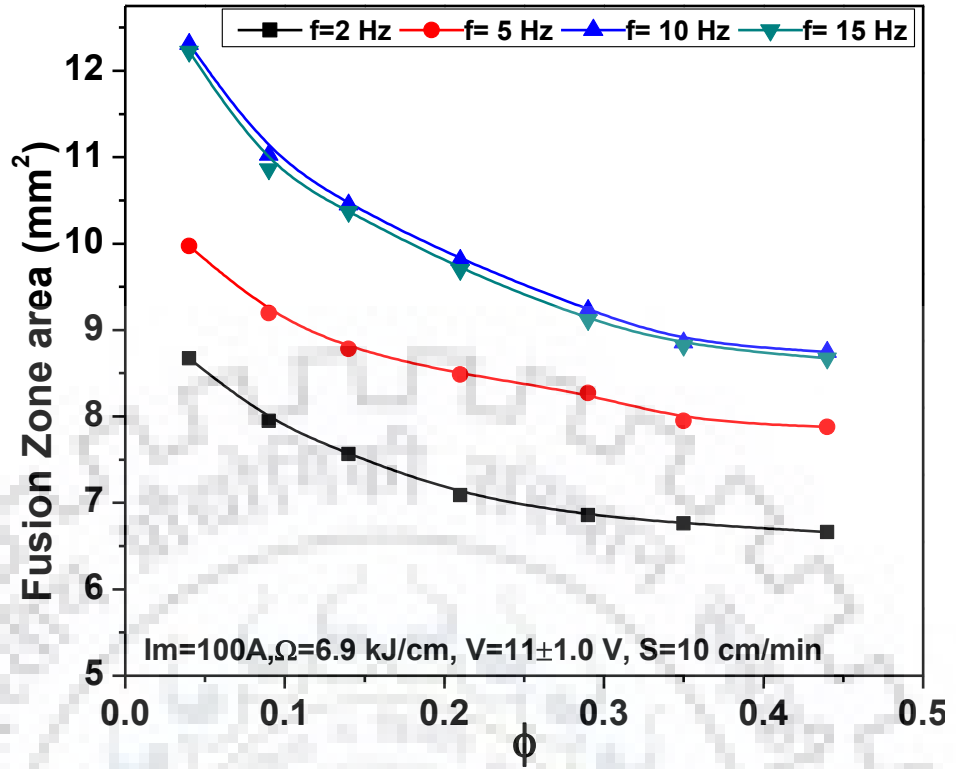
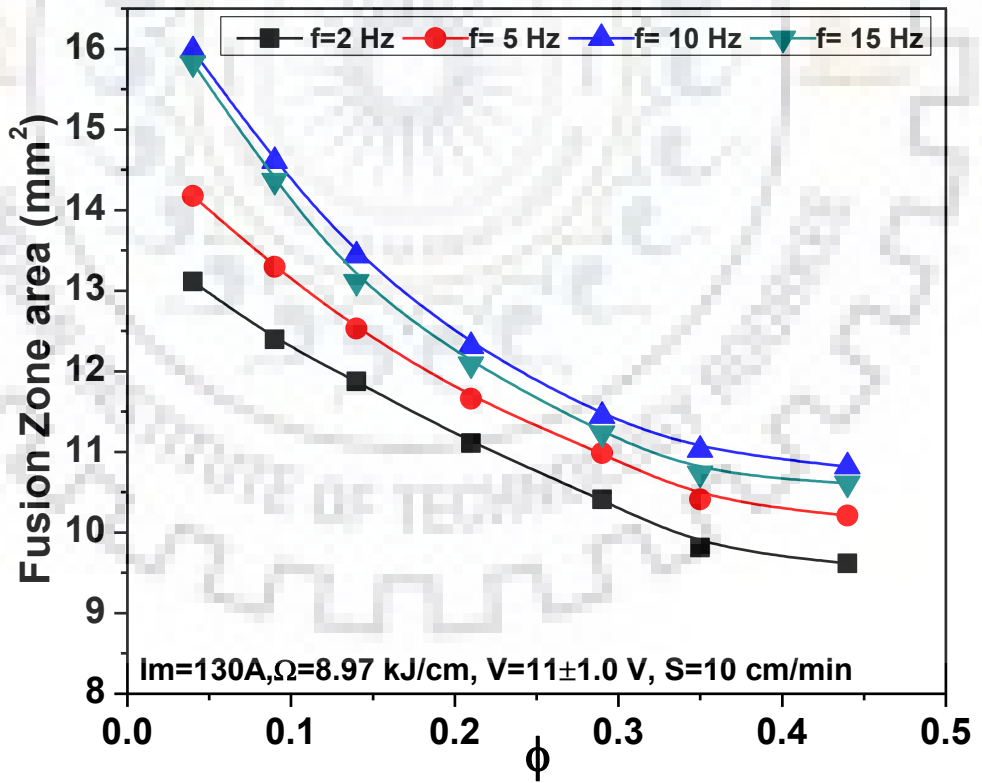


Fig. 6.21 At a given arc voltage of $11\pm 1\text{V}$, the effect of ϕ and f on width of HAZ under different I_m of 100, 130 and 170 A respectively.



(a)



(b)

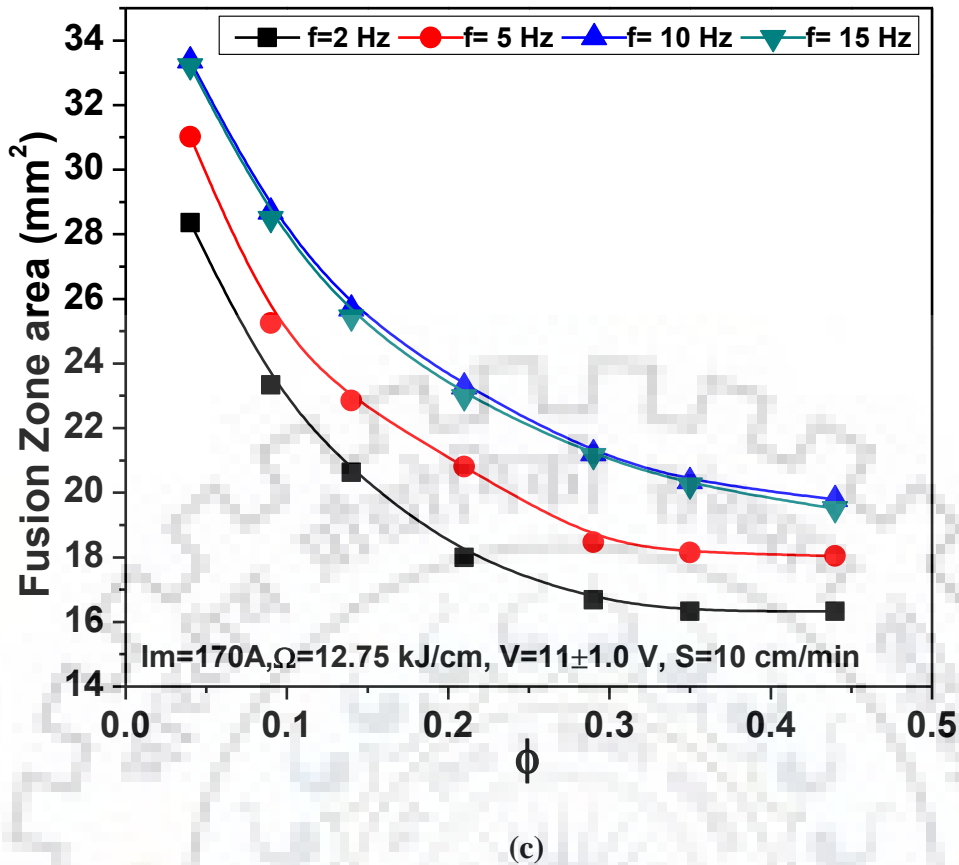


Fig. 6.22 At a given arc voltage of $11\pm 1V$, the effect of ϕ and f on fusion zone area under different mean current of 100, 130 and 170 A respectively.

6.2.3 Summary

Basic understandings of the effect of single pass C-TIGA and P-TIGA processes have been revealed in this study in terms of modified zone geometry like depth of penetration, width of fusion zone, width of HAZ and the fusion zone area. The studies on characteristics of the variation in arcing parameters (Arc current and travel speed) and their effect on heat input provides the effective utilization of the C-TIGA process for surface modification of materials. It is also observed from the results that in the P-TIGA process the effective control of ϕ and f at a given heat input significantly improves the geometrical characteristics of modified zone. However, it is interestingly observed that the use of P-TIGA process gives higher depth of penetration, higher width of fusion zone, lower width of HAZ and higher fusion zone area at relatively lower heat input as compared to that of the C-TIGA process. The precise control of heat buildup in fused zone by using appropriate ϕ and f in P-TIGA process effectively increases the depth of penetration, bead width and fusion zone area more than $30\pm 10\%$ as compared to that obtained in case of the C-TIGA process at the same arc current and heat input.

6.3 Analytical estimation of thermal characteristics

The size and shape of fusion zone in the TIG arcing process affect the mechanism and kinetics of solidification and thus, the microstructure and properties of the modified zone. The size and shape of the fusion pool along with the size and shape of its heat affected zone also affects the thermally introduced stresses that act on the modified zone leading to formation of residual stresses and distortion. In C-TIGA process, the size of fusion pool is controlled by the arc current, travel speed and heat input (Ω) while in P-TIGA process it is further governed by I_m , ϕ and pulse parameters in P-TIGA process. However, both the processes are governed by the isotherms and thermal cycle that may be predicted out of solutions of the heat flow equations. Thus, it is very much necessary to study the effect of these arcing parameters on isotherm and thermal cycle in order to critically understand, predict and ultimately control the final modified zone to a maximum extent for desired properties of substrate surface to perform under given service conditions.

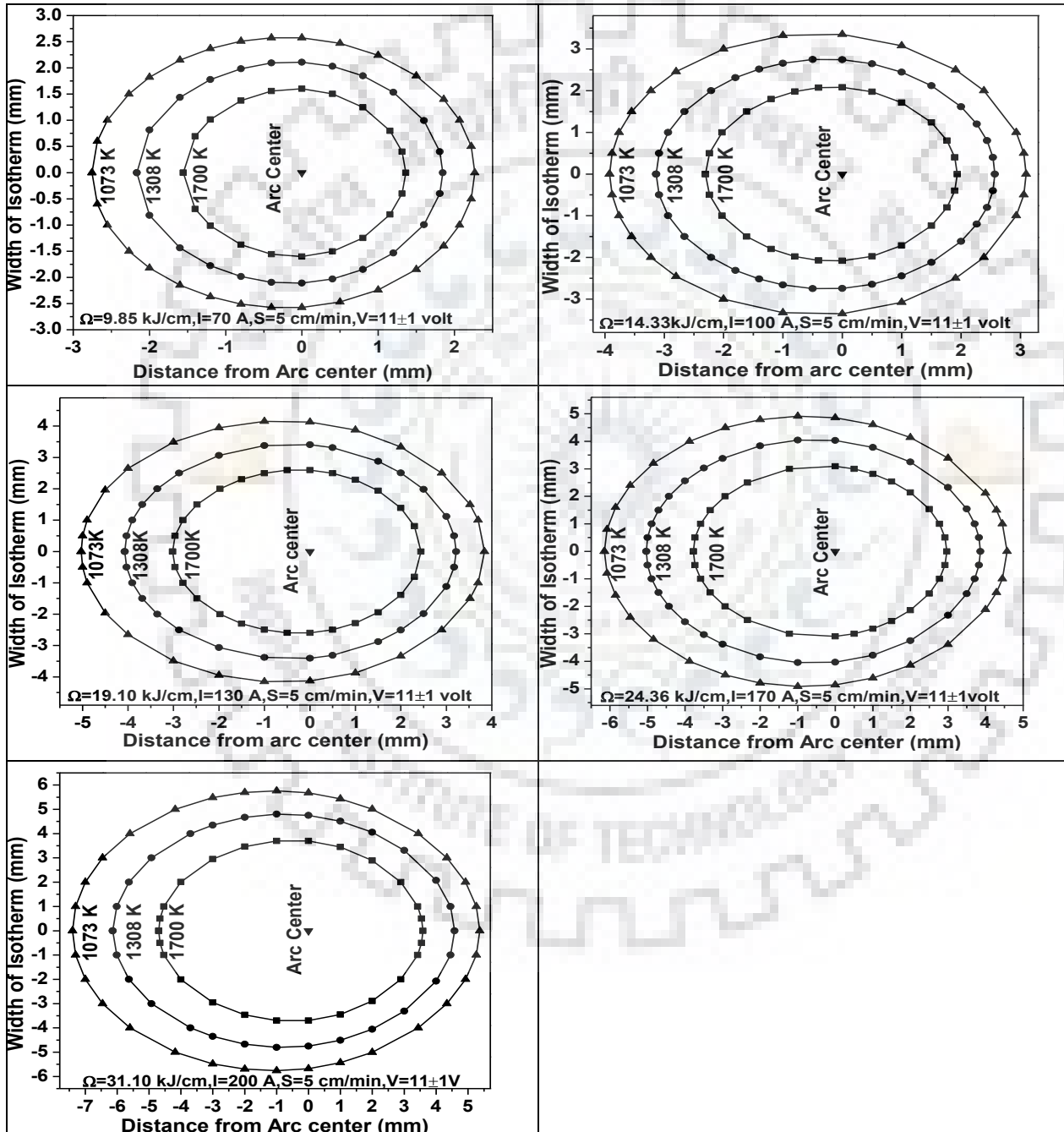
6.3.1 Analytical estimation of thermal characteristics for single pass C-TIGA process

The size of fused pool and HAZ is dictated by the isotherm produced in the substrate by the heat input as a function of operating current, arc voltage and travel speed of the C-TIGA process. The isothermal curves in both the planes of x-y and y-z, thermal cycle and cooling rate are estimated by the expression of heat flow as stated in chapter 5.

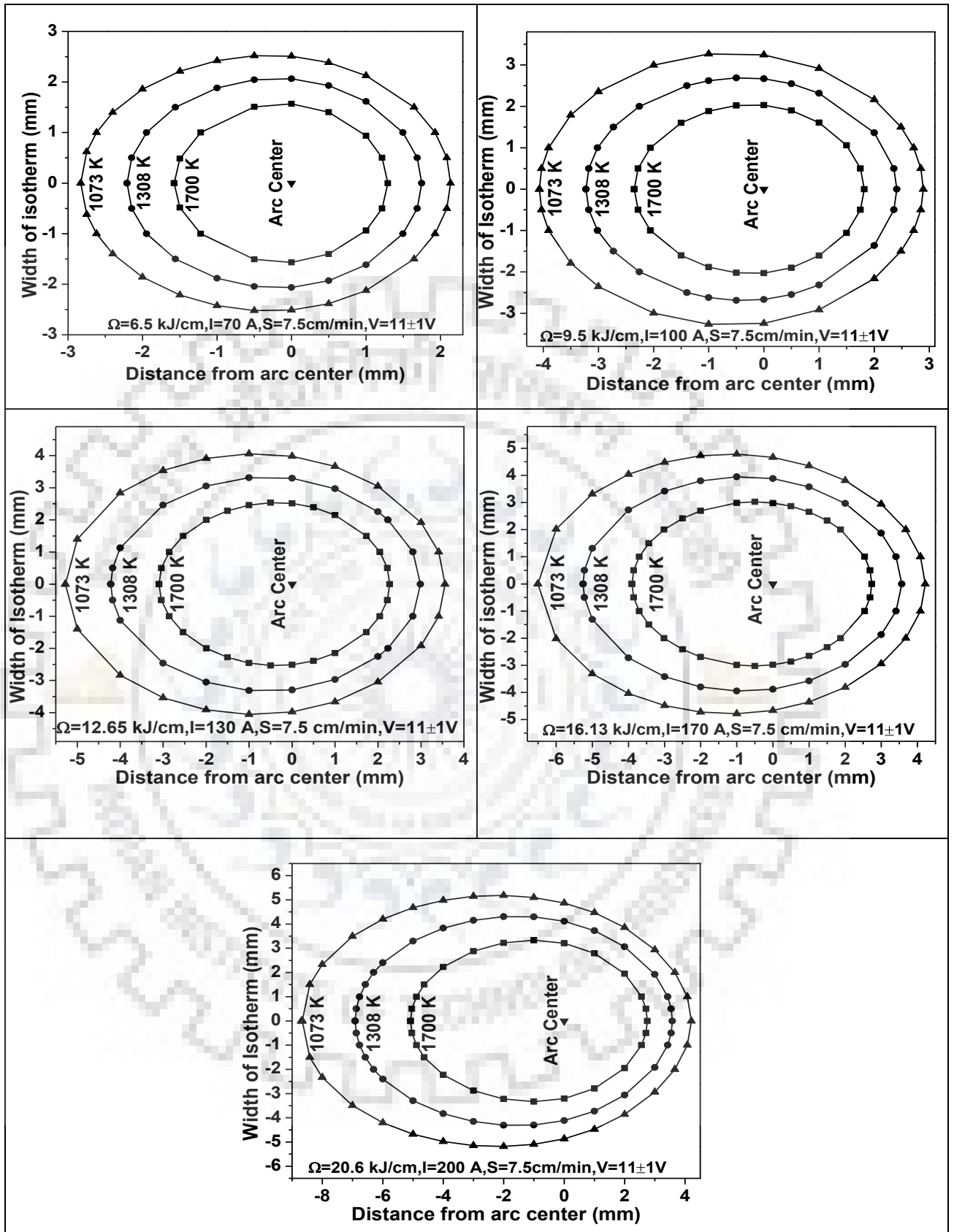
6.3.1.1 Isothermal curve in x-y and y-z plane

At a given arc voltage of 11 ± 1 V the variation in arc current and travel speed from 70 to 200 A and 5 to 15 cm/min, respectively, on fusion isotherm at the XY plane on the surface and YZ plane of the cross section have been shown in Figs. 25 (a-d) and 26 (a-d). It is observed from Figs. 25 (a-d) that the width and length of the isotherm increases with the increase of arc current at a given travel speed (S). Similarly the Figs. 26 (a-d) depict that the width and depth of modified zone increases with the increase in arc current at a given travel speed. This is primarily attributed to the increment in heat transferred to the fusion pool from the arc with the increase of arc current at given travel speed. It has been also observed from the figures that the increase of travel speed (S) at a given I and V reduces the width, length and depth of the isotherm. This is attributed to the reduction of the heat transferred to the fusion zone from the arc with the reduction of heat input (Ω). It is further observed that increase of Ω at a given I, which is achieved through the reduction of welding speed, increases the length of the fusion pool and depth of modified zone. This may have primarily happened because of its ability to cool the molten fusion pool to a relatively higher extent due to availability of comparatively

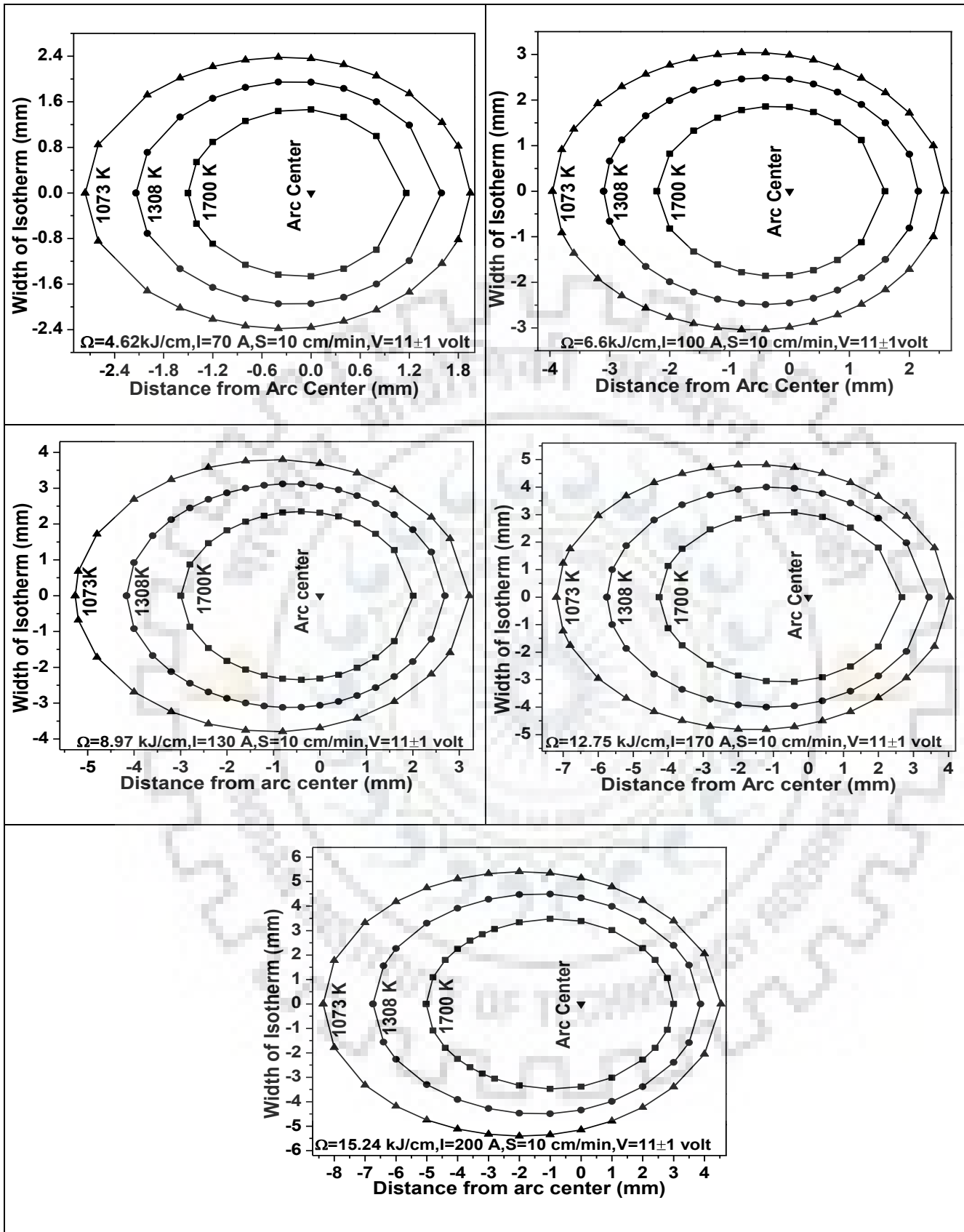
more time at lower welding speed and higher Ω . The increment in travel speed at a constant arc current reduces the energy input per unit length, which is responsible for distribution of energy into the workpiece. The increment in travel speed reduces the distribution of energy into the system. The Fig. 26 (a-d) also shows a comparison between the predicted and measured geometry of the modified zone at arc current and travel speed of 70 to 200 A and 5 to 15 cm/min respectively. The figure shows that the predicted geometry of modified zone is quite close to their experimental observations with an accuracy of $4\pm 2\%$.



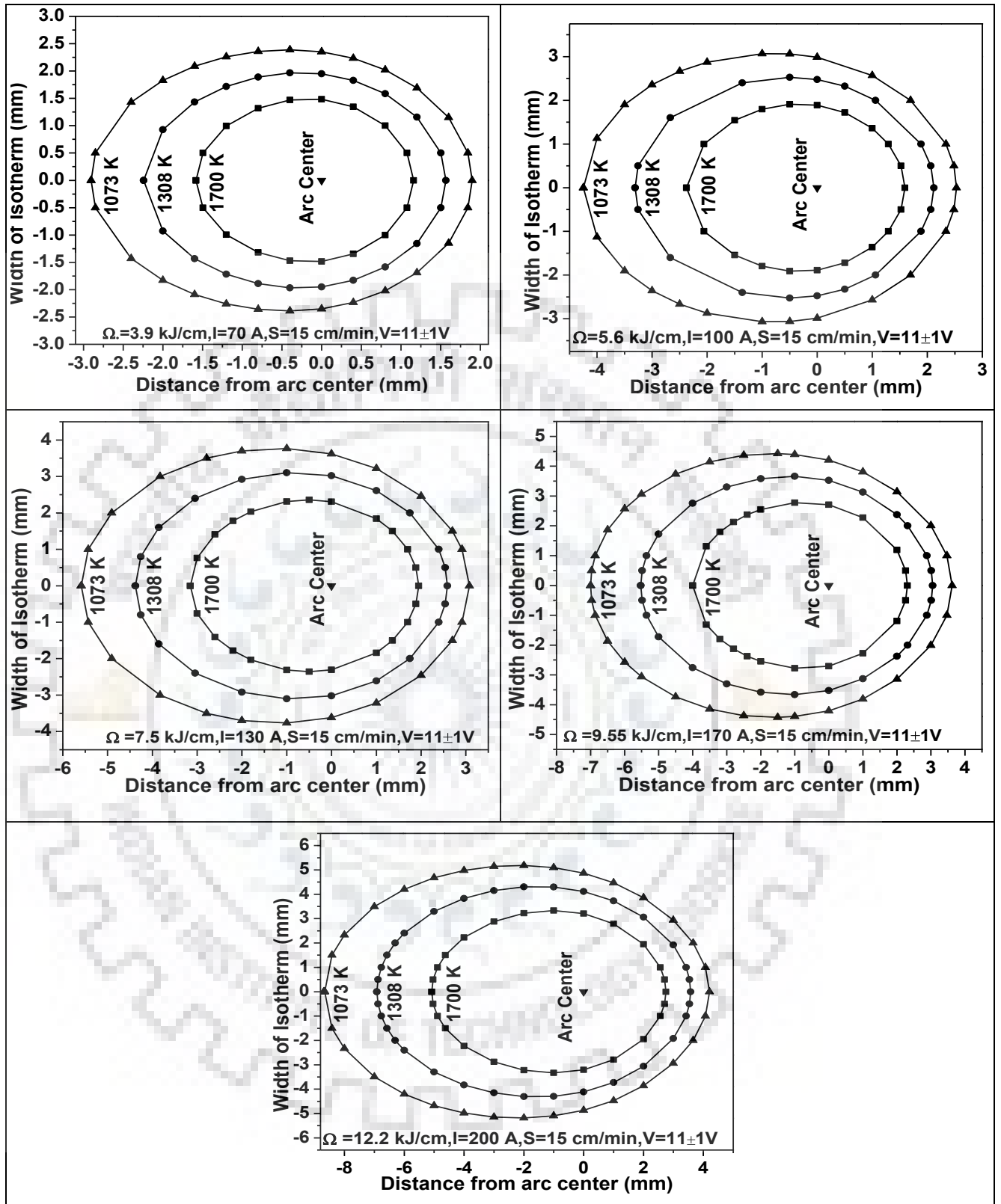
(a)



(b)



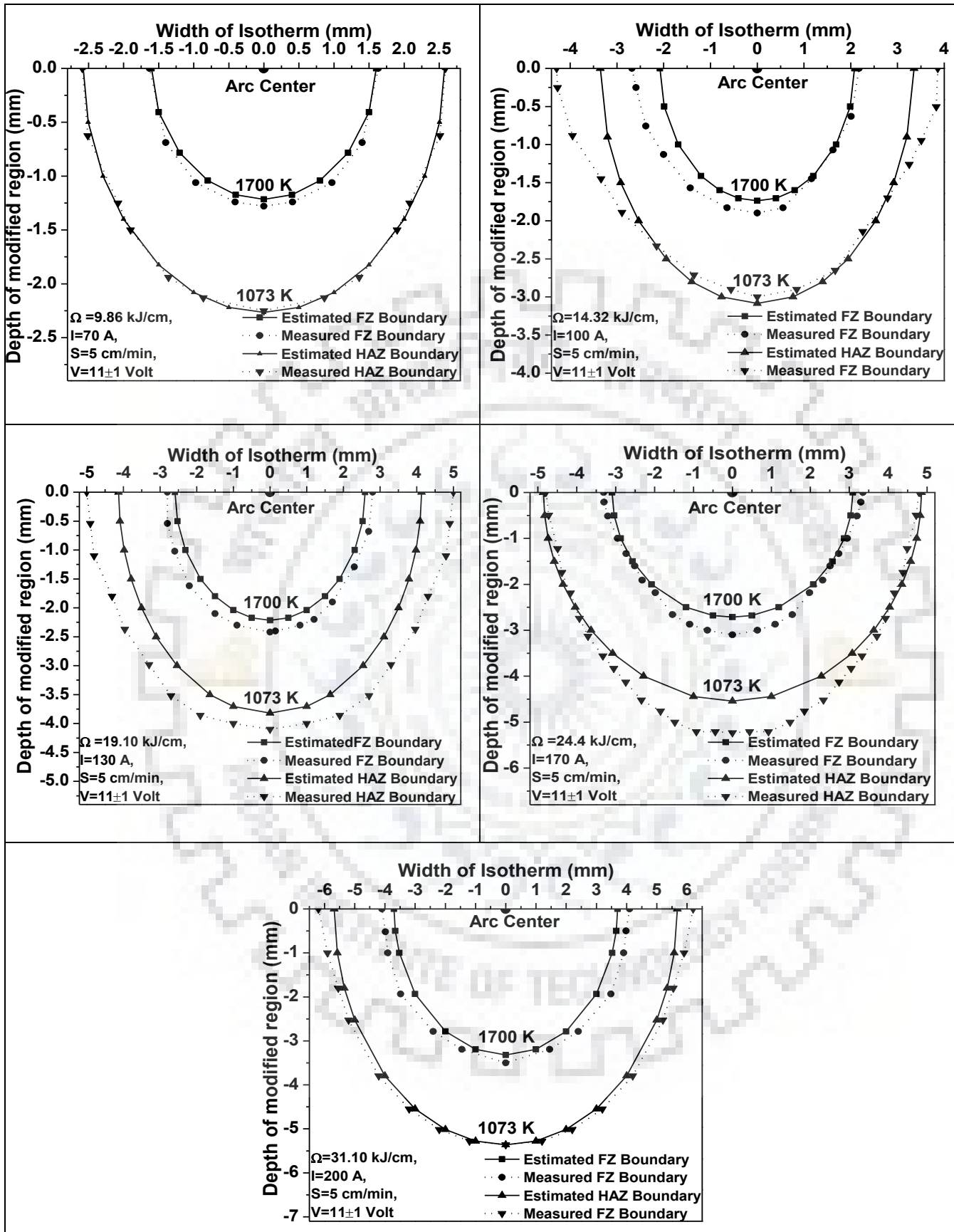
(c)



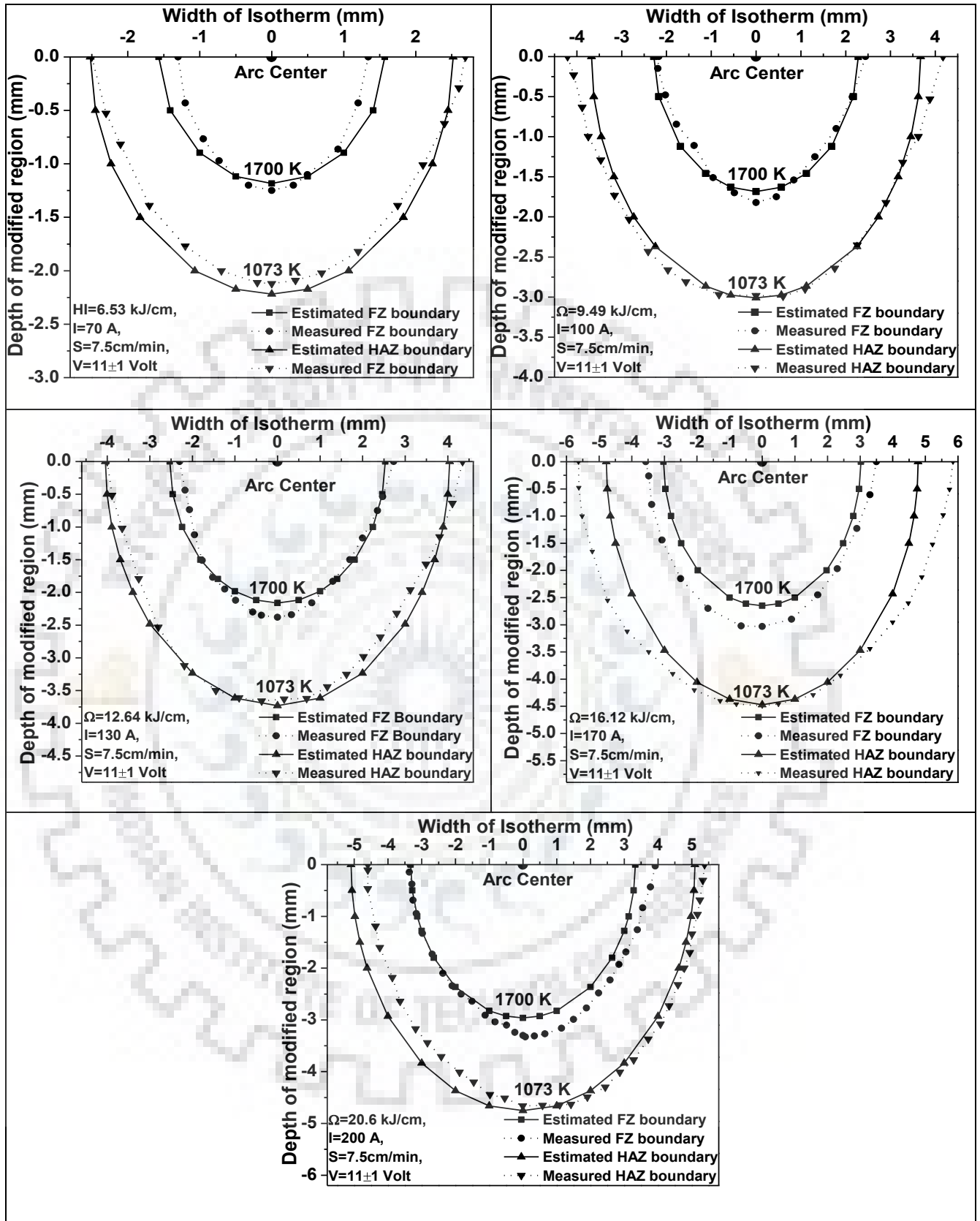
(d)

Fig. 6.23

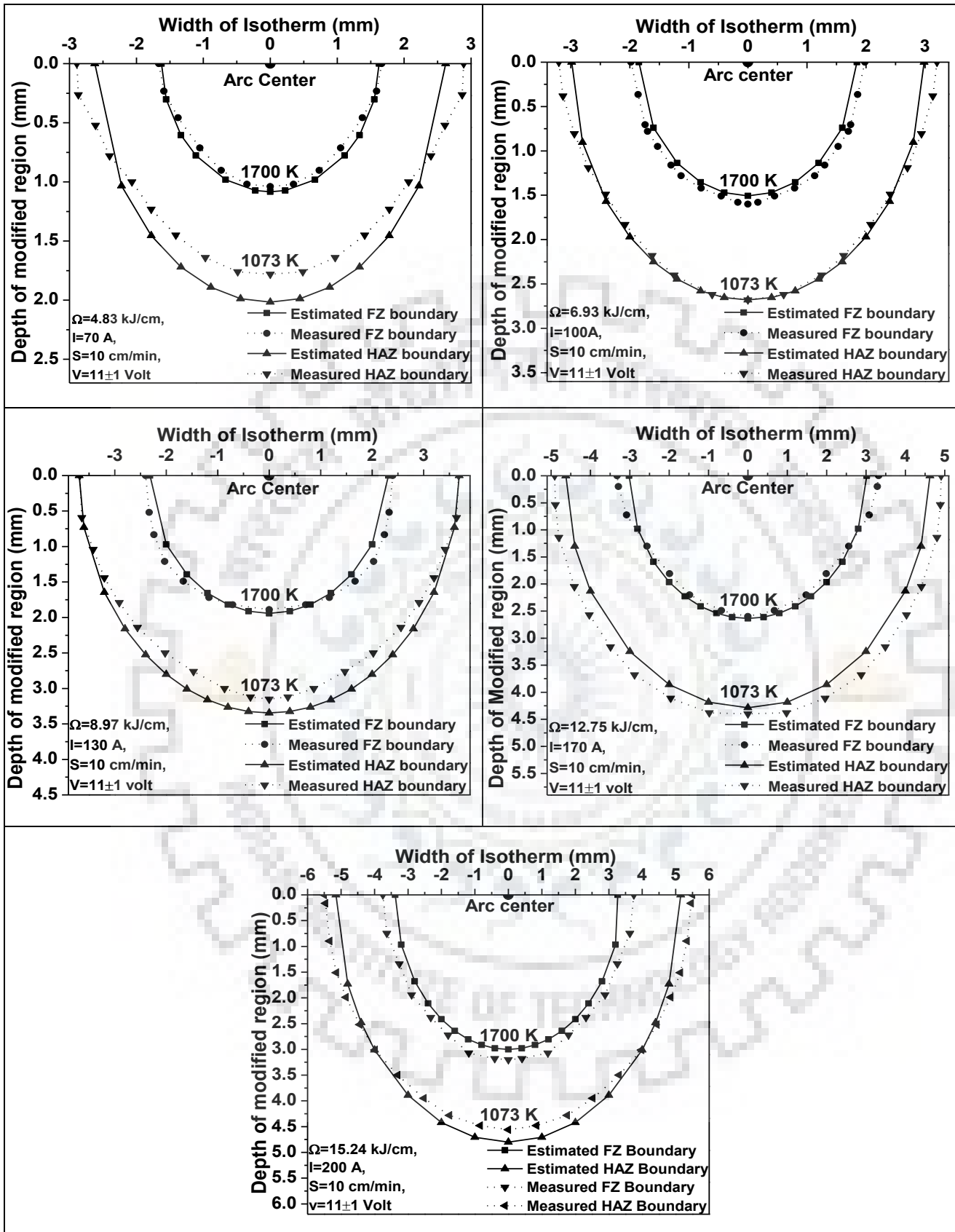
The effect of arcing current and heat input on estimated isotherms in XY plane at given arc voltage $11 \pm 1 \text{ V}$ and varied travel speed of (a) 5 cm/min (b) 7.5 cm/min (c) 10 and (d) 15 cm/min .



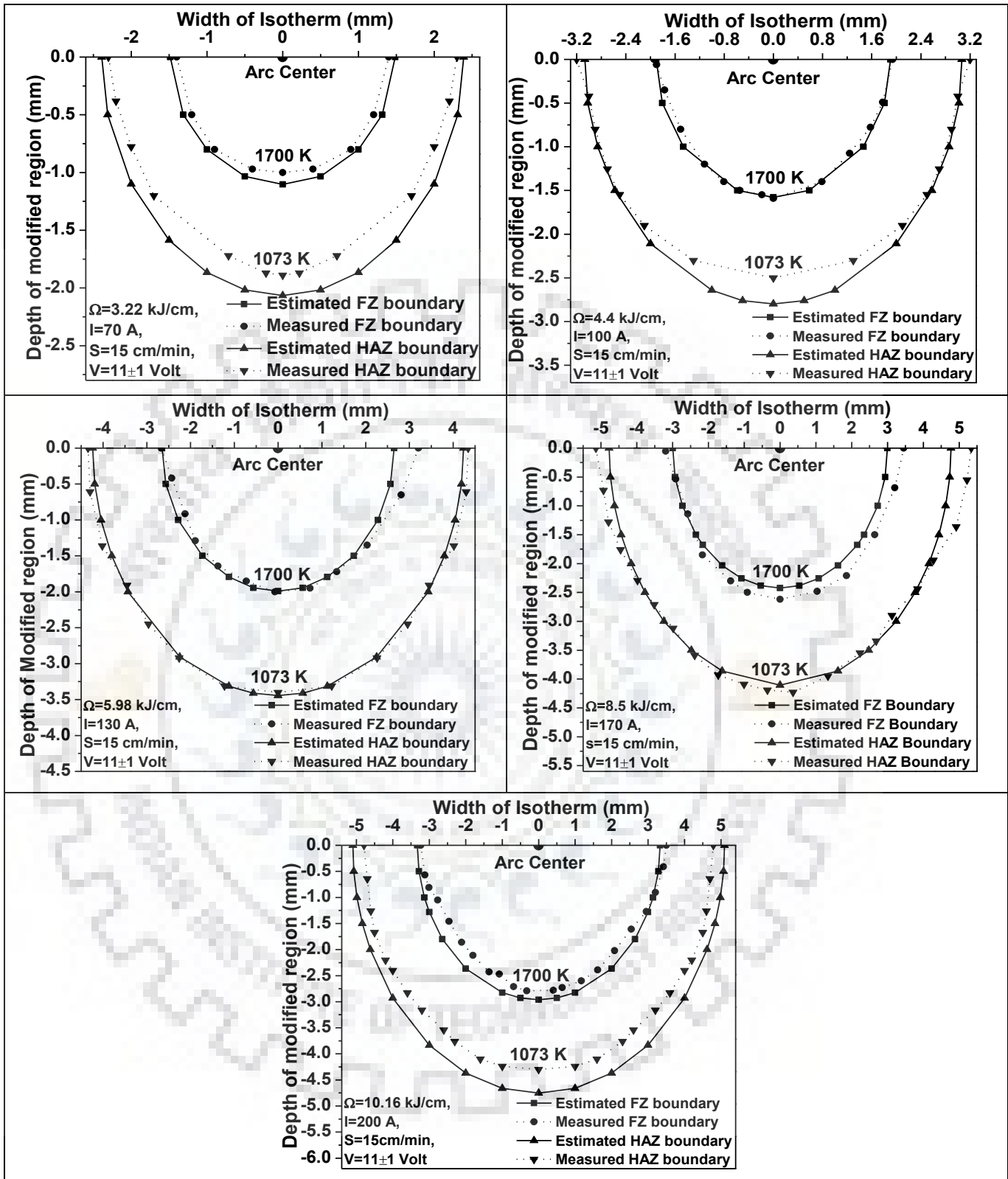
(a)



(b)



(c)



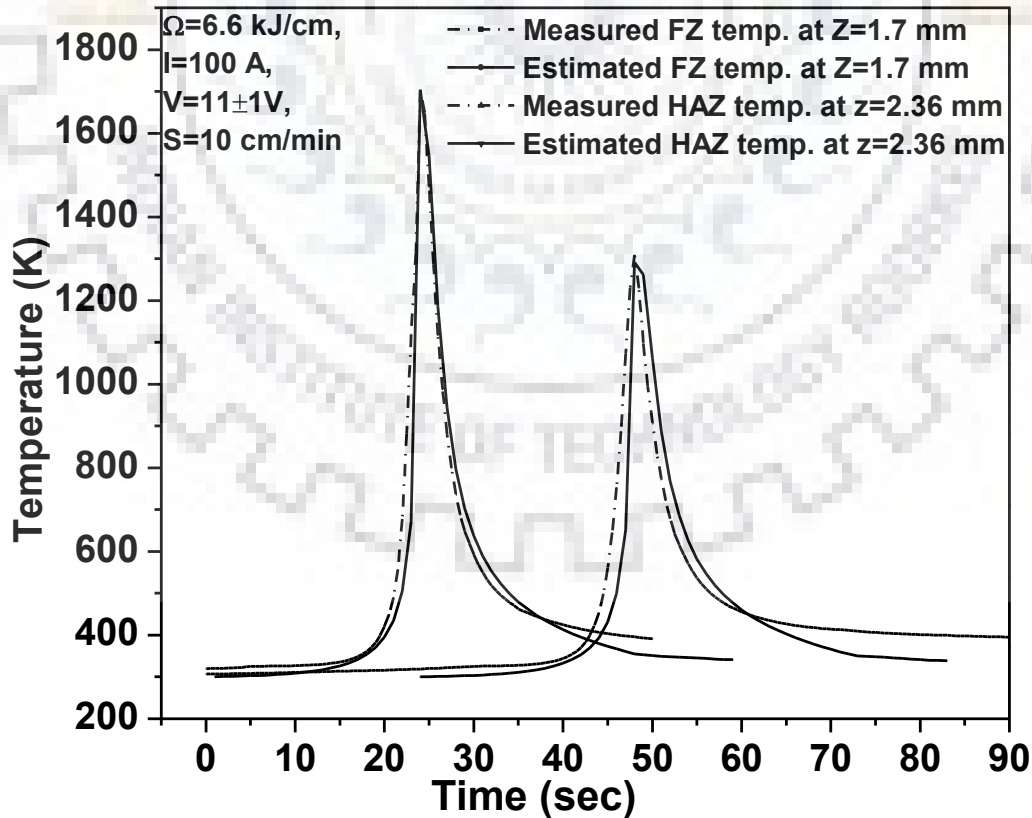
(d)

Fig. 6.24

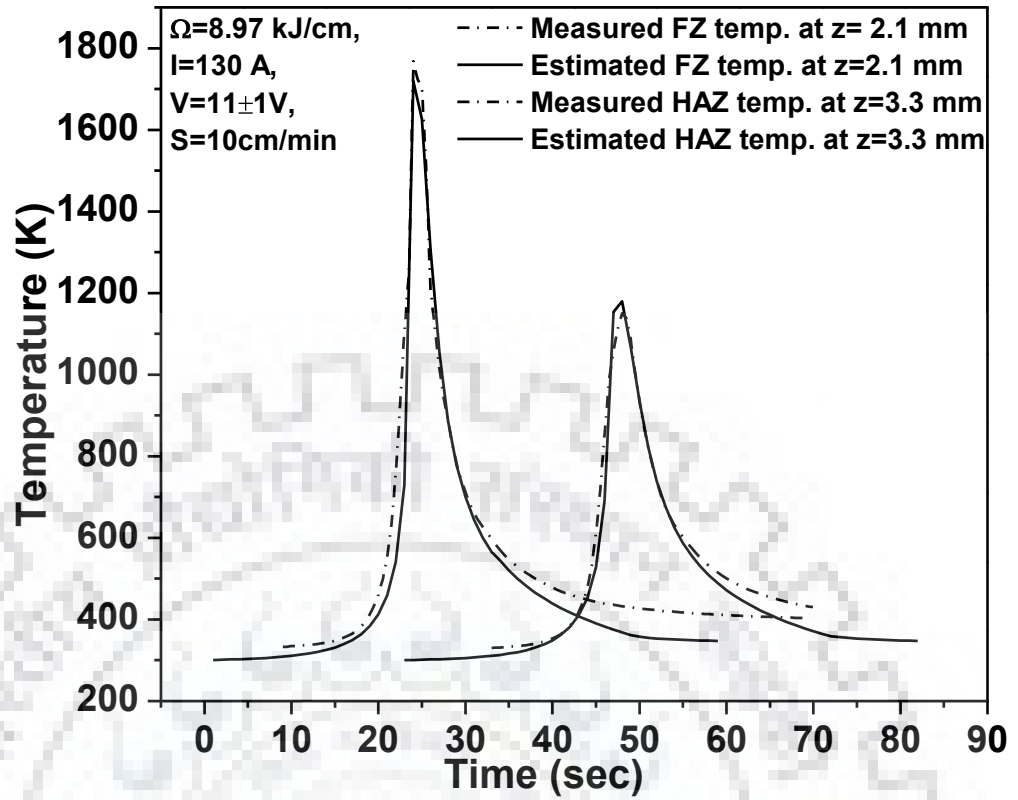
The effect of arcing current and heat input on estimated and measured isotherms in YZ plane at given arc voltage of 11 ± 1 V and varied travel speed of (a) 5 cm/min (b) 7.5 cm/min (c) 10 and (d) 15 cm/min.

6.3.1.2 Thermal Cycle

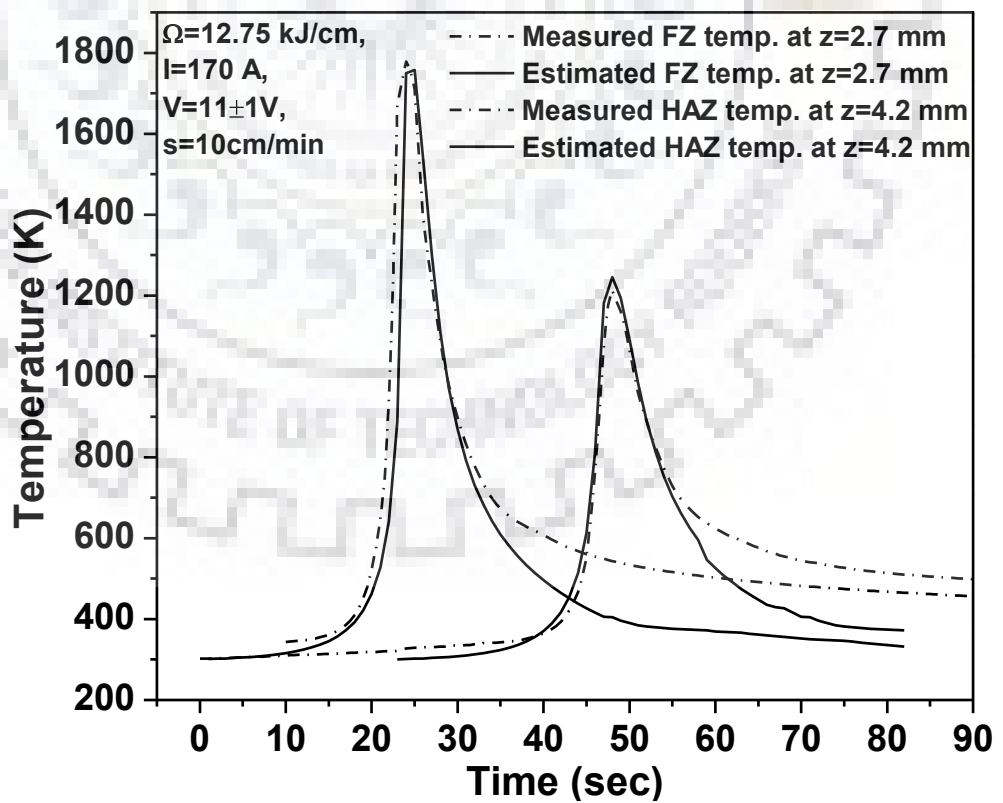
Thermal cycle shows variation in temperature with respect to time of a location inside and adjacent to the fused zone. At a given arc voltage and travel speed of 11 ± 1 V and 10 cm/min respectively, the effect of arc current and Ω , lying in the range of 100-200 A and 6.6–15.24 kJ/cm respectively, on estimated and measured thermal cycle of the fused zone and matrix (HAZ) adjacent to FZ is shown in Fig. 6.27 (a-d). The measured thermal cycle represents the characteristics of a point at a depth of Z axis corresponding to close approximation of its estimated value. It is observed that the increase in Ω with the increase of arc current reduces the cooling rate (CR). At higher heat input a lower area of the heat sink is available for heat transfer from the FZ to the surrounding matrix of base metal which may cause a lower CR at the intercritical temperature range (800–500 °C). But when the heat input is lowered from 15.24 to 4.83 kJ/cm due to lowering of arcing current from 200 to 70 A, a larger area of the available heat sink for heat transfer may cause a higher CR in the intercritical temperature range. This is attributed to increase in size of the fused pool at higher heat input that enhances the temperature of wider area of surrounding base metal and reduces its temperature gradient from the effective heat sink leading to lowering of CR.



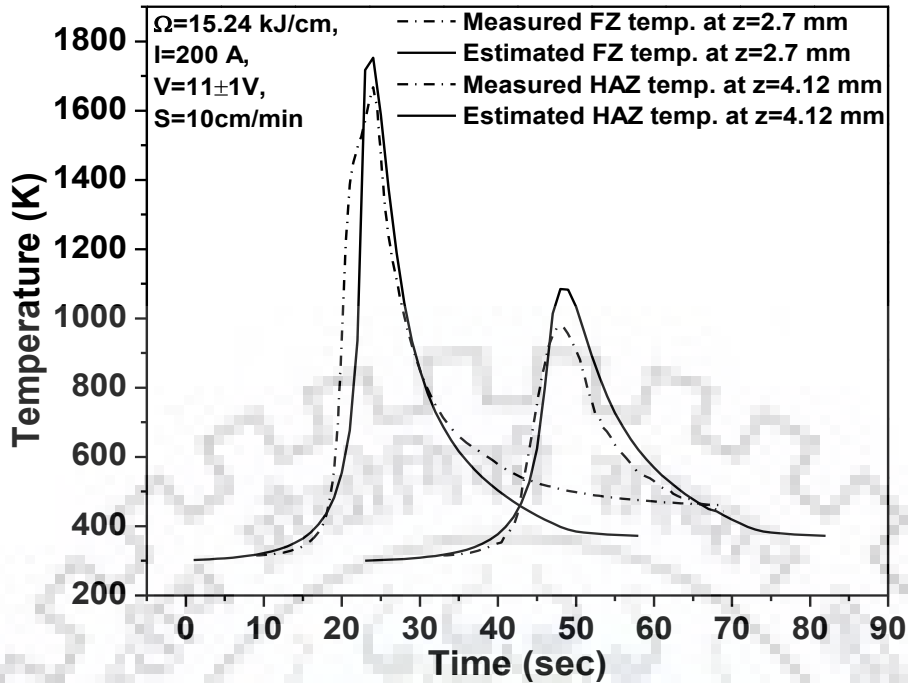
(a)



(b)



(c)



(d)

Fig. 6.25 Comparison of the estimated and measured weld thermal cycle at different combination of arc current and heat input of (a) 100 A; 6.6 kJ/cm (b) 130 A; 8.37 kJ/cm (c) 170A; 12.75 kJ/cm and (d) 200A, 15.24 kJ/cm

Table 6.1: Comparison of the estimated and measured peak temperature of FZ and HAZ at different operating parameters.

Operating parameters		Fusion Zone Temperature (T_p)		HAZ Temperature (T_p)	
I (A)	Ω (kJ/cm)	Estimated (K)	Measured (K)	Estimated (K)	Measured (K)
100	6.6	1703	1703.37	1291	1308
130	8.97	1719	1768	1180	1151
170	12.75	1757	1779	1245	1213
200	15.24	1753	1669	1085	977

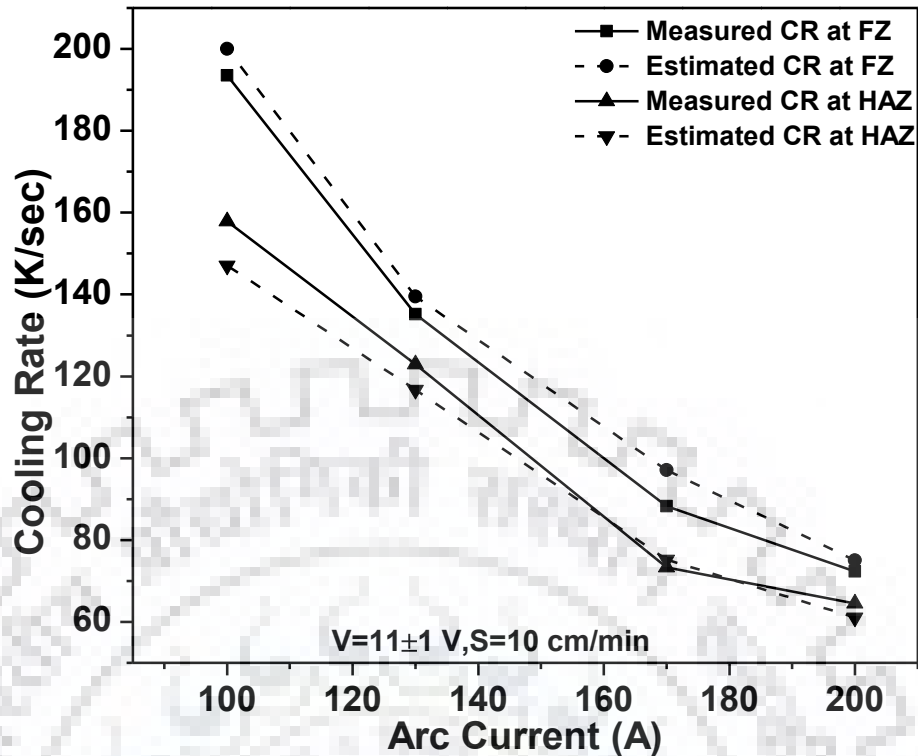


Fig. 6.26 Comparison of estimated and measured cooling rate at intercritical temperature range (800-5000C).

The table 6.1 shows the estimated and measured peak temperature of the FZ and HAZ at different arcing parameters. There is the 10 to 15 % variation in the peak temperature at the FZ and HAZ. Fig. 6.28 shows the estimated and measured CR at the intercritical temperature range evaluated from the respective thermal cycle plots. The figure shows that CR decreases with the increase in heat input on variation in arcing current from 100 to 200 A. The figure also shows that the estimated magnitude of CR is similar to its measured value with an accuracy of average variation $4 \pm 1\%$. The variation of isotherm and CR from the peak temperature dictates the final phase transformation of the fused zone and HAZ.

6.3.2 Analytical estimation of thermal characteristics for single pass P--TIGA process

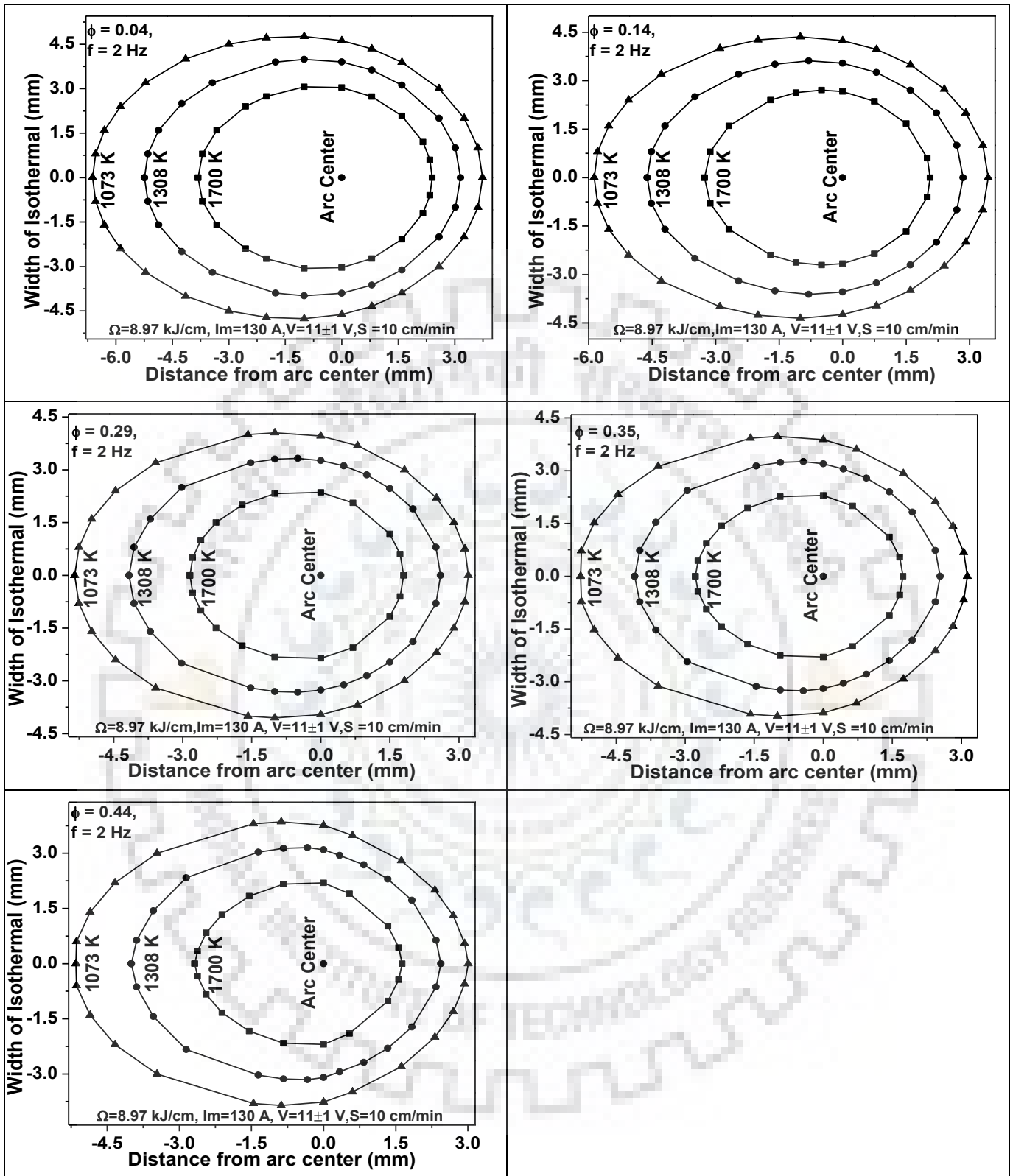
In the P-TIGA process the size and shape of the fusion pool along with the size and shape of the heat affected zone is dictated by the mean current (I_m), heat input (Ω), and pulse current parameters and governed by the isotherms predicted out of solutions of the heat flow equations. Thus, it is very much necessary to study the effect of these parameters on isotherms in order to critically understand, predict and ultimately control the final modified zone up to a maximum extent for desired performance of case hardenable AISI 8620 steel.

6.3.1.1 Isothermal curve in x-y and y-z plane

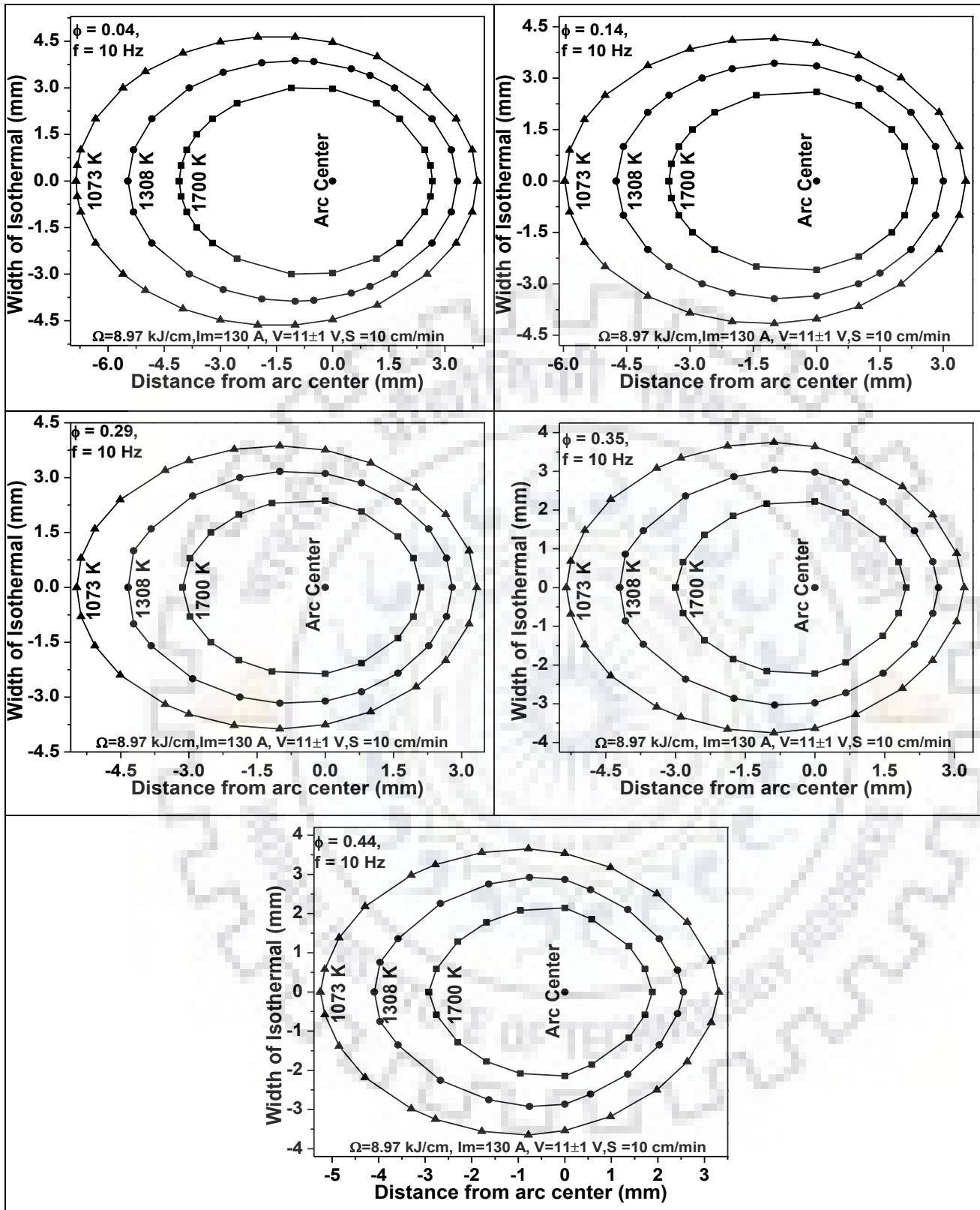
At a given arc voltage and travel speed of $11 \pm 1V$ and 10 cm/min, the isotherms of modified zones on AISI 8620 steel plates are estimated by Eqs. 5.3 and 5.4 (Chap.5.5.3) at two

levels of I_m and different pulse parameters. At varying I_m to 130 and 170 A, the typical estimated fusion isotherms in XY plane at different pulse frequencies of 2 and 10 Hz and ϕ lying in the range of 0.04-0.44 respectively have been shown in Figs. 6.29 (a and b) and 6.30 (a and b) respectively. It appears from the figures that the length and width of the isotherms decrease with the increase of ϕ at a given I_m and f . The figures also reveal that the increase of I_m and f from 130 to 170 A and 2 to 10 Hz enhances the length and width of isotherms at a given ϕ . Such a variation in the length and width of isotherm as a function of ϕ and f may be primarily attributed to the variation of the heat build-up in the fusion pool.

Similarly, at a varying I_m of 130 and 170 A, the typical fusion isotherms of the cross section (yz plane) at different f of 2 and 10 Hz and ϕ lying in the range of 0.04-0.44 have been shown in Figs. 6.31 (a and b) and 6.32 (a & b) respectively. The figures also compare the estimated fusion isotherm with the measured isotherm to find the acceptability of the analytical modelling. It appears from the figures that the depth and width of the modified zone reduces with the increase of ϕ at the same Ω and f . It further appears from the figures that the increase in frequency enhances the depth and width of the modified zone at a given ϕ . Further observations of figures reveal that the increase in I_m also increases the width and depth of the modified zone at same ϕ and f respectively. The variations of depth and width of modified zone as shown in figures are primarily governed by heat build-up into the workpiece due to the variation of ϕ , f and I_m .

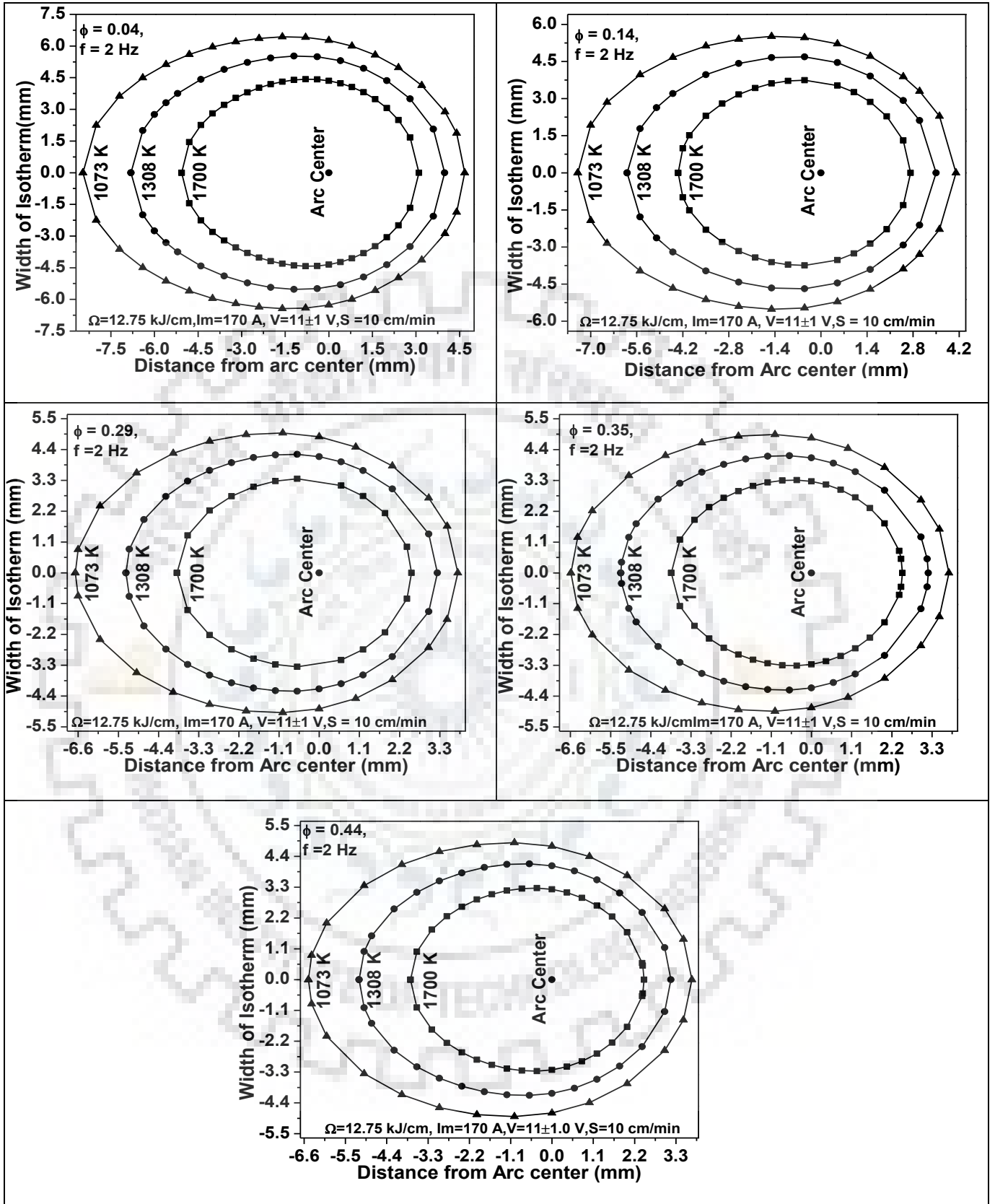


(a)

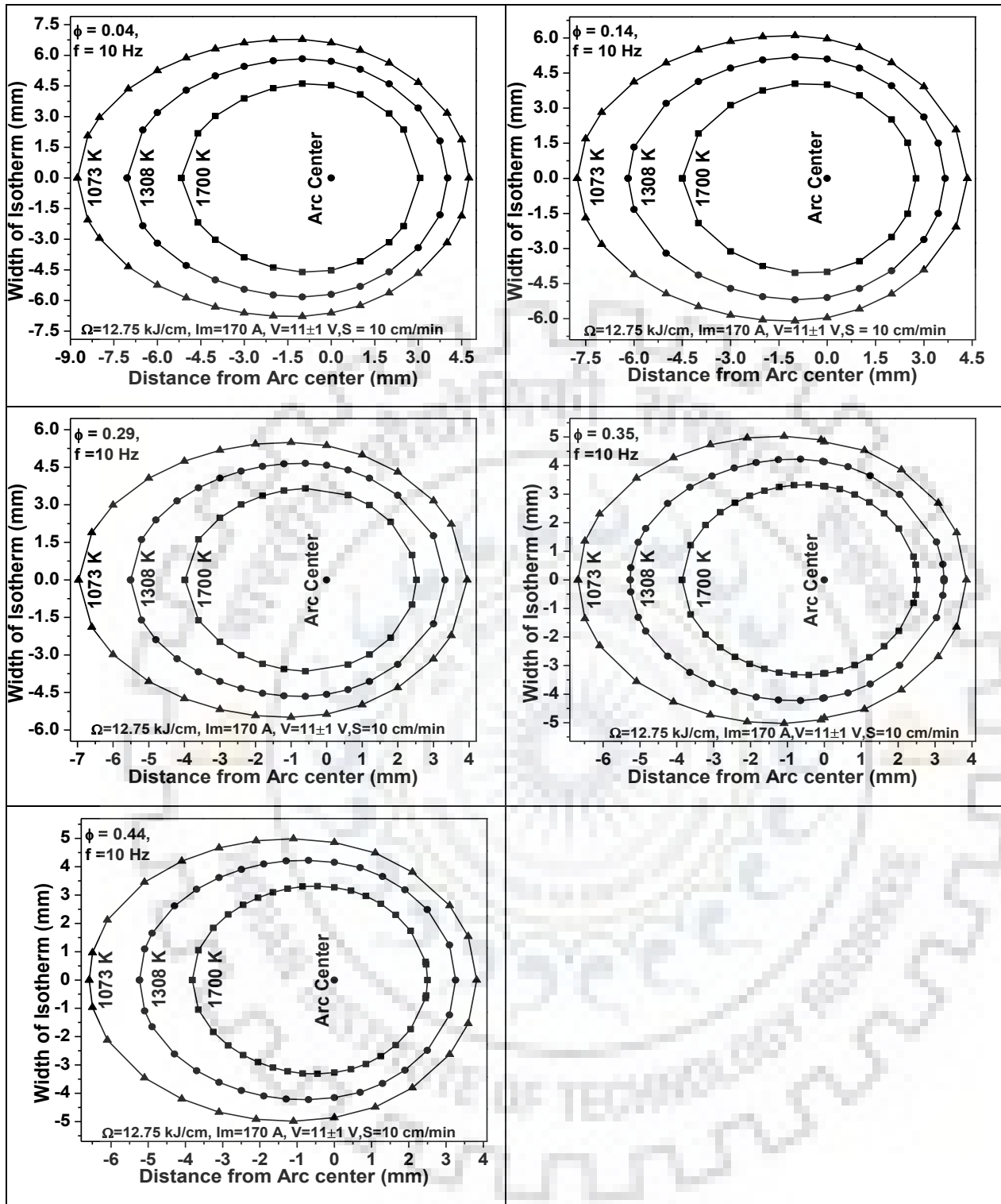


(b)

Fig. 6.27 Estimated isotherms in XY plane at given I_m of 130 A under varied ϕ from 0.04 to 0.44 and pulse frequency of (a) 2 Hz (b) 10 Hz.



(a)

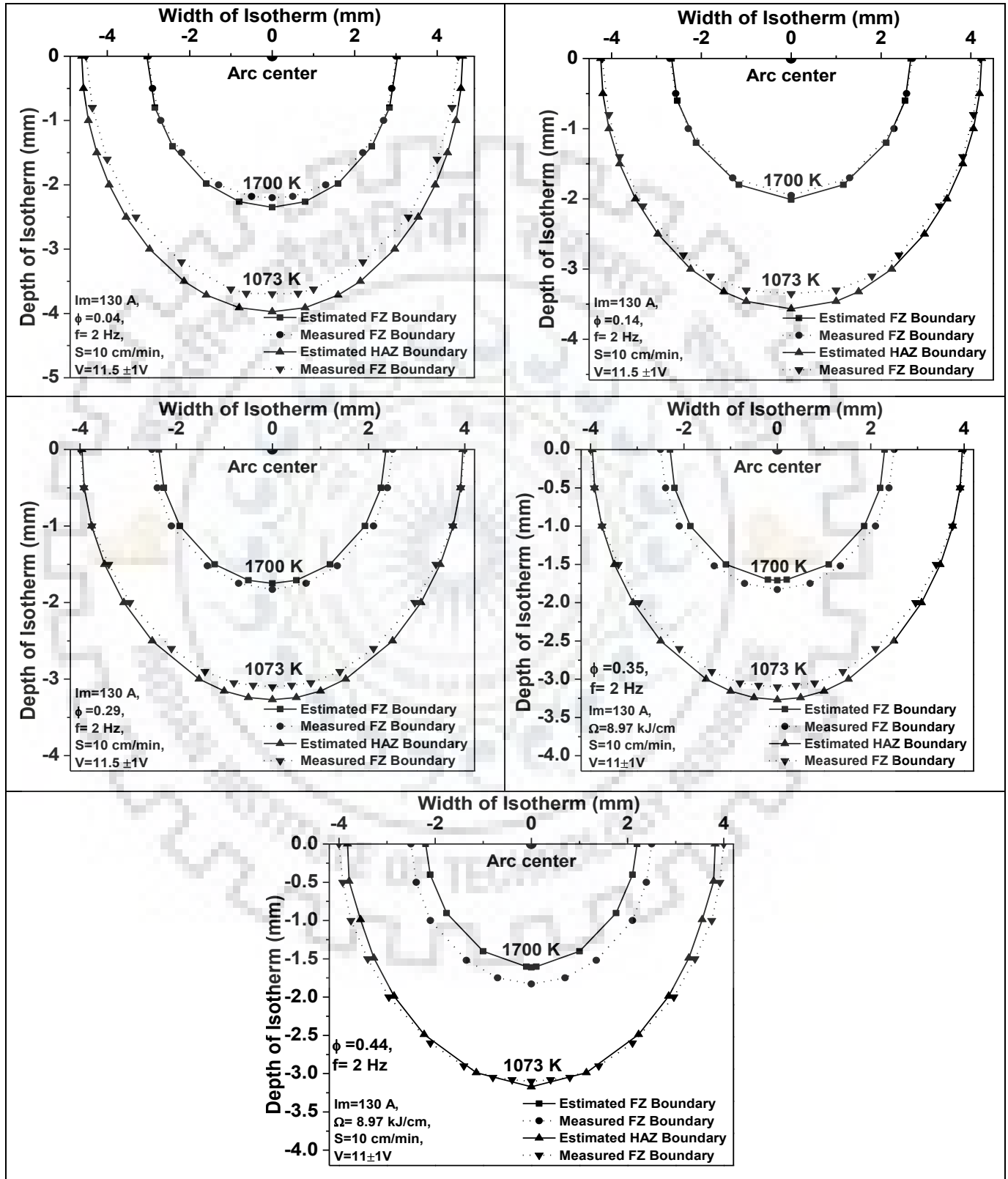


(b)

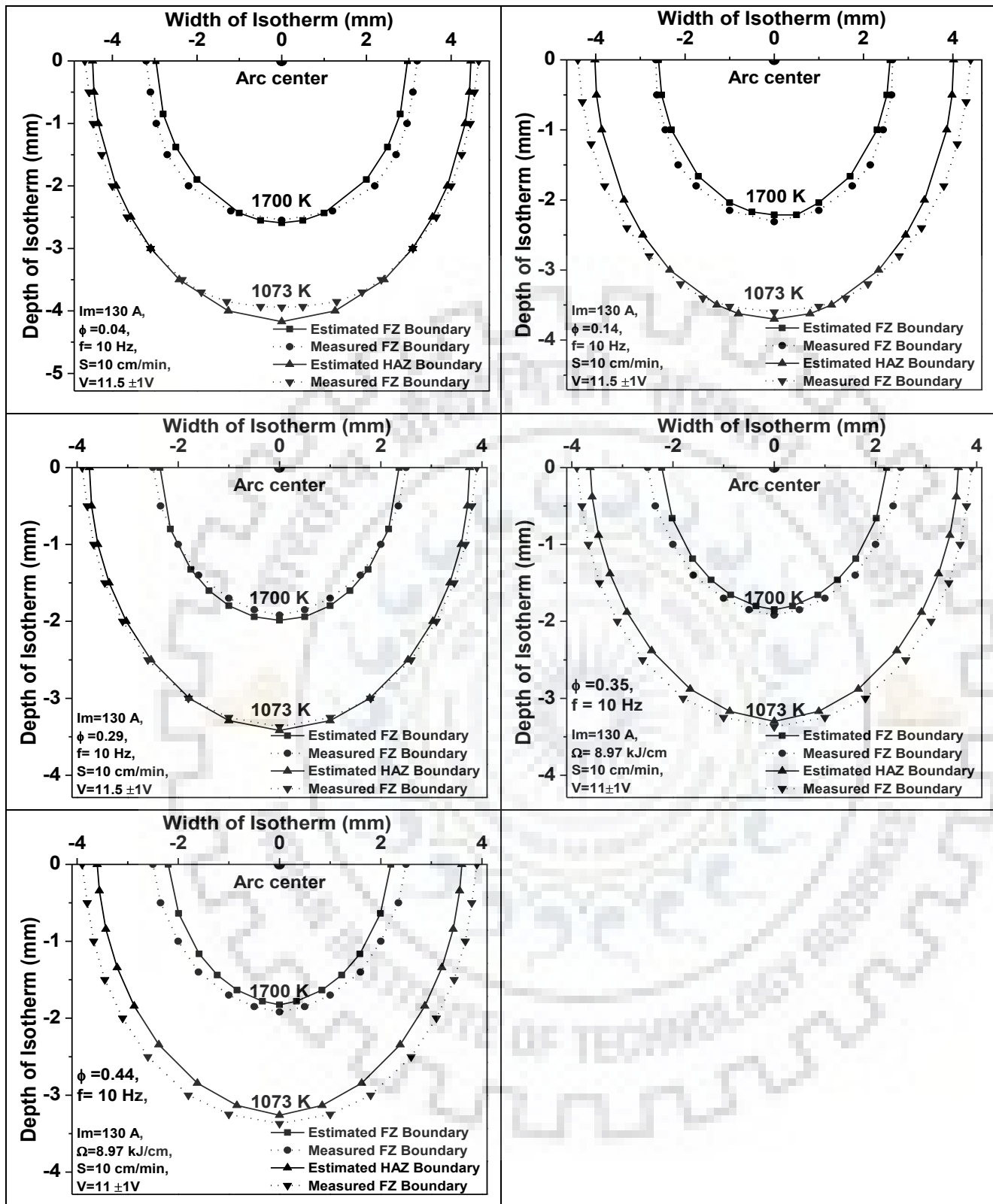
Fig. 6.28 Estimated isotherms in XY plane at given I_m of 170 A under varied ϕ from 0.04 to 0.44 and pulse frequency of (a) 2 Hz (b) 10 Hz.

The Figs. 6.31 and 6.32 also show a comparison between the predicted and measured geometry of the modified zone at I_m of 130 and 170 A respectively. The figure shows that the predicted geometry of modified zone is quite close to their experimental observations with accuracy of 3 ± 2 %. In the line of that observed in Figs. 6.31 and 6.32 here also the figure

shows that the predicted shape and size of the modified zone at the stated I_m and pulse parameter is largely in agreement with their corresponding measured shape and size of the fusion pool.

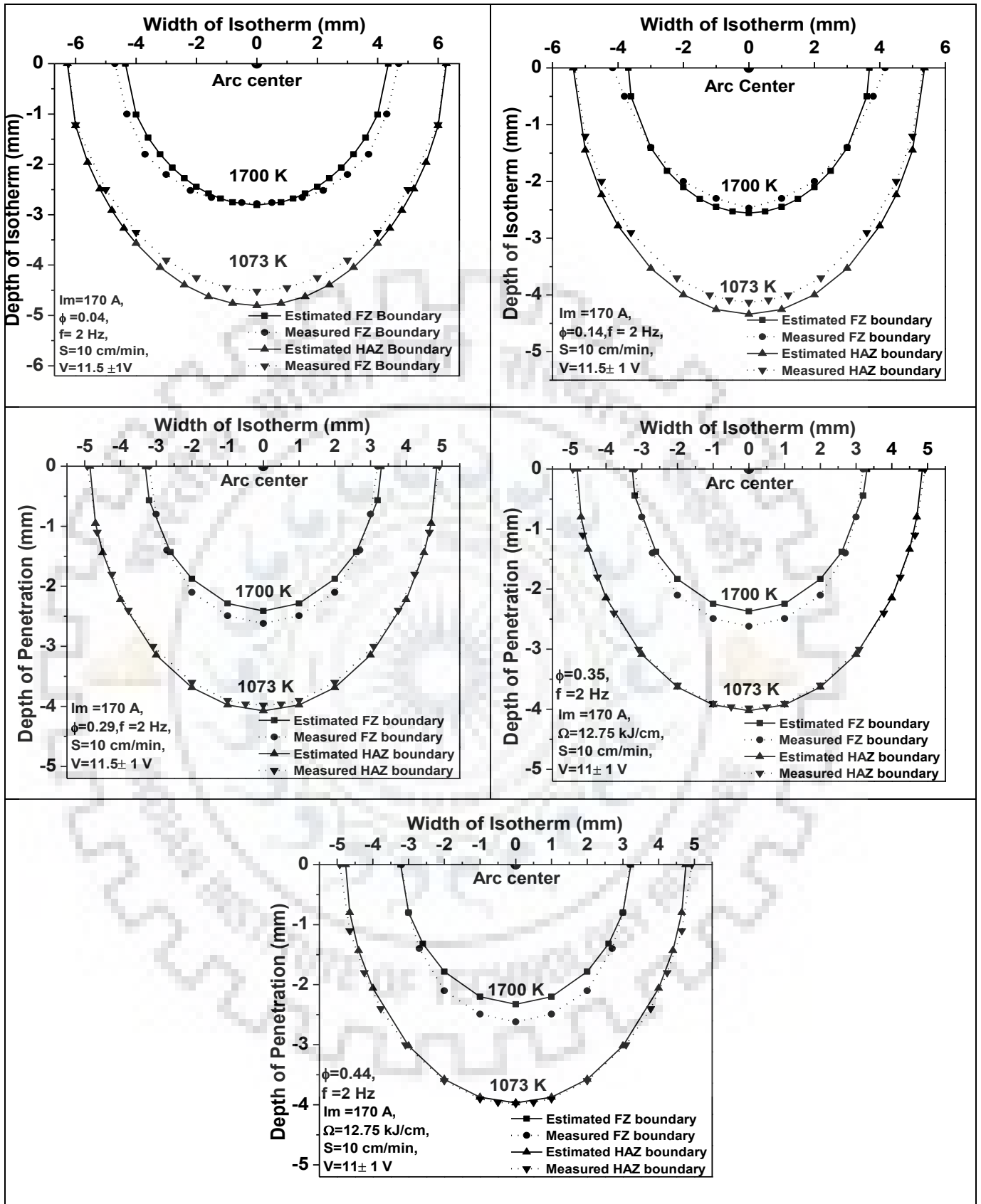


(a)

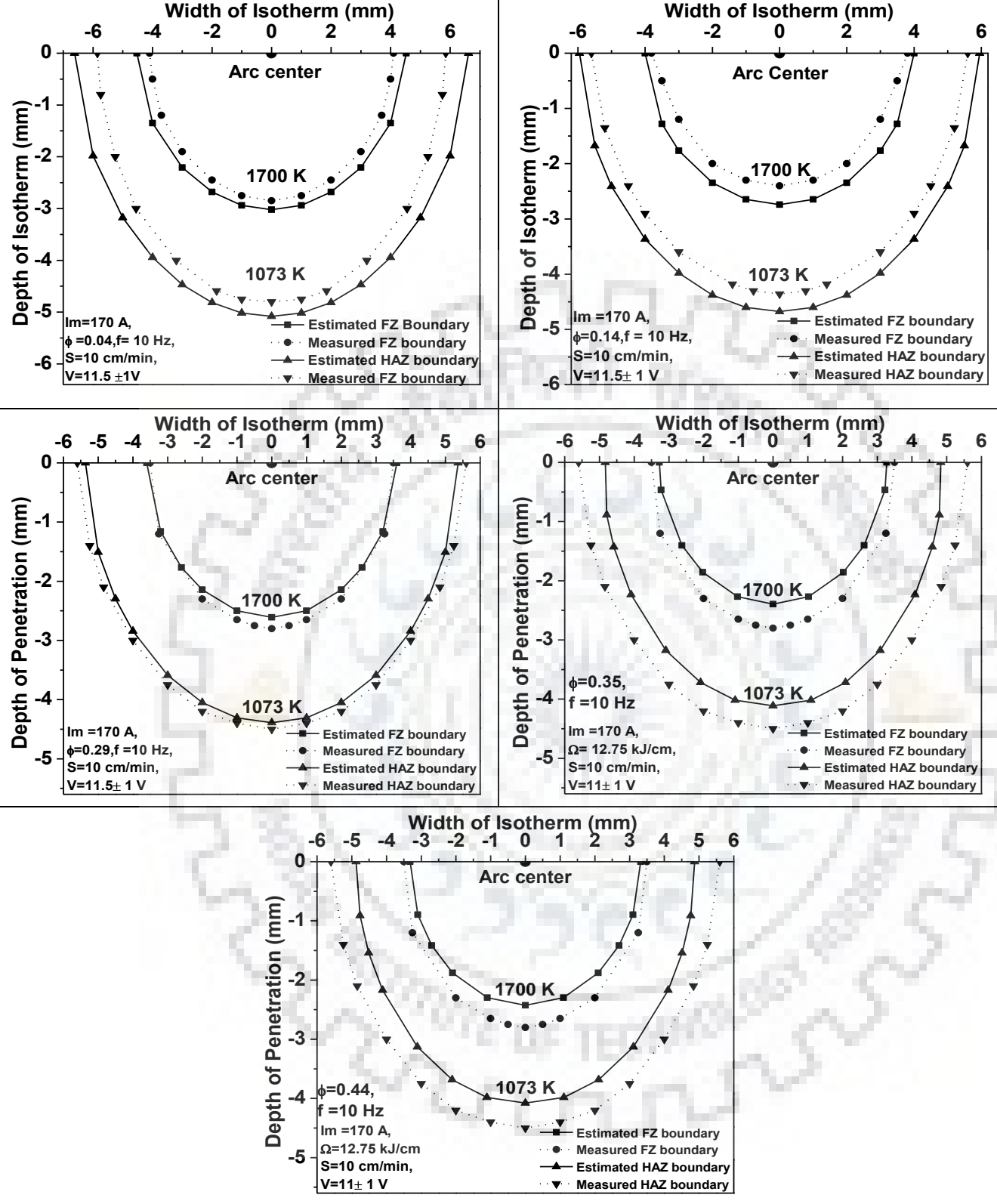


(b)

Fig. 6.29 Estimated and measured isotherms in YZ plane at given I_m of 130 A under varied ϕ from 0.04 to 0.44 and f of (a) 2 Hz (b) 10 Hz.



(a)

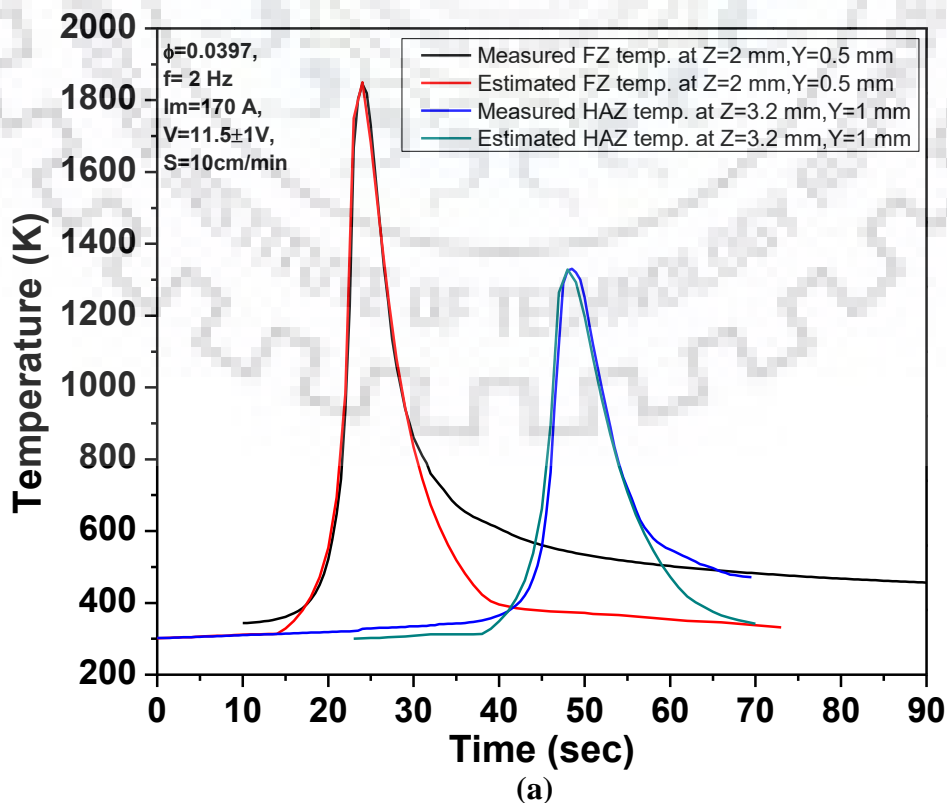


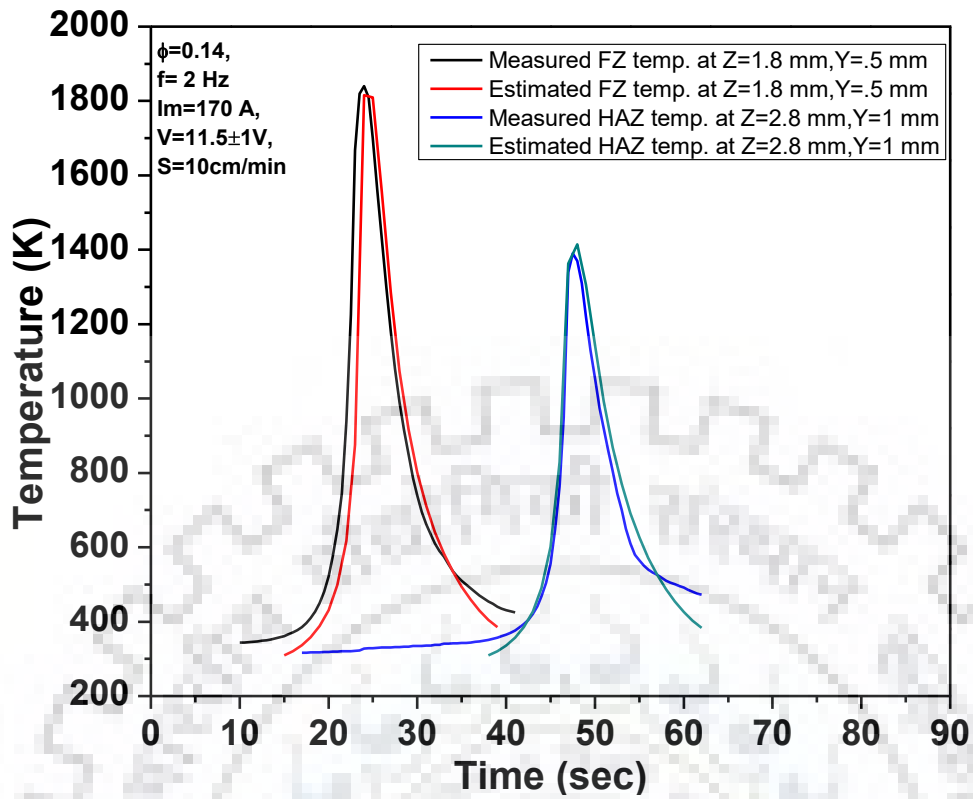
(b)

Fig. 6.30 Estimated and measured isotherms in YZ plane at given I_m of 170 A under varied ϕ from 0.04 to 0.44 and f of (a) 2 Hz (b) 10 Hz.

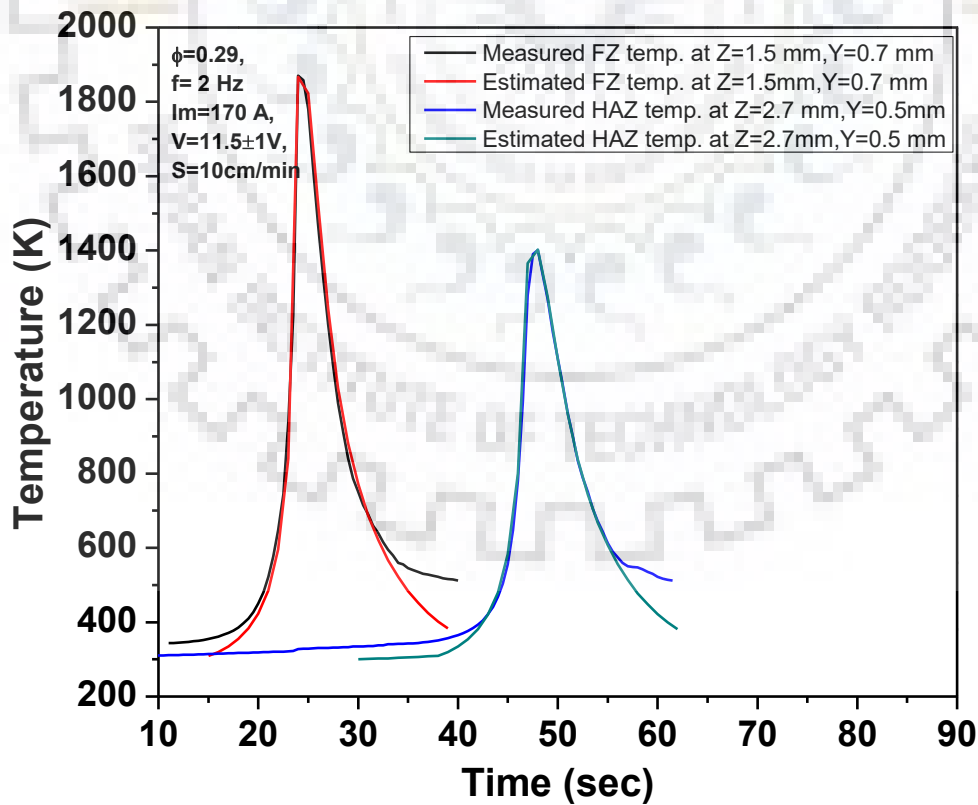
6.3.2.2 Thermal Cycle

At a given arc voltage, travel speed and pulse arc frequency of 11 ± 1 V, 10 cm/min and 2 Hz, the effect of ϕ , lying in the range of 0.04–0.44, on estimated and measured thermal cycle of the fused zone and matrix (HAZ) adjacent to FZ is shown in Fig. 6.33 (a-d). The measured thermal cycle represents the characteristics of a point at a depth of Z axis corresponding to close approximation of its estimated value. It is observed from the figure that the increase in ϕ increases the cooling rate (CR). At lower value of ϕ a lower area of the heat sink is available for heat transfer from the FZ to the surrounding matrix of base metal which may cause a lower CR at the intercritical temperature range (800–500 °C). But when the ϕ is increased from 0.04 to 0.44, a larger area of the available heat sink for heat transfer may cause a higher CR in the intercritical temperature range. This is attributed to increase in size of the fused pool at lower ϕ that enhances the temperature of the wider area of surrounding base metal and reduces its temperature gradient from the effective heat sink leading to lowering of CR. Fig. 6.34 shows the estimated and measured CR at the intercritical temperature range evaluated from the respective thermal cycle plots. The figure shows that CR increases with the increase in ϕ on variation in ϕ from 0.04 to 0.44. The figure also shows that the estimated magnitude of CR is similar to its measured value with an accuracy of average variation $3\pm 1\%$. The table 6.2 shows the comparison of the estimated and measured peak temperatures at the FZ and HAZ during P-TIGA process.

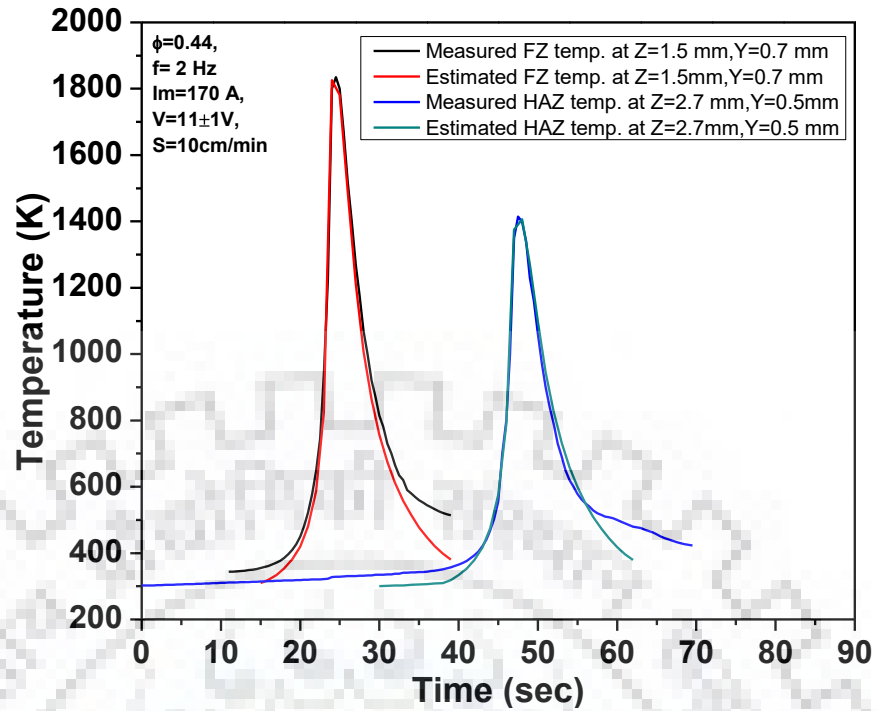




(b)



(c)



(d)

Fig. 6.31 Comparison of the estimated and measured weld thermal cycle at different ϕ value of (a) 0.0397 (b) 0.14 (c) 0.29 and (d) 0.44 at a given mean current, arc voltage and travel speed of 170 A, 11±1 V and 10 cm/min respectively.

Table 6.2: Comparison of the estimated and measured peak temperature of FZ and HAZ at different operating parameters in P-TIGA process.

Operating parameters		Fusion Zone Temperature (T_p)		HAZ Temperature (T_p)	
ϕ	I_m (A)	Estimated (K)	Measured (K)	Estimated (K)	Measured (K)
0.04	170	1850	1845	1328	1330
0.14		1840	1816	1415	1390
0.29		1860	1845	1412	1400
0.44		1826	1835	1406	1415

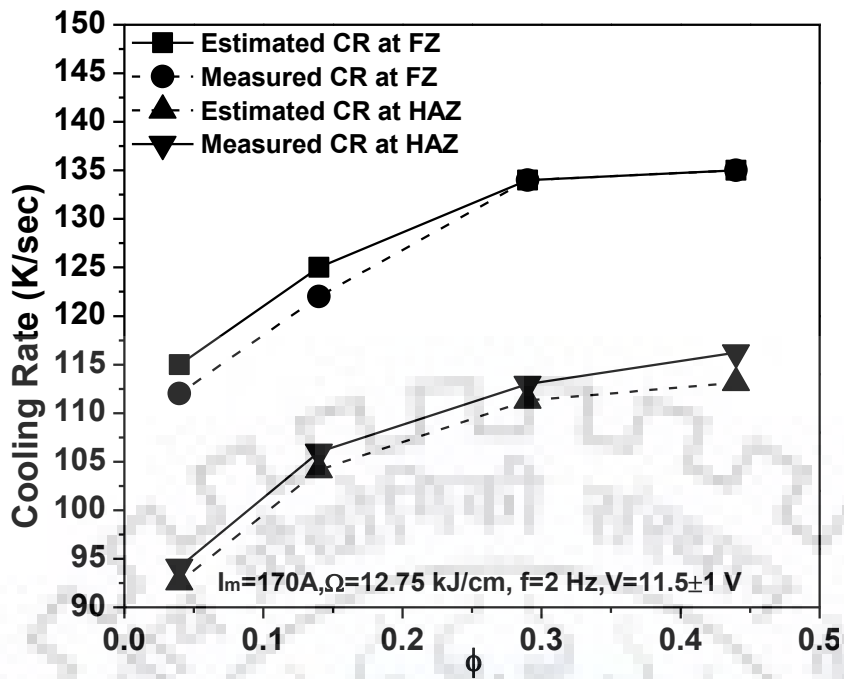


Fig. 6.32 Comparison of estimated and measured cooling rate at intercritical temperature range (800-5000 °C).

At varying I_m of 130 and 170 A, the typical estimated CR in the intercritical temperature range at f of 2 and 10 Hz and ϕ lying in the range of 0.04-0.44 respectively have been shown in Figs. 6.35 (a and b) respectively. The CR is estimated for both the region (FZ and HAZ) respectively. It is observed from figure that the increase of ϕ increases the CR at the given I_m and f . The increase of f reduces the CR at the given ϕ and Ω in both the regions of FZ and HAZ which may have happened due to additional heat build-up in the matrix. The variation of isotherm and CR from the peak temperature dictates the final microstructure of fused zone and HAZ.

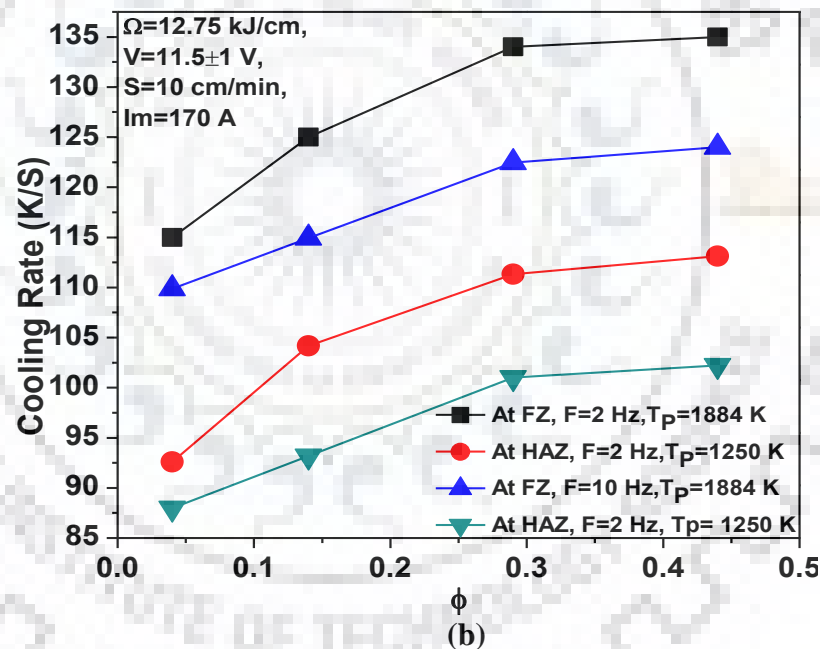
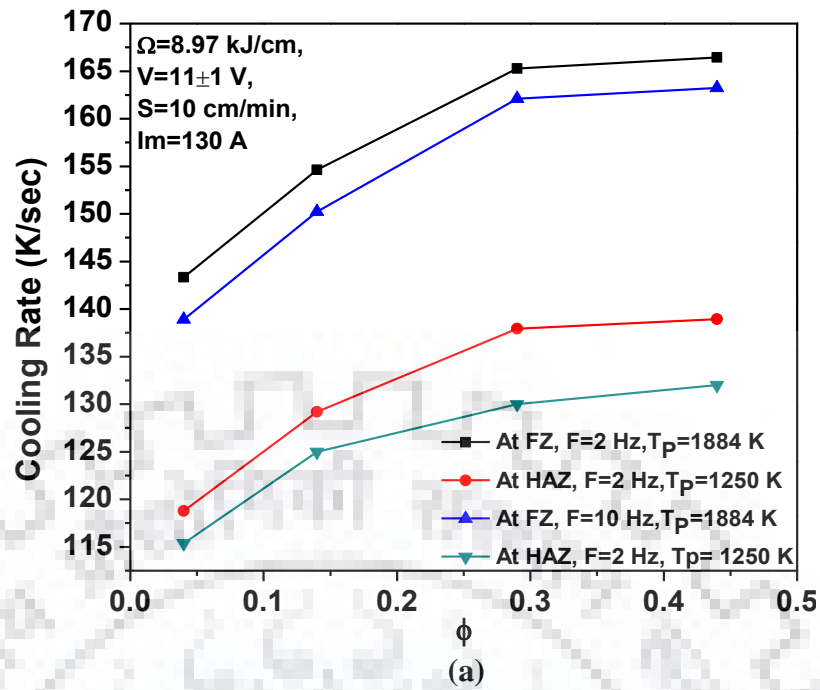


Fig. 6.33 Effect of ϕ on cooling rate in the intercritical temperature range with variation of ϕ from 0.04 to 0.44 and f of 2 and 10 Hz at different I_m of (a) 130 A and (b) 170 A.

6.3.3 Summary

The effect of arcing parameters of both the processes (single pass C-TIGA and P-TIGA process) on isotherms and thermal cycle is predicted and analyzed. Analytical estimation of thermal characteristics of surface modification by TIGA processing can provide effective control of desired properties of surface modified substrate. Analytical approximation of the

depth of the fused modified zone and intercritical cooling rate lies well within 3–5% variation from the measured value.

6.4 Microstructural Studies

Microstructure strongly influences the mechanical and chemical properties of metallic materials at low and elevated temperature, which governs the applications in industrial practices. In this regard the type, morphology and proportion of the phases present in the matrix play the primary role, which is basically controlled by the thermal cycle of fused zone and its reheating and cooling from the peak temperature primarily controls the desired phase transformation at any location of the matrix.

The phase transformation in AISI 8620 steel dictated by the isotherms and thermal cycle primarily depends upon the arcing parameters in both of the single pass C-TIGA and P-TIG arcing processes. Thus, it is very much necessary to study the effect of these parameters on phase transformation in this steel in order to critically understand, predict and ultimately control the final microstructure of AISI 8620 steel for desired properties of the modified surface.

6.4.1 Microstructural studies for single pass C-TIGA process

The microstructure of the C-TIGA processed AISI 8620 steel is primarily studied as a function of heat input (Ω), arc current (I) and arc travel speed (S). The detailed discussions of the microstructure of the modified zone with respect to the arc parameters have been given below.

6.4.1.1 Effect of arcing parameters on microstructure of fusion zone

At a given V and S of $11\pm 1V$ and 10 cm/min respectively the microstructures of the fusion zone observed in case of single pass C-TIGA process operated at arc current of 100 and 170 have been typically shown in Figs. 6.36 (a and b) respectively. The FZ microstructures at different arc current reveal the cast dendritic morphology. The further observations on the figures reveal the coarsening of dendritic growth with the increase of arc current due to enhancement of Ω . Similarly, at a given V and S of $11\pm 1V$ and 10 cm/min respectively the microstructures of the single pass fusion zone processed at varying arc current of C-TIGA from 70 to 170 A as revealed at relatively higher magnification have been shown in Fig. 6.37 (i to v) respectively. It is observed from the figures that at the low arc current of 70 and 100 A the microstructures of FZ primarily consist of fully lath martensite. However, with the increase of arc current from 130, 170 and 200A the microstructure of the FZ is also found to have the lath martensite along with certain amount of bainite and pro eutectoid ferrite. This is in agreement

to the increase of cooling rate with the decrease of arc current (section 6.3.1) promoting the transformation of martensite whereas, a slower cooling rate at higher arc current indulges the formation of lath martensite along with bainite. In this regard the CCT curve (Fig. 6.5) and AISI 8620 steel, showing the effect of cooling rate (Fig. 6.6) on phase transformation of steel, confirms the formation of bainite phase at lower cooling rate and fully lath martensite at higher cooling rate in the matrix. The X-ray diffraction profile of the fusion zone of TIGA processed substrate at varying arc current from 70 to 200 A is shown in Fig. 6.38. The figure confirms the presence of characteristic peaks of martensitic phase present in the fused matrix, which is in agreement to the similar identification of martensite in low alloy steel as described by Tewary et al., (2014).

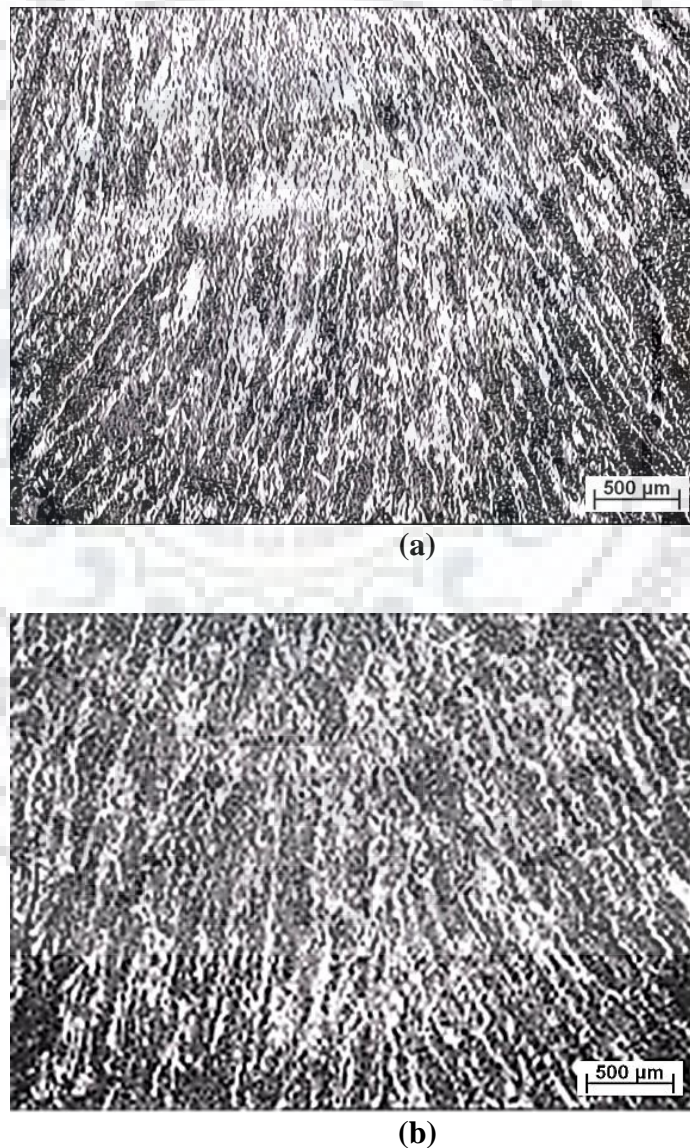


Fig. 6.34 Typical microstructure of FZ at FZ at different I of (a) 100 and (b) 170 A where the V and S are kept constant at 11 ± 1 V and 10 cm/min respectively.

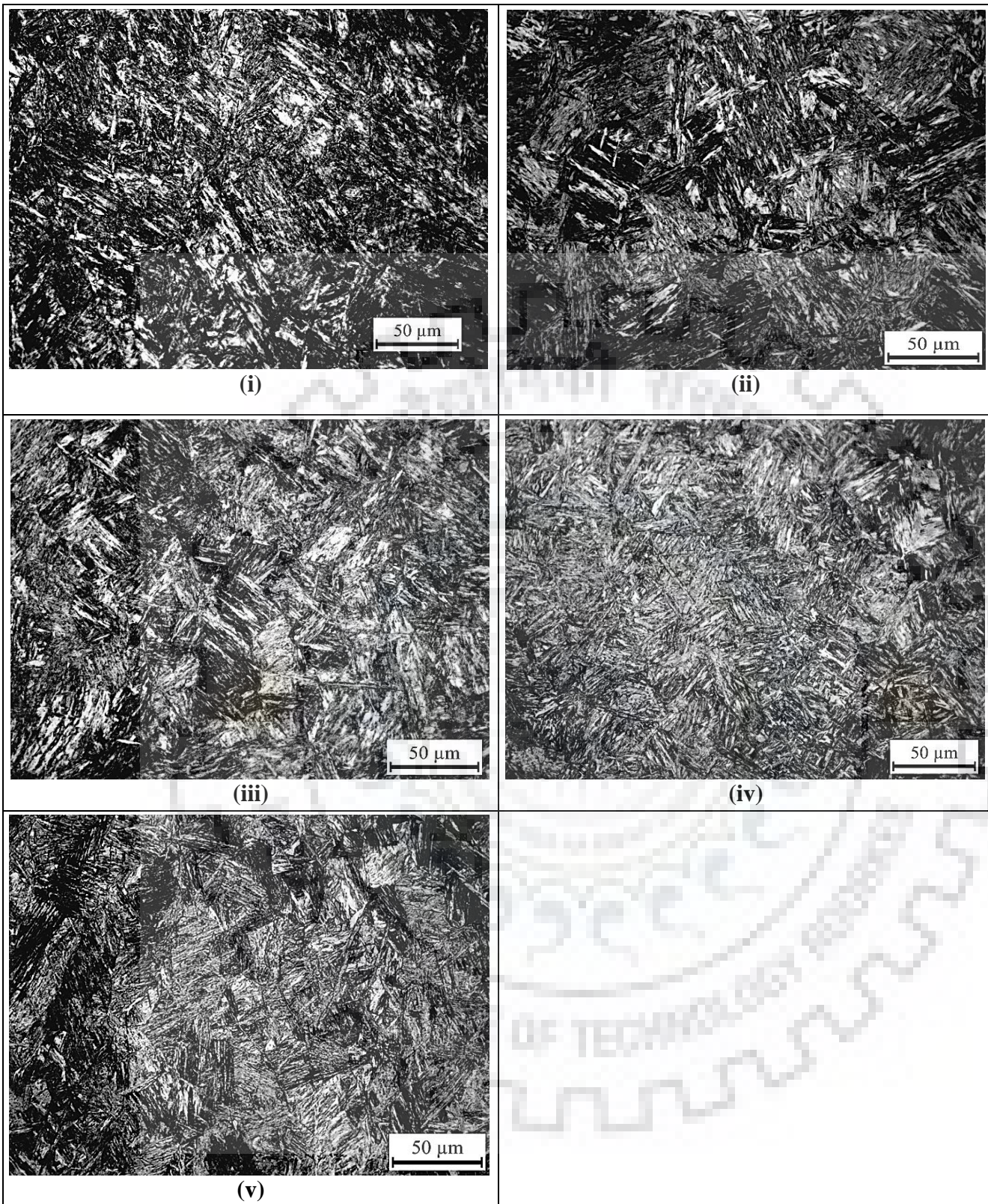


Fig. 6.35 Typical microstructure of fusion zone in single pass C-TIG arcing process under different arc current of (i) 70 (ii) 100 (iii) 130A (iv) 170 and (v) 200 A where the V and S are kept constant at 11 ± 1 and 10 cm/min respectively.

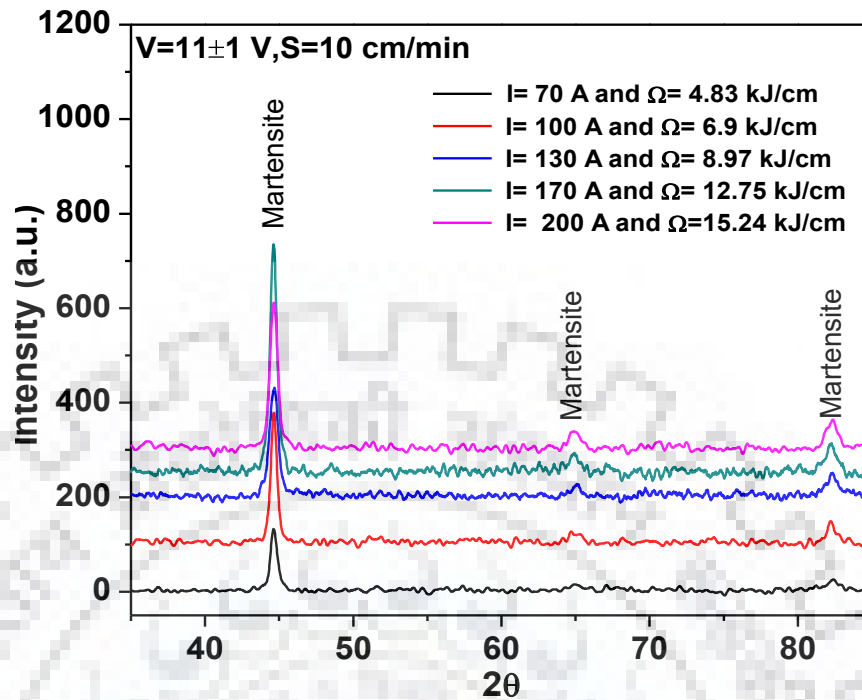


Fig. 6.36 XRD analysis of the modified surface at S and V of 10 cm/min and 11±1 V.

6.4.1.2 Effect of arcing parameters on microstructure of HAZ

At a given V and S the microstructure of the HAZ in case of using single pass C-TIGA process at varied arc current in five steps from 70 to 200 A, as revealed at a comparatively higher magnification, has been typically shown in Figs. 6.39 (i-v) respectively. The microstructure of HAZ of base metal adjacent to fusion line has been found thoroughly modified at the peak temperature raised to the range of 1000–1200 K (Fig. 6.27) and transformed to relatively finer grain with respect to that of the base metal (Fig. 6.1). The matrix is having transformation to martensite combined with bainite and allotriomorphic ferrite at its high CR (Fig. 6.28). At the comparatively higher cooling rate of low arc current of 70 A and 100 A the HAZ consists of a relatively higher proportion of martensite, that is compensated by formation of more bainite at the higher I of 130, 170 and 200 A due to reduction of CR. It is also noted that at the higher arc current the transformation of HAZ is having more proeutectoid ferrite than that observed in case of the lower arc current.

At a given V and S, the increase of arc current increases the Ω which reduces the cooling rate of modified zone because of comparatively lower temperature gradient between different locations within the fused pool [Robert W. Messler 1999], but increases fluid flow velocity and thus enhances the dendrite growth significantly. This has primarily happened due to increase of the fusion pool area as well as weld pool temperature with the increase of Ω .

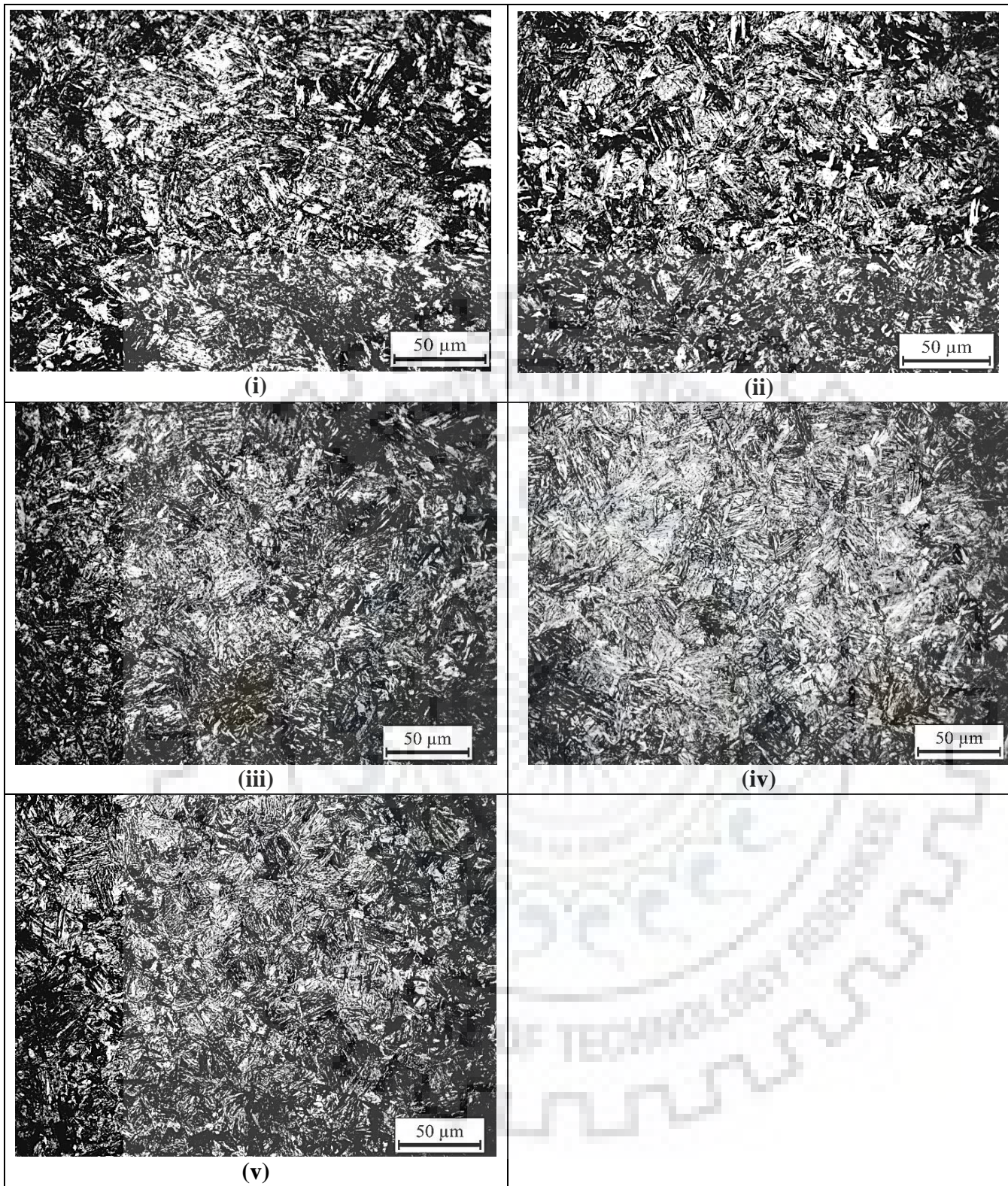


Fig. 6.37 Typical microstructure at HAZ using single pass C-TIG arcing process under different arc current of (i) 70 A (ii) 100 (iii) 130A (iv)170A and (v) 200 A where the V and S are kept constant at 11 ± 1 and 10 cm/min respectively.

6.4.2 Microstructural studies for single pass P-TIGA process

This subsection presents the effect of single pass P-TIGA process on the microstructure of the AISI 8620 steel controlled by operating pulse parameters. The detailed discussions of the microstructure of the FZ and HAZ with respect to pulse parameters have been given below.

6.4.2.1 Effect of pulse arcing parameters on microstructure of fusion zone

At a given arc voltage and travel speed of 11 ± 1 V and 10 cm/min, the typical variation in the microstructure of the fusion zone at relatively lower magnification with respect to ϕ of 0.04, 0.21 and 0.44 at f of 2 and 10 Hz have been shown in Fig. 6.40 respectively, where the I_m is kept constant at 170 A. The fusion zone has been found to have cast dendritic morphology. It has been observed from the figure that with the increase of ϕ at a given f , the microstructure of fusion zones becomes relatively finer. This is largely attributed to decreases of fusion zone size and size of isotherm with the increase of ϕ (Figs. 6.20 and 6.29 - 6.32) resulting in enhancement of cooling rate. Similarly, at a given ϕ the increase in f from 2 to 10 Hz the microstructure becomes relatively coarser due to increase in molten fusion pool size and size of isotherm with the increases of f (Figs. 6.20 and 6.29 - 6.32) resulting in reduction of cooling rate. The effect of frequency and ϕ has been given in detail in subsection 6.3.2

Similarly, at a given arc voltage and travel speed of 11 ± 1 V and 10 cm/min, the typical phases present in the microstructure of the fusion zone at relatively higher magnification with respect to varied ϕ from 0.04 to 0.44 at f of 2 and 10 Hz have been shown in Figs. 6.41 to 6.44 respectively where the I_m is kept at 130 and 170 A. It is observed from the figures that the microstructure of FZ primarily consist of lath martensite with proportionate amount of bainite and proeutectoid ferrite. The proportion of bainite and proeutectoid ferrite reduces with the increase of ϕ at the same I_m and f . This is largely attributed to decreases of fusion pool temperature and size of isotherm with the increase of ϕ resulting in enhancement of cooling rate due to increase of conduction and convection heat losses from the fusion pool due to comparatively higher temperature gradient as these types of heat transfer are function of temperature gradient. The further observations from the figures depicted that at a given ϕ and I_m the increase in f reduces the proportionate of lath martensite and increases the amount of bainite and ferrite.

The X-ray diffraction profile of the fusion zone of TIGA processed substrate at varying f of 2 Hz and 10 Hz and ϕ of 0.04 and 0.44 is shown in Figs. 6.45 (a & b) while the I_m is kept at 130 and 170 respectively. The figure confirms the presence of characteristic peaks of martensitic phase in the fused matrix.

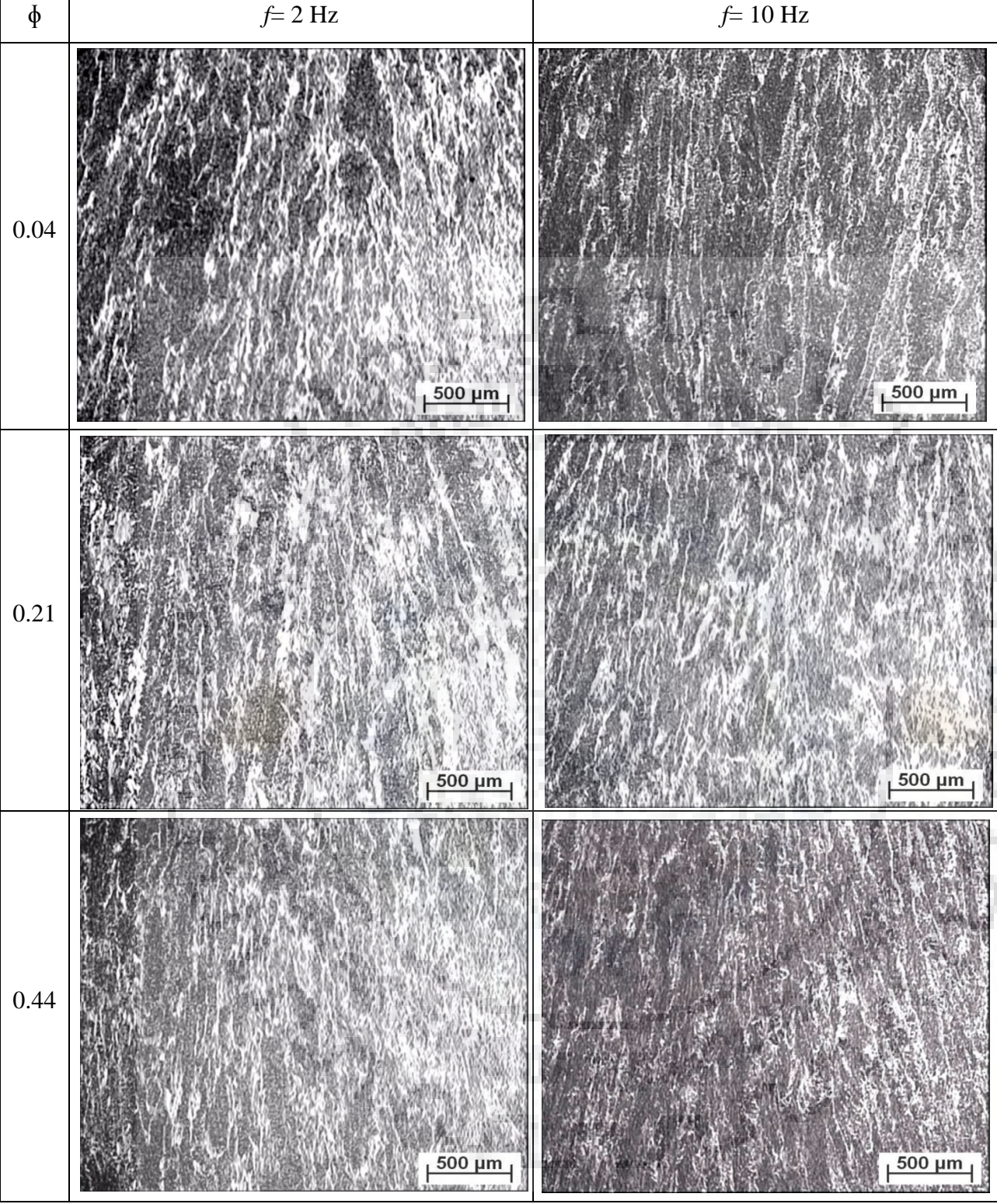


Fig. 6.38 Typical microstructure of FZ showing the effect of ϕ and f at a given I_m of 170A.

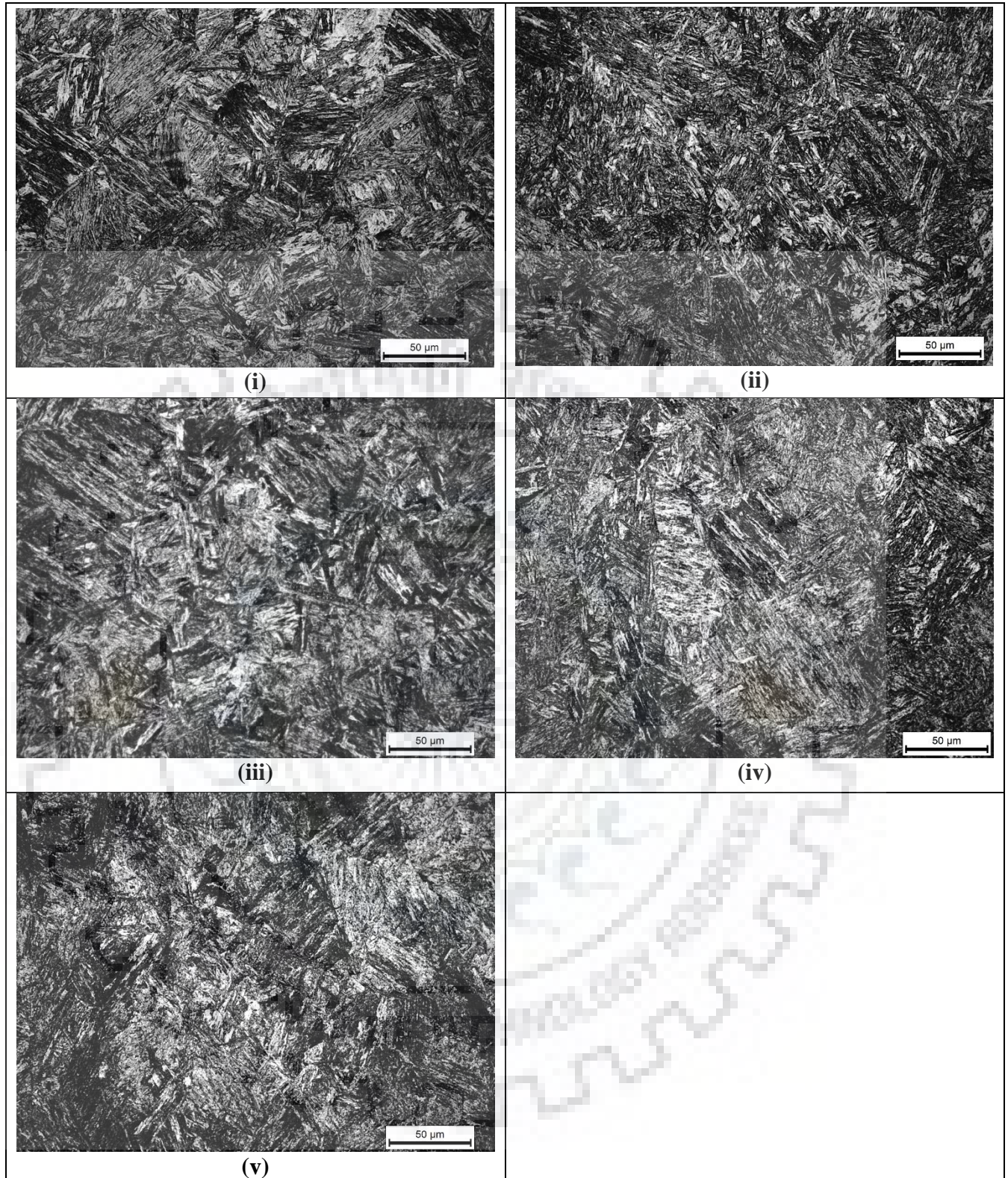


Fig. 6.39 Typical microstructure of fusion zone by single pass P-TIG arcing process under varied ϕ from (i) 0.04 to (v) 0.44 0.44 at an I_m and f of 130 A and 2 Hz respectively.

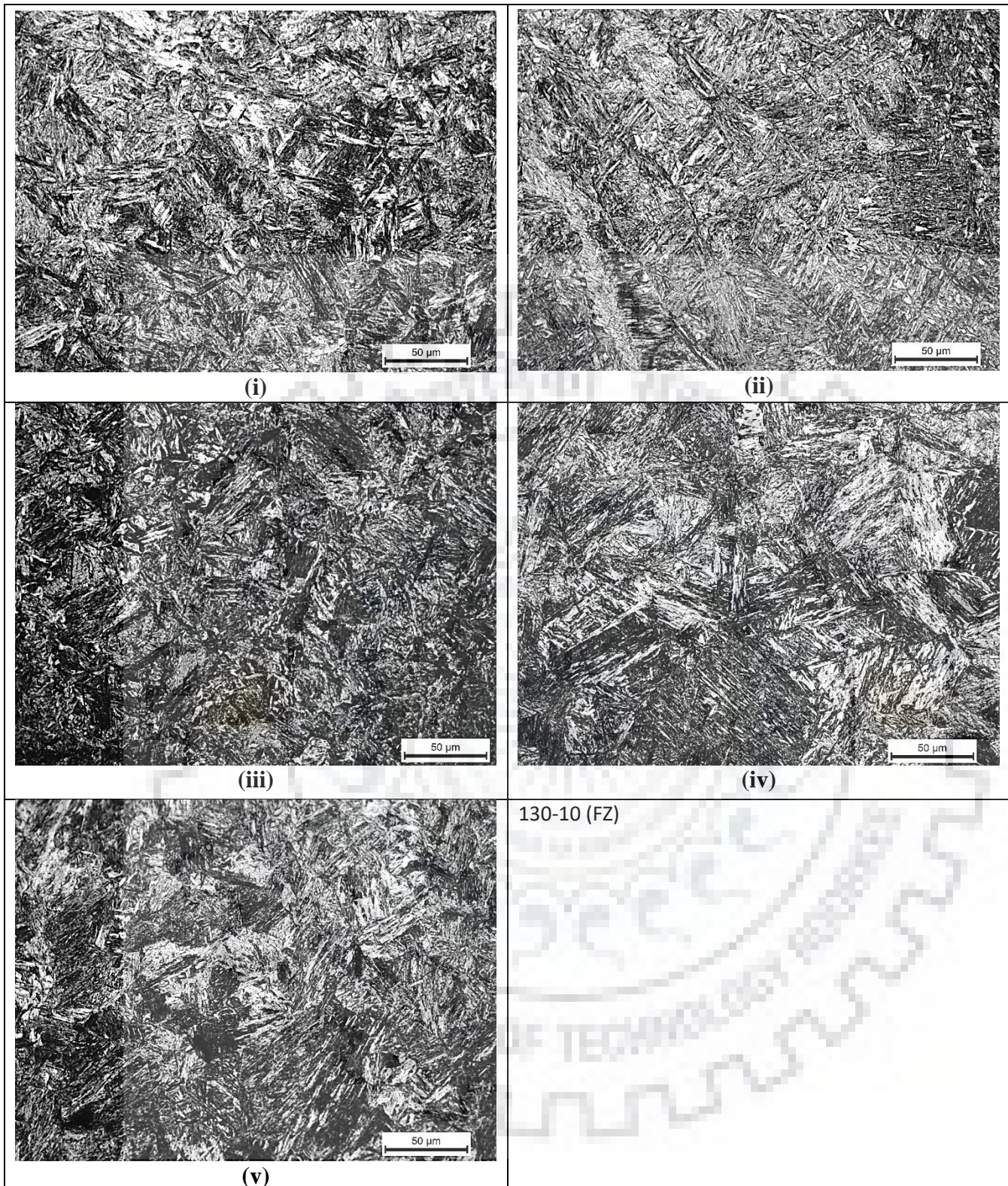


Fig. 6.40 Typical microstructure of fusion zone by single pass P-TIG arcing process under different ϕ value of (i) 0.04 (ii) 0.14 (iii) 0.29 (iv) 0.35 and (v) 0.44 at an I_m and f of 130 A and 10 Hz respectively.

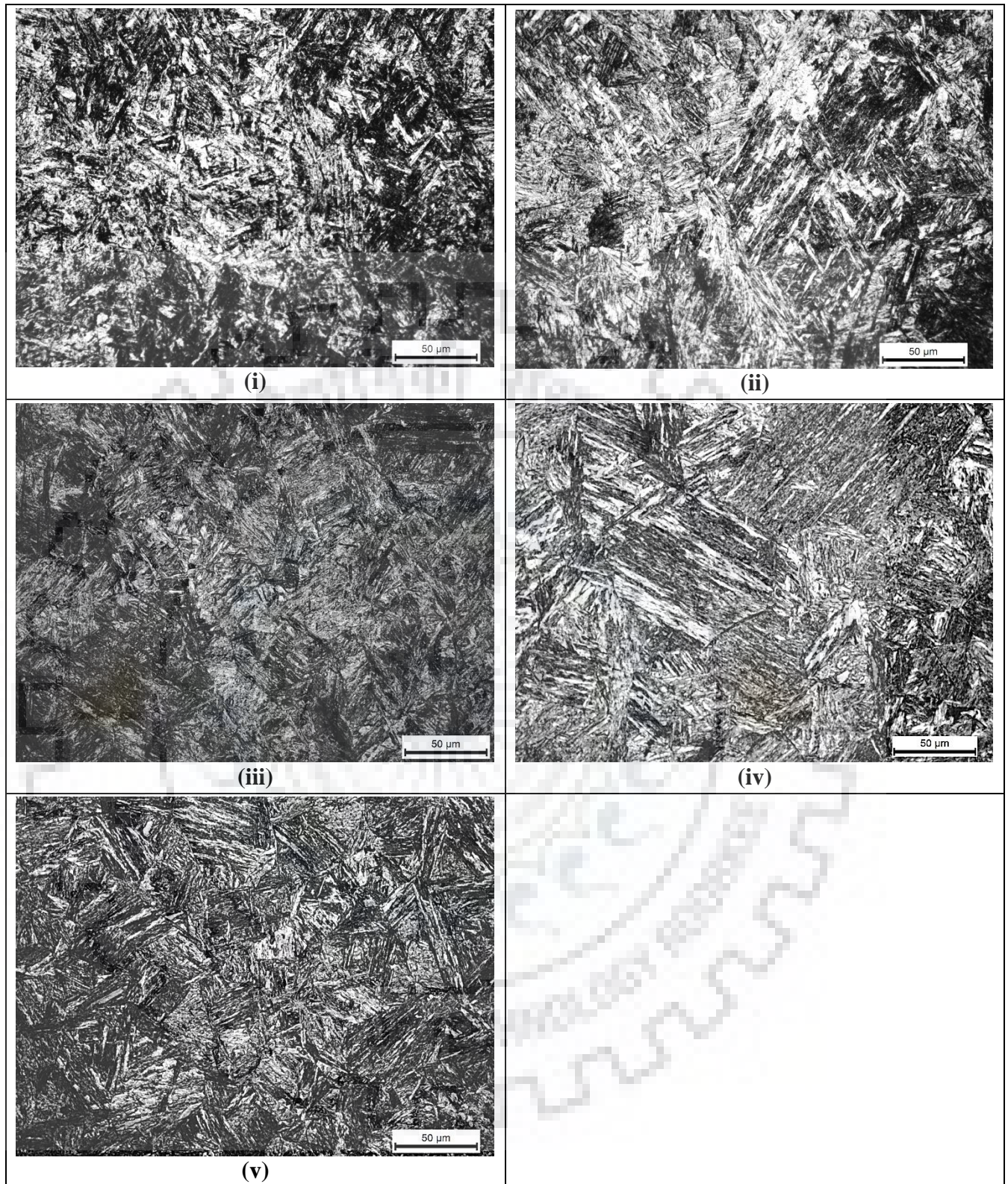


Fig. 6.41 Typical microstructure of fusion zone by single pass P-TIG arcing process under different ϕ value of (i) 0.04 (ii) 0.14 (iii) 0.29 (iv) 0.35 and (v) 0.44 at an I_m and f of 170 A and 2 Hz respectively.

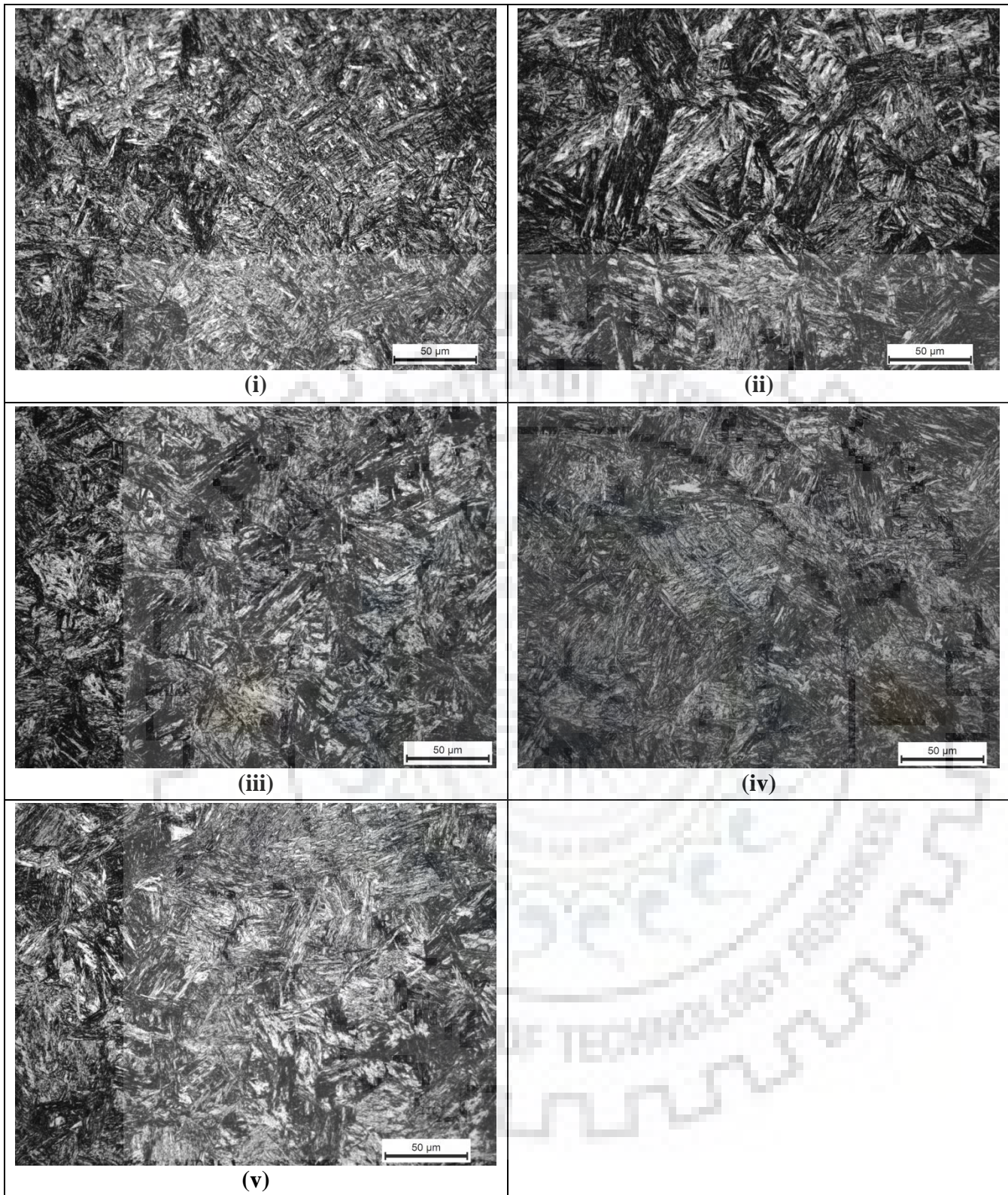


Fig. 6.42 Typical microstructure of fusion zone by single pass P-TIG arcing process under different ϕ value of (i) 0.04 (ii) 0.14 (iii) 0.29 (iv) 0.35 and (v) 0.44 at a I_m and f of 170 A and 10 Hz respectively.

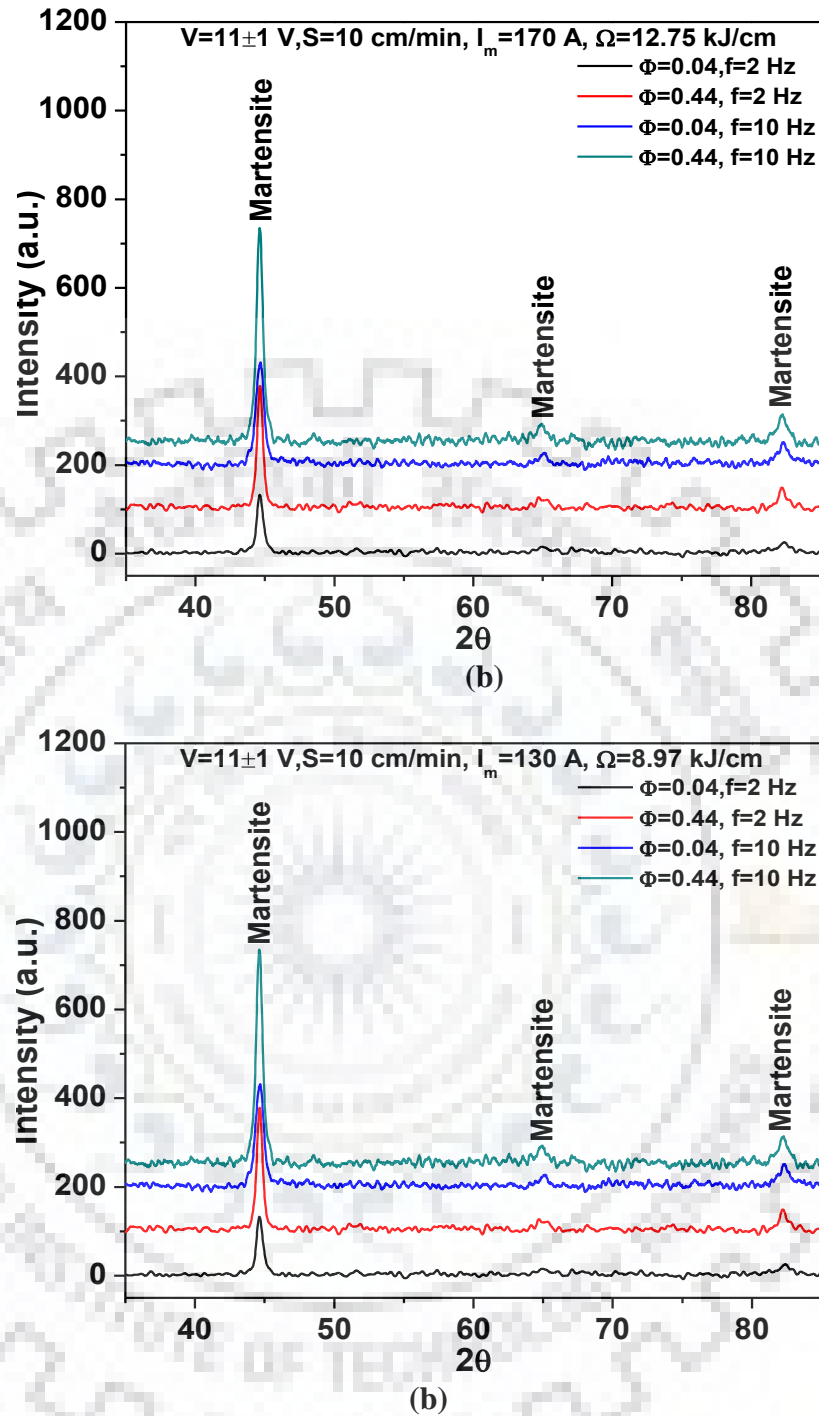


Fig. 6.43 XRD analysis of P-TIGA treated surface at I_m of (a) 130 (b) 170 A.

6.4.2.2 Effect of pulse arcing parameters on microstructure of HAZ

At a given arc voltage and travel speed of 11 ± 1 V and 10 cm/min respectively, the typical variation in microstructure of HAZ with variation in ϕ from 0.04 to 0.44 at two levels of frequency as 2 and 10 Hz have been shown in Figs. 6.46 to 6.49 respectively, where the I_m is 130 and 170 A. It has been observed that with the increase of ϕ at a given I_m and Ω , the microstructure of HAZ becomes relatively finer that consists of uniformly distributed refined

lath martensitic with some proportion of bainite and proeutectoid ferrite. The proportion of bainite and proeutectoid ferrite reduces with the increase of ϕ at the same I_m and f .

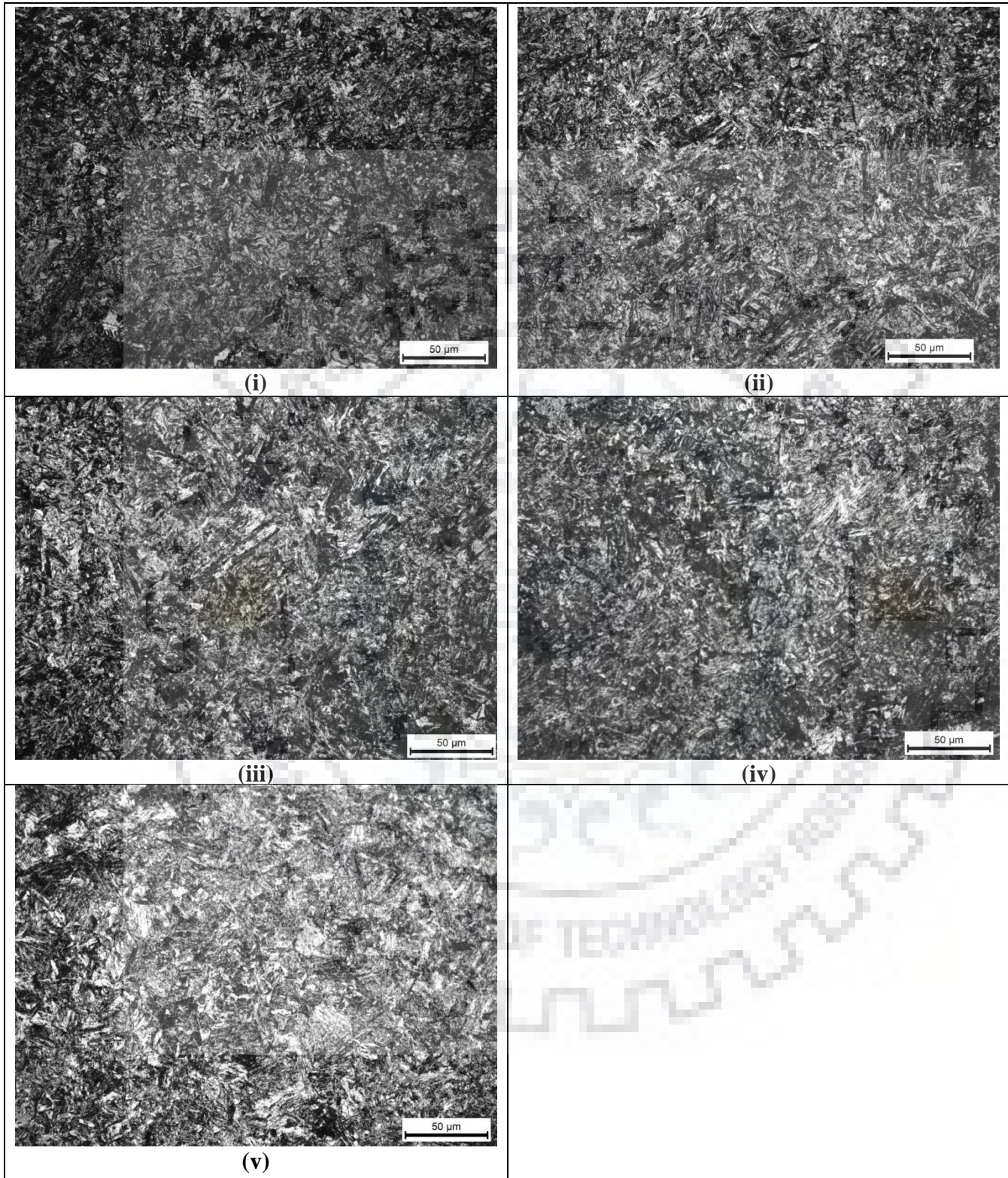


Fig. 6.44 Typical microstructure of HAZ by single pass P-TIG arcing process under different ϕ value of (i) 0.04 (ii) 0.14 (iii) 0.29 (iv) 0.35 and (v) 0.44 at an I_m and f of 130 A and 2 Hz respectively.

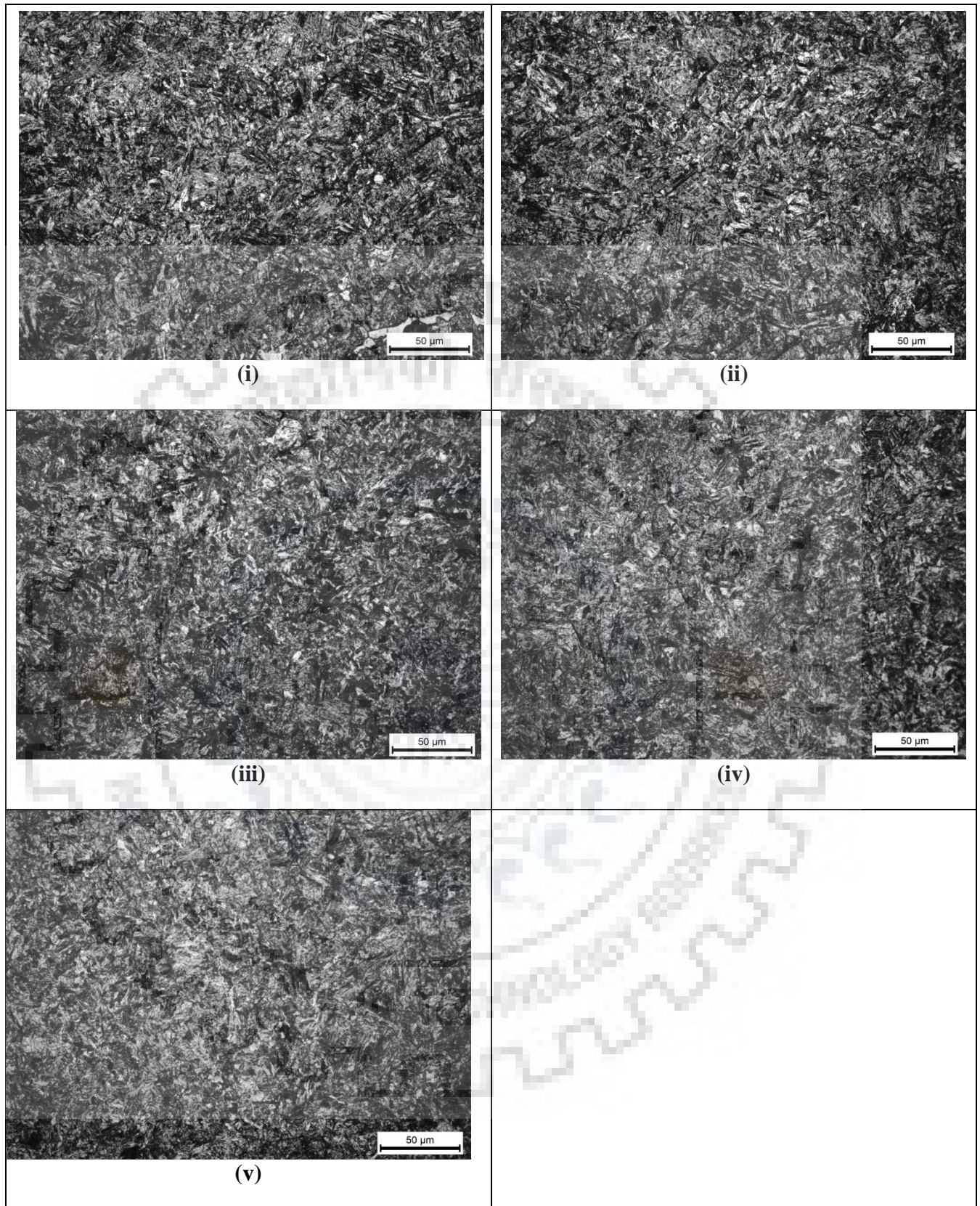


Fig. 6.45 Typical microstructure of HAZ by single pass P-TIG arcing process under different ϕ value of (i) 0.04 (ii) 0.14 (iii) 0.29 (iv) 0.35 and (v) 0.44 at I_m and f of 130 A and 10 Hz.

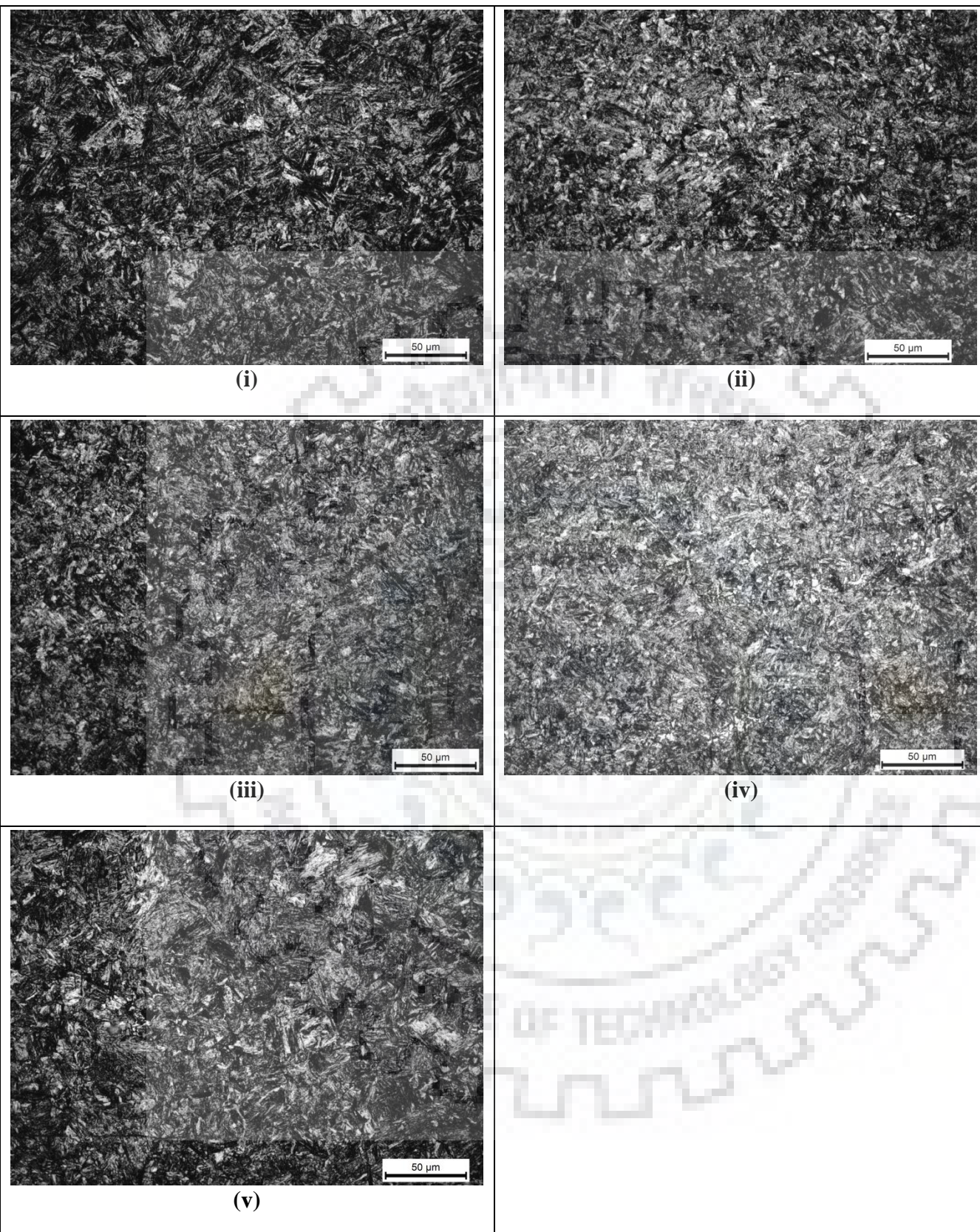


Fig. 6.46 Typical microstructure of HAZ by single pass P-TIG arcing process under different ϕ value of (i) 0.04 (ii) 0.14 (iii) 0.29 (iv) 0.35 and (v) 0.44 at a I_m and f of 170 A and 2 Hz.

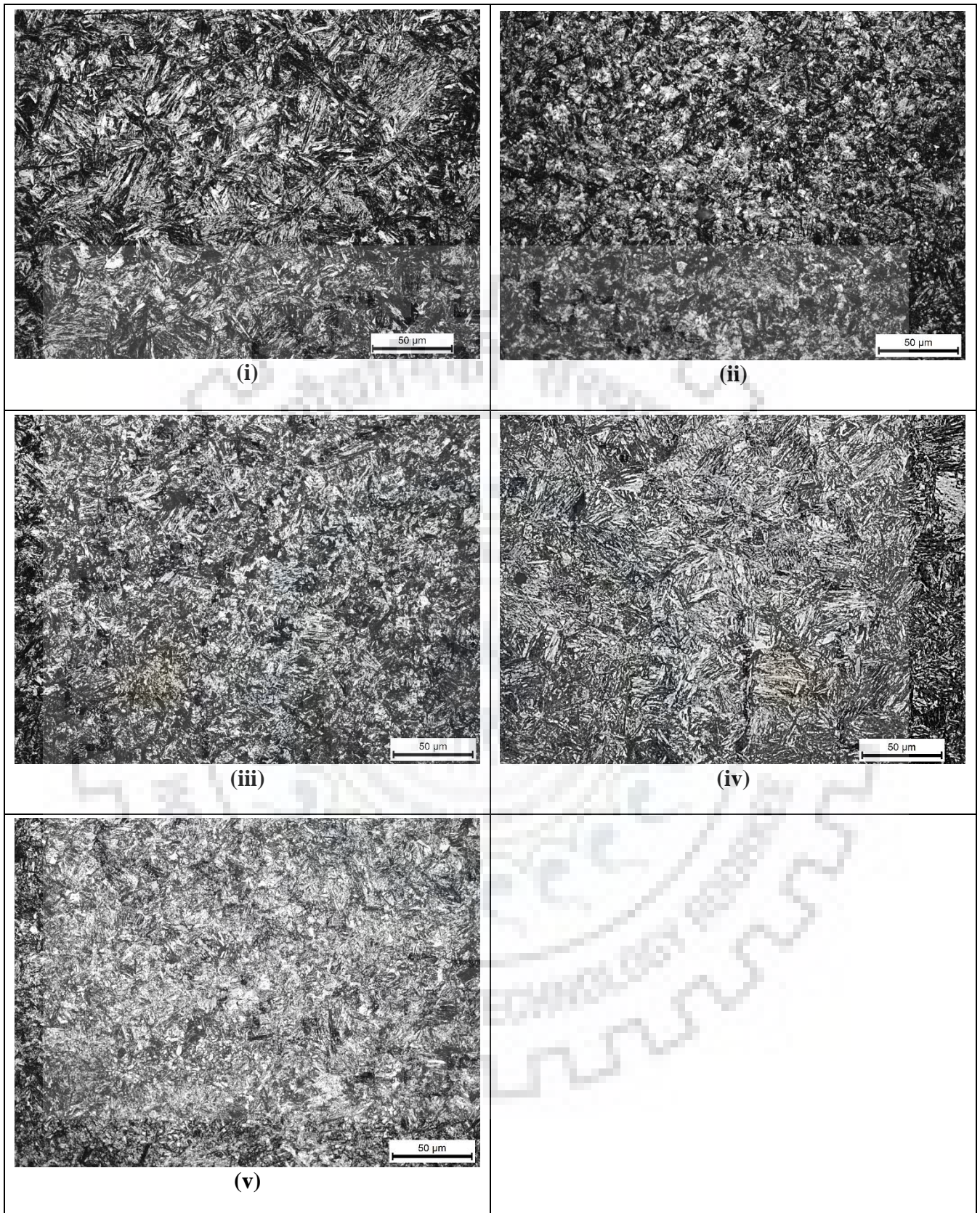


Fig. 6.47 Typical microstructure of HAZ by single pass P-TIG arcing process under different ϕ value of (i) 0.04 (ii) 0.14 (iii) 0.29 (iv) 0.35 and (v) 0.44 at I_m and f of 170 A and 10 Hz.

It is clear that with increasing ϕ at a given I_m and f , the cooling rate (Figs. 6.34 and 6.35) increases which promotes the lath martensite phase and at the same time the volume fraction of bainitic and ferrite reduces. The CCT curve (Fig. 6.4) confirms the formation of fully martensitic structure in the obtained range of cooling rate. The further observations from the figures depict that at a given ϕ and I_m the increase in f reduces the fraction of refined lath martensite and increases the amount of bainite ferrite and proeutectoid ferrite. It may have primarily happened due to additional heat buildup which retards the cooling rate and promotes the lower proportion of refined lath martensite.

6.4.3 Summary

Microstructures of the FZ and HAZ can be varied significantly with respect to Ω under the operating parameters in single pass C-TIGA process. The microstructure of FZ and HAZ is primarily dictated by the isotherm, heating and cooling rate. The metallurgical characteristics of the modified fused and heat affected zones of the base metal are governed by the proportionate transformation of martensite, bainite and pro eutectoid ferrite. In case of P-TIGA process the microstructure of the AISI 8620 surface is effectively controlled by the ϕ and f of the process parameters. The metallurgical characteristics of the modified FZ and HAZ of the base metal are regulated by the proportionate transformation of refined lath martensite with bainite ferrite and proeutectoid ferrite. As compared to single pass C-TIGA process, the P-TIGA process gives more refined microstructure at lower Ω and I_m .

6.5 Hardness Study

The hardness and its distribution in the matrix play an important role to increase the wear resistance and toughness of a case hardenable low alloy steel. The hardness of the case hardenable AISI 8620 steel is primarily governed by the isotherms and thermal cycle (heating and cooling rate) of the TIGA process. The present study involves understanding the effect of TIGA parameters of both single pass C-TIGA and P-TIGA processes on the hardness and its distribution in this steel. The hardness of base material (AISI 8620 steel) used in this study has been found as 220 ± 10 VHN.

6.5.1 Effect of single pass C-TIGA process on Hardness of FZ and HAZ

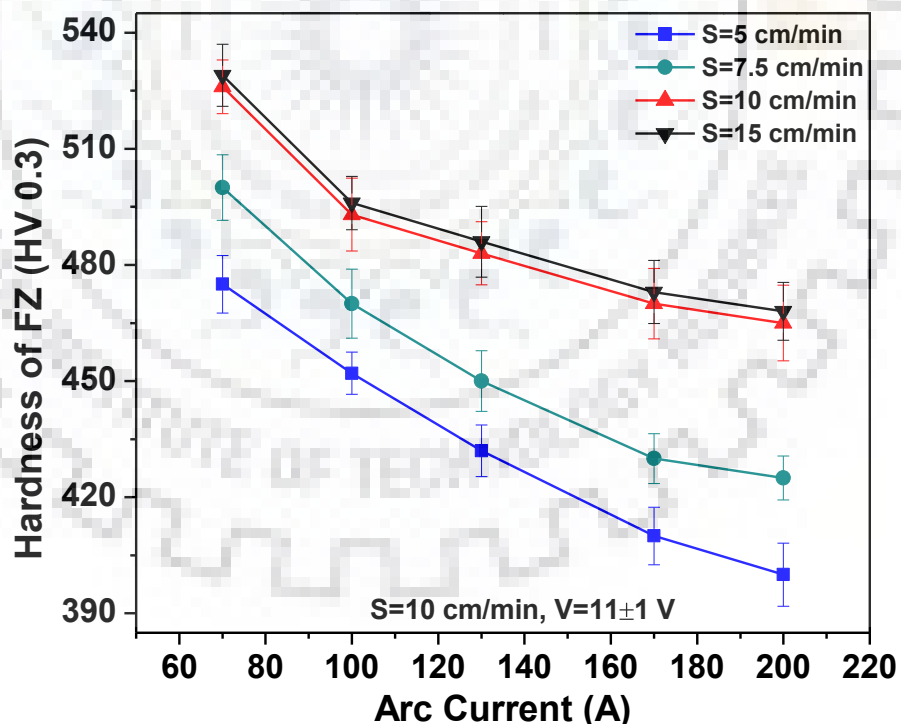
At a given arc voltage of 11 ± 1 V the effect of variation in arc current (I) and travel speed (S) on the hardness of fusion zone and HAZ have been shown in Figs. 6.50 (a and b) respectively. The figures show that the increase in arc current from 70 to 200 A significantly decreases the hardness of fusion zone and its HAZ. It has been further observed that the hardness of FZ and HAZ increases appreciably with the increase of travel speed. The figures

reveal that the hardness of the FZ and HAZ at any I and S is comparatively much more than that of the base metal (220 ± 10 VHN), which might have largely happened due to favorable phase transformation as discussed earlier. In HAZ it has happened primarily through a process of re-crystallization and phase transformation as a function of heating and cooling rate which are largely governed by the heat input and temperature gradient in the fusion pool dictated by the arcing parameters [Ghosh et al., 2009]. The decrease in arc current at a given travel speed and the increase in travel speed at a given arc current reduces the heat input that increases the size of fusion pool and consequently enhances its cooling rate. The high cooling rate is primarily responsible for the fully lath martensitic structure (refer to sec. 6.4) which is relatively hard as clearly reflected in the figure. Finally the presence of varied amount of different phases in the fused and heat affected zones as discussed in section 6.4 is reflected in their matrix hardness. The empirical correlations of hardness of FZ and HAZ with I and S have been worked out as follows.

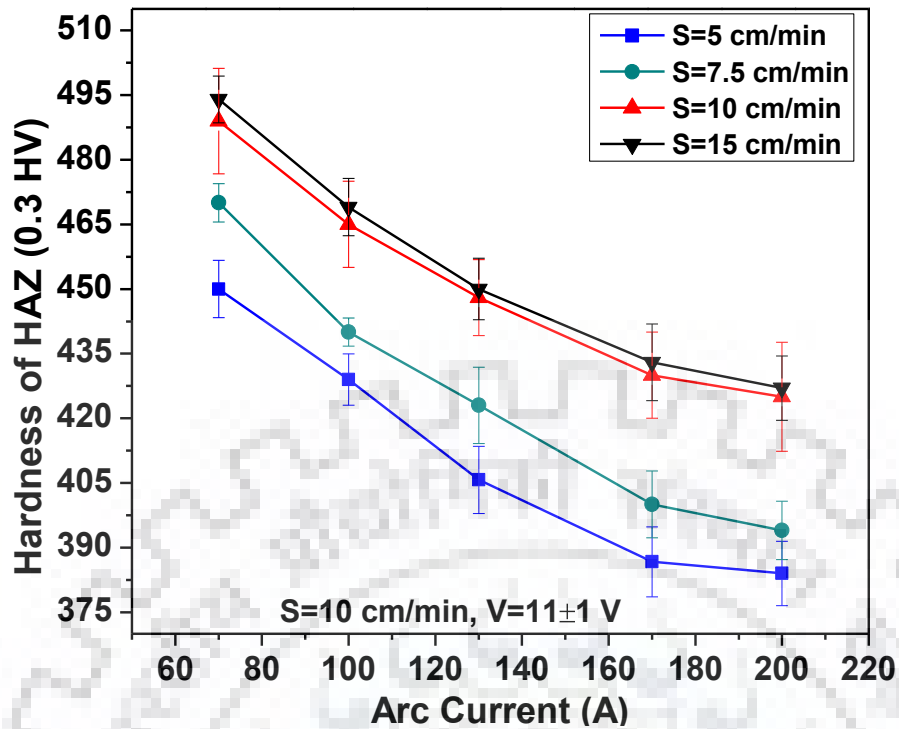
At $V=11\pm 1$ V

$$H_{FZ} = 4.77S - 0.76I + 3.40 \times 10^{-2} IS + 490.62 \quad (6.37)$$

$$H_{HAZ} = 5.53S - 0.61I + 1.13 \times 10^{-2} IS + 457.75 \quad (6.38)$$



(a)



(b)

Fig. 6.48 The effect of arc current and travel speed on hardness of (a) FZ and (b) HAZ at an arc voltage of 11 ± 1 V.

At different arc current of 70, 130 and 200 A the distribution of hardness across the region starting from the fusion zone through HAZ to base material is shown in Fig. 6.51. The figure shows that as one proceeds from the fused modified zone to HAZ the hardness falls till it reaches the stable hardness (220 ± 10 VHN) of base metal. It is observed that with the increase of arc current from 70 to 200 A the fusion zone of high hardness (about 525-470 VHN respectively) extends from about 0.8 to 3.0 mm, respectively with a backup of relatively lower hardness HAZ lying in the range of about 470 to 420 VHN respectively. At the low and high arc current of 70–200 A the fine grain, low hardness compare to FZ and tougher HAZ backup due to formation of lath martensite (Thalow et. al, 1987) is found to be extended up to about 1.5 and 2.5 mm followed by base metal. In view of the above it may be assumed that the use of TIGA processing is effective to produce high surface hardness with tougher inner core.

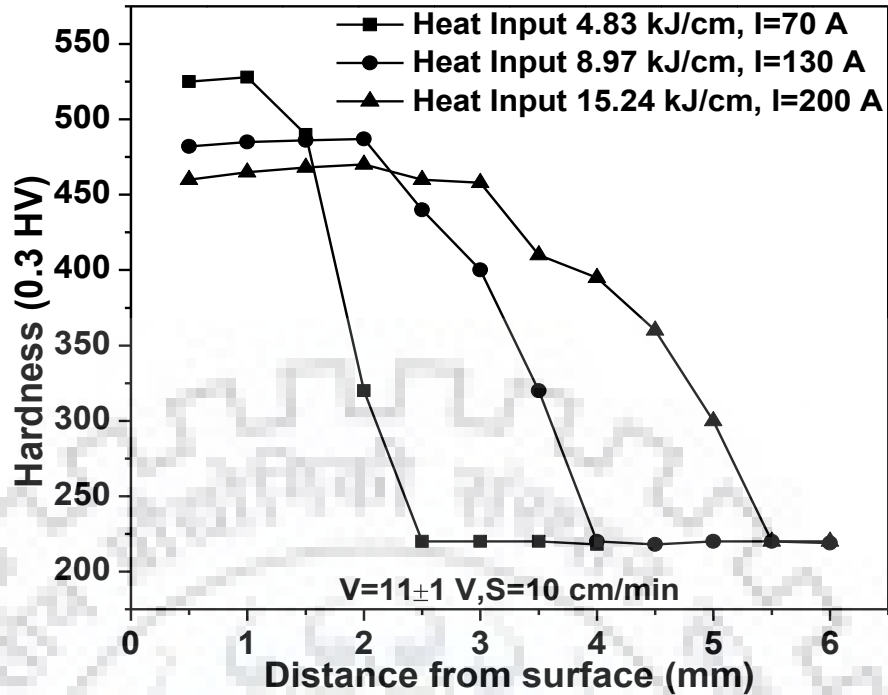


Fig. 6.49 Distribution of hardness across the region starting from the fusion zone through HAZ to base metal at different arc current of 70, 130 and 200 A.

6.5.2 Effect of single pass P-TIGA process on hardness of FZ and HAZ

At different Ω of 6.9, 8.97 and 12.75 kJ/cm raised at the I_m of 100 ± 1 , 130 ± 2 and 170 ± 1 A respectively, the effect of variation in ϕ and f in the range of 0.04 to 0.44 and 2 to 15 Hz respectively on the hardness of fusion zone and HAZ has been shown in Figs 6.52 (a-c) and 6.53 (a-c) respectively. The Figs. 6.52 (a-c) and 6.53 (a-c) depict that hardness of FZ and HAZ significantly increases with the increase of ϕ at a given f while the Ω remains constant. But it is observed that the hardness of FZ and HAZ reduces with the increase of f from 2 to 10 Hz followed by an insignificant change in it with a further increase of f to 15 Hz. The increase in hardness with the increase of ϕ may be primarily attributed to decrease in fusion pool size enhancing cooling rate which control the microstructure of the modified zone as discussed in section 6.4 respectively. Similarly the decrement in hardness with the increase of f may be primarily attributed to increase the heat build-up in molten pool which increases the fusion zone size and hence reduces the cooling rate. The proportionate variation of phases (lath martensite, bainite and ferrite) is reflected in the hardness data. The empirical correlations of hardness in the FZ and HAZ as a function of f and ϕ at different Ω has been worked out as follows.

For Fusion Zone

$$\text{At } I_m=100 \text{ A} \quad H_{FZ} = -0.97f + 58.18\phi + 0.06f\phi + 507.20 \quad (6.39)$$

$$\text{At } I_m=130 \text{ A} \quad H_{FZ} = -1.02f + 60.98\phi + 0.10f\phi + 499.07 \quad (6.40)$$

$$\text{At } I_m=170 \text{ A} \quad H_{FZ} = -1.34f + 77.73\phi + 0.56f\phi + 483.97 \quad (6.41)$$

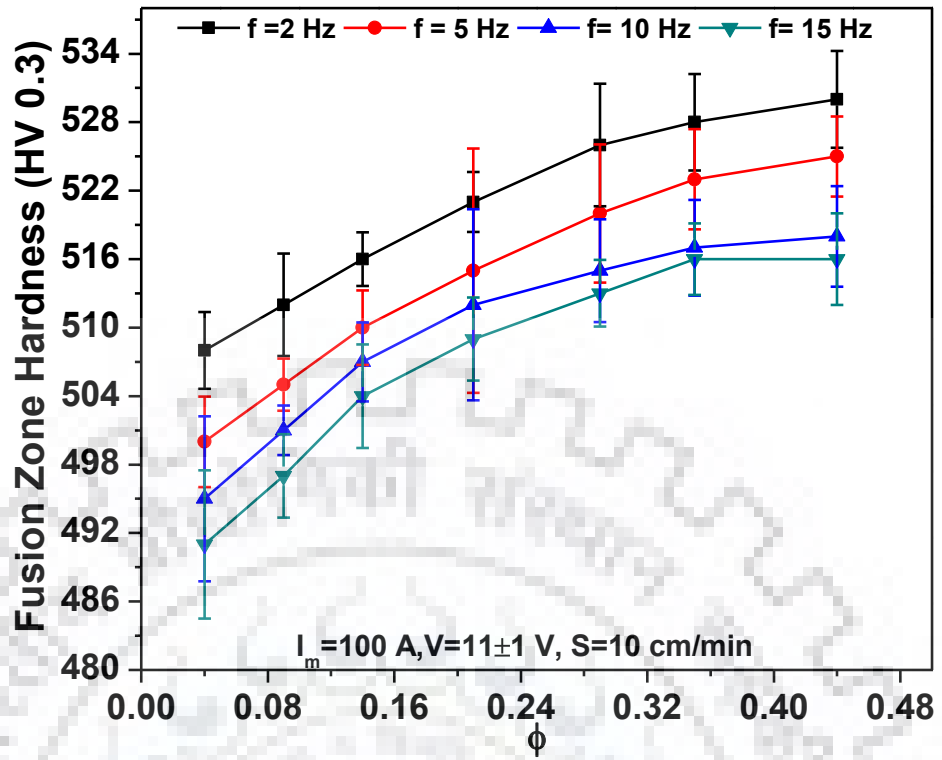
For HAZ

$$\text{At } I_m=100 \text{ A} \quad H_{FZ} = -0.97f + 58.18\phi + 0.06f\phi + 507.20 \quad (6.42)$$

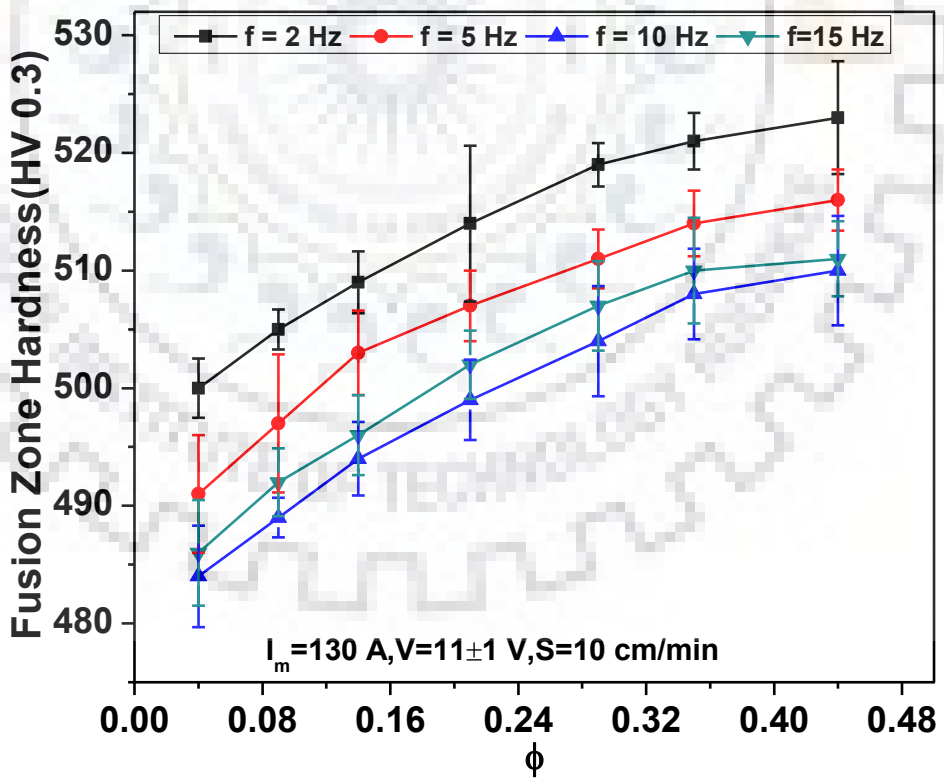
$$\text{At } I_m=130 \text{ A} \quad H_{FZ} = -1.02f + 60.98\phi + 0.10f\phi + 499.07 \quad (6.43)$$

$$\text{At } I_m=170 \text{ A} \quad H_{FZ} = -1.34f + 77.73\phi + 0.56f\phi + 483.97 \quad (6.44)$$

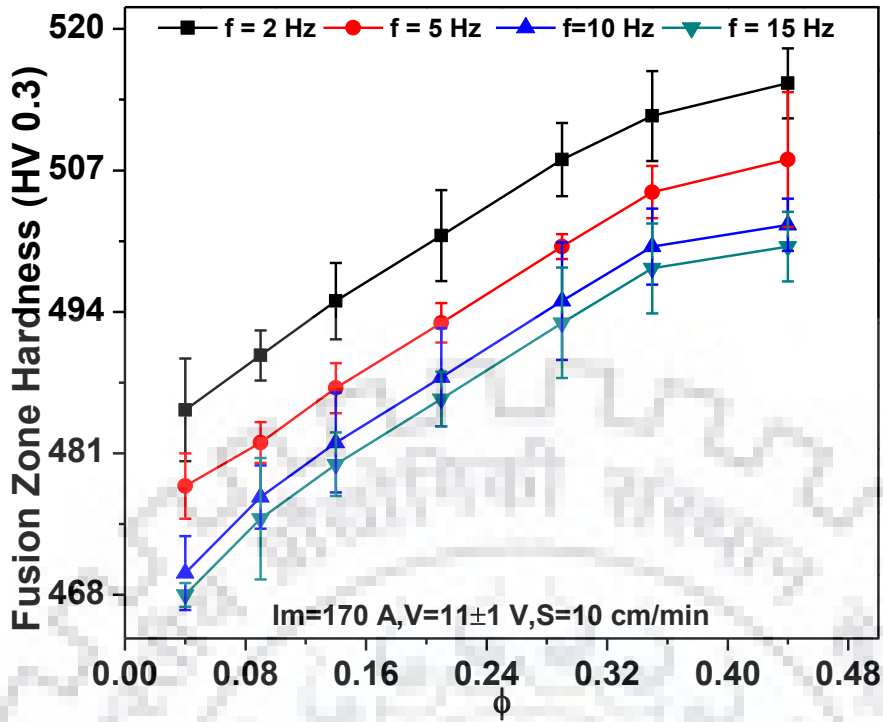
At different I_m of 100, 130 and 170 A, the effect of variation in ϕ and f in the distribution of hardness across the region starting from the fusion zone through HAZ to base material is shown in Figs. 6.54 (a and b), 6.55 (a and b) and 6.56 (a and b) respectively. The figures show that as one proceeds from the fused modified zone to HAZ the hardness falls till it reaches the stable hardness (220 ± 10 VHN) of base metal. It is observed from the figures that at a given f and I_m the increase of ϕ from 0.04 to 0.44 appreciably reduces the hardness of FZ with a backup of relatively lower hardness in HAZ. Further it is also observed that with the increase of pulse frequency from 2 to 10 Hz at a given I_m and ϕ increases the maximum hardness of fusion zone. With the increase in f and ϕ the comparatively fine grain, low hardness compare to FZ and tougher HAZ backup is found to be extended up to about 1.5 to 3 mm followed by base metal. In view of the above it may be assumed that the use of P-TIGA processing is effective to produce high surface hardness with tougher inner core as compared to C-TIGA process with versatile application of pulse parameters.



(a)

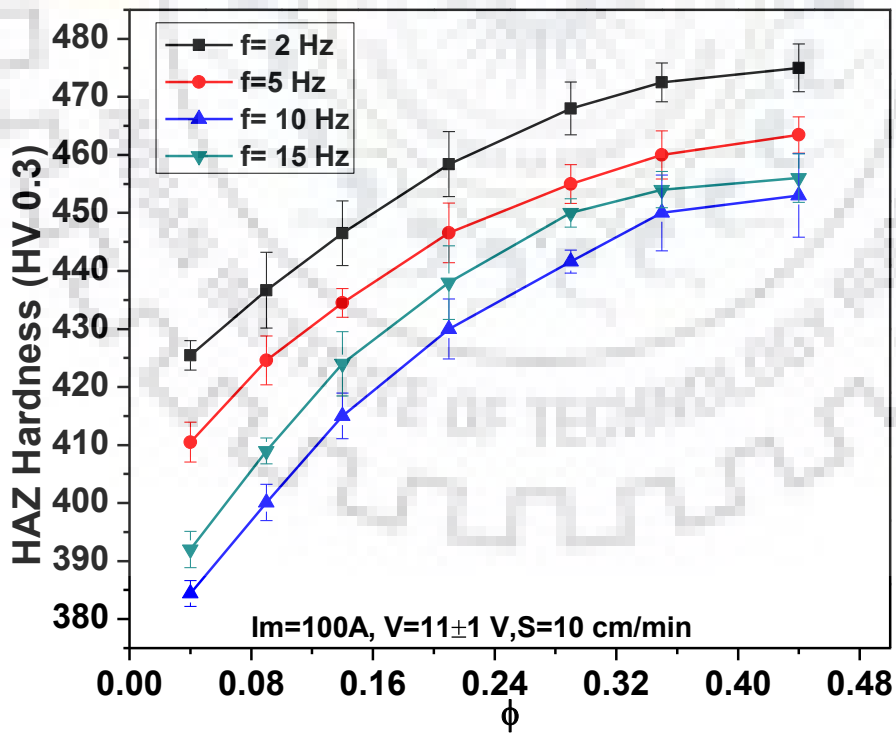


(b)

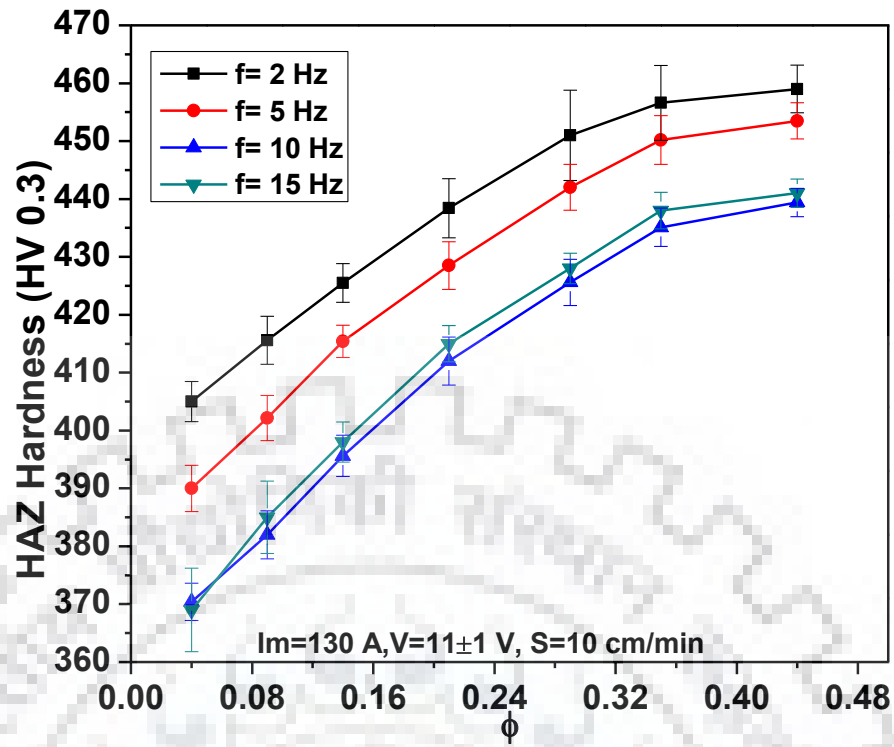


(c)

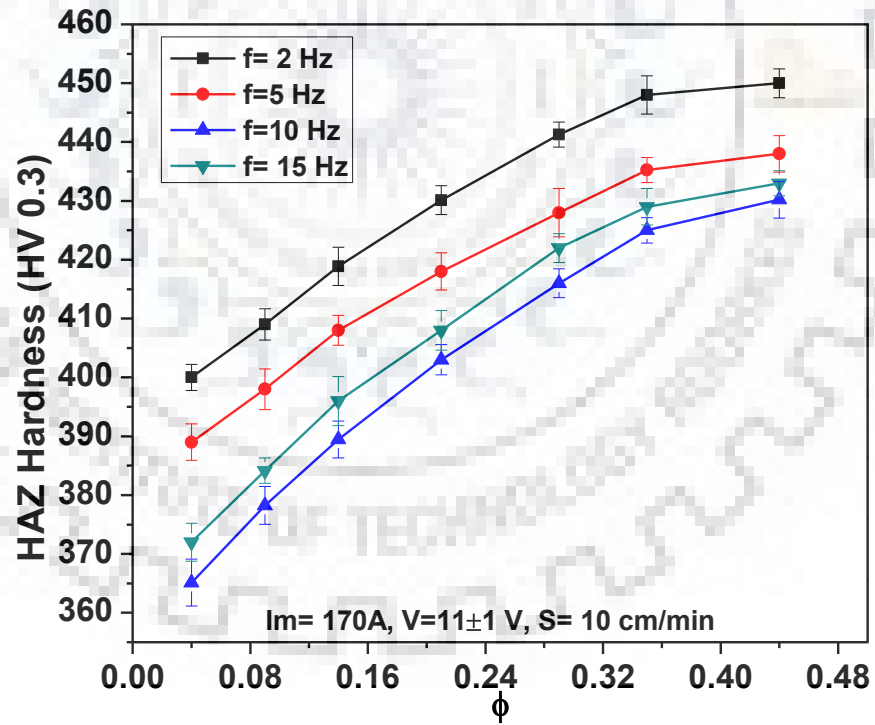
Fig. 6.50 Effect of ϕ and f on hardness of fusion zone at I_m and Ω of (a) 100A; 6.9 kJ/cm (b) 130 A; 8.97 kJ/cm and (c) 170 A; 12.75 kJ/cm.



(a)

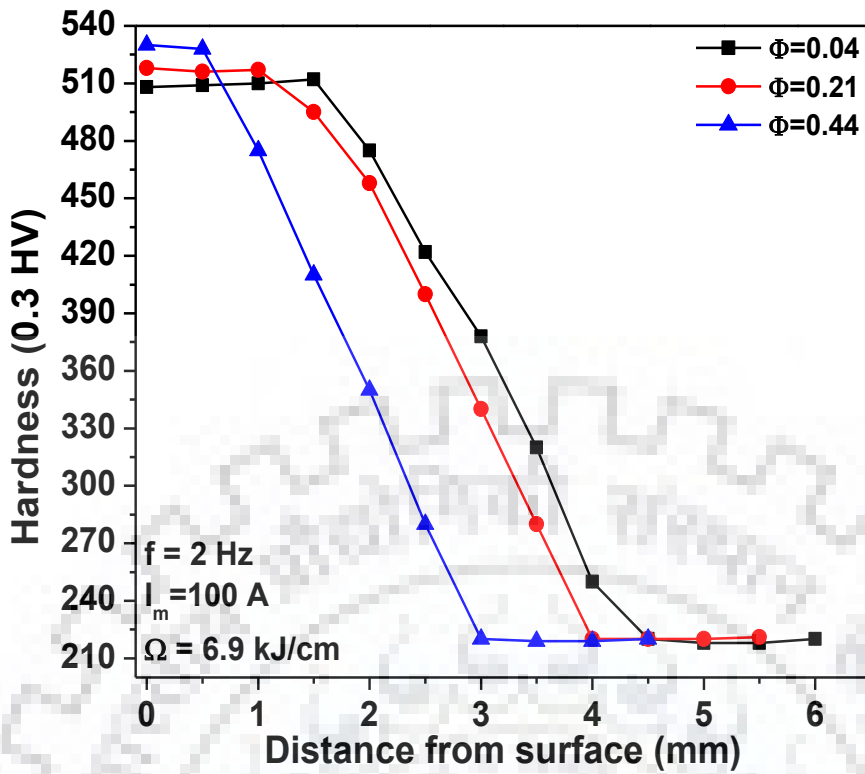


(b)

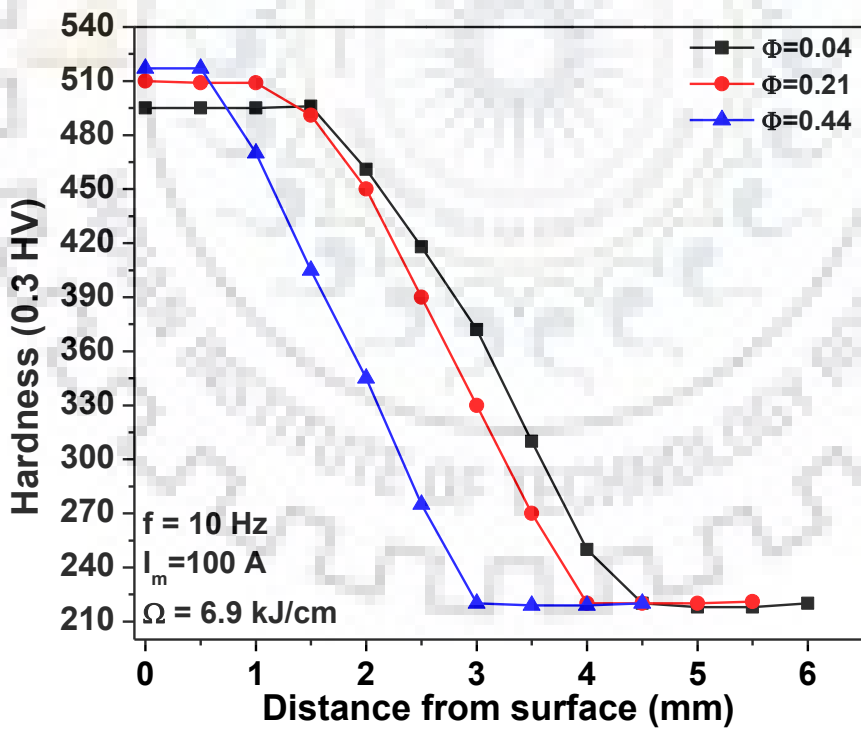


(c)

Fig. 6.51 Effect of ϕ and f on the hardness of HAZ at I_m and Ω of (a) 100A; 6.9 kJ/cm (b) 130 A; 8.97 kJ/cm and (c) 170 A; 12.75 kJ/cm.



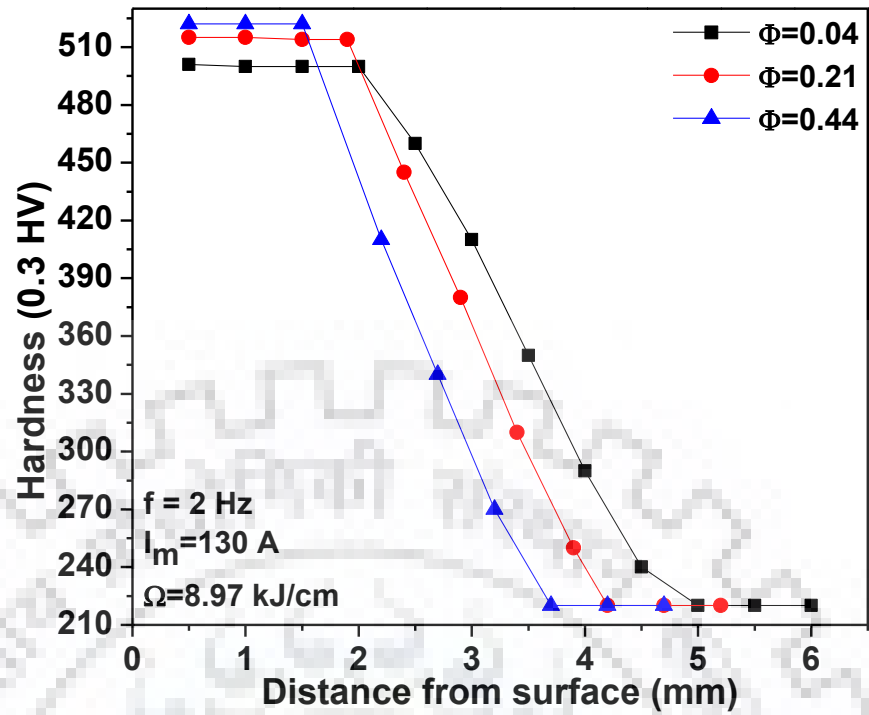
(a)



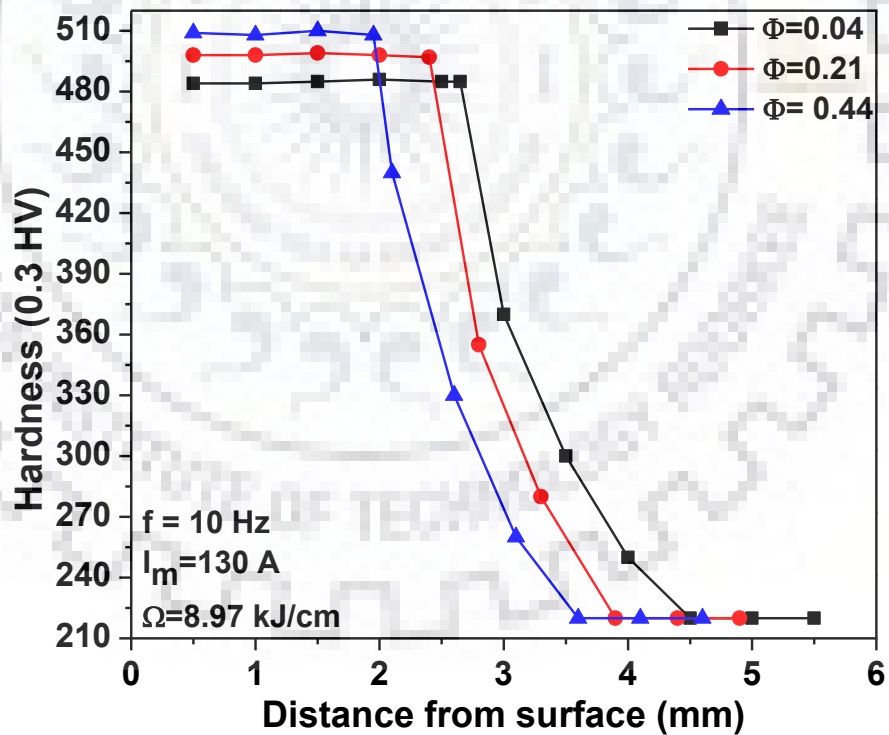
(b)

Fig. 6.52

Distribution of hardness across the region starting from the fusion zone through HAZ to base metal at different f of (a) 2 Hz and (b) 10 Hz at a given I_m of 100 A.



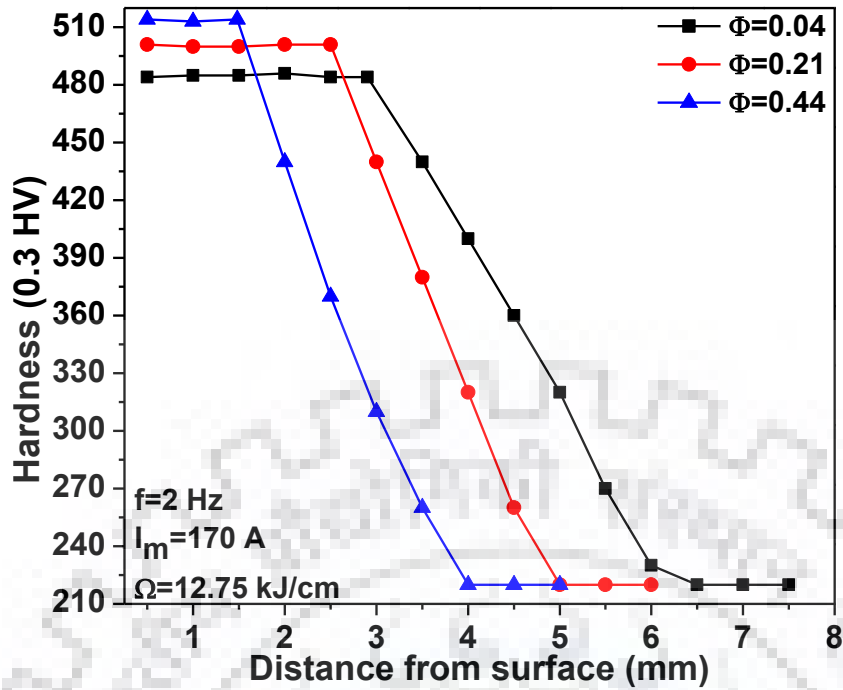
(a)



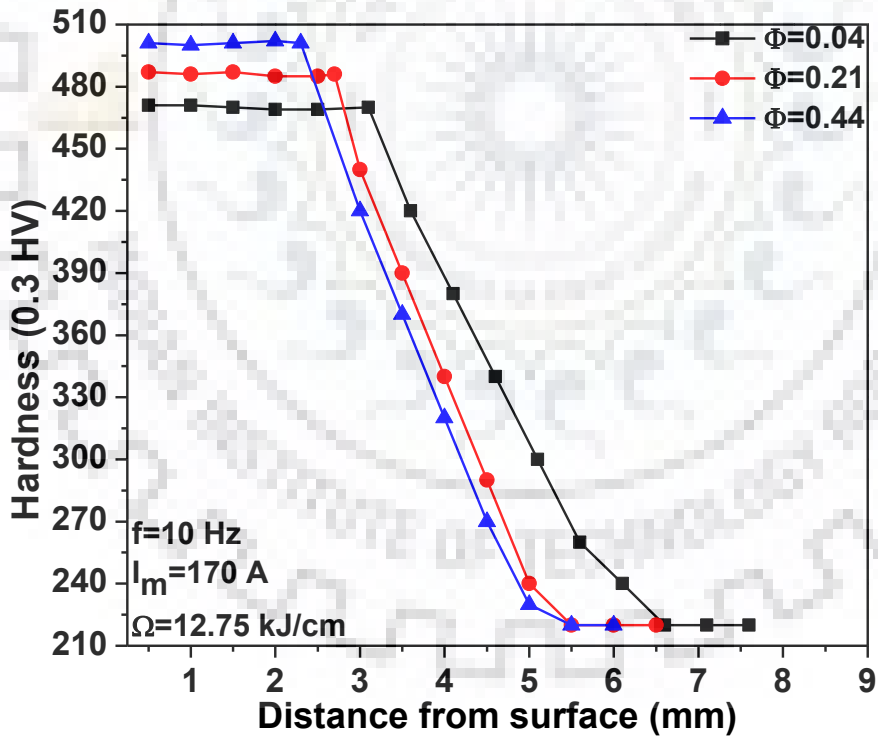
(b)

Fig. 6.53

Distribution of hardness across the region starting from the fusion zone through HAZ to base metal at different f of (a) 2 Hz and (b) 10 Hz at a given I_m of 130 A.



(a)



(b)

Fig. 6.54 Distribution of hardness across the region starting from the fusion zone through HAZ to base metal at different f of (a) 2 Hz and (b) 10 Hz at a given I_m of 170 A.

6.5.3 Summary

The effect of single pass C-TIGA and P-TIGA processes have been revealed in this study in terms of hardness of FZ and HAZ along with the distribution of hardness within them. It is observed that the variation of arcing and its travel parameters (I and S) in C-TIGA process significantly affects the improved hardness of the substrate surface (FZ) with a backup of refined and comparatively lower hardness of HAZ. It is also observed from the results that in the P-TIGA process the effective control of ϕ and f at a given heat input significantly increases the hardness of base material. However, it is interestingly observed that the use of P-TIGA process gives higher hardness in the fusion zone and heat affected zone at relatively lower Ω as compared to that of the C-TIGA process. The precise control of heat buildup in fused zone by using appropriate ϕ and f in P-TIGA process effectively increases the hardness of FZ and HAZ more than $20\pm 10\%$ as compared to that obtained in case of the C-TIGA process at the same arc current and heat input. As compared to base material the hardness of the FZ and HAZ is increased upto $127\pm 20\%$ and $77\pm 25\%$ respectively.

6.6 Multipass TIGA process

This section presents the observations in multi-pass surface modification of AISI 8620 steel plate using C-TIGA and P-TIGA processes over a relatively larger substrate surface area in order to analyze the effectiveness of the TIGA process for industrial applications. In case of the single pass C-TIGA and P-TIGA processes, the arcing parameters are optimized and used for larger surface area modification. The study involves understanding the effect of multi-pass treatment of substrate surface in terms of microstructural modification and hardness distribution in the matrix.

6.6.1 Multi-pass C-TIGA process

The multi-pass C-TIGA process is applied over the substrate surface at optimized parameters on the basis of hardness and depth of penetration as discussed in the case of single pass C-TIGA process. The effect of multi-pass treatment using C-TIGA process is studied and compared in terms of microstructural features and hardness distribution in its different thermally affected regions.

6.6.1.1 Microstructural studies

At a given arc voltage and travel speed of 11 ± 1 V and 10 cm/min respectively the effect of multi-pass C-TIGA process on the microstructures of different locations of the modified zone at the arc current of 170 A has been shown in Figs. 6.57. The multi-run process altered the characteristics and morphology of the fused and HAZ of the previous run through tempering by

the subsequent passes. The effect of tempering is clearly seen in Figs. 6.57 (ii to v). The microstructure of FZ shown in Fig. 6.57 (i) reveals the presence of cast dendritic structure with large patches of lath martensite and proeutectoid ferrite after the last (4th) pass. The Fig. 6.57 (ii and iii) shows the microstructure of FZ affected by subsequent passes (Ist, IInd and IIIrd passes). The microstructure of reheated FZ reveals smaller patches of tempered martensite along with bainite and ferrite as shown in Fig. 6.57 (ii) and the refinement of grains is observed in Figs. 6.57(iii). The Figs. 6.57 (iv and v) show the HAZ and reheated refine HAZ of the multi pass modified zones. The bainite and proeutectoid ferrite with some retained austenite are visible in the microstructure shown in Fig. 6.57 (iv). The refinement of grains is observed in Fig. 6.57(v) having elimination of martensite and bainite phases in the matrix. The temperature of the FZ of first pass reaches above austenizing temperature AC3 after second subsequent pass which reduces the dendritic morphology (Figs. 6.57(ii)) and produces acicular ferrite and bainite in the matrix. The temperature of the reheat refined fusion zone (Figs. 6.57(iii)) reaches between the AC1 and AC3 austenizing temperature ranges which has refined the microstructure. The effect of tempering in HAZ is observed in Figs. 6.57 (iv and v) where the austenizing temperature is below AC1. The appreciable refinement of grains is observed in reheated refined HAZ (Fig. 6.57(v)).

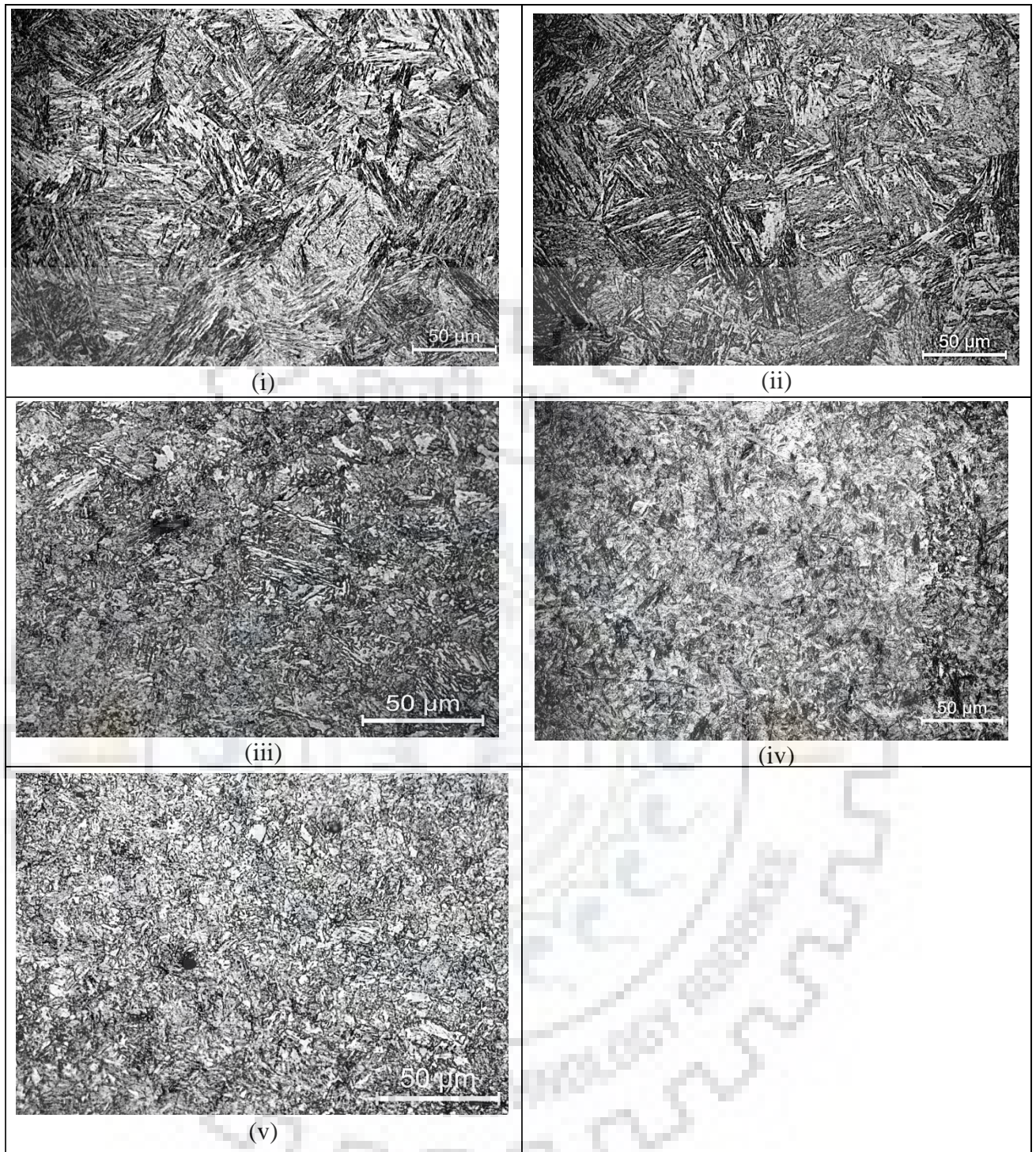


Fig. 6.55 Microstructures of different modified zones of multi-pass C-TIGA processed substrate at an arc current of 170 A; (i) Reheated FZ (ii) FZ (iii) Reheat refined FZ (iv) HAZ (v) Reheat refined HAZ.

6.6.1.2 Hardness Study

At the optimum arc current of 170 A, with respect to maximum effect of multi-pass C-TIGA processing on matrix hardness, its distribution in the matrix is shown in Fig. 6.58. The figure shows the typical distribution of hardness at different thermally affected zones of the

matrix as typically referred in Fig. 5.14. The second pass changes the characteristics of FZ and HAZ of first pass due to tempering effect. The second pass creates the reheated and reheats refined FZ over the FZ of the first pass. The similar zones are created by the third and fourth passes in the FZ and HAZ of the previous passes. So the area under the first, second and third passes may be recognized as stabilized modified zone and area under the fourth pass as unstabilized region. The hardness of the stabilized regions is varying from 410 VHN at reheated FZ to 450 VHN at reheat refined FZ. The variation of hardness in stabilized zone is occurred due to multi-pass TIGA process which has subsequently tempered the microstructure of FZ and HAZ of the prior passes. The variation in hardness reflects the nature of phase transformation in the different location of the modified matrix by using different C-TIGA parameters.

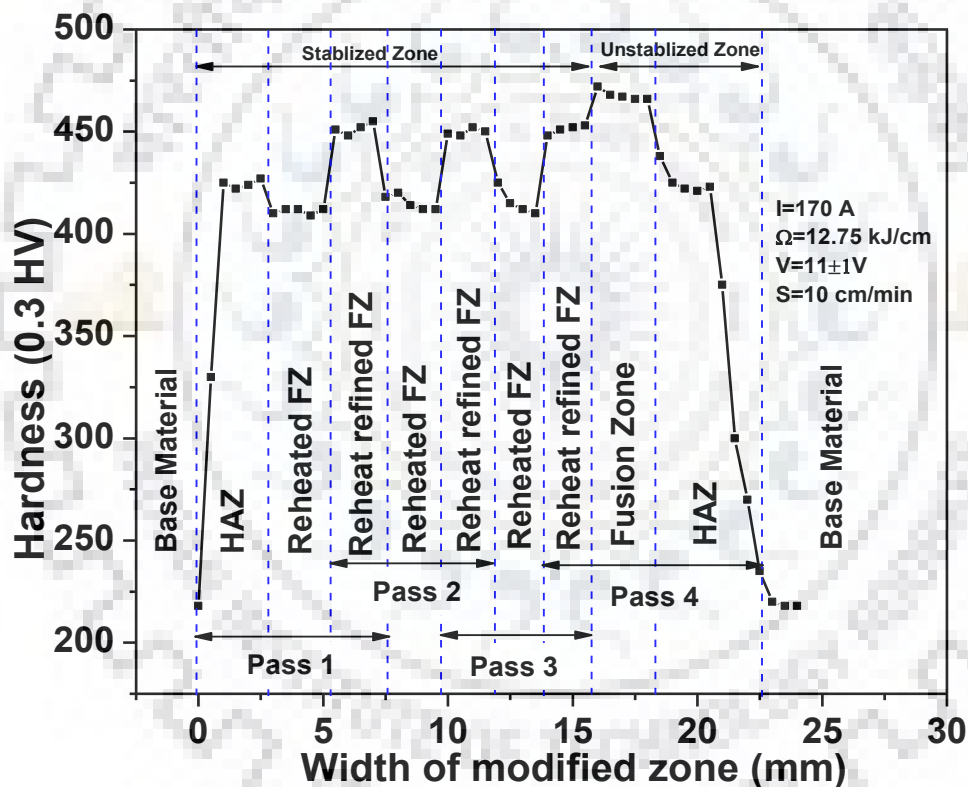


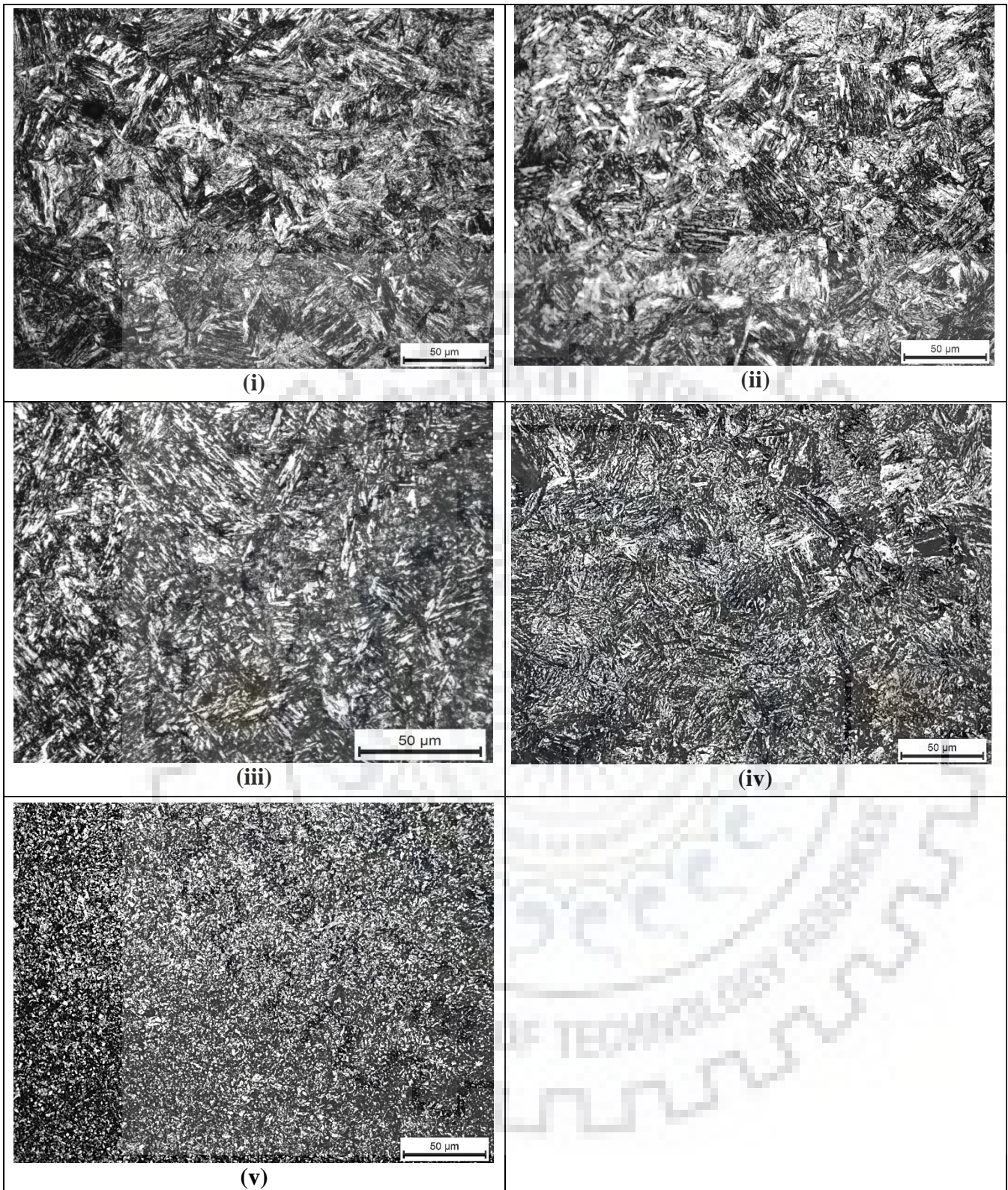
Fig. 6.56 Effect of multi-pass C-TIGA process in the distribution of hardness in the modified zone at an arc current of 170 A.

6.6.2 Multi-pass P-TIGA process

The multi-pass P-TIGA process is applied over the substrate surface at optimized parameters as discussed in chapter 5. The effect of multipass treatment using P-TIGA process is studied and compared in terms of microstructural features and hardness distribution in its different thermally affected regions.

6.6.2.1 Microstructural studies

At a given arc voltage and travel speed of 11 ± 1 V and 10 cm/min respectively, the microstructures of different locations of the modified zone at varying ϕ of 0.04 and 0.44 at two different levels of f of 2 and 10 Hz have been shown in Figs. 6.59 (a and b) and 6.60 (a and b) respectively. The ϕ and f are varied at the mean current of 170 A. It is observed from the figure that similar to multi-pass C-TIGA process the multi-pass P-TIGA process also changes the characteristics and morphology of the fused and HAZ of the previous pass through tempering by the subsequent passes. The microstructure of the FZ after the last (4th) pass as shown in Figs. 6.59(i) and 6.60 (i) reveals the cast dendritic structure with larger patches of lath martensite phase. The Figs. 6.59 (ii and iii) and 6.61 (ii and iii) show the effect of subsequent passes (iind, iiird and ivth passes) on the microstructure of FZ. It is observed from the figures (Figs 6.59 (ii) and 6.60 (ii)) that the microstructure of reheated FZ contains refined and smaller patches of tempered lath martensite along with lower and upper bainite, whereas the microstructure of the double reheated zone (Figs. 6.59 (iii) and 6.60 (iii)) is having uniformly distributed refined martensite plates. The Figs. 6.59 (iv and v) and 6.60 (iv and v) shows the microstructure of HAZ and reheated refine HAZ of the multi pass modified zones. The bainite and proeutectoid ferrite with some retained austenite are visible in the microstructure shown in Figs. 6.59 (iv) and 6.60 (iv). The refinement of grains is observed in Figs. 6.59 (v) and 6.60 (v) with absence of martensite and bainite phases in the matrix. The mechanism to understand the effect of multi-pass treatment is explained in subsection 6.5.5.1 which is considered practically similar in case of P-TIGA process.



(a)

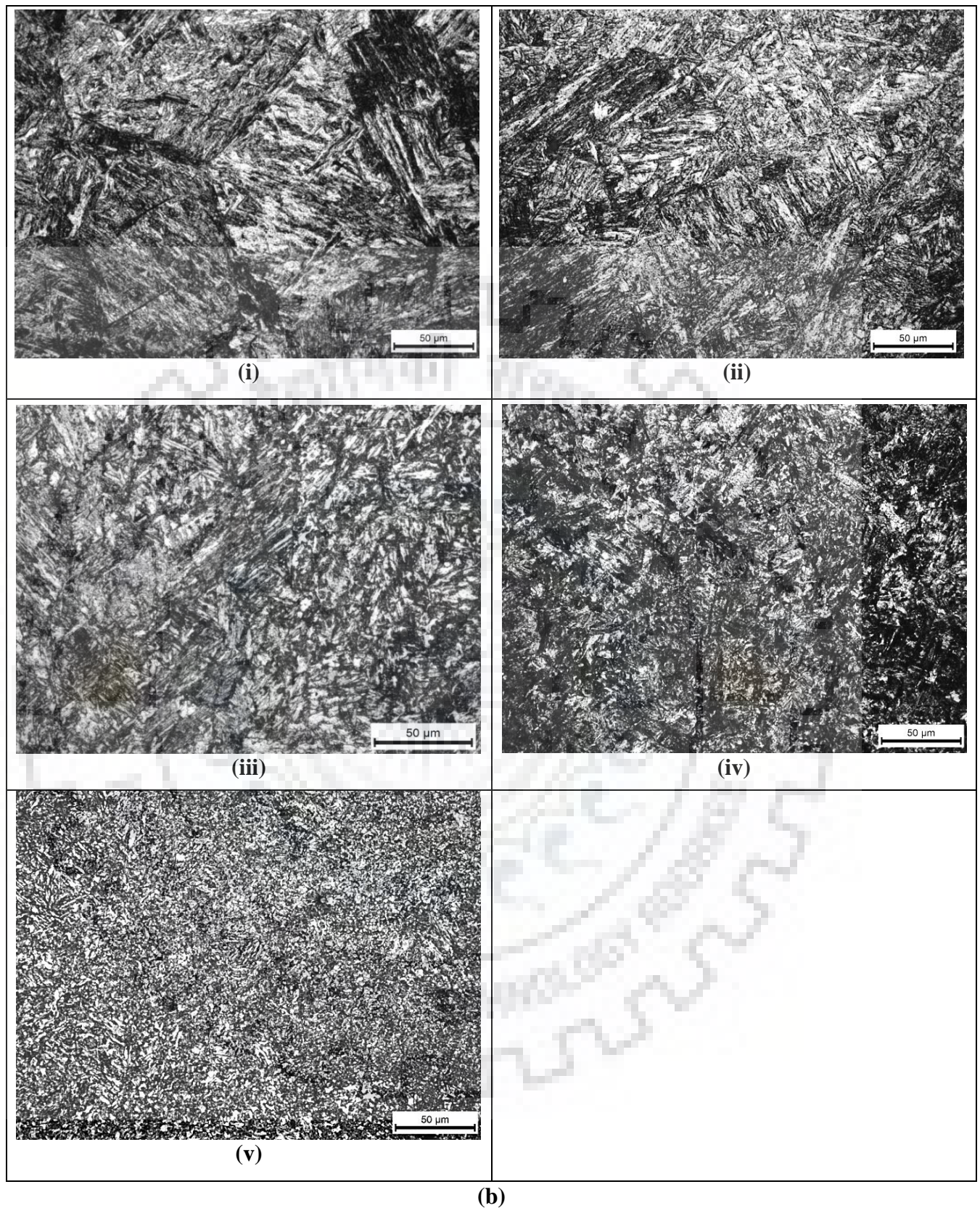
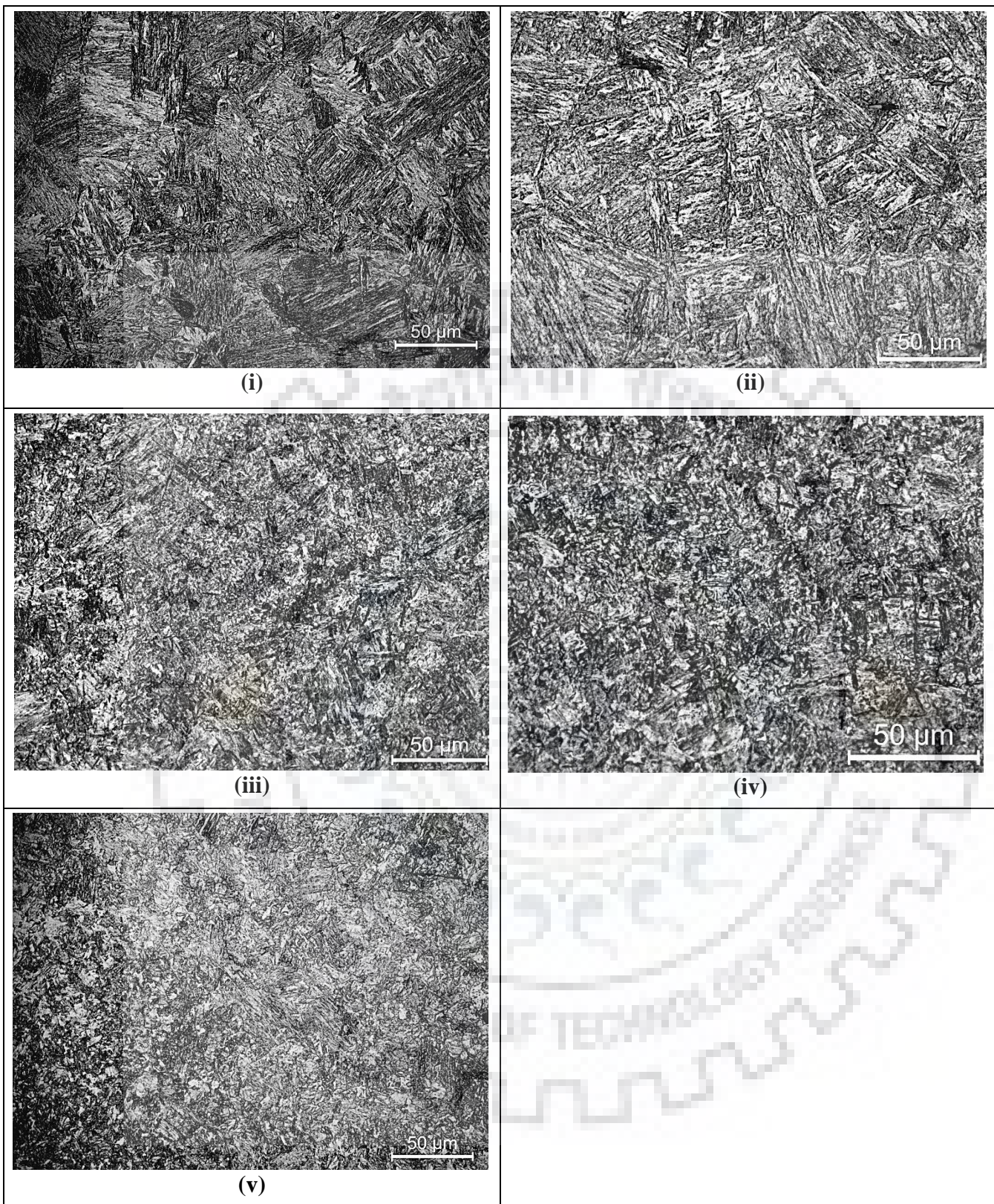
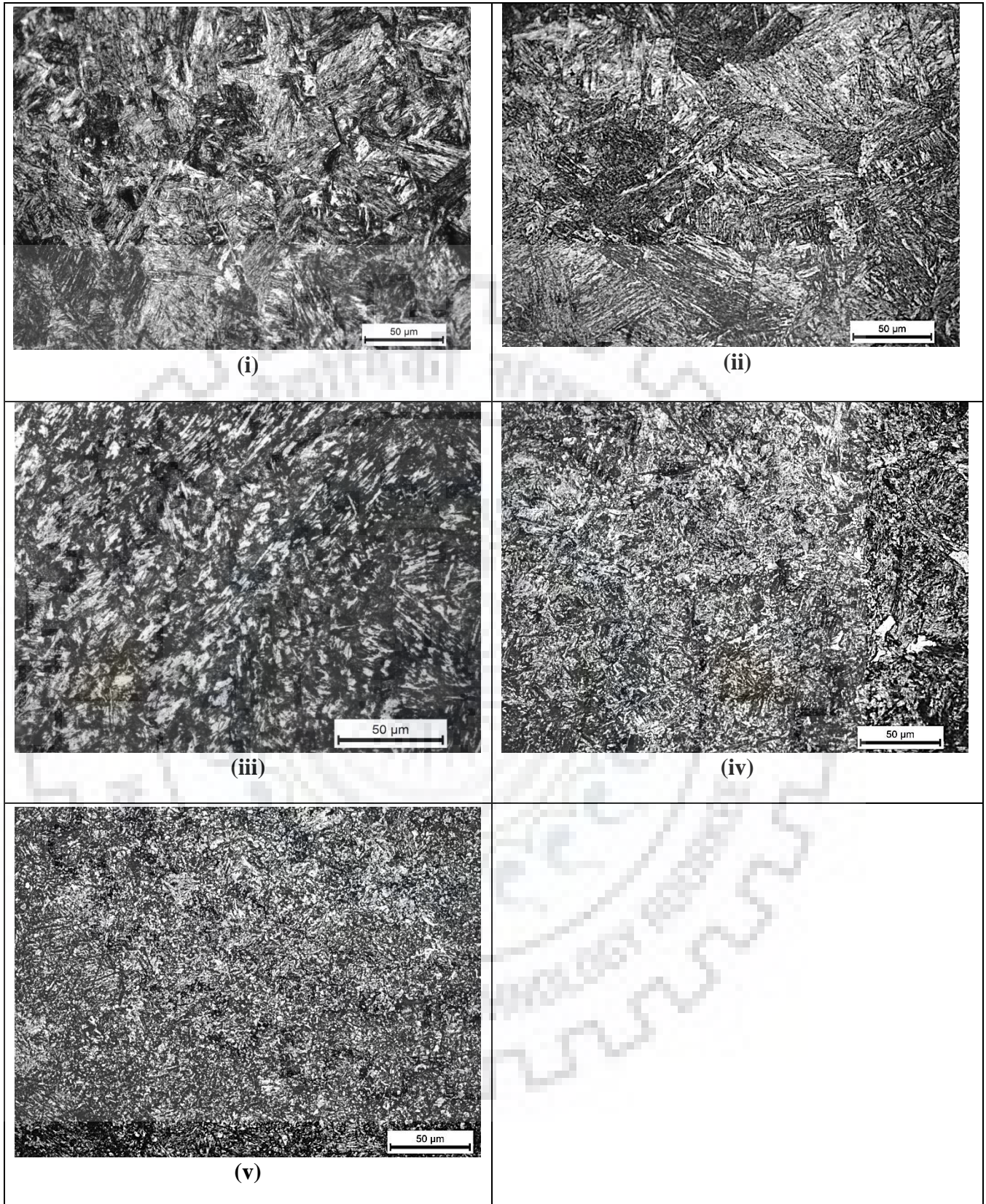


Fig. 6.57 Effect of multi-pass P-TIGA process on microstructures of different modified zones designated as (i) FZ (ii) Reheated FZ (iii) Reheat refined FZ (iv) HAZ (v) Reheat refined HAZ at a varied ϕ of (a) 0.04 and (b) 0.44 with f and I_m of 2 Hz and 170 A respectively.



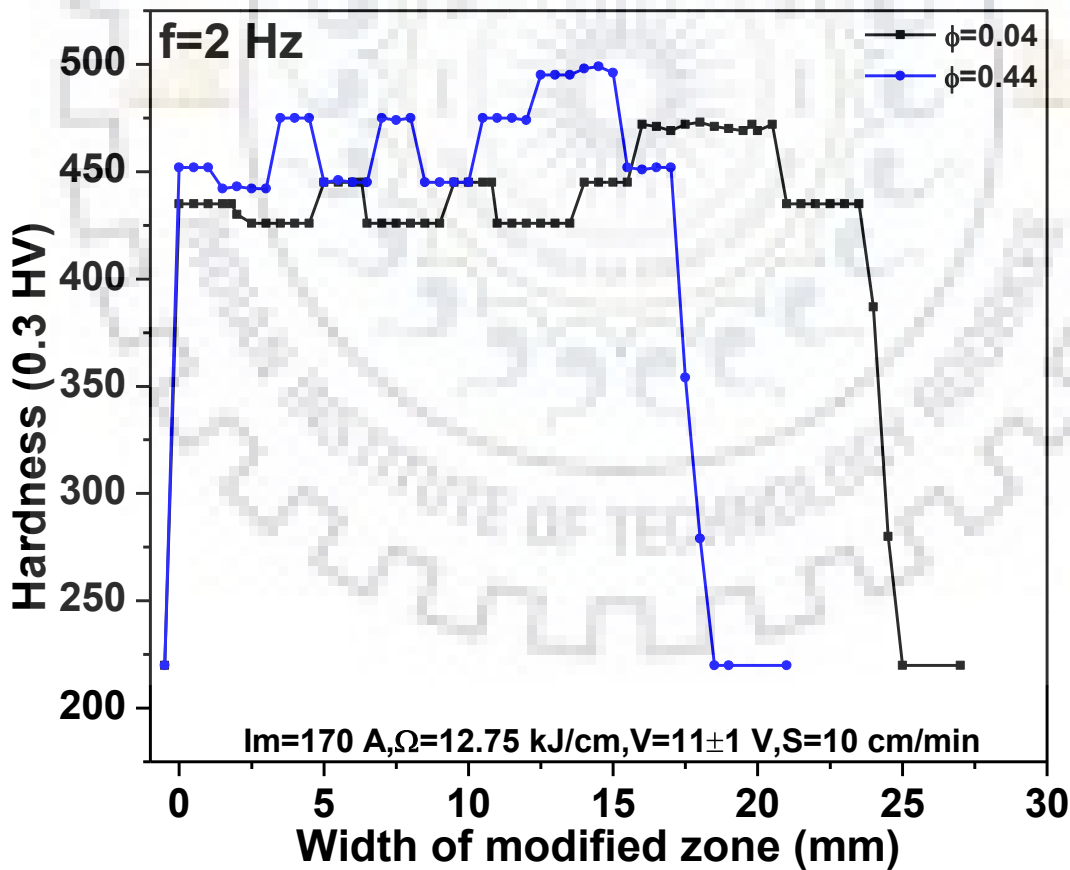
(a)



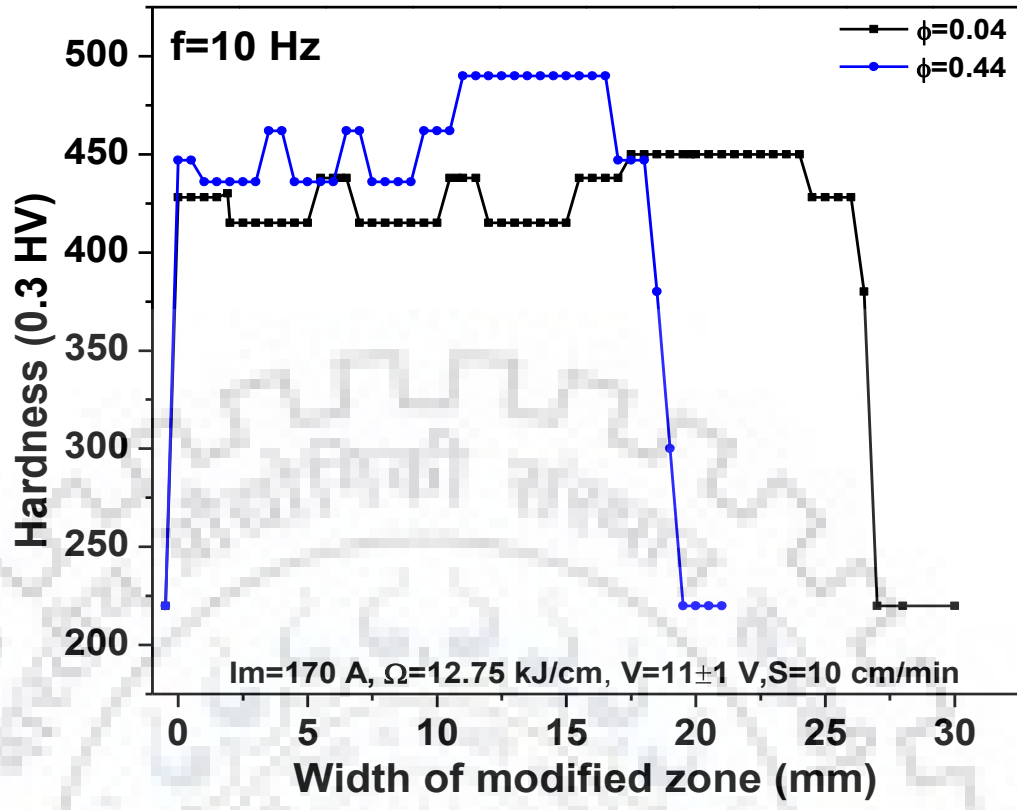
(b)
Fig. 6.58 Effect of multi-pass P-TIGA process on microstructures of different modified zones designated as (i) FZ (ii) Reheated FZ (iii) Reheat refined FZ (iv) HAZ (v) Reheat refined HAZ at a varied ϕ of (a) 0.04 and (b) 0.44 with f and I_m of 10 Hz and 170 A respectively.

6.6.2.2 Hardness Study

At a given arc voltage and travel speed of 11 ± 1 V and 10 cm/min respectively, the hardness distribution in the modified zone at varying ϕ of 0.04 and 0.44 in different f of 2 and 10 Hz have been shown in Figs. 6.61 (a and b) respectively, where the I_m was kept constant as 170 A respectively. It is observed from the figures that the hardness of the stabilized region (explained in the section 6.6.1.2) is varied in the range of 436 ± 13 and 460 ± 21 VHN at the ϕ of 0.04 and 0.44 while the f is kept at 2 Hz. Similarly, at the frequency of 10 Hz the hardness of the stabilized region is found to varied in the range of 427 ± 16 and 449 ± 18 VHN at the ϕ of 0.04 and 0.44 respectively. The variation of hardness in stabilized zone is occurred due to multi-pass P-TIGA process which has subsequently tempered the microstructure of FZ and HAZ of the prior passes. It is further observed from the figure that the width of modified zone increases with the decrease in ϕ and increase in f . The variation in hardness is attributed to the proportion of phase transformation in the different location of the modified matrix by using different P-TIGA parameters as discussed earlier.



(a)



(b)

Fig. 6.59 Distribution of hardness at a varied ϕ of (a) 0.04 and (b) 0.44 at a I_m and f of 170 A and 10 Hz respectively.

6.6.3 Summary

The multi-pass C-TIGA and P-TIGA processes are significantly used for modification of larger surface area to match the needs of industrial applications, especially for large bearings. The microstructures of stabilized zone primarily consist of tempered lath martensite followed by bainite and proeutectoid ferrite. The microstructure of different zones is primarily depends upon the C-TIGA and P-TIGA parameters. The effect of tempering is clearly observed in the distribution of the hardness in the modified zone. The hardness in the stabilized zone is found as 80 ± 20 % more than the base metal. However, the hardness of the modified zone using multi-pass TIGA process is reduced up to 8 ± 5 % due to effect of tempering as compared to the single pass TIGA process. Similarly, the hardness and width of the stabilized zone found 15 ± 3 % more in P-TIGA process at a given I_m or arc current respectively used in the arcing process.

6.7 Residual stress analysis

The residual stresses play an important role to determine the mechanical and chemical properties of metallic component. The effects of residual stresses may be beneficial or detrimental to service requirement depending upon the nature of residual stresses present, either

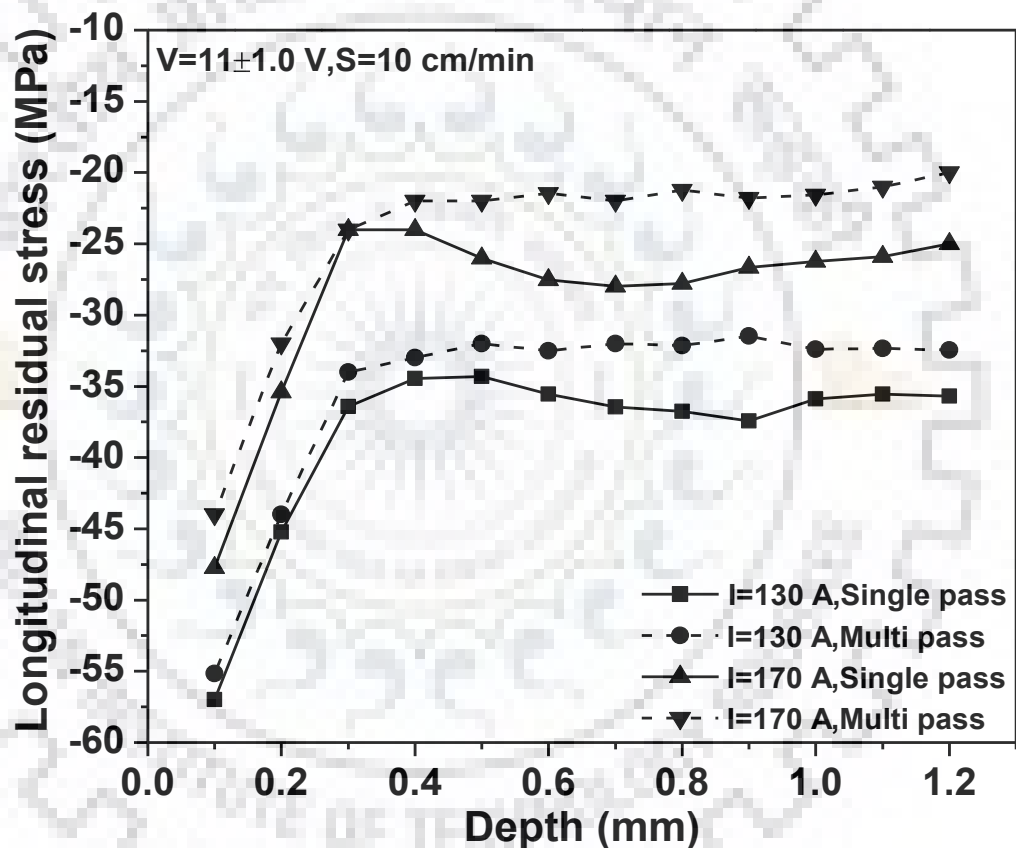
it compressive or tensile form. The tensile residual stress is detrimental to the matrix because it reduces the wear and fatigue properties. Whereas the compressive stress is beneficial for the engineering components because it increases their wear resistance and fatigue properties. Thus, this section presents the residual stress analysis of the single pass and multi-pass TIGA processed substrate surface treated at different parameters.

6.7.1 Effect of single and multi-pass C-TIGA process on residual stresses

At a given arc voltage and travel speed of 11 ± 1 V and 10 cm/min respectively, the effect of arc current on the longitudinal and transverse residual stresses developed in modified surface of the AISI 8620 steel is shown in Fig. 6.62 (a and b). The figure shows that at a given arc current of 130 and 170 A the surface modification by single and multi-pass C-TIGA processes develop compressive longitudinal and transverse residual stresses in the matrix, where the magnitude of stresses increases with the increase of arc current. It is also noticed that the magnitude of compressive residual stresses reduces as one travels deeper into the modified zone up to a depth of about 0.3–0.4 mm followed by an insignificant change in it with further increase of depth upto about 1.2 mm in base metal. It is also noticed that the depth of sharp reaction of decrease in residual stress is found to be limited to about 0.3 and 0.4 mm in case of both the longitudinal and transverse residual stresses. At the arc current of 130 A the compressive longitudinal and transverse residual stresses is found maximum about 57 and 78 MPa respectively for single pass and about 55 and 75 MPa respectively for multi pass processed within a depth of about 0.1 mm from the surface. However, at the higher arc current of 170 A the compressive longitudinal and transverse residual stresses at the similar depth from the surface is found maximum about 47 and 68 MPa respectively for single pass and 44 and 60 MPa respectively for multi pass processes. The longitudinal residual stresses at a larger depth of the matrix modified at 130 and 170 A are found to reduce up to about 37 and 25 MPa in single pass and 32 and 20 MPa respectively in multi pass followed by an insignificant change in them at further depth of the matrix. The transverse residual stresses at deep inside the matrix modified at 130 and 170 A is found to be reduced to almost of a similar order of about 22 and 16 MPa respectively in single pass and 18 and 15 MPa respectively followed by no significant change in them at further depth of base metal. During surface modification of AISI 8620 steel by C-TIGA process, the martensitic transformation in the matrix under the prevailing thermal cycle with significantly high cooling rate as stated in the section 6.3 above may have contributed to development of compressive residual stresses in the matrix. This is also in agreement to the observations reported by Grigoriants Alexander (1994) in case of laser beam

melting of carbon structural steel. However, in this regard its contribution also on the mechanical effect of distortion cannot be ignored.

It is further observed from the figures that the longitudinal and transverse residual compressive stresses in multipass C-TIGA process is slightly lower as compared to single pass C-TIGA process. During multi-pass C-TIGA process the microstructure of stabilized zone primarily consist of tempered martensite with some amount of bainite and ferrite (sub-section 6.6.1). The tempering of lath martensite due to subsequent passes reduces the residual compressive stresses in the matrix of base metal.



(a)

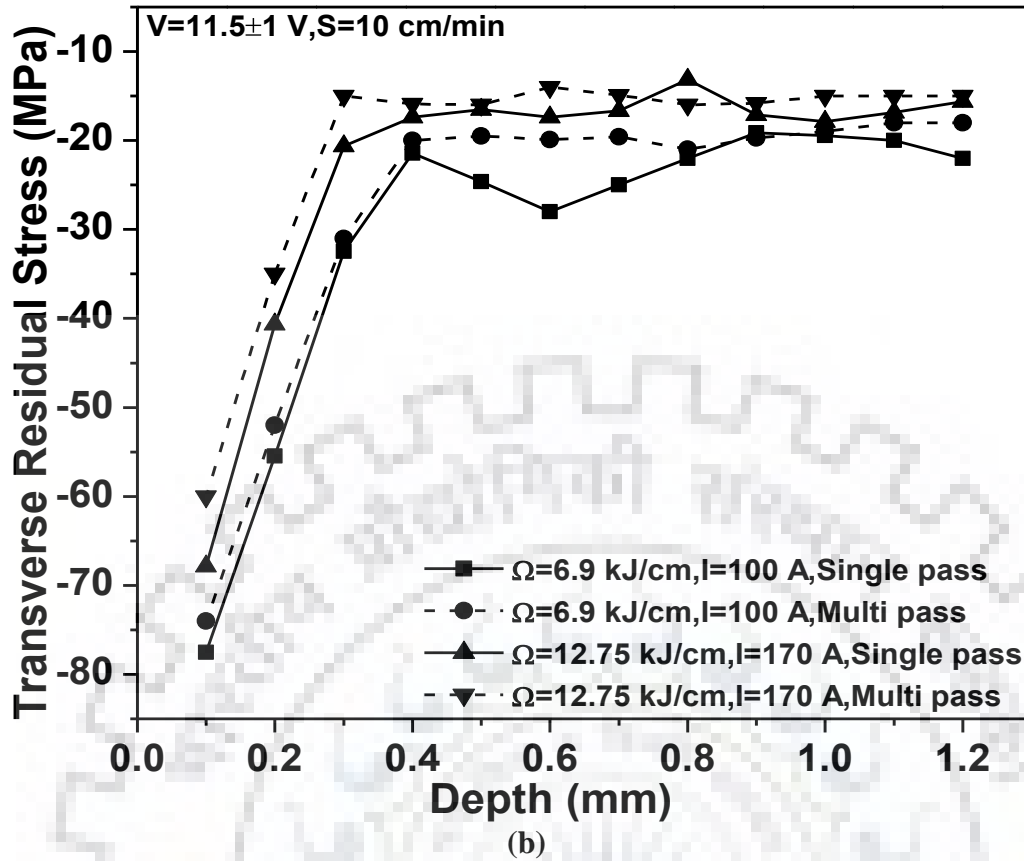
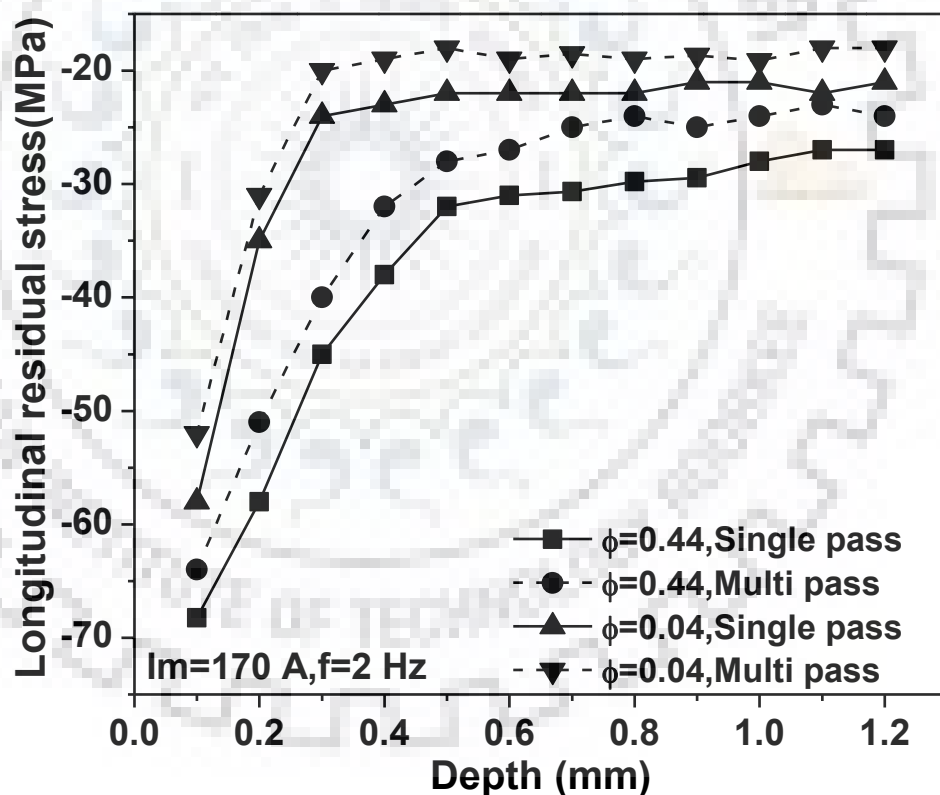


Fig. 6.60 The effect of C-TIGA process on (a) longitudinal and (b) transverse residual stress at the modified zone using single and multi-pass mode.

6.7.2 Effect of single and multi-pass P-TIGA process on residual stresses

At a given arc voltage and travel speed of 11 ± 1 V and 10 cm/min respectively, the longitudinal and transverse residual stresses in the FZ of the single pass P-TIGA and stabilized zone in multi pass P-TIGA processes at varying ϕ of 0.04 and 0.44 have been shown in Figs. 6.63 (a and b) whereas the I_m and f are kept as of 170 A and 2 Hz respectively. The figure shows that at varying ϕ of 0.04 and 0.44 the surface modification by single and multi-pass P-TIGA processes also develop compressive longitudinal and transverse residual stresses in the matrix, where the magnitude of stresses increases with the increase of ϕ . It is also noticed that the magnitude of compressive residual stresses reduces as one travels deeper into the modified zone up to a depth of about 0.25–0.43 mm followed by an insignificant change in it with a further depth of about 1.2 mm in base metal. Similar to C-TIGA process the depth of sharp reaction to decrease in residual stress is found to be limited to about 0.3 and 0.4 mm in case of both the longitudinal and transverse residual stresses. At the lower ϕ of 0.04 the compressive longitudinal and transverse residual stresses is found maximum about 58 and 65 Mpa respectively for single pass and about 52 and 62 Mpa respectively for multi pass within a depth of about 0.1 mm from the surface. However, at the higher ϕ of 0.44 the compressive

longitudinal and transverse residual stresses at the similar depth close to the surface is found maximum about 68 and 65 Mpa respectively for single pass and 64 and 62 Mpa respectively for multi pass processes. The longitudinal residual stresses in a larger depth of the matrix modified at ϕ of 0.04 and 0.44 are found to reduce up to about 21 and 27 Mpa respectively in single pass and 18 and 24 Mpa respectively in multi pass followed by an insignificant change in them at further depth of travel. Whereas the transverse residual stresses at deep inside the matrix modified at ϕ of 0.04 and 0.44 is found to reduce to almost of a similar order of about 18 and 24 Mpa respectively in single pass and 16 and 20 Mpa respectively in multipass followed by no significant change in them at further depth of base metal. During surface modification of AISI 8620 steel by P-TIGA process the increase in ϕ from 0.04 to 0.44 increases the proportion of lath martensitic structure in the matrix under the prevailing thermal cycle with significant cooling rate as stated in the section 6.3.2 may also have contributed to development of compressive residual stresses in the matrix.



(a)

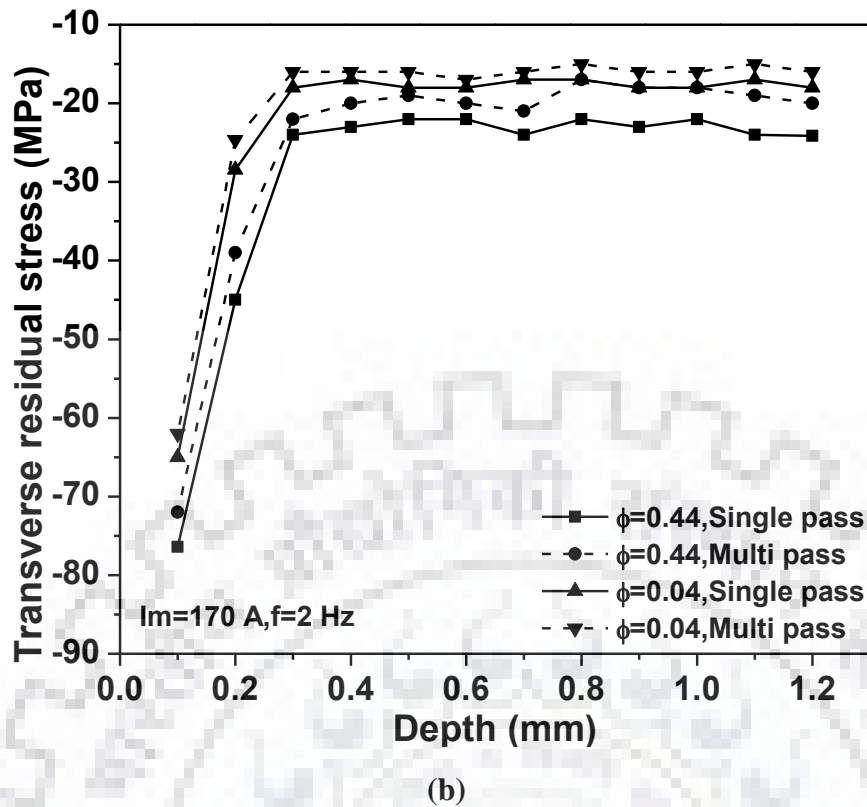


Fig. 6.61 The effect of P-TIGA process on (a) longitudinal and (b) transverse residual stress at the modified zone using single and multi-pass mode.

It is further observed from the figures that the longitudinal and transverse residual compressive stresses in multipass P-TIGA process is relatively low as compared to those of the single pass P-TIGA process. During multi-pass P-TIGA process the microstructure of stabilized zone primarily consists of tempered refined martensite with some amount of bainite and ferrite (sub-section). The tempering of lath martensite due to subsequent passes reduces the residual compressive stresses in the matrix of base metal as discussed above.

6.7.3 Summary

While operated at different parameters the effect of single pass and multi pass C-TIGA and P-TIGA process on residual stresses have been revealed in this study. It is observed that the use of TIGA process introduces compressive stresses into the substrate surface which is beneficial for mechanical and wear properties. It is observed that the increase of arc current reduces the compressive stresses in both the single and multi-pass mode of C-TIGA process. Similarly, it is also observed that the increase of ϕ increases the compressive residual stresses in the modified zone treated by both the single and multi-pass mode of P-TIGA process at the given I_m and f . Compared to C-TIGA process the P-TIGA process introduces relatively higher compressive stresses at the modified zone.

6.8 Dry sliding wear behavior of TIGA processed AISI 8620 steel plates

This section presents the effect of single pass and multi-pass C-TIGA and P-TIGA processes on the tribological behavior of surface of AISI 8620 steel modified at optimized parameters. Wear studies using a pin-on-disc tests were carried out at a constant load and sliding speed. The variation in coefficient of friction and wear rate was analyzed with respect to different C-TIGA and P-TIGA parameters. Wear surface is also analyzed to study the wear mechanism of the modified matrix. In this regards the volume loss, specific wear rate and average coefficient of friction (COF) of base material are found as 2.56 mm^3 , $2.75 \times 10^{-5} \text{ mm}^3\text{N}^{-1}\text{m}^{-1}$ and 0.65 ± 0.04 respectively, which are considered as a base to improve the wear properties of the substrate by its surface modification.

6.8.1 Effect of C-TIGA process on dry sliding wear

6.8.1.1 Effect of C-TIGA process on wear behavior of modified AISI 8620 steel

The variation of volume loss at a constant load and sliding speed of 20 N and 2.55 m/s respectively for varying C-TIGA parameters is shown in Fig. 6.64. It is observed that the volume loss gradually increases up to sliding distance of 5500 m. However, with the decrease of arcing current from 170 to 100A, the volume loss decreases. The drop of volume loss may have attributed to the increase in hardness of the substrate due to hard phase transformation in the matrix by increased cooling rate at low arcing current as discussed earlier. The similar effect of hardness on volume loss was observed by Tyagi et al., 2002. They claimed that the wear volume of the metal reduces with the increase of martensite fraction in the low alloy steel. The figure also shows that the volume loss of the base materials is higher than that of the C-TIGA processed surface of AISI 8620 steel, which may be attributed to relatively lower hardness of the base metal. Further it is observed that at a given arcing parameters volume loss of the multi-pass treated surface is higher than that of the single pass treated surface. This may have happened due to the reduction of hardness by tempering of the matrix.

Similarly the variation of specific wear rate at a constant load and sliding speed of 20 N and 2.55 m/s respectively with varying C-TIGA parameters are shown in Fig. 6.65. The figure shows that with the increase of arc current the specific wear rate increases due to reduction in cooling rate by increasing the fusion pool size which reduces the hardness of the modified zone as discussed earlier. Further observations from the figure depict that the wear rate of the modified zone of multi-pass C-TIGA process is lower than the wear rate of single pass C-TIGA processed sample prepared at the same arcing current. This is attributed to the effect of tempering on the hardness of the modified zone. The effect of C-TIGA parameters on the hardness of the modified zone is given in detail in section 6.5. The lowering of hardness with

the increase of arc current finally increases the wear rate of the modified zone. In this regards the influence of hardness on the wear rate is addressed by Archard's equation [Archard, 1953]:

$$Q = kW/H$$

Where Q is wear volume per unit sliding distance; k is the wear coefficient; W is the applied load and H is the hardness of the faying surface.

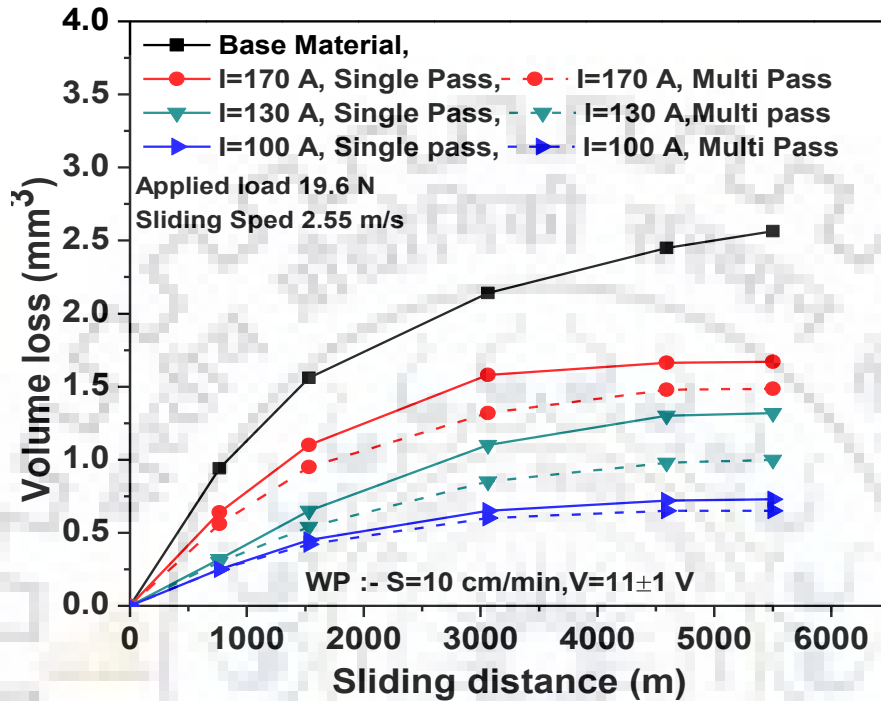


Fig. 6.62 Effect of C-TIGA process on volume loss of the modified surface.

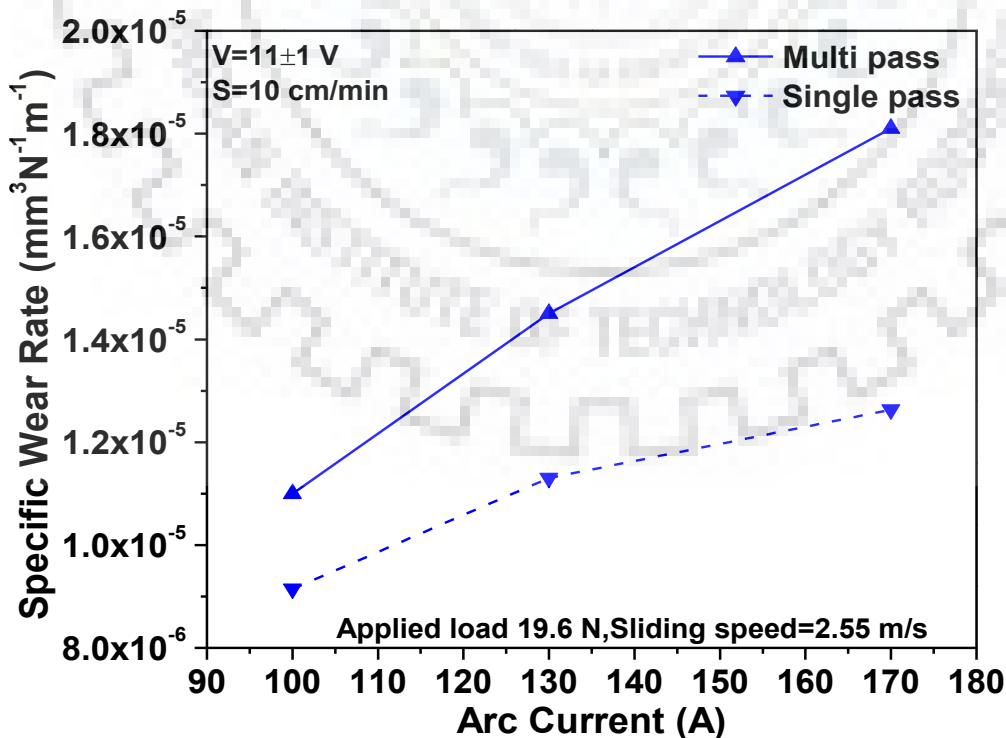


Fig. 6.63 Effect of C-TIGA process at different arcing current on wear rate of the modified surface.

6.8.1.2 Effect of C-TIGA process on Coefficient of friction (COF) of modified AISI 8620 steel

The average coefficient of friction (COF) at a constant load and sliding speed of 20 N and 2.5 m/s respectively under varying C-TIGA parameter (arcing current) is shown in Fig. 6.66. The figure shows that the increase of arc current from 100 to 170 A, enhances the average COF in case of both the single pass and multi-pass C-TIGA process. The figure further depicts that at a given arc current the modified surface produced by the multi-pass C-TIGA process gives relatively more COF as compared to that observed in case of using the single pass C-TIGA process. The coefficient of friction primarily depends upon the deformation of the surface asperities, adhesion of the flat regions of the sliding surfaces and ploughing of the sliding surfaces by wear particle and hard asperities. Due to increase of matrix hardness under the C-TIGA processing, the asperities became harder and are not easily worn out resulting in lower COF value which is reflected in the figure. It is already discussed in the previous chapters that the increase of arc current reduces hardness of the substrate surface due to decrease in cooling rate. However, the C-TIGA processed surface primarily consists of lath martensite structure which is a relatively harder phase. The increase of arc current reduces the fraction of martensitic phase in the matrix. Due to which the COF increases with the increase of arc current.

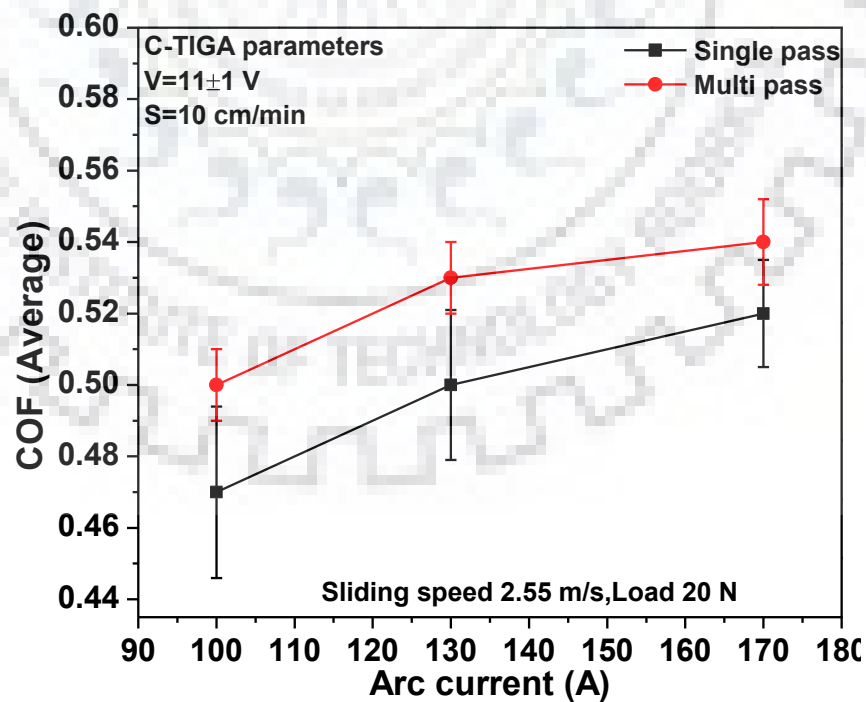


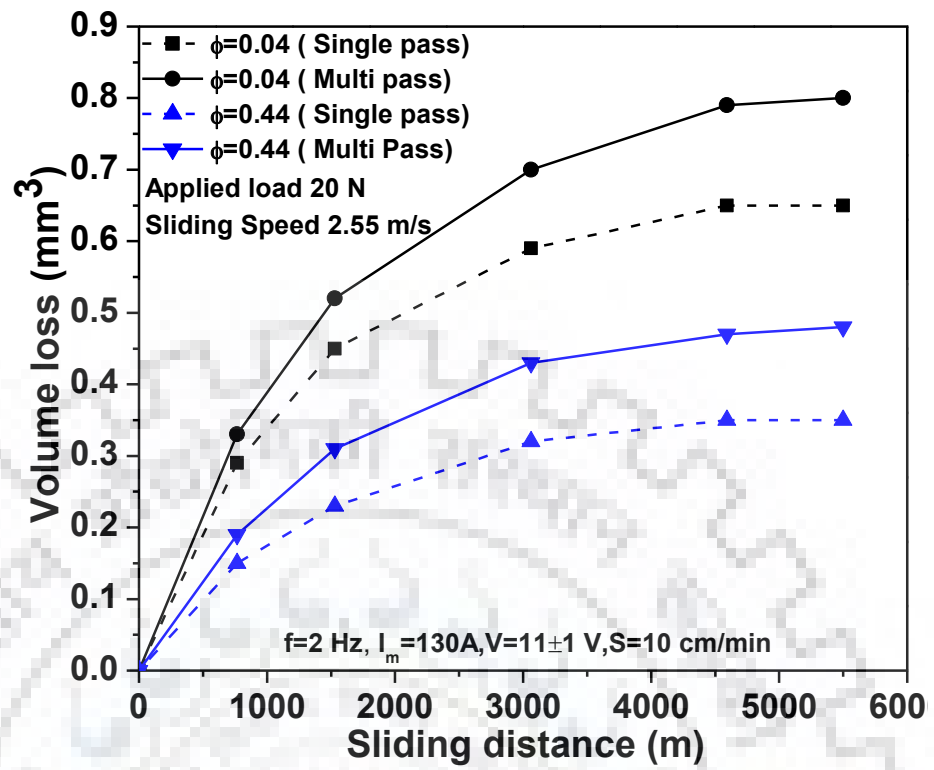
Fig. 6.64 Effect of arc current on the COF of the modified C-TIGA processes substrate surface.

6.8.2 Effect of P-TIGA process on dry sliding wear

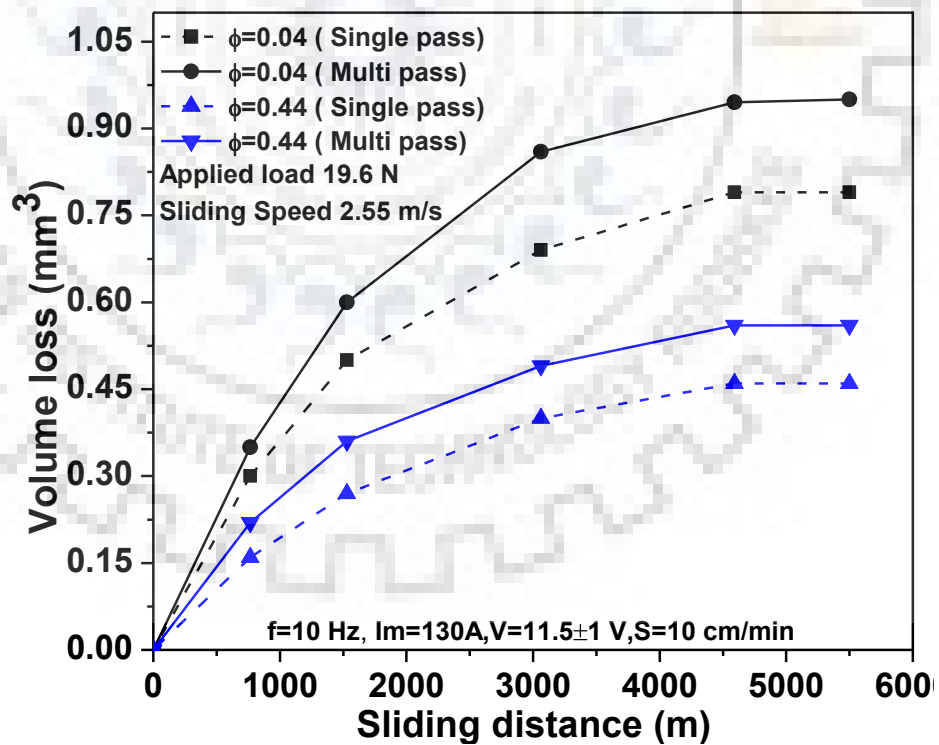
6.8.2.1 Effect of P-TIGA process on wear behavior of AISI 8620 steel

The variation of volume loss at a constant load and sliding speed of 20 N and 2.55 m/s respectively for varying P-TIGA parameters at the I_m of 130 and 170 A are shown in Fig. 6.67 (a and b) and Fig. 6.68 (a and b) respectively. Similar to C-TIGA process it is observed from the figure that in P-TIGA process the volume loss gradually increases up to sliding distance of 5500 m in both the I_m of 130 and 170 A. It is further observed that at a given f and I_m , the increase of ϕ from 0.04 to 0.44 reduces the volume loss for both the single pass and multi pass treated substrate surface. The drop of volume loss can be attributed to the increase in hardness of the substrate due to decrease in ϕ by reducing fusion zone size that results an increase of cooling rate (section 6.5). Similarly, at a given ϕ the variation of pulse frequency from 2 to 10 Hz increases the volume loss for both of the C-TIGA and P-TIGA processes. This is attributed to increase in heat buildup into the material by increasing the f resulting reduction in cooling rate. The reason behind the increase in hardness has been discussed in details in previous sections. Further observations from the figure depict that the volume loss of the multi-pass treated sample is relatively higher than the single pass treated surface at the given pulse parameters which may be attributed to the reduction of hardness due to tempering of phases in the matrix.

Similarly the variation of specific wear rate at a constant load and sliding speed of 20 N and 2.55 m/s respectively for varying P-TIGA parameters at the pulse frequencies of 2 and 10 Hz are shown in Figs. 6.69 (a and b) respectively where the I_m is kept constant at 130 A. The figures show that with the increase of ϕ the specific wear rate decreases due to reduction in fusion pool size resulting enhancement of cooling rate at the given I_m . The increase of cooling rate increases the hardness of the matrix by increasing the fraction of martensite in it. The figure further depicts that wear rate of the modified zone for multi-pass P-TIGA process is lower than the wear rate of single pass C-TIGA processed sample at the given I_m and f which is attributed to the effect of tempering on the hardness of the modified zone. The increased pulse frequency from 2 to 10 Hz increases the heat buildup into the substrate by reducing interruption of energy. The increase of f reduces the cooling rate which is described in detail in section 6.5.2. So increase in f reduces the cooling rate which increases the specific wear rate at the given I_m . In this regards the influence of hardness on the wear rate is addressed by Archard's equation as given above to understand the effect of hardness with respect to cooling rate and phase transformation.

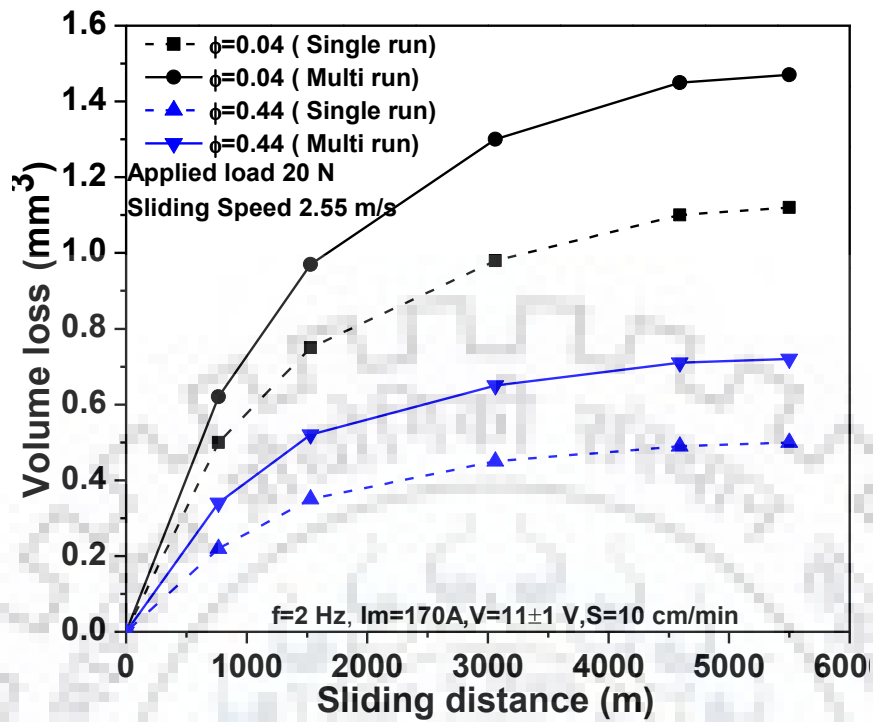


(a)

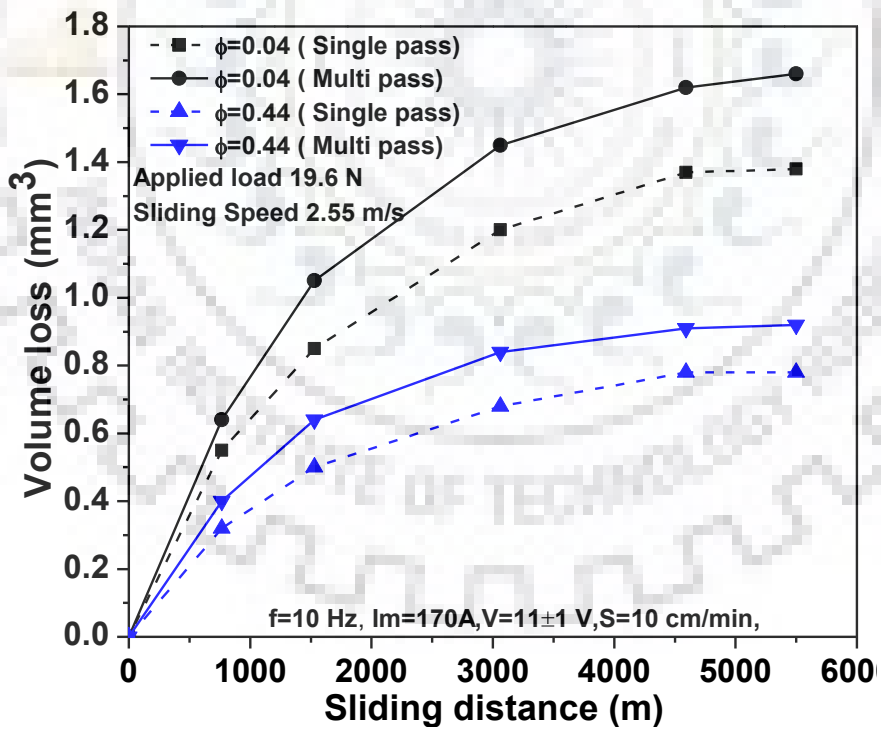


(b)

Fig. 6.65 Effect of ϕ on volume loss by Single pass and Multi pass P-TIGA process at the f of (a) 2 and (b) 10 Hz where the I_m is 130 A.

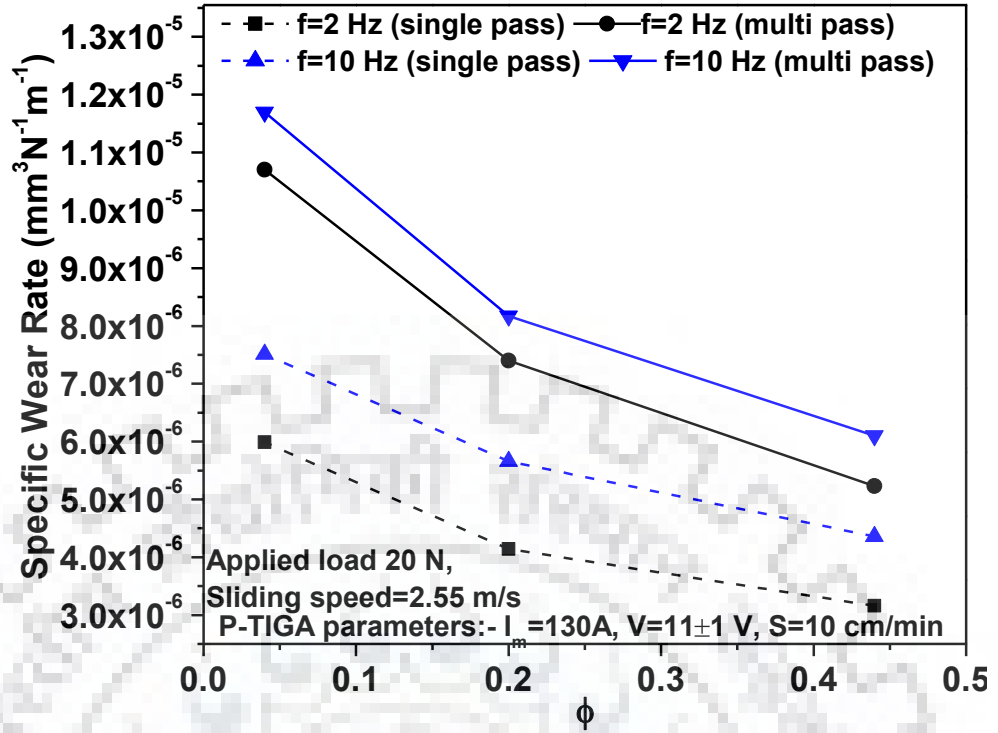


(a)

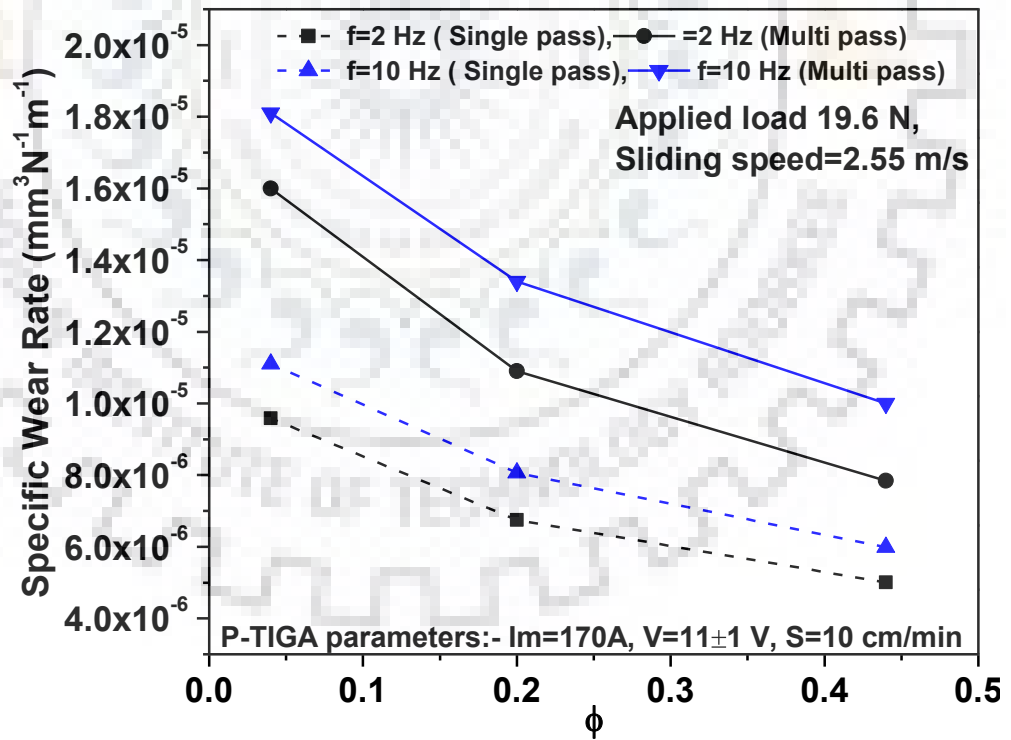


(b)

Fig. 6.66 Effect of ϕ on volume loss by Single pass and Multi pass P-TIGA process at the f of (a) 2 and (b) 10 Hz where the I_m is 170 A.



(a)



(b)

Fig. 6.67 Effect of ϕ on Specific wear rate during Single pass and Multi pass P-TIGA process at f of (a) 2 and (b) 10 Hz with $I_m=130\text{ A}$.

6.8.2.2 Effect of P-TIGA process on Coefficient of friction (COF)

The average coefficient of friction (COF) at a constant load and sliding speed of 20 N and 2.55 m/s respectively for varying P-TIGA parameters (I_m , f and ϕ) are shown in Fig. 6.70. The figure shows that the increase in ϕ from 0.04 to 0.44 decreases the average COF of both the single pass and multi-pass P-TIGA processes at a given I_m and f . Further the figure depicts that at a given ϕ and I_m there is an increase of COF in both the cases of single pass and multi pass P-TIGA processed surface with the increase of f from 2 to 10 Hz. The increase in hardness plays an important role in decreasing COF because the asperities became harder and are not easily worn out. The effect of P-TIGA parameters on hardness of the modified zone is already stated in the sections 6.5 and 6.6 respectively.

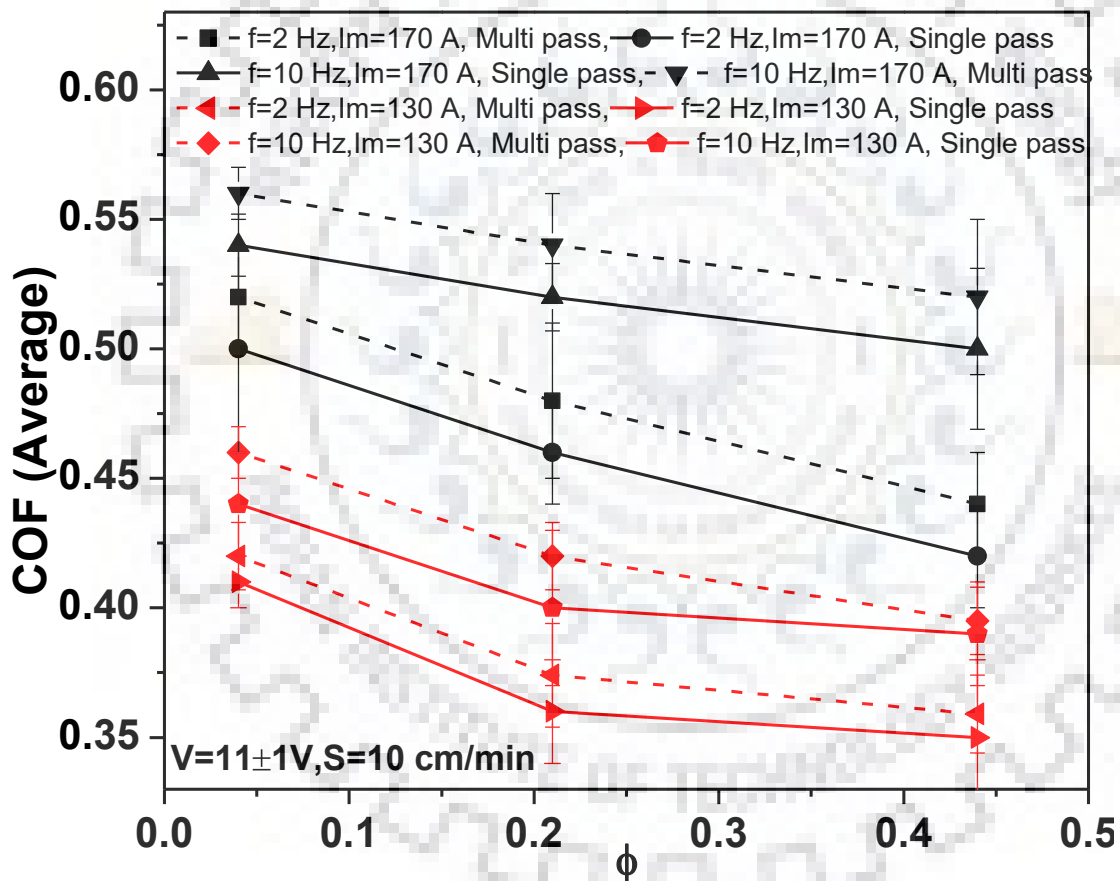


Fig. 6.68 Effect of P-TIGA parameters on the COF of the modified P-TIGA processes substrate surface.

6.8.3 Wear mechanism

The wear behavior of metallic materials is largely governed by the phase transformation, residual stresses and hardness of the substrate surface. The studies reveal that the TIGA hardened samples exhibit lower wear rate than that of the as received samples. It is

observed from the Figs. 6.64, 6.67 and 6.68 that the wear volume loss increases with the increase of sliding distance. The surface of the engineering component exhibit asperities. During the relative motion between the two bodies the asperities makes contact to each other and the surfaces evolve to better conformity to each other. An initial relatively rapid wear occurs by the removal of initial asperities, initial oxide layers and surface contaminants of the matrix. At the beginning of the test the oxidation of the faying surface starts and progresses with frictional heating started by sliding. This oxide layer further prevents the wear and thus reduces the wear loss and rate of wear. Thus, wear volume is relatively high in the starting stage as compared to that of the later stage.

Similarly, the wear rate increases with the increase of arc current in C-TIGA parameters and decreases with the increase of ϕ and reduction of f in case of P-TIGA process. The wear rate primarily depends upon the fraction of lath martensite present in the modified substrate matrix. A lower wear rate at a constant load may be explained primarily on the basis of the hardness imparted by incorporation of martensite phase in the modified zone. The effect of martensitic % on the wear rate is well explained by the Tyagi et al., 2002. They reported that the wear rate is directly proportional to the real area of contact and the steel containing higher amount of martensite is able to show a lower wear rate. The other factor contributing to the observed behavior of wear rate may be the extent of transfer oxide layer and the nature of adhesion of the compacted transfer layer to the pin surface. Similarly the decrease in wear coefficient may be attributed to the decreasing wear rate domination over the decrease in real area of contact due to increasing hardness. It is well known that the wear of materials occurs when one or both surfaces are in relative motion to one another. Wear is propagated by means of mechanical and chemical effects followed by frictional heating. So the wear mechanism may be broadly classified into adhesive, abrasive followed by oxidizing.

6.8.4 The SEM analysis of wear surfaces

The SEM analysis of wear surfaces formed during the dry sliding provides an important tool to disseminate the wear behavior of the steels more accurately. The Figs 6.71, 6.72 and 6.73 show the SEM micrographs of the worn surfaces of as received base material and the C-TIGA and P-TIGA processed base metal respectively. When the asperities of the pin material came in contact of the asperities of disc material, the material of the pin is detached from the pin in the form of wear debris. The wear debris act as hard grit particles in between the surface which slides as well as roll and create further abrasion of the base material. The increase in hardness causes rapid formation of oxide layer, which prevents further wear of the material and also reduces the coefficient of friction. The Fig. 6.71 shows the worn surface of the as-received

base material which shows the delamination of the surface due to lower hardness. Micro cracks are also observed in the worn surface of the pin material due to wear. The relatively low hardness of the base material causes the slow formation of oxide layer in the base material resulting a higher volume loss, wear rate and coefficient of friction. Similarly, the Fig. 6.72 (a and b) shows the worn surfaces of the single pass and multi pass C-TIGA processed surface produced at an arc current of 130 and 170 A respectively. The figs. 6.72 (a(i) and b(i)) shows the formation of oxide layer over the pin material which reduces the volume loss, wear rate and COF in single pass C-TIGA processed sample. However, in case of multi-pass C-TIGA process (Figs. 6.72 (a(ii) and b(ii)) the oxide layer forms in the substrate surface but due to comparatively lower hardness it may have broken by debris particles resulting a little increment in the volume loss, wear rate and COF.

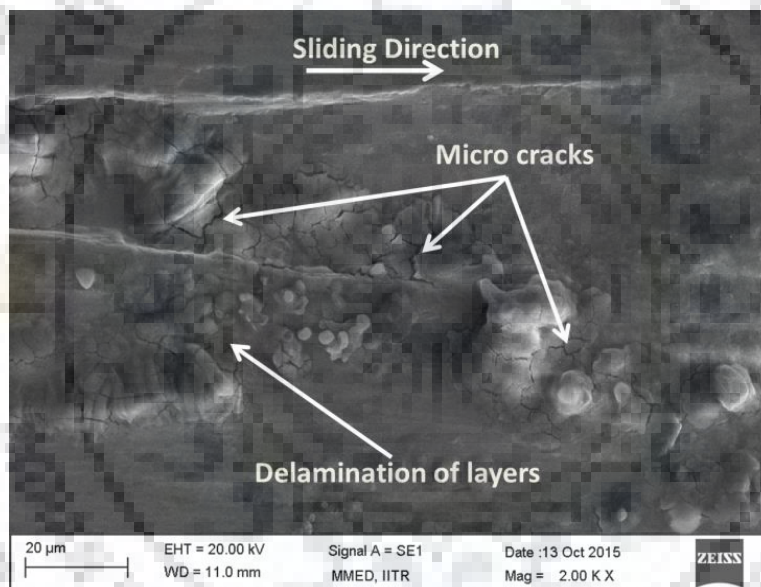
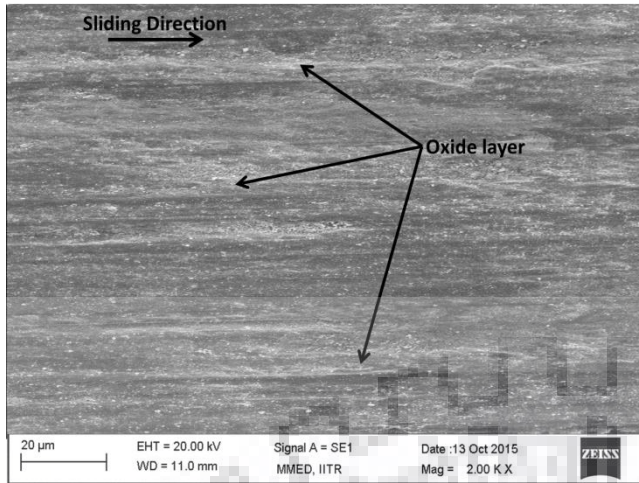
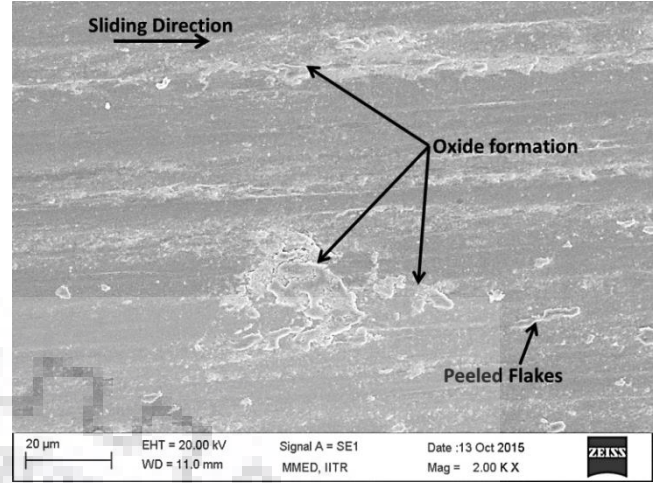


Fig. 6.69 The SEM Micrograph of as received base metal.

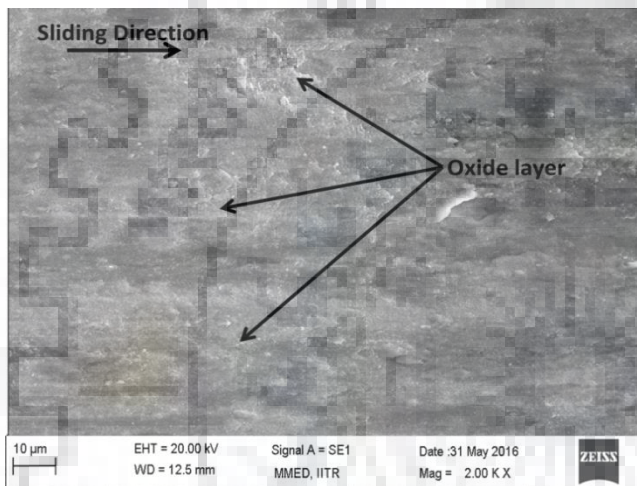
The Fig. 6.73 (a and b) presents the SEM micrographs of the single pass and multi pass P-TIGA processed surface at the varied ϕ of 0.04 and 0.44, whereas the f and I_m are kept as 2 Hz and 130 A respectively. It is observed from the figures that the increase of ϕ from 0.04 to 0.44 generates oxide layer over both the single pass and multi pass P-TIGA processed surface. This oxide layer protects the surface from further wear and reduces wear rate, wear volume and COF. However in case of the multi-pass P-TIGA process (Fig. 6.73 a(ii) and b(ii)) the oxide layer brakes from certain places which relatively increases the wear rate, wear volume and COF. So the wear of AISI 8620 is primarily regulated by the adhesive, abrasive and then followed by oxidizing wears mechanism.



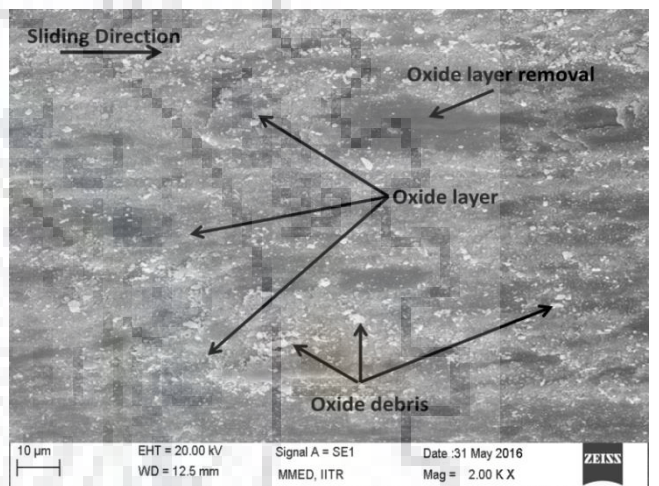
a(i)



a(ii)

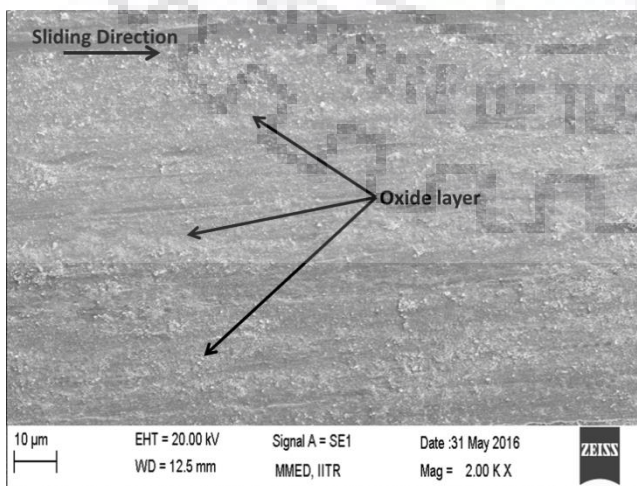


b(i)

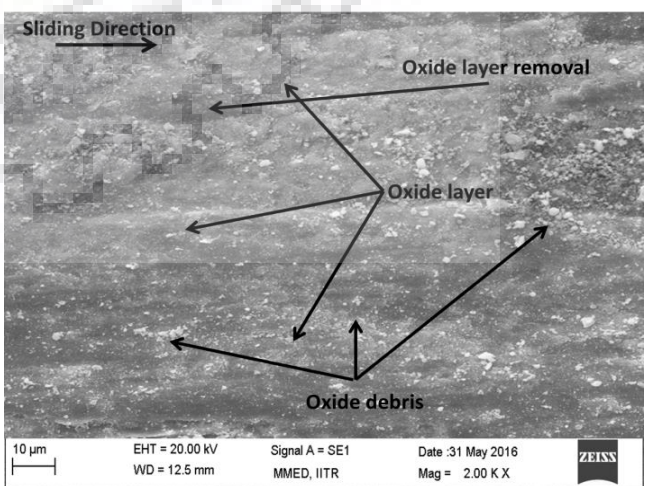


b(ii)

Fig. 6.70 The SEM micrographs of worn surfaces of the substrate modified by the single and multi-pass C-TIGA processes operated at the arc current of (a) 130 A and (b) 170 A.



a(i)



a(ii)

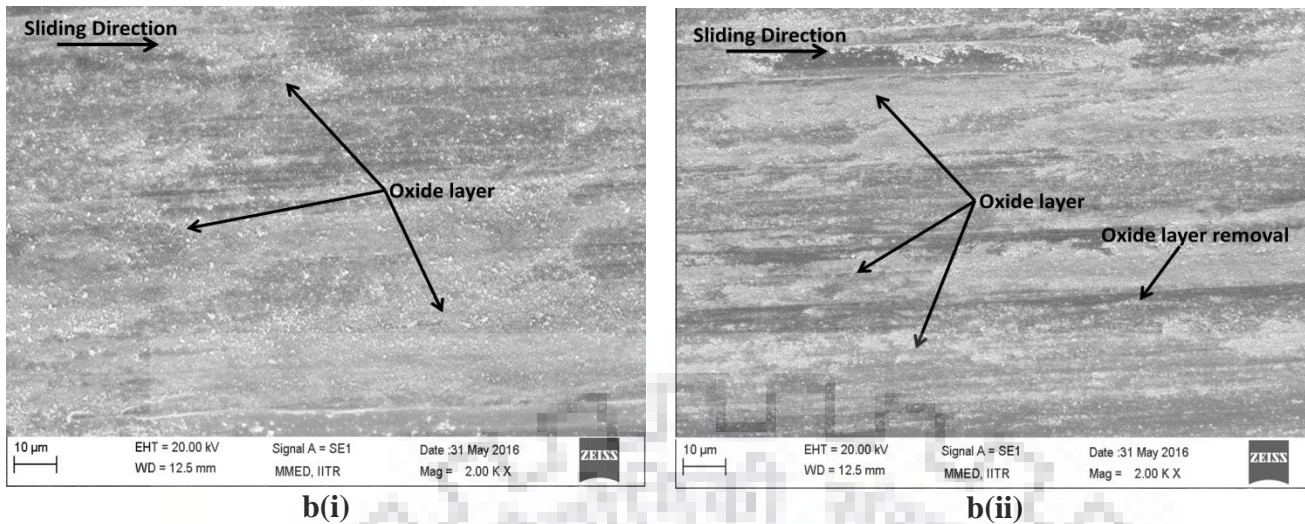


Fig. 6.71 The SEM micrographs of worn surfaces of the substrate modified by single and multi-pass P-TIGA operated at the ϕ of (a) 0.04 and (b) 0.44 while I_m and f are 170 A and 2 Hz respectively.

6.8.5 Summary

The C-TIGA and P-TIGA processes are successfully used to modify the surface properties in terms of the wear and frictional properties. The effect of hardness rise is clearly reflected in the improvement of wear volume, wear rate and coefficient of friction resulting in reduction of volume loss under dry sliding process. The use of TIGA process successfully reduces the wear rate and the average coefficient of friction as compared to those of the as received AISI 8620 steel base material. The average reduction of wear rate is found as $50 \pm 10\%$ during processing at optimum TIGA parameters. The microstructure modification of the surface, generation of residual compressive stresses over the surface and hardness increment play the primary role in improving wear resistance. Finally as compared to C-TIGA process, the P-TIGA process has been found more effective to produce a modified surface having lower wear rate and average COF.

CHAPTER 7

CONCLUSIONS

The specific observations made from different facets of the present work have already been given in the corresponding chapters. The final generic conclusions drawn from the present work can be summarized as follows.

1. The TIG arcing has been found as a significantly effective process which can be successfully used for surface modification of bearing steel (AISI 8620) in order to produce the bearing components satisfying the minimum requirement of properties as per the ASTM standards. Further the TIGA process has the ability to produce superior properties in case hardenable bearing components to those are currently available in the commercial market just by controlled phase transformation in the matrix without any alloying or mass deposition on the surface.
2. The surface modification of AISI 8620 steel can be done by continuous tungsten inert gas arcing (C-TIGA) and pulse tungsten inert gas arcing (P-TIGA) arcing processes. However out of these two processes P-TIGA process has been found much more efficient and beneficial to produce the best combination of surface properties in AISI 8620 steel. The geometric characteristics (Bead width and Depth of penetration) of P-TIGA processed surface is found $40\pm 15\%$ more than C-TIGA processed substrate surface with reduction in HAZ width around $20\pm 5\%$ at the same parameters.
3. Surface properties of the base material is primarily governed by the isotherm and thermal cycle created by the use of TIGA process parameters which are found to be more precisely controlled under P-TIGA process. This is because of it has availability of more number of controlling parameters than the C-TIGA process, affecting the thermal characteristics of the modified zone.
4. It is established that summarized influence of pulse parameters define by the hypothetically established dimensionless factor ϕ , can be effectively used to control the thermal characteristics resulting desired phase transformation and properties in the fusion modified zone and its HAZ in the AISI 8620 steel. The proper control of ϕ makes superior change in thermal characteristics and properties of bearing steel as compared to C-TIGA process parameters at the same Ω and arc current.

5. In order to determine the necessary control of parameters to achieve desired properties and thermal characteristics, a thermal model is established and justified by experimental verification as a guide to govern and control the arcing parameters to achieve desired phase transformation and properties in the modified zone.
6. The hardness of the modified zone as compared to base metal increases up to 127 ± 20 % and 77 ± 25 % respectively for the P-TIGA and C-TIGA processes respectively. However at the same arc current and Ω the P-TIGA process increases the hardness of the modified zone more than 20 ± 10 % as compared to that obtained in case of the C-TIGA process. The hardness of the modified zone using multi-pass TIGA process is reduced up to 5 ± 2 % due to the effect of tempering as compared to single pass TIGA process. Similarly, the hardness and width of the stabilized zone found 15 ± 3 % more in P-TIGA process as compared to C-TIGA process at the same arc current.
7. The single and multi-pass C-TIGA and P-TIGA processes, introduces residual compressive stresses over the modified zone. In C-TIGA process the increase in arc current reduces the compressive stresses over the surface. Similarly, in P-TIGA process the increase in ϕ increases the compressive residual stresses in the modified zone of single and multi-pass mode at the given pulse parameters. As compared to the C-TIGA process the P-TIGA produces relatively higher compressive stresses over the surface.
8. The use of C-TIGA and P-TIGA process successfully reduces the wear rate and the average coefficient of friction as compared to that of the as received base material. The average reduction of wear rate is found as 50 ± 10 %, depending upon the TIGA parameters. The microstructure modification of the surface, generation of residual compressive stresses over the surface and hardness increment are the key factors for improving wear resistance. Finally as compared to the C-TIGA process, the P-TIGA process has been found to give significantly lower wear rate (about 30 %) and COF about 20 ± 5 .
9. It may be concluded that the both C-TIGA and P-TIGA processes are suitable for surface modification of AISI 8620 steel for industrial application in terms of achieving significantly high surface hardness and high depth of required modified zone along with high compressive stresses and better wear resistance of the matrix. However in this regard the P-TIGA process is found superior to the C-TIGA process in terms of higher depth of modified zone, lower HAZ width, higher hardness, higher compressive stresses and higher wear resistance.

10. The variation of ϕ from 0.04 to 0.44 in P-TIGA process at the optimized mean current of 130 A gives the superior properties in terms of high hardness, wear resistance and high compressive stresses over the substrate surface.
11. For industrial application, multi pass TIG arcing process is applied over the surface which significantly increases the surface characteristics. However, some reduction in properties is found due to tempering of modified zone which are acceptable under the requirement of bearing properties as per the ASTM standards





SCOPE FOR FUTURE WORK

In light of the understanding on the work presented in this report, it is realised that following aspects of studies have to be carried out further to improve the reliability and performance of modified surface by TIGA process.

1. Fatigue and fracture analysis of the modified surface should be tried, in order to understand the effect of the TIGA process on the performance of modified materials surface.
2. The effect of TIGA process should be tried for other materials like aluminium, magnesium and titanium etc. to better utilization of the process.
3. The distortion analysis should be performed in order to understand the effect of TIGA process because the process creates high residual stresses over the surface.
4. The TIGA process can be used for alloying the nano particle over the substrate surface to increase the surface properties of the materials.
5. The wear analysis may be tried at different loads and sliding speeds to understand the detailed analysis of the wear mechanism.
6. TEM analysis may be performed to understand the phase transformation in detail.



REFERENCES

1. **Andrés A.**, Cardona A., Risso J. and Víctor D. F., [2011], “Finite element modeling of welding processes.”, *Applied Mathematical Modelling*, Vol. 35 (2), pp. 688–707.
2. **Apple C.A.** and Krauss G., [1973], “Microcracking and fatigue in a carburized steel.”, *Metallurgical Transactions A*, Vol. 4 (5), pp. 1195–1200.
3. **Arivarasu, M.**, Devendranath R., K., and Arivazhagan, N., [2014], “Comparative studies of high and low frequency pulsing on the aspect ratio of weld bead in gas tungsten arc welded AISI 304L Plates.”, *Procedia Eng.* 97, pp. 871–880.
4. **Arthur E.K.**, Ampaw E., Kana M.G.Z., Akinluwade K.J., Adetunji A. R. and Adewoye O.O., [2015], “Indentation size effects in pack carbo-nitrided AISI 8620 steels”, *Mater. Sci. Eng. A.*, Vol. 644, pp. 347–357.
5. **Asi, O.**, Can, A.Ç., Pineault, J., Belassel, M., [2007], “The relationship between case depth and bending fatigue strength of gas carburized SAE 8620 steel.”, *Surf. Coatings Technol.*, Vol. 201, pp. 5979–5987.
6. **Atamert, S.** and Bhadeshia, H. K. D. H., [1989], “Comparison of the microstructures and abrasive wear properties of stellite hardfacing alloys deposited by arc welding and laser cladding.”, *Metall Trans. A*, Vol. 20 (6), pp. 1037–1054.
7. **Bakshi, S.R.** and Harimkar S.P., [2015] “Surface Engineering for Extreme Conditions.”, *JOM*, Vol. 67, pp. 1526-1527.
8. **Balasubramanian, V.**, Ravisankar, V. and Reddy, M. G., [2008], “Effect of pulsed current welding on fatigue behaviour of high strength aluminium alloy joints.”, *Mater. Des.*, Vol. 29, pp. 492–500.
9. **Bardelcik, A.**, Salisbury, C.P., Winkler, S., Wells, M.A. and Worswick, M.J., [2010], “Effect of cooling rate on the high strain rate properties of boron steel.”, *Int. J. Impact Eng.*, Vol. 37, pp. 694–702.
10. **Barkoula, N.M.**, Alcock, B., Cabrera, N.O., Peijs, T., [2008], “Fatigue properties of highly oriented polypropylene tapes and all-polypropylene composites.”, *Polym. Polym. Compos.*, Vol. 16, pp. 101–113.
11. **Batahgy A. M.**, Ramadan, R.A. and Moussa, A., [2013], “Laser Surface Hardening of Tool Steels- Experimental and Numerical Analysis.” *J. S. Engg. Mat. Ad. Tech.*, Vol. 3 (02), pp. 146–153.
12. **Béjar, M.A.** and Henríquez, R., [2009], “Surface hardening of steel by plasma-electrolysis boronizing.”, *Mater. Des.* 30, pp. 1726–1728.

13. **Bochnowski, W.**, [2010], “The influence of the arc plasma treatment on the structure and microhardness C120U carbon tool steel.”, Vol. 10, pp. 331–334.
14. **Boiko V. I.**, Valyaev A.N., Pogrebnyak A. D. and Uspekhi F. N., [1999], “Metal modification by high-power pulsed particle beams.”, Vol.169 (11), pp. 1243-1248.
15. **Briant, C.L.**, [1981], “The effect of nickel, chromium, and manganese on phosphorus segregation in low alloy steels.” Scripta Metallurgica, Vol. 15(9), pp. 1013-1018.
16. **Bugaev S.P.**, Korovin S.D., Koval N.N., Oks E.M., Proskurovsky D.I. and Sochugov N.S., [2002], “Intense low-energy electron and ion beams and their application. Conference Record of the Twenty-Fifth International Power Modulator Symposium”, High-Voltage Workshop., pp. 548-55.
17. **Calik, A.**, Duzgun, A., Ekinici, A.E., Karakas, S and Ucar, N., [2009], “Comparison of hardness and wear behaviour of boronized and carburized AISI 8620 steels.”, Acta Phys. Pol. A, Vol. 116, pp. 1029–1032.
18. **Calik A.**, [2009], “Effect of cooling rate on hardness and microstructure of AISI 1020 , AISI 1040 and AISI 1060 Steels.”, Int. J. Phys. Sci., Vol. 4, pp. 514–518.
19. **Cary, H.B.**, [1995], “Arc Welding Automation.”, 1st Edn., CRC Press, New York., ISBN: 10: 0824796454, pp: 325.
20. **Chatterjee, A.**, Moitra, A., Bhaduri, A.K., **Chakrabarti, D.**, Mitra, R., [2014], “Effect of heat treatment on ductile-brittle transition behaviour of 9Cr-1Mo steel.”, Procedia Eng. Vol. 86, pp. 287–294.
21. Chatterjee, S., **Pal, T.K.**, [2003], “Wear behaviour of hardfacing deposits on cast iron.”, Wear, Vol. 255, pp. 417–425.
22. Chatterjee, S. and **Pal, T.K.**, [2006], “Solid particle erosion behaviour of hardfacing deposits on cast iron-Influence of deposit microstructure and erodent particles.”, Wear, Vol. 261, pp. 1069–1079.
23. **Chen, S.B.**, Lou, Y. J., WU L. and Zhao, D. B., [2000], “ Intelligent Methodology for Sensing , Modeling and Control of Pulsed GTAW : Part 1 Bead on plate welding.”, Welding research supplement, pp. 151s–163s.
24. **Chiumenti M.**, Miguel C., Salmi A., Carlos A., Narges D. and Kazumi M., [2010] “Finite element modeling of multi-pass welding and shaped metal deposition processes.”, Computer Methods in Applied Mechanics and Engineering, Vol. 199, pp. 2343-2359.
25. **Clare, A.**, Oyelola, O., Folkes, J. and Farayibi, P., [2012], “Laser cladding for railway repair and preventative maintenance.”, J. Laser Appl., Vol. 24 (3), pp. 032404-32414.

26. **Collins J.A.**, [1993], “Failure of Materials in Mechanical Design: Analysis, Prediction, Prevention.”, 2nd ed. New York: John Wiley & Sons.
27. **Cook, G.E.** and Hussam, E. D., [1985], “The Effect of high-Frequency pulsing of a welding arc.”, IEEE trans. Ind. App., Vol 1A-21 (5), pp. 1294–1299.
28. **David A. P.**, Easterling, K.E and Sherif, M., [2009], “Phase Transformations in Metals and Alloys.”, CRC Press, London,
29. **Davis C.L.** and King J.E., [1993], “Effect of cooling rate on intercritically reheated microstructure and toughness in high strength low alloy steel.”, Mater. Sci. Technol., Vol. 9, pp. 8–15.
30. **Damborenea, D. J.**, [1998], “Surface modification of metals by high power lasers.”, Surf. Coatings Technol., Vol. 100-101, pp. 377–382.
31. **De, A.** and DebRoy T., [2011], “A perspective on residual stresses in welding. Sci. Technol.” Weld. Join., Vol. 16, pp. 204–208.
32. **De A.**, Walsh C., Maiti S.K. and Bhadeshia H.K.D.H., [2003], “Prediction of cooling rate and microstructure in laser spot welds, Sci. Technol.”, Weld. Join., Vol. 8, pp. 391–399.
33. **Dieter, G.E.**, [1988], “Mechanical Metallurgy”, *McGraw-Hill book company*, UK.
34. **Dieter, R.**, [1992], “Heat Effects of Welding: Temperature Field, Residual Stress, Distortion”, Springer-verlag, Newyork.
35. **Durgutlu, A.**, [2004], “Experimental investigation of the effect of hydrogen in argon as a shielding gas on TIG welding of austenitic stainless steel.”, Mater. Des., Vol. 25, pp. 19–23.
36. **Dziedzic, A.** and Bylica A, [2008], “The microstructure of HS 6-5-2 steel in the areas overlapping remelting obtained by the use of GTAW method.”, Vol. 8, pp. 47–52.
37. **Edmund I.**, [2009], “Cutting Data for Turning of Steel”, Industrial Press Inc., Newyork
38. **Erdogan M.** and Tekeli S., [2002], “The effect of martensite particle size on tensile fracture of surface-carburised AISI 8620 steel with dual phase core microstructure.”, Mater. Des., Vol. 23, pp. 597–604.
39. **Fan, F.G** and Kovacevic. R., [2004], “A unified model of transport phenomena in gas metal arc welding including electrode, arc plasma and molten pool”, *Journal of Physics D: Applied Physics*, Vol. 37, pp 2531–2544.
40. **Fan H.G.**, Shi Y.W. and Na S.J. [1997], “Numerical analysis of the arc in pulsed current gas tungsten arc welding using a boundary-fitted coordinate.” *Journal of Materials Processing Technology*, Vol. 72, pp. 437-445.

41. **Farahani, E.**, Shamanian, M. and Ashrafizadeh, F., [2012], “A Comparative Study on Direct and Pulsed Current Gas Tungsten Arc Welding of Alloy 617.”, *Int. J. on Manufacturing and Material Science*, Vol. 2(1), pp. 1–6.
42. **Farfan S.**, Rubio-Gonzalez C., Cervantes-Hernandez T. and Mesmacque G., [2004] “High Cycle Fatigue, Low Cycle Fatigue and Failure Modes of a Carburized Steel. *Intl. J. Fatigue*” Vol. 26(6),pp. 673–678.
43. **Franjo C**, Darko L. and Vojteh L., [2010], “Surface Modifications of Maraging Steels used in the Manufacture of moulds and dies.”, *Materials and Technology*, Vol. 44, pp. 85–91.
44. **Ghosh, P.K.**, [2017], “Pulse Current Gas Metal Arc Welding- *Materials Forming, Machining and Tribology*”, Springer Singapore,
45. **Ghosh, P.K.** and Kumar, R., [2015], “Surface Modification of Micro-Alloyed High-Strength Low-Alloy Steel by Controlled TIG Arcing Process.”, *Metall. Mater. Trans. A*, Vol. 46, pp. 831–842.
46. **Ghosh, P.K.** and Dorn, L., [1993], “Thermal behaviour of pulsed MIG Al-Zn-Mg weld – An analytical model analysis”, *International Journal on Joining of Materials*, Vol. 5(4), pp 143-150.
47. **Ghosh, P.K.** and Rai, B.K., [1998], "Correlations of pulse parameters and bead characteristics in pulsed current flux cored GMAW process", *Indian Welding Journal*, Vol. 31(4), pp.30-39.
48. **Ghosh, P.K.** and Sharma, V., [1991], “Weld bead chemistry and its characteristics in pulsed MIG welded Al-Zn-Mg alloy”, *Materials Transactions JIM*, Vol. 32(2), pp.145-150.
49. **Ghosh, P.K.**, [1996], “An analysis of weld characteristics as a function of pulse current MIG welding parameters”, *International Journal on Joining of Materials*, Vol. 8(4), pp. 157-161.
50. **Ghosh, P.K.**, Dorn, L., and Goecke, S.F. [2001], “Universality of co-relationships among pulse parameters for different MIG welding power sources“, *International Journal on Joining of Materials*, Vol. 13(2), pp. 40-47.
51. **Ghosh, P.K.**, Goyal, V. K., Dhiman, H.K., Kumar, M., [2006] “Thermal and metal transfer behaviour in pulsed current GMA weld deposition of Al-Mg alloy”, *Sci. Technol. Weld. Joining*, Vol. 11(2), pp. 232-42.

52. **Ghosh, P.K.**, Dorn, L., Hubner, M. and Goyal, V.K., [2007 (a)], “Arc characteristics and behaviour of metal transfer in pulsed current GMA welding of aluminium alloy”, *Journal of Materials Processing Technology*, Vol. 194, pp. 163-175.
53. **Ghosh, P.K.**, Kulkarni, S.G., Kumar, M. and Dhiman, H.K., [2007 (b)], “Pulsed current GMAW for superior weld quality of austenitic stainless steel sheet”, *ISIJ International*, Vol. 47(1), pp. 138–45.
54. **Ghosh, P.K.**, Dorn, L., Kulkarni, S. and Hoffmann, F., [2008], “Arc characteristics and behaviour of metal transfer in pulsed current GMA welding of stainless steel”, *Journal of Material Processing Technology*, Vol. 209, pp. 1262-1274.
55. **Goyal, V.K.**, Ghosh, P.K., Saini, J.S., [2008 (b)] “Analytical studies on thermal behaviour and geometry of weld pool in pulsed current gas metal arc welding”, *J. Met. Proc. Tech*, Vol. 209, pp. 1318-1336.
56. Grigoriants A. G., [1994], “Basics of Laser Material Processing”, CRC Press, Florida, pp. 150-160.
57. **Grum J.**, [2007], “Comparison of different techniques of laser surface hardening.”, *J. Achiev. Mater.*, Vol. 24, pp. 17–25.
58. **Grum J.** and Ferlan D., [1997], “Residual internal stresses after induction hardening and grinding.”, In: Proceedings of the 17th ASM Heat Treating Society Conference, Indianapolis, Indiana, 1997, pp 629–639.
59. **Grum, J.**, Božič, S. and Zupančič, M., [2001], “Influence of quenching process parameters on residual stresses in steels.”, *Metalurgija*, Vol. 40, pp. 0–13.
60. Guguloth, K., Sivaprasad, S., **Chakrabarti, D.** and Tarafder, S., [2014], “Low-cyclic fatigue behavior of modified 9Cr-1Mo steel at elevated temperature.”, *Mater. Sci. Eng. A*, Vol. 604, pp. 196–206.
61. **Guile, A. E.**, [1984], “Electric arcs: their electrode processes and engineering applications.”, *IEE Proc. A Phys. Sci. Meas. Instrumentation, Manag. Educ. Rev.*, Vol. 131(7), pp.450-480.
62. Häßler, M., Rose, S., **Füssel, U.**, Schneider, H.I. and Werner, C., [2014], “TIG narrow gap welding -new approaches to evaluate and improve the shielding gas coverage and the energy input.”, *Weld. World*, Vol. 59, pp. 71–76.
63. Hertel, M., **Füssel, U.** and Schnick, M., [2014], “Numerical simulation of the plasma-MIG process - Interactions of the arcs, droplet detachment and weld pool formation.”, *Weld. World*, Vol. 58, pp. 85–92.

64. **Hiroshi A.** and Mitsuyasu Y., [2003], “Simulation of surface temperature of metals irradiated by intense pulsed electron, ion and laser beams.”, *Surface and Coatings Technology*, Vol. 169-170, pp. 219-222.
65. **Inoue, T.**, Nagaki, S., Kishino, T. and Monkawa, M., [1981], “Description of transformation kinetics, heat conduction and elastic-plastic stress in the course of quenching and tempering of some steels.”, *Ingenieur-Archiv*, Vol. 50, pp. 315–327.
66. **Ivanov Y.F.**, Rotshtein V.P., Proskurovsky D.I., Orlov P.V., Polestchenko K.N., Ozur G.E. and Goncharenko I.M., [2000], “Pulsed electron-beam treatment of WC–TiC–Co hard-alloy cutting tools: wear resistance and microstructural evolution.”, *Surface and Coatings Technology*, Vol. 125:1-3, pp. 251-256.
67. **Ivanov Y.**, Matz W., Rotshtein V., Günzel R. and Shevchenko N., [2002], “Pulsed electron-beam melting of high-speed steel: structural phase transformations and wear resistance.”, *Surface and Coatings Technology*, Vol. 150:2-3, pp. 188-198.
68. **Kah, P.**, Martikainen, J., [2013], “Influence of shielding gases in the welding of metals.”, *Int. J. Adv. Manuf. Technol.*, Vol. 64, pp. 1411–1421.
69. **Kanchanomai C.** and Limtrakarn W., [2008], “Effect of Residual Stress on Fatigue Failure of Carbonitrided Low-Carbon Steel.” *Journal of Materials Engineering and Performance*, Vol. 17(6) , pp. 879–887.
70. **Karl-Erik T.**, [1984], “Steel and Its Heat Treatment”, Sec. editin, Oxford publication, Sweden.
71. Karmakar, A., Sahu, P., Neogy, S., **Chakrabarti, D.**, Mitra, R., Mukherjee, S., Kundu, S., [2017], “Effect of Cooling Rate and Chemical Composition on Microstructure and Properties of Naturally Cooled Vanadium-Microalloyed Steels.”, *Metall. Mater. Trans. A*, Vol. 48 (4), pp. 1–15.
72. **Khan, T.I.**, Rizvi, S.A. and Matsuura, K., [2000], “The effect on wear behaviour of H13 tool steel surfaces modified using a tungsten arc heat source.”, *Wear*, Vol. 244, pp. 154–164.
73. **Kim, W.H.** and Na, S.-J., [1998], “Heat and fluid flow in pulsed current GTA weld pool.”, *Int. J. Heat Mass Transf.*, Vol. 41, pp. 3213–3227.
74. **Kobasko, N.I.**, Totten, G.E.L and Canale, C.F., [2007], “Intensive Quenching:Improved Hardness and Residual Stress.”, *Heat Treatment of Metals*, Vol. 32 (5), pp. 84–89.
75. **Kobasko, N.I.**, [2010], “Stress State of Steel Parts During Intensive Quenching.” *ASTM International*.

76. **Korkut, M.H.**, Yilmaz, O. and Buytoz, S., [2002], “Effect of aging on the microstructure and toughness of the interface zone of a gas tungsten arc (GTA) synthesized Fe-Cr-Si-Mo-C coated low carbon steel.”, *Surf. Coatings Technol.*, Vol.157, pp. 5–13.
77. **Kobasko, N. I.**, [2012], “Steels of optimal chemical composition combined with intensive quenching.”, *Int. Heat Treat. Surf. Eng.*, Vol. 6, pp. 153–159.
78. **Kumar, A.** and Sundarrajan, S., [2009], “Optimization of pulsed TIG welding process parameters on mechanical properties of AA 5456 Aluminum alloy weldments.”, *Mater. Des.*, Vol. 30, pp. 1288–1297.
79. **Kumar P.**, Kolhe K. P. and Morey S. J, [2011], “Process Parameters Optimization of an Aluminium Alloy with Pulsed Gas Tungsten Arc Welding (GTAW) Using Gas Mixtures.”, *Mater. Sci. Appl.*, Vol. 2, pp. 251–257.
80. **Kikuchi S.**, Sasago A. and Komotori J., [2009], “Effect of simultaneous surface modification process on wear resistance of martensitic stainless steel.”, *Journal of Materials Processing Technology*, Vol. 209 (20), pp. 6156–6160.
81. **Kim W.H.** and Na S.J. [1998], “Heat and fluid flow in pulsed current GTA weld pool.”, *Heat and Mass Transfer*, Vol. 41, pp. 3213–3227
82. **Kobasko, N. I.** and Morganyuk V. S., [1985], “Numerical Study of Phase Changes, Current and Residual Stresses in Quenching Parts of Complex Configuration,” *Proceedings of the 4Th International Congress on Heat Treatment of Materials, Berlin, Germany*, Vol. 1, pp. 465-486.
83. **Kobasko, N. I.**, [1992], “Intensive Steel Quenching Methods. Theory and Technology of Quenching”, Springer-Verlag, New York, N.Y., pp. 367-389.
84. **Kobasko, N. I.**, [1975], “Method of Overcoming Self-Deformation and Cracking During Quenching of Metal Parts”, *Metallovedenie and Termicheskay Obrabotka Metallov (in Russian)*, Vol. 4 , pp. 12-16.
85. **Kolbus L. M. S**, Payzant E. A. , Cornwell P. A. , Watkins T. R. , Babu S. S. , Dehoff R. R. , Lorenz M. , Ovchinnikova O. ,and Duty C. [2015], “Comparison of Residual Stresses in Inconel 718 Simple Parts Made by Electron Beam Melting and Direct Laser Metal Sintering”, *Metallurgical and Materials Transactions A*, Vol. 46 (3), pp. 1419–1432.
86. **Kristoffersen H.** and Vomacka P., [2001], “Influence of process parameters for induction hardening on residual stresses.” *Materials & Design*, Vol. 22 (8), pp. 637–644.

87. **Kuang H. T.** and Jie M. H., [2013], “Arc Efficiency Assisted Finite Element Model for Predicting Residual Stress of TIG Welded Sheet.”, *Journal of Computers*, Vol. 8(9), pp. 2182-2189.
88. **Labudovic, M.** and Kovacevic, R., [2001] “The Use of Laser/GTAW Combination for Surface Modification of Ti-6Al-4V Alloy.”, *J. Mater. Sci. Technol.*, Vol. 17(2), pp.-237-239.
89. **Lampman S.**, [1991], “Introduction to surface hardening of steels.”, *ASM Handbook-Heat Treat*, Vol. 4, pp. 259–267.
90. **Lee M.K.**, Kim G.H., Kim K.H., Kim W.W., [2006], “Effects of the surface temperature and cooling rate on the residual stresses in a flame hardening of 12Cr steel.”, *Journal of Materials Processing Technology*, Vol. 176 (3), pp. 140–145.
91. **Lee, S. C.** and Ho Weio-Youe, [1989] “The effects of surface hardening on fracture toughness of carburized steel.”, *Metallurgical Transactions A*, Vol. 20 (3), pp. 519-525.
92. **Leggatt, R.H.**, [2008], “Residual stresses in welded structures.”, *Int. J. Press. Vessel. Pip.*, Vol. 85, pp. 144–151.
93. **Leskovšek, V.**, Podgornik, B. and Nolan, D., [2008], “Modelling of residual stress profiles in plasma nitrided tool steel.” *Materials Characterization*, Vol. 59 (4), pp. 454-461.
94. **Lin R.** and Ericsson T., [1992] “Fatigue endurance limit and residual stress of steels surface hardened by rapid heating.”, In: *Proceedings of the 3rd ECRS, Frankfurt/Main, Germany*, 4–6/11, pp 505–514.
95. **Li, P.J.** and Zhang, Y.M., [2001], “Precision Sensing of Arc Length in GTAW Based on Arc Light Spectrum.”, *J. Manuf. Sci. Eng.*, Vol. 123 (1), pp. 62-65.
96. **Liu, Q.**, Yang, C.H., Ding, K., Barter, S.A. and **Ye, L.**, [2007], “The effect of laser power density on the fatigue life of laser-shock-peened 7050 aluminium alloy”, *Fatigue & Fracture of Engineering Materials & Structures*, Vol. 30, pp. 1110-1124.
97. **Lu J.Z.**, Luo K.Y., Dai F.Z., Zhong J.W., Xu L.Z. and Yang C.J., [2012], “Effects of multiple laser shock processing (LSP) impacts on mechanical properties and wear behaviors of AISI 8620 steel.”, *Mater. Sci. Eng. A.*, Vol. 536, pp. 57–63.
98. Mandal, S., Tewary, N.K., Ghosh, S.K., **Chakrabarti, D.** and Chatterjee, S., [2016], “Thermo-mechanically controlled processed ultrahigh strength steel: Microstructure, texture and mechanical properties.”, *Mater. Sci. Eng. A*, Vol. 663, pp. 126–140.

99. **Mangonon, P. L.**, [1976], “Effect of alloying elements on the microstructure and properties of a hot-rolled low-carbon low-alloy bainitic steel.”, *Metallurgical Transactions A*, Vol. 7(9), pp 1389–1400.
100. **Manti, R.** and Dwivedi, D.K., [2007], “Microstructure of Al-Mg-Si weld joints produced by pulse TIG welding.”, *Mater. Manuf. Process.*, Vol. 22, pp. 57–61.
101. Manvatkar, V.D., Gokhale, A.A., Jagan Reddy, G., Venkataramana, A. and **De, A.**, [2011], “Estimation of melt pool dimensions, thermal cycle, and hardness distribution in the laser-engineered net shaping process of austenitic stainless steel.”, *Metall. Mater. Trans. A Phys. Metall. Mater. Sci.*, Vol. 42, pp. 4080–4087.
102. **Matlock, D.K.**, Alogab, K. A. and Richards, M.D., Speer, J.G., [2005], “Surface processing to improve the fatigue resistance of advanced bar steels for automotive applications.”, *Mater. Res.*, Vol. 8, pp. 453–459.
103. **Mazar Atabaki, M.**, Nikodinovski, M., Chenier, P., Ma, J., Liu, W., Kovacevic, R., [2014], “Experimental and numerical investigations of hybrid laser arc welding of aluminum alloys in the thick T-joint configuration.”, *Opt. Laser Technol.*, Vol. 59, pp. 68–92.
104. **Mencík J.**, [2013], “Mechanics of Components with Treated or Coated Surfaces.” Springer Science & Business Media, Vol. 42.
105. **Messler, R. W. Jr.**, [1999], “Principles of welding” *John Wiley and sons*, New York.
106. **Meyers M.A.** and Wittman C.L., 1990, “Effect of metallurgical parameters on shear band formation in low-carbon (~0.20 Wt Pct) steels.”, *Metall. Trans. A*, Vol. 21, pp. 3153–3164.
107. **Ming D. J.** and Yih-fong, T., [2004], “Optimisation of electron-beam surface hardening of cast iron for high wear resistance using the Taguchi method.”, *Int. J. Adv. Manuf. Technol.*, Vol. 24, pp. 190–198.
108. **Mohamadzadeh, H.**, Saghafian, H. and Kheirandish, S., [2009], “ Sliding Wear Behavior of a Grey Cast Iron Surface Remelted by TIG.”, *Mater. Sci. Technol.*, Vol. 25, pp. 622–628.
109. **Mohanty, O.N.**, [1994], “Residual stresses in heat treatment.”, Tata steel, Jamshedpur, <http://eprints.nmlindia.org/5773/1/pp1-9.PDF>.
110. **Mohseni, E.**, Zalnezhad, E., Sarhan, A.A.D. and Bushroa, A.R., [2014], “A Study on surface modification of al7075-t6 alloy against fretting fatigue phenomenon.”, *Adv. Mater. Sci. Eng.*, Vol. 2014, pp. 17.

111. Montross, C.S., Wei, T., **Ye, L.**, Clark, G. and Mai, Y.W., [2002], “Laser shock processing and its effects on microstructure and properties of metal alloys: A review.”, *Int. J. Fatigue* Vol. 24, pp. 1021–1036.
112. **Murphy, A.B.**, Tanaka, M., Yamamoto, K., Tashiro, S., Sato, T. and Lowke, J.J., [2009], “Modelling of thermal plasmas for arc welding: the role of the shielding gas properties and of metal vapour.”, *J. Phys. D. Appl. Phys.*, Vol 42, pp. 20.
113. **Murphy, A. B.**, Tanaka, M., Tashiro, S., Sato, T. and Lowke, J.J., [2009], “A computational investigation of the effectiveness of different shielding gas mixtures for arc welding.”, *J. Phys. D. Appl. Phys.*, Vol. 42, pp. 115-205.
114. **Murphy, A. B.**, Tanaka, M., Yamamoto, K., Tashiro S, Sato, T. and Lowke, J. J. [2009], “Modelling of thermal plasmas for arc welding: the role of the shielding gas properties and of metal vapour.” *Journal of Physics D: Applied Physics*, Vol. 42(19), pp. 20.
115. Murray, J.W., **Clare, A.T.**, [2016], “Morphology and Wear Behaviour of Single and Multi-layer Electrical Discharge Coatings.”, *Procedia CIRP* 42, pp. 236–239.
116. **Nadkarni, S. V.**, [2010], “Modern Arc Welding Technology”, Ador Welding Limited, New Delhi.
117. **Needham, J.C.**, [1965], “Pulse controlled consumable electrode welding arcs”, *British welding Journal*, Vol. 12(4), pp. 191-197.
118. **Nemani ,A.V.**, Sohi, M. H, Amadeh, A. A. and Ghaffari M,[2016], “Liquid-phase surface melting of Ti-6Al-4V.” *Argon and nitrogen atmospheres*, Vol. 2 (1), pp. 115-122.
119. **Nemchinsky, V.A.**, [1997], “Electrode evaporation in an arc with pulsing current”, *Journal of Physics D: Applied Physics*, Vol. 30, pp. 2895–2899.
120. **Nemkov, V.S.** and Goldstein, R.C., A., [2004], “Design Principles for Induction Heating and Hardening Processing.”, *Handbook of Metallurgical process design*, pp. 591-640.
121. **Nguyen N.T.**, Matsuoka Ohta, K., and Maeda Y., “Analytical Solutions for Transient Temperature of Semi-Infinite Body Subjected to 3-D Moving Heat Sources.”, *Weld. Res. Suppl. I*, pp. 265–274.
122. **Norman, A.F.**, Drazhner, V. and Prangnell, P.B., [1999], “Effect of welding parameters on the solidification microstructure of autogenous TIG welds in an Al–Cu–Mg–Mn alloy.”, *Mater. Sci. Eng. A*, Vol. 259, pp. 53–64.

123. **Orlowicz, A.U.W.**, Trytek, A., [2005], “Use of the GTAW method for surface hardening of cast-iron.”, *Weld. Int.*, Vol. 19, pp. 341–348.
124. **Ormanova M.**, Petrov P and Kovacheva D., [2017], “Electron beam surface treatment of tool steels.”, *Vacuum*, Vol. **135**, pp. 7-12.
125. **Pal, K.** and Pal, S.K., [2011], “Effect of pulse parameters on weld quality in pulsed gas metal arc welding: A review.”, *J. Mater. Eng. Perform.*, Vol. 20, pp. 918–931.
126. Pashby, I. R., **Barnes, S.** and Bryden, B. G., [2003], “Surface hardening of steel using a high power diode laser.”, *Journal of Materials Processing Technology*, Vol. 139, pp. 585-588.
127. **Picraux, S.T.** and L.E. Pope, [1984], “Tailored surface modification by ion implantation and laser treatment.”, *Science*, Vol. 226, pp. 615-622.
128. **Phillips, I.T.S.**, Costa, K.D., I, R., Chambers and T. V, Hill, R., [1994], “Pulse welding process.” United States Patent No. US4273988 A.
129. Prakash G. G., Pramod S. L., Chandran Prathap, Zhang Cheng, Agarwal Arvind, Fabijanic Daniel, and **Bakshi Srinivasa Rao.**, [2013], “Microstructure and wear properties of Ni-Cu-Cr-Al multi-component coatings prepared by plasma spraying”, **TMS Annual Meeting and Exhibition**, San Antonio, USA
130. **Praveen, P.**, Yarlagadda, P.K.D.V. and Kang, M.J., [2005], “Advancements in pulse gas metal arc welding”, *Journal of Materials Processing Technology*, Vol. 164–165, pp. 1113–1119.
131. **Przybylowicz, K.**, [1999], “Advantages and limitations of steel boronizing process.”, *Inzynieria Materialowa*, Vol. 20(5), pp. 251-254.
132. **Qi, B.J.**, Yang, M.X., Cong, B.Q. and Liu, F.J., [2013], “The effect of arc behavior on weld geometry by high-frequency pulse GTAW process with 0Cr18Ni9Ti stainless steel.”, *Int. J. Adv. Manuf. Technol.*, Vol. 66, pp. 1545–1553.
133. **Quintino, L.** and Allum, C.J., [1984], “Pulsed GMAW: Interactions between process parameters, Part I”, *Welding and Metal Fabrication*, Vol. 16(4), pp. 126-129.
134. **Rajasekaran, S.**, Kulkarni, S.D., Mallya, U.D. and Chaturvedi, R.C., [1998], “Droplet detachment and plate fusion characteristics in pulsed current gas metal arc welding”, *Welding Journal*, Vol. 6, pp. 254s-268s.
135. Rajeev G.P., Kamaraj M., and **Srinivasa R. Bakshi.**, [2014] “Comparison of Stellite Coatings on Valve Steel Material Prepared by Plasma Transferred Arc and Cold Metal Transfer Techniques.” **2014 TMS Annual Meeting and Exhibition**, San Diego, USA.

136. **Randhawa, H.S.**, Ghosh., P.K., and Gupta, S.R., [2000], “Some basic aspects of geometrical characteristics of pulsed current vertical-up GMA weld”, *ISIJ International*, Vol. 40 (1), pp. 71-76.
137. **Randhawa, H.S.**, Ghosh., P.K., and S.R. Gupta, [1998], “Geometric characteristics of pulsed current positional GMA weld”, *ISIJ Int.*, Vol. 38(4), pp. 276-284.
138. Ray, A., Arora, K.S., Lester, S., **Shome, M.**, [2014], “Laser cladding of continuous caster lateral rolls: Microstructure, wear and corrosion characterisation and on-field performance evaluation.”, *J. Mater. Process. Technol.*, Vol. 214, pp. 1566–1575.
139. **Razzak, M.A.**, [2012], “Heat treatment and effects of Cr and Ni in low alloy steel.”, *Mater. Sci.*, Vol. 34, pp. 1439–1445.
140. **Reddy G. M.**, Gokhale A. A. and Rao, K.P., [2013], “Optimisation of pulse frequency in pulsed current gas tungsten arc welding of aluminium–lithium alloy sheets.”, *Materials Science and Technology*, Vol. 14(1), pp. 61-66.
141. Reich, M., Osten, J., Milkereit, B., Kalich, J., **Füssel, U.** and Kessler, O., [2014], “Short-time heat treatment of press hardened steel for laser assisted clinching.” *Mater. Sci. Technol.*, Vol. 30, pp. 1287–1296.
142. **Renk T.J.**, Provencio P.P., Prasad S.V., Shlapakovski A.S., Petrov A.V., Yatsui K., Jiang W and Suematsu H., [2004], “Materials modification using intense ion beams.”, *Proceedings of the IEEE*, Vol. 92(7), pp. 1057-1081.
143. **Richard L. L.**, [1973], “Welding and Welding Technology”, McGraw Hill, 1st edition, Newyork.
144. **Rosenthal, D.**, [1941], “Mathematical theory of heat distribution during welding and cutting.” *Welding Res. Suppl.*, pp. 220s-234s.
145. **Rotshtein, V.P.**, Proskurovsky, D.I., Ozur, G.E., Ivanov, Y.F. and Markov, A.B., [2004], “Surface modification and alloying of metallic materials with low-energy high-current electron beams.”, *Surface and Coatings Technology* , Vol. 180-181, pp. 377-381.
146. **Rowan, O.K.**, Sisson, R.D., [2009], “Effect of Alloy Composition on Carburizing Performance of Steel.”, *J. Phase Equilibria Diffus.*, Vol 30, pp. 235–241.
147. Samanta, S., Das, S., **Chakrabarti, D.**, Samajdar, I., Singh, S.B. and Haldar, A., [2013], “Development of multiphase microstructure with bainite, martensite, and retained austenite in a Co-containing steel through quenching and partitioning (Q&P) treatment.”, *Metall. Mater. Trans. A, Phys. Metall. Mater. Sci.*, Vol. 44, pp. 5653–5664.

148. **Saedi, H.R.** and Unkel, W., [1988], “Arc and Weld Pool Behavior for Pulsed Current GTAW.”, *Weld. Res. Suppl.*, pp. 247s-255s.
149. **Sakai T.**, Morita Y., Iwao T. and Yumoto M., [2010], “Heat transfer and heat efficiency of pulsed arc as a function of current frequency.”, *IEEE International Conference on Plasma Science*.
150. Sandip, P. H., **Srinivasa R. Bakshi** and Arvind Agarwal, [2013], “Recent Developments in Surface Engineering of Materials.”, *JOM*, Vol. 65, pp. 739-740.
151. Schnick M, **Fuessel U.**, Hertel M, Haessler M, Kohoff A S and Murphy A. B. [2010], “Modelling of gas–metal arc welding taking into account metal vapour” *J. Phys. D: Appl. Phys.*, Vol. 43, pp 11.
152. Schnick, M., Rose, S., **Füssel, U.**, Mahrle, A., Demuth, C. and Beyer, E., [2012], “Experimental and Numerical Investigations of the Interaction between a Plasma Arc And a Laser.”, *Weld. World*, Vol. 56, pp. 93-100.
153. **Schöpfel A.** and Störzel. K., [1997], “Optimization of process parameters for induction heat treating by means of numerical simulation.”, In: *Proceedings of the 17th ASM Heat Treating Society Conference including the 1st International Heat Treating Symposium, Indianapolis*, pp. 595–600.
154. Shariff S. M., **Pal, T. K.**, Padmanabham and G., Joshi, [2010], “ Sliding wear behaviour of laser surface modified pearlitic rail steel.”, *Surface Engg.*, Vol. 26, pp.199-208.
155. **Shiple, R.J.** and Moore, D.A., [2002], “ASM Handbook-Analysis of Distortion and Deformation.” Vol. 11, pp. 1047–1058.
156. **Shirali, A.A.** and Mills, K.C., [1993], “The effect of Welding Parameters on Penetration in GTA Welds.”, *Weld. J.*, pp. 347s–353s.
157. Singh, A., **Srinivasa R. B.**, Agarwal A. and Sandip P. Harimkar, [2010], “Microstructure and Tribological Behavior of Spark Plasma Sintered Iron-based Amorphous Coatings”, *Materials Science and Engineering A*, Vol. 527, pp. 5000-5007.
158. **Singh J**, [1995], in: Y. Pauleau (Eds.), “Materials and Processes for Surface and Interface Engineering”, E-Publishing, Inc. France., pp. 347–406.
159. **Shome, M.**, [2007], “Effect of heat-input on austenite grain size in the heat-affected zone of HSLA-100 steel.”, *Mater. Sci. Eng. A*, Vol. 445-446, pp.454–460.
160. **Shome, M.** and Mohanty, O.N., [2006], “Continuous cooling transformation diagrams applicable to the heat-affected zone of HSLA-80 and HSLA-100 steels.”, *Metall. Mater. Trans. A*, Vol. 37, pp. 2159–2169.

161. **Shome, M.**, Gupta, O.P. and Mohanty, O.N., [2004], “A modified analytical approach for modelling grain growth in the coarse grain HAZ of HSLA steels.”, *Scr. Mater.*, Vol. 50, pp. 1007–1010.
162. **Shome, M.**, Gupta and Mohanty, O.N., [2004], “Effect of simulated thermal cycles on the microstructure of the heat-affected zone in HSLA-80 and HSLA-100 steel plates.” *Metall. Mater. Trans. A.*, Vol. 35, pp. 985–996.
163. Speidel, A., Lutey, A.H.A., Mitchell-Smith, J., Rance, G.A., Liverani, E., Ascari, A., Fortunato, A., **Clare, A.**, [2016], “Surface modification of mild steel using a combination of laser and electrochemical processes.”, *Surf. Coatings Technol.*, Vol. 307, pp. 849–860.
164. **Stava, E. K.**, [1990], “Method and apparatus for TIG welding.”, U.S. Patent No. 4,947,021.
165. **Stephan, E.**, Johannes, Z., Roland, B., Roland, N., Gerhard, P and Bernd, R., [2015], “Advanced Gas Tungsten Arc Weld Surfacing Current Status and Application.”, *Soldag. Inspeção*, Vol. 20(3), pp. 300–314.
166. **Stott, F.H.**, Wood, G.C. and Stringer, J., [1995], “The influence of alloying elements on the development and maintenance of protective scales.”, *Oxid. Met.*, Vol. 44, pp. 113–145.
167. **Suresh, M.V.**, Vamsi Krishna, B., Venugopal, P. and Prasad R. K., [2004], “Effect of pulse frequency in gas tungsten arc welding of powder metallurgical preforms.”, *Sci. Technol. Weld. Join.*, Vol. 9, pp. 362–368.
168. **Tadamalle A.P.**, Ramjee E. and Reddy K. V, [2014], “Estimation of Weld Pool Geometry and Cooling Rate in Laser Welding”, All India Manufacturing Technology, Design and Research Conference, pp. 1–7.
169. **Terent, V.F.**, Michugina M.S., Kolmakov A.G., Kvedaras V., Čiuplys V., Čiuplys A. and Vilys J., [2007], “The effect of nitriding on fatigue strength of structural alloys.” *Mechanika*, Vol. 2(64), ISSN 1392 - 1207.
170. **Tewary N.K.**, Syed B., Ghosh S.K., Kundu S., Shariff S.M. and Padmanabham G., [2014], “Microstructural evolution and mechanical behaviour of surface hardened low carbon hot rolled steel.”, *Mater. Sci. Eng. A.*, Vol. 606, pp. 58–67.
171. **Thompson, S. W.**, Vin Col, D. J., Krauss, G., [1990], “Continuous cooling transformations and microstructures in a low-carbon, high-strength low-alloy plate steel” *Metallurgical Transactions A*, Vol. 21 (6), pp. 1493–1507.

172. **Tong, Z.**, Zhentai, Z. and Rui, Z., [2013], “A dynamic welding heat source model in pulsed current gas tungsten arc welding.”, *J. Mater. Process. Technol.*, Vol. 213, pp. 2329–2338.
173. **Totten, G. E.**, [2002], “Handbook of Residual Stress and Deformation of Steel.”, ASM International, Ohio, USA
174. **Totten, G. E.** and Liang, H., [2005], “Surface modification and mechanism : Friction, stress and reaction engineering.” Marcel Dekker, Inc, New York.
175. **Traidia A.** and Roger F. [2011], “Numerical and experimental study of arc and weld pool behaviour for pulsed current GTA welding.”, *International Journal of Heat and Mass Transfer*, Vol. 54, pp. 2163–2179.
176. **Traidia, A.**, Roger, F. and Guyot, E., [2010], “Optimal parameters for pulsed gas tungsten arc welding in partially and fully penetrated weld pools.”, *Int. J. Therm. Sci.*, Vol. 49, pp. 1197–1208.
177. **Tsai, C.L.** and Hou, C.A., [2013], “Theoretical Analysis of Weld Pool Behavior in the Pulsed Current GTAW Process.”, *J. Heat Transfer*, Vol. 110, pp. 160–165.
178. **Tseng, K.H.** and Chou, C.P., [2001], “Effect of pulsed gas tungsten arc welding on angular distortion in austenitic stainless steel weldments.” *Science and Technology of Welding and Joining*, Vol. 6(3), pp. 149-153.
179. **Uzlov, I. G.** and Danchenko, N. I. [1971] “Effect of cooling rate during quenching on the properties of carbon steel”, *Metal Science and Heat Treatment*, Vol.13(5), pp 407–409.
180. **Venkatramani, N.**, [2002], “Industrial plasma torches and applications.”, *Curr. Sci.*, Vol. 83, pp. 254–262.
181. **Voort, G. F. V.** and Lucas, G.M., [2009], “Microstructural characterization of carburized steels.” *Heat Treat. Prog.*, pp. 37–42.
182. Walker, J.C., Cook, R.B., Murray, J.W., **Clare, A.T.**, [2013], “Pulsed electron beam surface melting of CoCrMo alloy for biomedical applications.”, *Wear*, Vol. 301, pp. 250–256.
183. Walker, J.C., Murray, J.W., Nie, M., Cook, R.B., **Clare, A.T.**, [2014], “The effect of large-area pulsed electron beam melting on the corrosion and microstructure of a Ti6Al4V alloy.”, *Appl. Surf. Sci.*, Vol. 311, pp. 534–540.
184. **Wang, L.**, Wood, R.J.K. and Sun, J., [2008], “Unlubricated metal on metal sliding contact and its acoustic emission signatures.”, 3rd World Congress on Engineering

- Asset Management and Intelligent Maintenance Systems Conference, Springer11, pp. 1614-1624.
185. **Wavare S. B.** and. Ramgir M. S, [2015], Magnetic Arc Blow in Arc Welding Affects Weld Bead Parameters, *J. Mat. Sci. Mech. Engg.*, Vol. 2, pp. 38-40.
186. Yang, C.H., Hodgson, P.D., Liu, Q.C. and **Ye, L.**, [2008], “Geometrical effects on residual stresses in 7050-T7451 aluminum alloy rods subject to laser shock peening”, *Journal of Materials Processing Technology*, Vol. 201(1-3), pp. 303-309.
187. **Yang, M.**, Qi, B., Cong, B., Liu, F., Yang, Z., [2013], “Effect of pulse frequency on microstructure and properties of Ti-6Al-4V by ultrahigh-frequency pulse gas tungsten arc welding.”, *Int. J. Adv. Manuf. Technol.*, Vol. 68, pp. 19–31.
188. **Yasumoto, K.**, Nagamichi, T, Yasuhiro, Maehara, Y. and Gunj, K, [1987], “Effects of alloying elements and cooling rate on austenite grain growth in solidification and the subsequent cooling processes of low alloy steels.” *I.S.I.J*, Vol. 73(14), pp. 1738-1745.
189. Yip, M. W., **Barnes, S.** and Sarhan, A., [2014], “Effects of laser cladding of silicon carbides particles and iron based powder.”, *Applied Mechanics and Materials*, Vol. 548-549, pp. 289-293.
190. Yip, M W, **Barnes, S.**, [2013], “CO₂ laser cladding of mild steel using iron based powder and silicon carbide particles.”, 4th International Conference on Material and Manufacturing Technology (ICMMT 2013), Seoul, Korea, 11-12 May 2013, Published in *Advanced Materials Research: Material and Manufacturing Technology IV*, pp. 269-272.
191. Yip, M. W., **Barnes, S.** and Sarhan, A., [2014], “Effects of laser cladding of silicon carbides particles and iron based powder.”, 3rd International Conference on Informatics, Environment, Energy and Applications (IEEA 2014), Shanghai, China.
192. **Yousefieh, M.**, Shamanian, M. and Saatchi, A., [2011], “Influence of Heat Input in Pulsed Current GTAW Process on Microstructure and Corrosion Resistance of Duplex Stainless Steel Welds.”, *J. Iron Steel Res. Int.*, Vol. 18, pp. 65–69.
193. Zähr, J., **Füssel, U.**, Hertel, M., Lohse, M., Sende, M. and Schnick, M., [2012], “Numerical and Experimental Studies of the Influence of Process Gases in Tig Welding Numerical and Experimental Studies of the Influence of Process Gases in Tig Welding.”, *Weld. World*, Vol. 56, pp. 85–92.

LIST OF PUBLICATIONS

1. P.K.Ghosh and **Ravindra Kumar**, “Surface Modification of Micro-Alloyed High-Strength Low-Alloy Steel by Controlled TIG Arcing Process”, Metallurgical and Materials Transactions A, 46 (2015), pp. 831–842
2. **Ravindra Kumar**, P.K.Ghosh and Sudhir Kumar, “Thermal and metallurgical characteristics of surface modification of AISI 8620 steel produced by TIG arcing process”, Journal of Materials Processing Technology, 240 (2017), pp. 420–431

